

WL-TR-95-2068

ADVANCED DEMONSTRATION OF FUEL INJECTOR/  
FLAMEHOLDER FOR HIGH SPEED RAMBURNERS

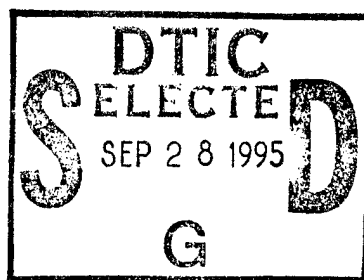


S. ALAN SPRING  
CLIFFORD E. SMITH  
ANDY D. LEONARD

CFD RESEARCH CORPORATION  
3325 TRIANA BLVD  
HUNTSVILLE AL 35805

MAY 1995

FINAL REPORT



APPROVED FOR PUBLIC RELEASE; DISTRIBUTION IS UNLIMITED.

19950926 138

AEROPROPULSION AND POWER DIRECTORATE  
WRIGHT LABORATORY  
AIR FORCE MATERIEL COMMAND  
WRIGHT PATTERSON AFB OH 45433-7251


DTIC QUALITY INSPECTED 8

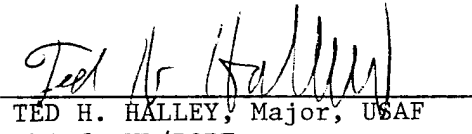
# NOTICE


When Government drawings, specifications, or other data are used for any purpose other than in connection with a definitely Government-related procurement, the United States Government incurs no responsibility or any obligation whatsoever. The fact that the government may have formulated or in any way supplied the said drawings, specifications, or other data, is not to be regarded by implication, or otherwise in any manner construed, as licensing the holder, or any other person or corporation; or as conveying any rights or permission to manufacture, use, or sell any patented invention that may in any way be related thereto.

This report is releasable to the National Technical Information Service (NTIS). At NTIS, it will be available to the general public, including foreign nations.

This technical report has been reviewed and is approved for publication.

  
CHARBEL N. RAFFOUL  
Program Monitor  
Experimental Research Branch  
Advanced Propulsion Division

  
TED H. HALLEY, Major, USAF  
Chief, WL/POPT  
Experimental Research Branch  
Advanced Propulsion Division

  
WILLIAM C. BURSON, Ph.D.  
Acting Chief, WL/POP  
Advanced Propulsion Division

Accession For	
NTIS CRA&I	<input checked="checked" type="checkbox"/>
DTIC TAB	<input type="checkbox"/>
Unannounced	<input type="checkbox"/>
Justification	
By	
Distribution /	
Availability Codes	
Dist	Avail and/or Special
A-1	

If your address has changed, if you wish to be removed from our mailing list, or if the addressee is no longer employed by your organization please notify WL/POP, WPAFB, OH 45433-7251 to help us maintain a current mailing list.

Copies of this report should not be returned unless return is required by security considerations, contractual obligations, or notice on a specific document.

# REPORT DOCUMENTATION PAGE

Form Approved  
OMB No. 0704-0188

Public reporting burden for this collection of information is estimated to average 1 hour per response, including the time for reviewing instructions, searching existing data sources, gathering and maintaining the data needed, and completing and reviewing the collection of information. Send comments regarding this burden estimate or any other aspect of this collection of information, including suggestions for reducing this burden, to Washington Headquarters Services, Directorate for Information Operations and Reports, 1215 Jefferson Davis Highway, Suite 1204, Arlington, VA 22202-4302, and to the Office of Management and Budget, Paperwork Reduction Project (0704-0188), Washington, DC 20503.

1. AGENCY USE ONLY (Leave blank)		2. REPORT DATE MAY 1995		3. REPORT TYPE AND DATES COVERED FINAL	
4. TITLE AND SUBTITLE ADVANCED DEMONSTRATION OF FUEL INJECTOR/FLAMEHOLDER FOR HIGH SPEED RAMBURNERS				5. FUNDING NUMBERS C F33615-92-C-2288 PE 65502 PR 3005 TA 02 WU 0Y	
6. AUTHOR(S) ALAN SPRING CLIFFORD E. SMITH ANDY D. LEONARD					
7. PERFORMING ORGANIZATION NAME(S) AND ADDRESS(ES) CFD RESEARCH CORPORATION 3325 TRIANA BLVD. HUNTSVILLE AL 35805				8. PERFORMING ORGANIZATION REPORT NUMBER	
9. SPONSORING/MONITORING AGENCY NAME(S) AND ADDRESS(ES) AEROPROPULSION AND POWER DIRECTORATE WRIGHT LABORATORY AIR FORCE MATERIEL COMMAND WRIGHT PATTERSON AFB OH 45433-7251				10. SPONSORING/MONITORING AGENCY REPORT NUMBER WL-TR-95-2068	
11. SUPPLEMENTARY NOTES  Technical Monitor - Dr. A. S.Nejad (WL/POPT, WPAFB OH 45433-7251)					
12a. DISTRIBUTION/AVAILABILITY STATEMENT APPROVED FOR PUBLIC RELEASE; DISTRIBUTION IS UNLIMITED.				12b. DISTRIBUTION CODE	
13. ABSTRACT (Maximum 200 words) The combustion efficiency of ramburner technology is mixing-limited. Therefore, significant gains are possible if the fuel-air mixing can be increased without a significant increase in pressure loss or a decrease in flame stability. Several design concepts were explored in this report that increase the fuel-air mixing by generating large axial vortices downstream of the flameholder. The baseline flameholder for this project was the Integral Fuel Injector/Flameholder (IFF) used in previous studies by United Technologies Research Center (UTRC). CFD solutions were completed on the baseline design and 28 advanced configurations. Most designs did improve fuel-air mixing, but also increased the cold pressure loss by several fold. The most promising designs used the momentum of the fuel to contribute to the axial thrust, thereby reducing the pressure loss.  Isothermal experimental tests were conducted at Wright Laboratory in parallel with CFD analysis. A complete data set was taken for one baseline model, while several advanced models were screened for pressure loss. The baseline tests showed that a regular pattern of alternating vortices were shed from the base of the flameholder. Simultaneous three-component laser Doppler velocimeter (LDV) measurements were taken, providing mean velocities and Reynolds stresses at various axial locations downstream of the flameholder. The CFD analysis consisted of 2-D and 3-D time-accurate simulations, with various turbulence models including standard k-ε model, RNG k-ε model, and full Reynolds stress model. The analysis showed that the 3-D effects from the presence of the walls were significant. 3-D time accurate calculations with the RNG k-ε turbulence model were necessary to accurately predict the isothermal flowfield. Good overall agreement was shown between CFD analysis and measurements.					
14. SUBJECT TERMS flameholder, fuel-air mixing, ramburner, CFD, LDV measurements, turbulence modeling				15. NUMBER OF PAGES 202 X	
				16. PRICE CODE	
17. SECURITY CLASSIFICATION OF REPORT UNCLASSIFIED	18. SECURITY CLASSIFICATION OF THIS PAGE UNCLASSIFIED	19. SECURITY CLASSIFICATION OF ABSTRACT UNCLASSIFIED	20. LIMITATION OF ABSTRACT SAR		

# TABLE OF CONTENTS

	<u>Page</u>
PREFACE	viii
NOMENCLATURE	ix
EXECUTIVE SUMMARY	1
1.0 INTRODUCTION	3
1.1 Background	3
1.2 Flameholder Theory	4
1.3 Improved Concepts	7
2.0 TECHNICAL OBJECTIVES AND APPROACH	10
3.0 ISOTHERMAL BASELINE EXPERIMENTAL TESTS	11
3.1 Overview	11
3.2 Test Facility	11
3.3 Model Definition	13
3.4 Inlet Conditions	14
3.5 LDV Hardware	14
3.5.1 Far-Field Transmitting Optics	14
3.5.2 Near-Field Transmitting Optics	14
3.5.3 LDV Receiving Optics	16
3.5.4 Data Acquisition and Postprocessing	16
3.5.5 LDV Seed Selection	18
3.6 Experimental Results - Baseline IFF	19
3.6.1 One-Component Far Field Data	19
3.6.2 Three-Component Far Field Data	22
3.6.3 Three-Component Near Field Data	31
4.0 ISOTHERMAL NUMERICAL INVESTIGATION OF BASELINE IFF CONFIGURATION	47
4.1 CFD Code	47
4.2 Computer	48
4.3 Geometry and Grid	48
4.4 Numerical Technique	51
4.5 Numerical Results	54



5.0	ADVANCED MODEL NUMERICAL TESTS	75
5.1	Computational Method	75
5.2	Inlet Conditions	76
5.3	Advanced Flameholder Models	77
5.3.1	Baseline Model	77
5.3.2	Advanced Model ADV2	79
5.3.3	Advanced Model ADV3	92
5.3.4	Advanced Model ADV4	96
5.3.5	Advanced Model ADV5	96
5.3.6	Advanced Model 6	102
5.3.7	Advanced Model 7	105
5.3.8	Advanced Model 8	106
5.4	Discussion	106
6.0	ISOTHERMAL EXPERIMENTAL TESTS: ADVANCED MODELS	109
6.1	Test Results	109
6.2	Pressure Losses	112
7.0	EXPERIMENTAL COMBUSTION TESTS	113
7.1	Test Section Design	113
7.2	Transition Section Design	115
7.3	Choke Block Design	116
7.4	Baseline Model Design	117
7.5	Miscellaneous Information	117
7.6	Test Cancellation	119
8.0	NUMERICAL COMBUSTION TESTS	120
8.1	Experimental Data Set	120
8.2	Numerical Details	121
8.3	Numerical Results	122
9.0	CONCLUSIONS	133
10.0	REFERENCES	134
APPENDIX A. A NUMERICAL METHOD FOR THE SECOND-MOMENT TURBULENCE CLOSURE WITH APPLICATIONS		A-1
A.1	INTRODUCTION	A-2
A.2	GOVERNING EQUATIONS	A-3
A.3	NUMERICAL METHOD	A-5
A.3.1	Discretization	A-5
A.3.2	Evaluation of the Cell Face Stresses	A-7
A.3.3	Boundary Conditions	A-9

A.4	APPLICATIONS	A-11
A.4.1	Backward-Facing Step Flow	A-11
A.4.2	An Axisymmetric Faired Diffuser Flow	A-13
A.4.3	Confined Swirling Flow	A-17
A.5	CONCLUSIONS	A-28
APPENDIX B.	LASER DOPPLER VELOCIMETRY	B-1
B.1	LDV THEORY	B-2
B.2	STATISTICAL ANALYSES	B-5
APPENDIX C.	FORTRAN LISTING FOR LDV DATA REDUCTION	C-1

## LIST OF FIGURES

<u>Figure</u>	<u>Page</u>
1. Schematic of IFF Concept	4
2. Elliptical - Gutter Flameholder Tested by Williams et al.	6
3. Axial Vorticity Mechanism of Increased Fuel-Air Mixing	8
4. Concepts Numerically Tested in Phase I	9
5. Experimental Model Design	13
6. Near-Field Optical Set-Up for 3-D LDV System	15
8. Normalized rms Axial Turbulent Velocity Profiles at Far Field Stations; 1-D LDV	21
9. Frequency Spectra Upstream and Downstream of IFF Shows Vortex Shedding Frequency	23
10. Comparison Between 1-D and 3-D LDV Measurements Shows Good Agreement	24
11. Normalized Mean Axial Velocity Profiles at Far Field Stations; 3-D LDV	25
12. Normalized rms Axial Turbulent Velocity Profiles at Far Field Stations; 3-D LDV	26
13. Normalized Mean Transverse Velocity Profiles at Far Field Stations; 3-D LDV	27
14. Normalized rms Transverse Turbulent Velocity Profiles at Far Field stations; 3-D LDV	28
15. Normalized Mean Spanwise Velocity Profiles at Far field Stations; 3-D LDFV	29
16. Normalized rms Spanwise Turbulent Velocity Profiles at Far Field Stations; 3-D LDV	30
17. Bimodal PDF Occurs at Centerline Position for Transverse Components	32
18. Normalized Mean Axial Velocity Profiles at Near Field Stations; 3-D LDV	33
19. Normalized Mean Transverse Velocity Profiles at Near Field Stations; 3-D LDV	34
20. Normalized Mean Spanwise Velocity Profiles at Near Field Stations; 3-D LDV	35
21. Normalized uu turbulent Stress Distributions at Near Field Stations	36
22. Normalized vv Turbulent Stress Distributions at Near Field Stations	37
23. Normalized ww Turbulent Stress Distributions at Near Field Stations	38
24. Normalized uv Trubulent Stress Distributions at Near Field Stations	39
25. Normalized uw Trubulent Stress Distributions at Near Field Stations	40
26. Normalized vw Turbuulent Stress Distributions at Near Field Stations	41
27. Axial Mean Normal Stresses - Isotropy Check (Isotropic $uu/k = 2/3$ )	42
28. Transverse Mean Normal Stresses-Isotropy Check (Isotropic $vv/k = 2/3$ )	43
29. Spanwise Mean Normal Stresses - Isotropy Check (Isotropic $ww/k = 2/3$ )	44
30. Normalized Mean Spanwise Velocity profiles Indicate Presence of Vortex Flow; 1-D LDV	46
31. Baseline IFF Model used for Current Study	49

32.	Computational Grid used for Numerical Study of Baseline IFF	50
33.	Normalized Mean Axial Velocity and Velocity Gradient Distributions	55
34.	Normalized Mean Transverse Velocity and Velocity Gradient Distributions	56
35.	Normalized uu Turbulent Stress and Stress Gradient Distributions	57
36.	Normalized vv Turbulent Stress and Stress Gradient Distributions	58
37.	Normalized uv Turbulent Stress and Stress Gradient Distributions	59
38.	Streamlines Show Unsteady Vortex Motion Behind Example Bluff Body	60
39.	Normalized Mean Axial Velocity and Velocity Gradient Distributions	62
40.	Normalized Mean Transverse Velocity and Velocity Gradient Distributions	63
42.	Normalized vv Turbulent Stress and Stress Gradient Distributions	65
44.	Coarse Grid used for 3-D Unsteady Analysis	68
45.	Normalized Mean Axial Velocity and Velocity Gradient Distributions	70
46.	Normalized Mean Transverse Velocity and Velocity Gradient Distributions	71
47.	Normalized uv Turbulent Stress and Stress Gradient Distributions	72
48.	Normalized uu Turbulent Stress and Stress Gradient Distributions	73
49.	Normalized vv Turbulent Stress and Stress Gradient Distributions	74
50.	Computational Grid used for Baseline Performance Analysis	78
51.	3-D Model of ADV2 $\alpha$ 0, and Definition of $\alpha, \beta$	80
52.	3-D Model of ADV2 $\alpha$ 10	81
53.	3-D Model of ADV2 $\alpha$ 20	81
54.	3-D Model of ADV2 $\alpha$ 30	81
55.	Combustion Efficiency for ADV2 $\alpha$ Models Shows $\alpha$ 20 gives Superior Performance	82
56.	Large Scale Axial Vortices Enhance Fuel-Air Mixing; ADV2 $\alpha$ 20	83
57.	Strong Fuel Core Forms Above Ramp; ADV2 $\alpha$ 20	85
58.	3-D Model of ADV2 $\beta$ 20	86
59.	3-D Model of ADV2 $\beta$ -20	86
60.	Combustion Efficiency for ADV2 $\beta$ Models	87
61.	Model JETMOD Reduces Presence of Fuel Core	88
62.	Model JETMOD does not Improve Combustion Efficiency	89
63a.	Pressure Loss for All Models Analyzed	91
63b.	Pressure Loss for all Models Analysed	92
64.	Parametric Study on Ramp Angle, by Varying Tail Length	93
65.	3-D Model of ADV3	94
66.	Combustion Efficiency for ADV3 Models	95
67.	3-D Model of ADV3 Extended	97
68.	3-D Model of ADV4	97
69.	ADV4 with Fuel Injected Near Trailing Edge	98
70.	Combustion Efficiency for ADV4 Models	99
71.	3-D Model of ADV5	100
72.	Velocity Vectors from 2-D Analysis of ADV5 Show Attached Flow	101

73.	Combustion Efficiency for ADV5 Models	103
74.	3-D Model of ADV6 with Velocity Vectors Downstream of Flameholder	104
75.	2-D and 3-D Models of ADV7	105
76.	Schematic of ADV8	106
77.	Velocity Fields for ADV8 Model, with Two Fuel Injection Angles	107
78.	Advanced Model ADV2, as Tested with Three Ramps	110
79.	ADV7 Models as Tested	111
80.	Schematic of Combustion Test Section	114
81.	Schematic of IFF Mounting System for Combustion Tests	118
82.	A Schematic Drawing of the Validation Rig	120
83.	Grid for Reacting-Flow Case Modeling Sjunnesson Experiment	123
84.	Pressure History at Centerline, $x/11 = 1$ , Demonstrates Acoustic Pressure Waves in Tunnel	124
85.	Sequence of Flame Shapes for Triangular Flameholder with $\phi = 0.61$ ; Color Denotes Temperature (Blue = 288 K, Red = 1710 K)	125
86.	Instantaneous Velocity Vectors and Temperature Contours for the Flat Plate Flameholder with $\phi = 0.61$	129
87.	Time Histories of Pressure and Temperature Behind the Flat Plate Flameholder ( $\phi = 0.61$ )	129
88.	Instantaneous Velocity Vectors and Temperature Contours for Flat Plate Flameholder with $\phi = 0.55$	130
89.	Instantaneous Velocity Vectors and Temperature Contours for Triangular Flameholder with $\phi = 0.55$	130
90.	Pressure History Behind Triangular Flameholder with $\phi = 0.55$	131
A-2.	The Comparison of the Mean Streamwise Velocity	A-12
A-3.	The Calculated Streamlines -Top: the second-moment closure Bottom: the k- $\epsilon$ model	A-13
A-4.	The Comparison of the Turbulent Normal Stress Component	A-14
A-5.	The Comparison of the Turbulent Shear Stress Component	A-14
A-6.	The Geometry of the Axisymmetric Faired Diffuser	A-14
A-7.	The Comparison of the Mean Streamwise Velocity	A-16
A-8.	The Comparison of the Turbulent Shear Stress Component	A-17
A-10.	Sensitivity of the Computed Solution to the Inlet $\epsilon$	A-20
A-11.	Sensitivity of the Computed Solution to the Grid	A-21
A-12.	The Calculated Streamline Plots	A-23
A-13.	Radial Variation of the Mean Axial Velocity at Four Axial Locations	A-25
A-14.	Radial Variation of the Mean Swirl Velocity at Five Axial Locations	A-26
A-15.	Radial Variation of the Turbulent Kinetic Energy at Four Axial Locations	A-27
B-1.	Typical Dual Beam Laser Doppler Anemometer	B- 2
B-2.	Frequency Shifting Allows the Measurement of Negative Velocities	B- 4
C-1.	Definition of Correction Angles ( $\theta_g$ , $\theta_b$ )	C- 3
C-2.	Definition of Rotation Angle ( $\delta$ )	C-3
C-3.	Definition of Tilt Angle ( $\epsilon$ )	C-4

## PREFACE

This report is the Phase II Small Business Innovative Research (SBIR) Final Report under U.S. Air Force Contract No. F33615-92-C-2288. The goals of the project were to improve ramburner fuel-air mixing and combustion efficiency through the innovative design of the fuel injection/flameholding system, and to improve upon current CFD techniques for designing combustion systems by providing a detailed, high quality database for code validation. The project consisted of five major parts:

- 1) a numerical investigation of the baseline Integral Fuel injection/Flameholder (IFF) design, and advanced designs;
- 2) isothermal experimental tests of the baseline IFF design, and selected advanced designs;
- 3) numerical combustion tests of the baseline IFF design, and selected advanced designs;
- 4) design and fabrication of experimental hardware for combustion tests; and
- 5) numerical reacting analysis of an existing benchmark experiment.

Mr. Clifford E. Smith was the program manager and Mr. S. Alan Spring was the principal investigator and project engineer for CFD Research Corporation (CFDRC). The U.S. Air Force technical contract monitor was initially Ms. Lourdes Maurice, and later Dr. Abdi Nejad. For the experimental tests, the U.S. Air Force project engineer was Mr. Charbel Raffoul and Mr. Kevin Kirkendall of CFDRC helped in taking the measurements. Valuable assistance was attained from Mr. Milind Talpallikar, Dr. Andy Leonard, and Dr Yong Lai of CFDRC. The final manuscript was skillfully prepared by Ms. Marni Kent.

## NOMENCLATURE

$f$	Frequency
$k$	Turbulent Kinetic Energy
$u, v, w$	Mean Fluctuating Velocity Components
$x$	Axial Coordinate
$y$	Transverse Coordinate
$z$	Spanwise Coordinate
$H$	Base Height of IFF (0.5 inches)
$M$	Mach Number
$M_{\text{ref}}$	Reference Mach Number
$P$	Pressure
$Re_H$	Reynolds Number Based on Base Height $\frac{\rho U H}{\mu}$
$St$	Strouhal Number = $\frac{fH}{U}$
$T$	Temperature
$T_{\text{ref}}$	Reference Temperature
$U, V, W$	Reynolds Averaged Velocity Components
$U_{\text{ref}}$	Reference Axial Velocity
$\bar{U}$	Mean Velocity
$\varepsilon$	Turbulent Dissipation
$\mu$	Laminar Viscosity
$\mu_t$	Effective Turbulent Viscosity
$\rho$	Density
$\delta_{ij}$	Kronecker Delta ( $\delta_{ij} = 1$ if $i = j$ , $\delta_{ij} = 0$ if $i \neq j$ )
$\eta_{\text{comb}}$	Combustor Efficiency
$\phi$	Equivalence Ratio
$\tau$	Representative Time Scale

## EXECUTIVE SUMMARY

The combustion efficiency of current ramburner technology is mixing-limited. Therefore, significant gains are possible if the fuel-air mixing can be increased without a significant increase in pressure loss or a decrease in flame stability. Several design concepts were explored in this SBIR Phase II project that increase the fuel-air mixing by generating large axial vortices downstream of the flameholder. The baseline flameholder for this project was the Integral Fuel injector/Flameholder (IFF) used in previous studies by United Technologies Research Center (UTRC). CFD solutions were completed on the baseline design and 28 advanced configurations. Most designs did improve fuel-air mixing, but also increased the cold pressure loss by several fold. The most promising designs used the momentum of the fuel to contribute to the axial thrust, thereby reducing the pressure loss.

Isothermal experimental tests were conducted at Wright Laboratory in parallel with CFD analysis. A complete dataset was taken for one baseline model, while several advanced models were screened for pressure loss. The baseline tests showed that a regular pattern of alternating vortices were shed from the base of the flameholder. Simultaneous three-component laser Doppler velocimeter (LDV) measurements were taken, providing mean velocities and Reynolds stresses at various axial locations downstream of the flameholder. The CFD analysis consisted of 2-D and 3-D time-accurate simulations, with various turbulence models including standard  $k-\epsilon$  model, RNG  $k-\epsilon$  model, and full Reynolds stress model. The analysis showed that the 3-D effects from the presence of the walls were significant. 3-D time accurate calculations with the RNG  $k-\epsilon$  turbulence model were necessary to accurately predict the isothermal flowfield. Good overall agreement was shown between CFD analysis and measurements.

A water-cooled combustion test section was designed and fabricated to facilitate collection of CARS and LDV data at Wright Laboratory for combustng flameholder flows. After several delays, the tests were canceled, due to the lack of availability of the test facilities. In their place, further CFD studies were completed, modeling the reacting flow past a triangular flameholder in a duct (experiment by Sjunnesson, et al.). The results showed that the acoustic interactions between the combustng flow and the duct were of paramount importance at low (near blowout) equivalence ratios, and that small changes in the overall equivalence ratio dramatically affected the vortex shedding in the wake of the flameholder. The CFD analysis showed a longitudinal combustion instability at a lower equivalence ratio than was seen experimentally. More work is needed to accurately predict reacting flow in ducts.



Overall, the program was successful in developing a useful database for isothermal bluff body flows, suitable for CFD validation. The use of time-accurate, 3-D CFD analysis was shown to be necessary to accurately capture the unsteady flowfield downstream of the flameholder. In addition, the program showed that ramburner performance gains may still be possible using vortex generators with the flameholder, but that smaller gains must be accepted to avoid large pressure losses.

## 1.0 INTRODUCTION

### 1.1 Background

The advent of high speed cruise vehicles has brought about the need to develop efficient propulsion systems for the Mach 0-6 flight regime. The turboramjet is one such propulsion system. In its simplest form, the turboramjet is a gas turbine with a bypass ramjet built into the system. From take-off conditions through Mach 4 flight, the turbine engine powers the vehicle. Above Mach 3, the ramjet takes over and powers the vehicle up to Mach 6 or higher.

The development of the ramburner has several challenges. One of the technological challenges is the development of fuel injection/flameholding concepts capable of providing good fuel-air mixing, stable combustion characteristics, and low pressure loss. Conventional ramburners have used dump combustors, where the fuel is injected from the wall. But dump combustors often suffer from poor fuel-air mixing due to a lack of adequate fuel penetration, and poor performance due to an insufficient number of flameholders. Instream fuel injection and flameholding is thus preferred. Gas turbine augmentors employ instream devices. However, the conventional spraybars and v-gutter flameholders used in augmentors are not viable for high speed flight due to constraints placed on the system by the high temperatures associated with Mach 3+ flight. At high Mach numbers, the air entering the combustor is hot enough to autoignite the fuel at the injector, possibly causing structural damage to the downstream flameholder. Therefore, the instream fuel injector and flameholder must be close-coupled, and actively cooled.

Due to these requirements, the Integral Fuel injector/Flameholder (IFF) was selected as the baseline scheme by United Technologies Research Center (UTRC) in a recent turboramjet technology program for the Air Force.<sup>1-9</sup> A schematic of the IFF is shown in Figure 1. The IFF concept was originally conceived as an advanced augmentor scheme at United Technologies Pratt and Whitney for the PW1120 engine, and UTRC adapted the concept for ramburner applications. Since the coupled injection/flameholder unit is cooled by the incoming fuel, the IFF avoids structural damage caused by the autoignition of the fuel.

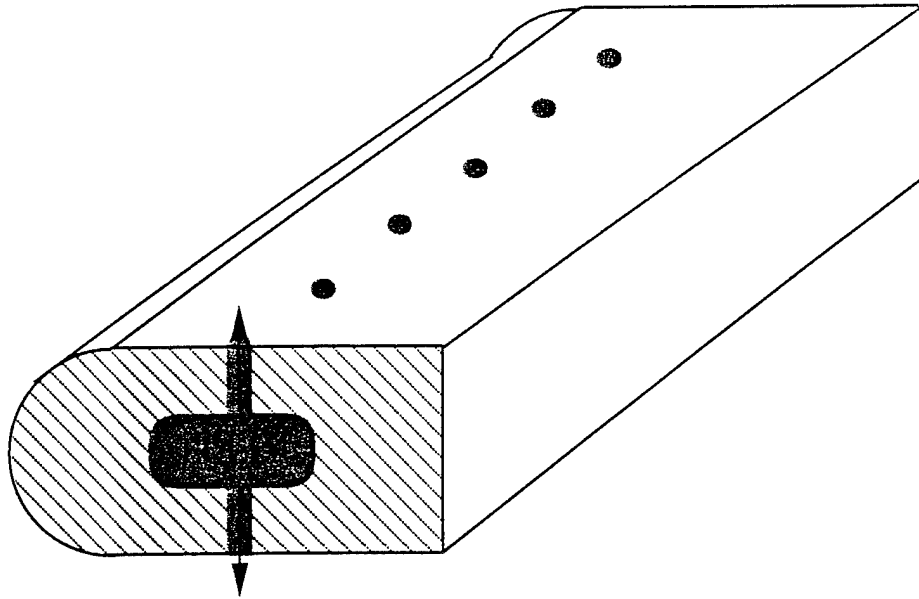


Figure 1. Schematic of IFF Concept

While the IFF is a good first design, the combustion efficiency of the IFF is generally mixing-limited. Therefore, concepts with enhanced fuel-air mixing are needed to reduce the ramburner length and increase combustion efficiency. Fuel-air mixing is strongly dependent upon the fuel penetration into the airstream. Low fuel penetration can provide good flameholder stability, but at the expense of fuel-air mixing. Likewise, high fuel penetration can result in improved mixing, but creates lean fuel mixtures directly behind the flameholder, leading to combustion instabilities.

## 1.2 Flameholder Theory

Bluff body flameholders have been studied for many years, due to their practical application of stabilizing flames in flowing combustible mixtures. Flame stabilization is necessary since the flowing gas stream can exceed the normal flame speeds of the fuel-air mixtures by orders of magnitude. The purpose of the flameholder is to produce a recirculation zone in which the combusting gases can reside and provide continuous ignition to the flowing mixture.

The detailed mechanisms of flameholding have been studied extensively, by examining the flow around the bluff body itself. In isothermal conditions, the flow in the wake of a bluff body consists of alternating vortices shed from the top and bottom of the bluff body. The vortices are shed at a nominal Strouhal number ( $fH/U$ ) of 0.2, producing a symmetrical double-vortex flow pattern in the mean flow of the wake. However, in combusting flow, the heat released from the combustion process reduces the instantaneous vortex formation, and produces a steady pair of counter-rotating vortices in the wake. As the equivalence ratio decreases in the

flame zone, the heat release also decreases. As the equivalence ratio in the recirculation zone approaches lean flammability limits, the alternating vortex structure reappears, leading to flame instabilities that eventually extinguish the flame.

Models of flame stability have generally followed two lines of reasoning. The first follows the idea that the recirculation zone in the wake of the bluff body acts as a well stirred reactor, with additional combustion products supplied by the flow outside of the recirculation zone. When the rate of supply of the fuel-air mixture exceeds the rate at which it can be burned, the flame gets extinguished. The second line of reasoning holds that the combustion takes place in the shear layer between the hot recirculation zone, and the fresh fuel-air mixture of the outer flow. Combustion is initiated as the two streams mix in the shear layer. If the gas is not ignited by the time the mixture within the shear layer has reached the end of the recirculation zone, combustion instabilities result. In other words, the residence time of the entrained mixture in the shear layer should exceed the reaction time for stable combustion.<sup>10</sup>

Research into flameholder stability indicates that the aerodynamic blockage plays a major role. The larger the flameholder, the larger the recirculation zone, and the better the flameholder stability. However, large blockages also create higher pressure loss, reducing the thrust performance of the engine. Therefore, flameholder design becomes a tradeoff between combustion stability and total pressure loss.

Typically, simple two-dimensional shapes have been used for flameholders, such as flat plates, v-gutters, and circular and rectangular cylinders. In some case, axisymmetric shapes have been used, such as discs and cones. There have been a limited number of studies on irregular shaped flameholders. Williams, et. al.<sup>11</sup>, have studied elliptically shaped, gutter-type flameholders (Figure 2), with spanwise slots cut near the trailing edge of the flameholder to facilitate gas sampling in the wake. They noticed that the presence of the slots increased the entrainment of fresh mixture, and increased the turbulence in the recirculation zone. Nicholson and Field<sup>12</sup> attempted to modify the wake characteristics of a flat plate flameholder by introducing a splitter plate at the centerline of the flameholder base. They reported only minor differences between the performance of the original flat plate and that of the modified plate. Other researchers examining similar splitter plate geometries<sup>13</sup> have noticed that the splitter plate reduces the turbulence in isothermal conditions by stabilizing the vortex shedding in the wake. Such differences would not be expected under combusting conditions. Also in an effort to modify the wake flow of a flameholder, Fail<sup>14</sup> attached streamwise tabs to the edges of a disc flameholder. The tabs had very little effect on the aerodynamic blockage of the disc, and had little effect on the flameholder stability. Stwalley, et. al.<sup>15</sup> have examined the use of v-gutter flameholders with slots of various widths cut into the trailing edge. The

purpose was to examine the flameholding characteristics of the irregular external surfaces of a damaged aircraft. They found that removing material from the trailing edge of the flameholder in a random fashion, always resulted in decreased flame stability. As more material was removed, and the shape approached the original shape, albeit with a smaller characteristic dimension, the flame stability improved. The pressure losses were reduced as material was removed, but this was a simple function of reduced blockage. Rizk and Lefebvre<sup>16</sup> have also noticed in their studies that single sided flameholders (such as a plate mounted on a wall) tend to provide better combustion stability, but more pressure loss, than a double sided instream flameholder. This is due to the stable single vortex produced behind a single sided flameholder.

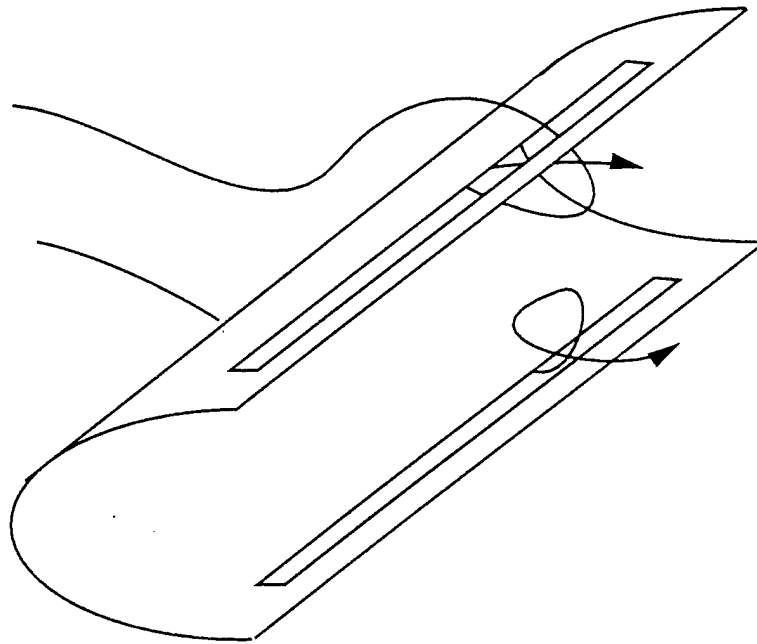


Figure 2. Elliptical - Gutter Flameholder Tested by Williams et al.

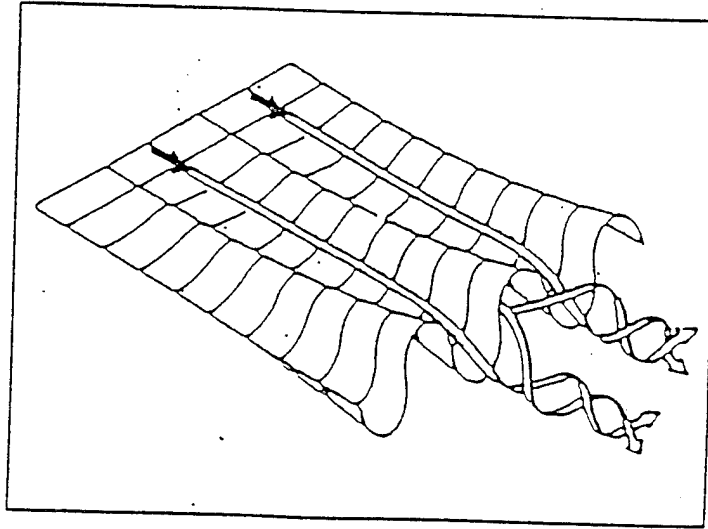
In general, the research shows that the stability of a flameholder is not significantly affected unless the aerodynamics of the wake are altered. Alteration by irregular geometry often leads to increased turbulence in the wake and reduced stability characteristics.

### 1.3 Improved Concepts

In the current study, new flameholder concepts have been introduced that build on the original IFF design. The new concepts all use the enhancement of large scale axial mixing to improve the fuel-air mixing of the IFF. The idea comes from the use of forced mixers developed for turbofan applications as shown in Figure 3. The mixers provide large scale axial vortices to enhance the mixing between the two fluids on each side of the plate. The mixers also increase the total area of the shear layer between the two fluids by convoluting the wake. When applied to the IFF, the two fluids above and below the mixer are the same, but there are regions of high fuel concentration that need to be mixed with the rest of the air.

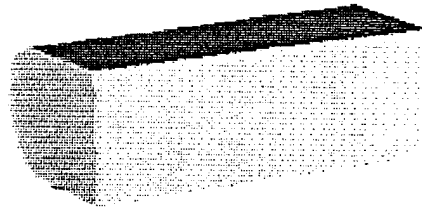
Lobed mixers have received the attention of the research community in recent years. McCormick and Bennett<sup>17</sup> have shown experimentally, that small scale horseshoe vortices are generated in the trough of the mixer plate, further enhancing mixing. They also showed that the thrust of the system was actually improved in addition to the increased mixing. Abdolfadl and Sehra<sup>18</sup> performed experimental tests on lobed mixers, varying the length and scallop of the mixer trailing edge. They found that the proper scalloping can increase mixing. Peschke and McVey<sup>19</sup> examined the use of lobed mixers positioned above a back-step flameholder to enhance mixing and combustion. They found that the lobed mixers increased mixing through the combustion region, increasing the flame front angle by a factor of four. No pressure measurements were reported. A numerical study was initiated by Malecki and Lord<sup>20</sup>, who found that Navier-Stokes methods were able to properly capture the physics behind the lobed mixer, by comparing to experimental data. Finally, Elliot, et al.<sup>21</sup>, conducted a joint numerical-experimental test, and showed that lower lobe-height/lobe-wavelength ratio produced stronger vortices. Although lobed mixers have proven capabilities in providing increased mixing, their application to ramjet combustors is not clear, due to the tradeoff between mixing and stability.

The Phase I study of this program evaluated two possible advanced concepts using the lobed mixer approach. The Convolute Lip IFF is shown in Figure 4, along with the Split-Notched IFF. The results in Phase I showed the potential for increased mixing, but did not directly examine the issues of total pressure loss and flame stability.

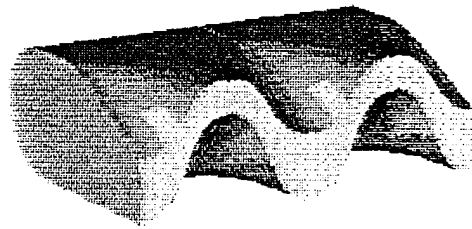


Lobed Mixer

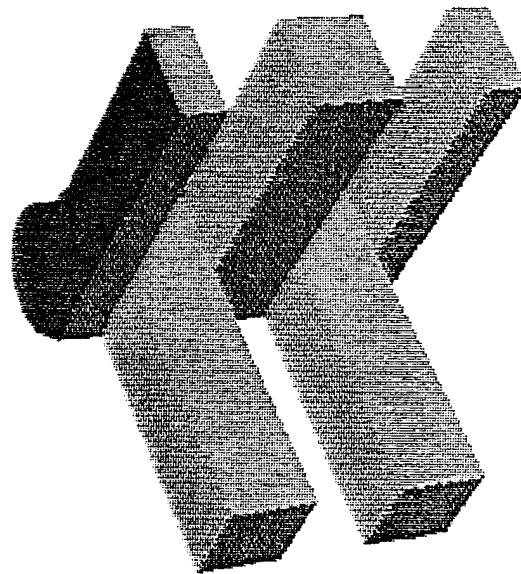
Figure 3. Axial Vorticity Mechanism of Increased Fuel-Air Mixing



IFF



CLIFF



SNIFF

Figure 4. Concepts Numerically Tested in Phase I



## 2.0 TECHNICAL OBJECTIVES AND APPROACH

The overall goal of this project was to develop a fuel injector/flameholder design that would provide increased fuel-air mixing with acceptable increases in the cold pressure loss. In addition, the program sought to develop an experimental data base for the validation of CFD software. The baseline design chosen for this study was the IFF configuration of United Technologies, shown in Figure 1.

A parallel CFD/experimental approach was defined for the Phase II program with the following objectives:

- 1) perform 3-D numerical studies of the baseline design and advanced designs. Then analyze the advanced designs and select the best candidate(s) for isothermal testing;
- 2) design, fabricate, and experimentally test the baseline design, and two advanced designs, at Wright Laboratory; compare the data to numerical results for possible numerical modeling improvements;
- 3) perform additional 3-D numerical studies based on experimental results, to obtain final candidate for combustion tests;
- 4) design and fabricate combustion test section to facilitate combustion tests; and
- 5) design, fabricate, and test baseline model and final advanced design under reacting conditions. Tests include LDV and CARS data under non-reacting and reacting conditions.

The first four objectives were successfully accomplished during this Phase II effort. The fifth task was not performed due to scheduling difficulties at Wright Laboratory. In its place, reacting CFD analysis was performed and compared to existing benchmark data.

### 3.0 ISOTHERMAL BASELINE EXPERIMENTAL TESTS

#### 3.1 Overview

The purpose of the isothermal experimental tests was to establish a baseline set of data for the validation of the CFD effort, and to test a selected set of advanced designs for possible further study in the combustion tests. The initial test matrix called for the extensive use of simultaneous 3-component LDV, along with Mie scattering test to determine species concentration levels during injection tests. This test program was very ambitious and would have provided a wealth of velocity, turbulence, mixing, and atomization data for both liquid and gaseous fuel injection. However, many difficulties were encountered, and the test matrix had to be severely curtailed. Only the baseline IFF, without injection, was thoroughly tested using the LDV. No injection tests were completed and no Mie scattering results were obtained.

The data taken for the baseline tests are presented in three main groups: 1) the single component LDV data, 2) the three-component near-field LDV data, and 3) the three component far-field LDV data. The single-component data were taken at the 13 far field axial stations, defined as  $x/H = -5, -3, 1, 1.5, 2, 3, 4, 6, 8, 10, 14, 18,$  and  $22$ . Single component data were taken to allow axial velocity measurements from the top of the tunnel to the bottom of the tunnel, providing a check on the conservation of mass from station to station, and lending confidence to the three-component measurements. The three-component measurements were taken in the far field, and in the near field, defined as axial stations  $x/H = 0.5, 0.6, 0.7, 0.8, 0.9, 1.0, 1.1,$  and  $1.2$ .

In addition to the baseline tests, one advanced model (ADV2) was tested using the LDV system. Vertical profiles were taken at  $x/H = 2.5$ , and  $z/H = 2.7, 2.0, 1.0, 0.0, -1.0,$  and  $-2.0$ . Spanwise profiles were taken at  $x/H = 4.0$ , and  $y/H = 1.5, 0.0,$  and  $-1.5$ . Several other model variations were briefly tested, in an effort to determine the peak crossflow velocity in the near wake of the flameholder. The conclusions from these tests are presented, along with an analysis of the measured pressure losses.

#### 3.2 Test Facility

The test facility was located in Test Cell 18 at the Aero Propulsion and Power Directorate of Wright Laboratory. The test stand was specifically designed and constructed to accommodate flow visualization and laser-based diagnostics. The 76 mm x 130 mm (3.0 in x 5.0 in) test section originally had full-view fused quartz windows on both sides, with a partial view window on the top. For the current study, the bottom of the tunnel was modified to also include a partial view window. The tunnel air was supplied by the facility compressors, allowing total pressure beyond 500 psia at ambient temperature. With choke blocks located downstream of

the test section, the free stream Mach number was fully variable between 0 and 1. Two sets of honeycomb and screens were used in a small settling chamber upstream of the test section to reduce the freestream turbulence, and provide uniform flow to the test section. Facility instrumentation included an array of absolute pressure transducers and thermocouples monitored by a micro-computer based system.

The original test conditions were designed to follow closely the earlier experimental tests of Hautman, et al.<sup>9</sup>, but at ambient temperature ( $M = 0.2$ ,  $p = 275$  KPa,  $T = 300$  K). However, initial testing indicated the presence of a low frequency pressure oscillation in the test section. Much time and effort was spent attempting to alleviate the problem. A new, larger settling chamber was designed and fabricated to damp the oscillations. The chamber included a high pressure loss core buster, intended to act as an acoustic barrier to small changes in the supply pressure. Unfortunately, this did not solve the problem.

The next tunnel modification involved powering the tunnel from an auxiliary air supply. Several options were explored, including the use of a Roots blower to provide high pressure air. However, the tunnel was finally connected to a 7.5 Hp centrifugal blower. This provided air pressures only slightly above ambient pressure at a peak Mach number of 0.08. It was determined that the lower Mach number would be sufficient to provide baseline CFD data, since the original flow conditions were well in the incompressible regime. The problem with the pressure oscillations were still present, however, even with the blower supplying the air. Additional testing concluded that using either the original small settling chamber or the larger one did not drastically affect the oscillations.

Therefore, attention turned to the components of the tunnel downstream of the test section. Since the choke blocks were no longer being utilized, the test section exit was no longer acoustically isolated from the downstream sections. The trials included: 1) removing the exit diffuser and allowing the test section to exhaust directly into the room, 2) allowing the test section to exhaust into a dump diffuser with no suction applied, and 3) attaching a long 7 inch diameter flex hose to the test section exit and exhausting the flow through a powered roof vent. The last configuration provided the most stable flow conditions although they were not ideal. The final configuration chosen for the tests were the 7.5 Hp blower with honeycomb at the blower exit, ducted into the small settling chamber, and into the test section through another layer of honeycomb.

For the final tunnel configuration, the free stream dynamic pressure was measured 8 inches upstream of the test section with a pitot static probe connected to both sides of a micromanometer. The total temperature was measured at the same axial location with a thermocouple inserted in the flow, and the static pressure was measured with an absolute pressure transducer connected to the side wall of the

tunnel. All reference conditions were recorded by hand during the acquisition of each data point in the test matrix.

### 3.3 Model Definition

The baseline IFF model was fabricated out of aluminum in three sections (Figure 5). The hemispherical nose had a radius of 0.25 inches. The rectangular center section followed with a length of 0.625 inches, and housed a fuel manifold for the injection tests. Finally a detachable base plate measuring 0.125 inches long was connected to the trailing edge. The base plate was detachable to allow the attachment of modified trailing edges to the IFF. The model was mounted in the test section directly to the side wall windows 4 inches downstream of the test section inlet, allowing free optical access to the entire geometry. The reference point for all data is defined as the vertical and spanwise centerlines at the IFF trailing edge. The total length of the IFF was 1.0 inches with a base height  $H = 0.5$  inches, giving a total blockage of 17% in the 3 inch high test section.

not to scale

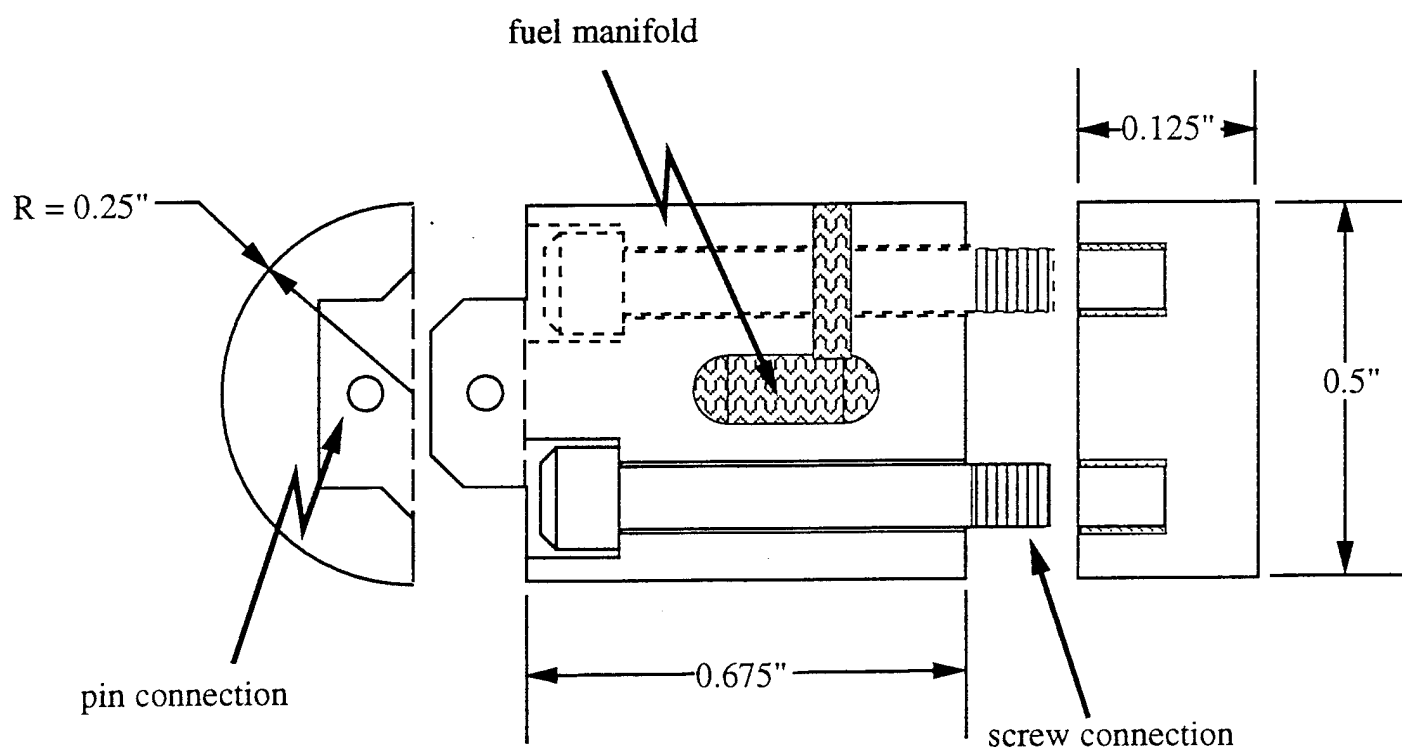


Figure 5. Experimental Model Design

### 3.4 Inlet Conditions

The measured inlet conditions changed slightly from test to test, since the entire test spanned a period of 01 year. Each data point was nondimensionalized with the actual freestream conditions. For reference purposes the following inlet conditions were specified.

$$U_{\text{ref}} = 24.5 \text{ m/sec}$$

$$T_{\text{ref}} = 295 \text{ K}$$

$$\text{Re}_H = 18,000$$

$$M_{\text{ref}} = 0.07$$

### 3.5 LDV Hardware

Two different optical systems were used for the far-field and the near-field tests. The differences were all contained within the transmitting optics; the set up for the receiving optics was the same for all tests. The entire system was mounted on a three-axis motion table capable of placing the measurement probe volume at any point in the test section with a resolution of  $\pm 0.03 \text{ mm}$ .

#### 3.5.1 Far-Field Transmitting Optics

The far field LDV system started with a 1 watt argon-ion laser. The laser beam was steered into a TSI Color Burst beam separator, where the beams were separated into their primary colors, polarized, split, and Bragg shifted. Fiber optic couplers transmitted the conditioned beams to the transmitting heads adjacent to the test section. The blue and green beams were directed through the side windows from a TSI model 9277 two-component fiber optic probe with a focal length of 450 mm, such that the green beams ran parallel to the tunnel and the blue beams ran perpendicular to the tunnel. The violet beams were directed through the top window via a TSI model 9274 single-component fiber optic probe. All three components were Bragg shifted 40 MHz to resolve the directional bias.

To ensure that all six beams from the three different components were focused at the same point in space, the beams were steered to pass through a  $35 \mu\text{m}$  pinhole oriented at 45 degrees to the vertical. The alignment was then further optimized by maximizing the 3-component data rate from a water mist passing through the probe volume.

#### 3.5.2 Near-Field Transmitting Optics

During the time between the far-field tests and the near-field tests, the two-component fiber optic probe was damaged. Although the unit was repaired, it was not returned in time for the near field tests. Therefore, the near field tests had to use an alternative optical train for the transmitting optics. The alternative method involved putting together a manual optic train from components available

throughout the laboratory. The process was very tedious but ultimately successful. Figure 6 shows a schematic of the system used for the near field tests. The beam from the argon-ion laser was first separated into the primary colors with a prism. The blue and green beams were then processed separately through a polarizer, beam splitter, and Bragg cell, before being focused into the test section. The beam orientation was rotated 45 degrees for the near field set up allowing the probe volume closer access to the base of the IFF. The violet beam from this laser was not used.

A second 1 watt argon-ion laser was used to generate the violet beam in the single color mode. This provided for a slight increase in the power available to the violet beam, which was found to be a limiting factor in the far field tests. The violet beam was then passed through the color burst separator to take advantage of the bragg cell internal to the system. The violet beams were then connected via fiber optic cables to the single component fiber optic probe and utilized as in the far field tests. Beam alignment between the different colors was accomplished in a manner similar to the far field tests, and all components were Bragg shifted 40 MHz.

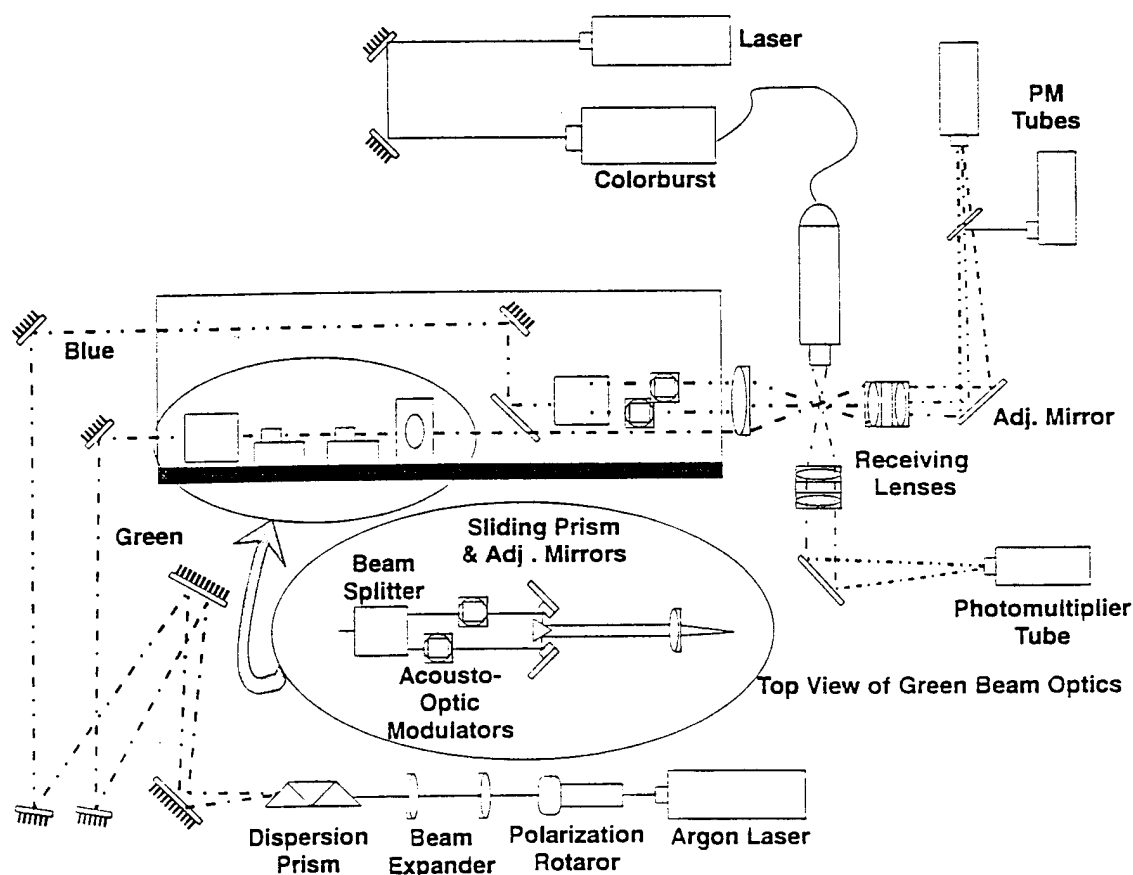


Figure 6. Near-Field Optical Set-Up for 3-D LDV System

### **3.5.3 LDV Receiving Optics**

All LDV channels were operated in a forward scattering mode to maximize the collected signals. The blue and green signals were collected with a 120 mm lens and passed through a dichroic filter. The filter passed the green light into a photomultiplier, and reflected the blue light into another photomultiplier. The violet light was also collected in the forward scattering mode and passed to a third photomultiplier.

The output from each photomultiplier was routed to TSI's IFA 750 Digital Burst Correlator and Analyzer. The IFA 750 was able to collect the data at a high rate of speed while performing a number of validation checks on each velocity realization. The signals were first conditioned by passing through high and low pass filters, set at 20 MHz and 100 MHz respectively, for each channel. One of the validations included the use of a user controlled coincidence window, defined as the amount of time allowed for each channel to produce a valid signal for a single particle. Realizations from different channels outside of the coincidence window are deemed to be from different particles and discarded. A window of 20 usec was selected for all the current LDV tests.

Another check was a count of the number of fringes crossed by a given particle. The user could set a minimum number of fringes that the particle must cross, or the signal was invalid. If any tests failed for any one of the channels, then the point was invalidated for all channels. A minimum of 8 fringes was chosen for this study. Valid data points were collected in a data buffer within the IFA 750 and downloaded to the controlling computer in blocks of 1024 points.

### **3.5.4 Data Acquisition and Postprocessing**

A 486-based personal computer was used to control the IFA 750 through the use of TSI's FIND software package. The software allowed the user to control every aspect of the IFA 750, and to view real-time histograms of the incoming signals. After the data was acquired, the software provided full data reduction and plotting capabilities.

During the course of the testing, some minor shortcomings were encountered with both the acquisition and reduction portions of the software. During data acquisition, the coincidence window was not always set properly, even though the software indicated that it was set. Cycling the coincidence window setting seemed to solve the problem. The difficulties with the reduction software were more difficult to alleviate. The FIND software made several assumptions that did not hold with the LDV configuration used in the current study. First, the software assumed that the green and blue components were perfectly orthogonal. Although this should be true, measurements indicated that the beams were nonorthogonal by approximately 1 degree. Second, the software assumed that any frequency shifting would be in the negative direction, relative to the local coordinate system. While this is generally

true for low speed axial measurements, it is arbitrary for flows with a net zero velocity, such as the cross-flow velocity components in a duct. In the current configuration, the blue beam was shifted in the positive direction. The FIND software would not accept a negative frequency shift, but would accept a negative fringe spacing. Such a solution is mathematically correct, however TSI recommended against using a negative fringe spacing, indicating that the software often uses hidden negative signs on certain variables to flag unrelated operations.

To resolve the reduction software problems, a new data reduction package was written to run independent of the TSI software. The new software was developed on a 486 based PC using the Lahey FORTRAN compiler, and read the raw data directly from the TSI binary packed files. The software included full control over all beam angles, and frequency shift directions and magnitudes. It also allowed for the inclusion of reference conditions to facilitate point-by-point normalization of the data. The new software was tested and validated against the FIND software and produced identical results for the test cases. Additional information on the new software, including the source code, is presented in Appendix C.

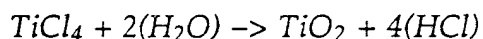
During the calculation of the flow statistics, additional measures were taken to remove spurious points. The velocity measurements were first transformed to the tunnel coordinate system for each validated realization. The Probability Density Functions (PDF) were then assembled for each velocity component at the given measurement station. The statistics of interest were calculated by the methods described in Appendix B. Finally, all velocity points were compared against a 3 sigma criteria. Any points falling outside of 3 sigma from the mean were discarded. If a point failed for any one of the three velocity components, then the point was removed from all components. All statistics were then recomputed with the spurious points removed. For the current study, 5120 validated points were collected from the IFA 750 at each station. Of these, typically 50 points were eliminated by the 3 sigma criterion.

Another source of error for LDV measurements is velocity bias. Velocity bias arises from the fact that turbulent flow is continuous and structured. Therefore, for a uniformly seeded flow, during the period of time that the flow is traveling faster than the true mean, the LDV will measure more particles than when the flow is traveling slower than the true mean. The simple arithmetic mean calculated from the collected measurements will then be artificially high. The higher the turbulence level, the greater the effect of the bias. Although several methods have been devised to correct for velocity bias, general acceptance of the post processing corrections is lacking. While the FIND software included velocity bias corrections, the new reduction software did not include such corrections, and no velocity bias corrections were made to the current data set.



### 3.5.5 LDV Seed Selection

The next problem involved the proper selection of seed material to use with the LDV system. Several different seed materials were tested. Initial tests used the chemical seeder designed by Craig, et. al.<sup>22</sup> The chemical seeder produced small titanium dioxide particles (0.2 - 1  $\mu\text{m}$ ) by reacting titanium tetrachloride with the water in the air supply, according to the following equation:



The titanium dioxide particles produced by the reaction make excellent seed particles, but titanium tetrachloride, and the reaction by-product, hydrochloric acid, are extremely corrosive and difficult to handle. Due to the hazards of using such corrosive seed material, alternative seeding methods were explored.

Aluminum oxide powder was the next seed material used for the tests. This finely ground powder supplied seed particles from 0.5 - 5 microns in diameter, provided the material was kept very dry. A new seeding device was fabricated using a hot plate and dry nitrogen purge system to keep the seed dry. The nitrogen system was then used to create a fluidized bed to inject the seed into the tunnel. While the system worked well at times, it was prone to clogging and would often surge, injecting large amounts of seed into the tunnel. Since uniform seed rates are desirable during data sampling, and from sample to sample, the surging problem was unacceptable. The aluminum oxide seed also had a tendency to build up on the IFF leading edge and would quickly coat the windows rendering the LDV system useless.

The last seeder tested was of the liquid glycerin type, and was fabricated by Rabe and Sabroske.<sup>23</sup> The liquid glycerin seeder produced liquid droplets of glycerin that ranged from 0.5 - 1.0  $\mu\text{m}$  in diameter. The seed rate was easily controlled and consistent. In general, the seed material did not collect on the windows, although the separation region directly behind the IFF became coated fairly quickly. When taking measurements in this area, the windows had to be cleaned after every 3 - 4 data points.

Peak data rates with all the seeders were between 15,000 and 20,000 per second in the single channel mode. During simultaneous 3-component data collection, the data rate dropped to 5000 per second in the free stream, and 1500 per second in the highly turbulent region behind the IFF. The windows were removed and cleaned whenever the data rate fell below 1000 per second.

### 3.6 Experimental Results - Baseline IFF

The data were taken in three main groups, designated as the one-component far field data, the three component far field data, and the three component near field data. The far field data were obtained with each color aligned directly with the velocity component being measured. Therefore, no coordinate transformation was required. However, such an arrangement prevented the measurement of normal velocities within 0.5 inches of a wall, due to partial blockage of the incoming laser beams. The near field data were taken with the blue and green beams rotated 45 degrees to the tunnel axis, to allow measurements to within 0.25 inches of the IFF. The data then had to be transformed to the tunnel coordinate system for processing.

#### 3.6.1 One-Component Far Field Data

The first data collected were the axial component at the far field stations. Since only the axial component was collected, data were taken in profiles from the floor to the ceiling of the test section. The velocity and turbulence profiles are presented in Figures 7 and 8, and show several basic features of the flow. First, the incoming flow profile is relatively flat and symmetric, indicating uniform inlet conditions. Second, the freestream turbulence is approximately 3%, with a maximum of 8% in the tunnel wall boundary layers. Finally, the presence of the wake is clearly seen in the velocity deficit and increased turbulence levels downstream of the IFF. Since no negative mean velocities were indicated in the wake, the recirculation zone ended within 1H of the IFF.

From the axial velocity profiles, the mass flux at each station was integrated by the trapezoidal rule, assuming that the flow was 2-D with constant density. The mass flow at each station agreed to within 2% of the first station, with the highest errors occurring in the near wake region ( $x/H = 1, 1.5, 2$ ). Such a result gives an indication that the measurements were taken correctly, and that velocity bias was not a problem. However, velocity bias will only be significant in regions of high turbulence, such as directly behind the IFF. But the region in the near wake also makes the smallest contribution to the mass flow, due to the velocity deficit. Therefore, velocity bias may still be significant even though the mass flow errors are small.

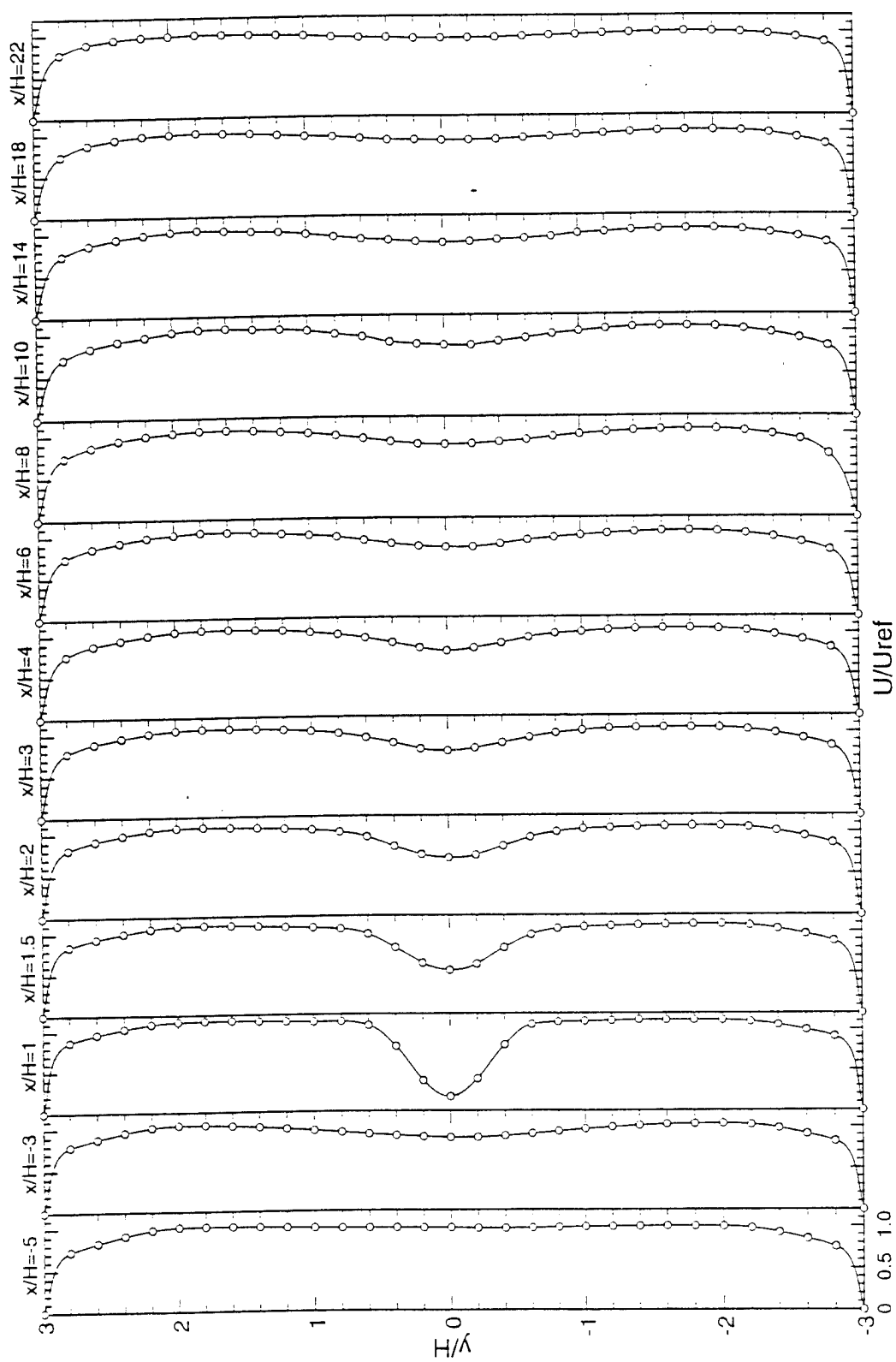


Figure 7. Normalized Mean Axial Velocity Profiles at Far Field Stations; 1-D LDV

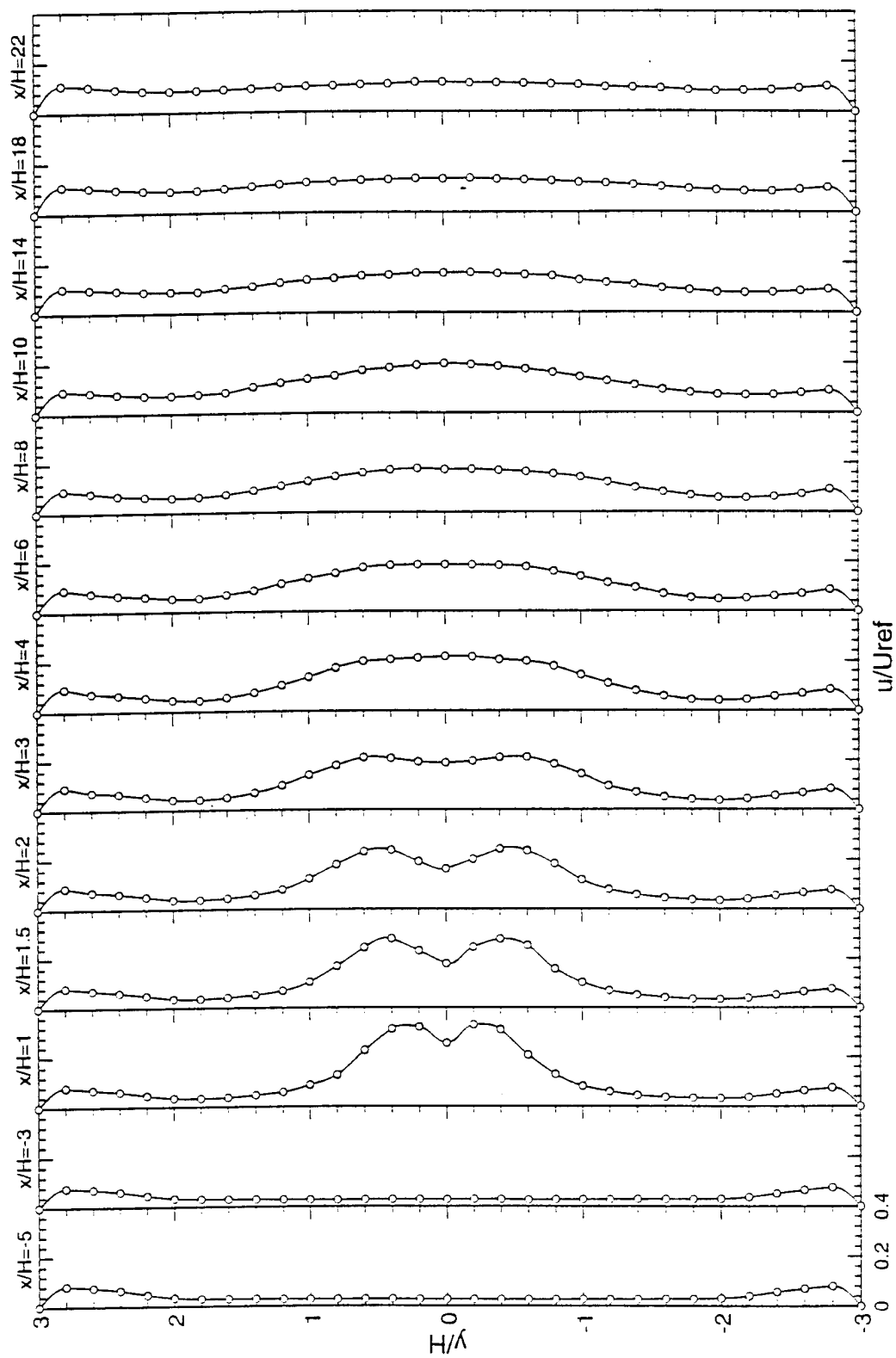


Figure 8. Normalized rms Axial Turbulent Velocity Profiles at Far Field Stations; 1-D LDV

Several samples along the centerline were analyzed using Fourier analyses to determine the vortex shedding frequency behind the IFF. Since the LDV data was taken by random samples whenever a particle passed through the probe volume, a transformation to uniform time intervals between data realizations was necessary. The FIND software provided a mechanism that averaged all data within a given time interval,  $dt$ . The entire data set was averaged to give one realization for every  $dt$  within the data set. A Fast Fourier Transform (FFT) routine then computed the frequency spectrum. Figure 9 shows the frequency spectrum as measured at  $x/H = -5$  and 2. A distinct frequency peak is noted at 454 Hz ( $St = 0.243$ ) for the downstream location, while the upstream location shows no dominant frequency. The dominant frequency was found to continue at all downstream stations at diminishing magnitudes until it disappeared at the last station,  $x/H = 22$ .

### **3.6.2 Three-Component Far Field Data**

After the single-component data were collected, all three components were collected at the far field stations. The general agreement for the axial component between the single component and three-component measurements was very good. A comparison is shown in Figure 10 at the near wake station of  $x/H = 1.0$ . This station is the most demanding station of the far field data, due to the high turbulence, and there is some discrepancy between the two data sets. While several possible errors were identified, the greatest error was due to the replacement of the model in the test section between the two tests. Every effort was made to maintain the model's attitude and position within the test section, but small errors were possible.

In addition to the conclusions drawn from the single-component data, the three-component data (presented in Figures 11-16) yielded the following information. The vertical velocity profiles indicated that the flow is turning back towards the centerline in the wake as the flow fills the low pressure region left behind the IFF. The maximum velocity gradients in the vertical direction were located at the centerline, and also marked the position of the highest turbulence intensity (75% at  $x/H = 1$ ). Likewise, the axial component's maximum velocity gradient was located in the shear layer at  $y/H = \pm 0.2$ , where the turbulence was also at its peak. The regions of maximum turbulence in the axial and transverse components did not spatially correspond, indicating that the turbulence was not isotropic.

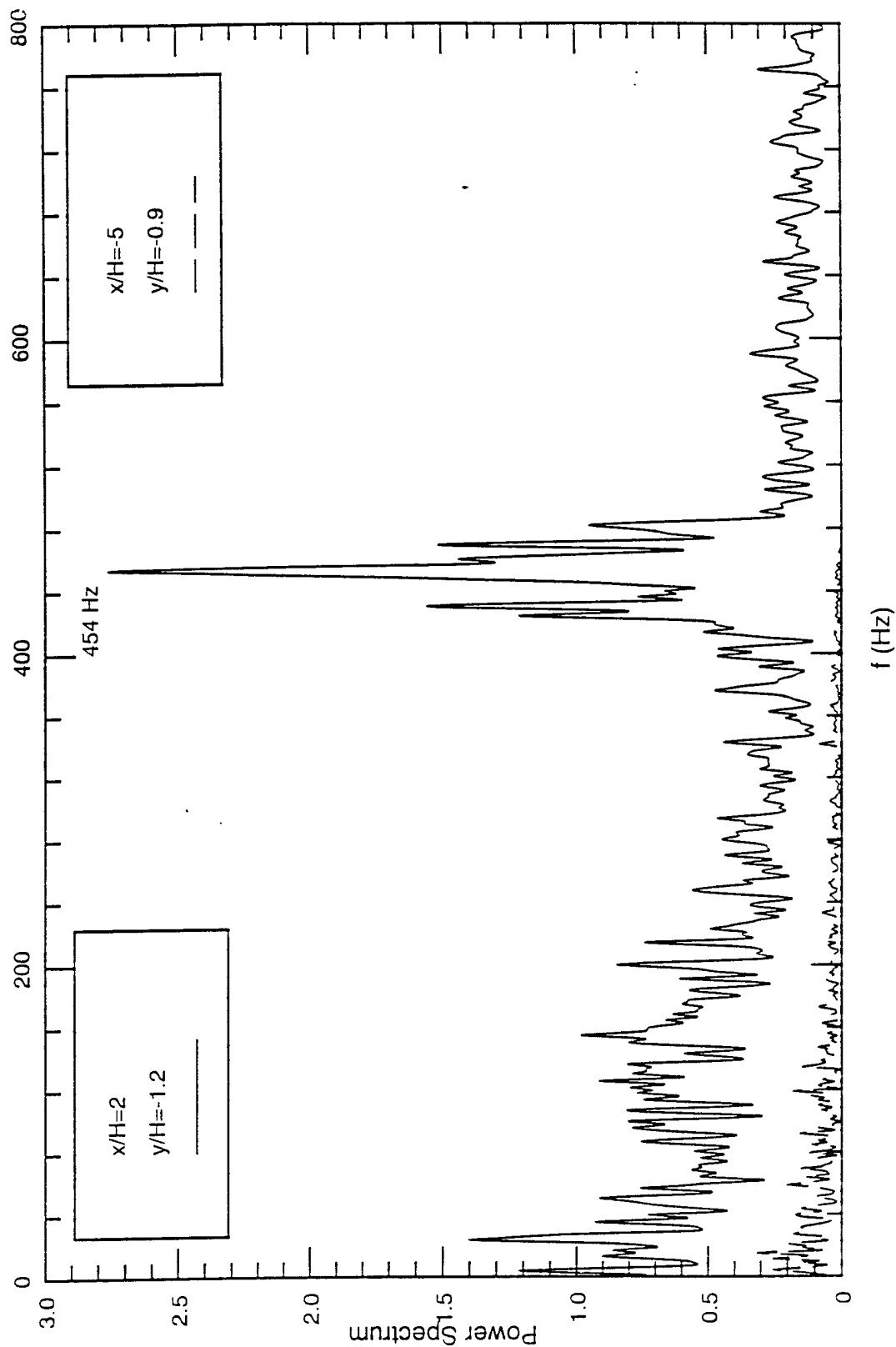


Figure 9. Frequency Spectra Upstream and Downstream of IFF Shows Vortex Shedding Frequency

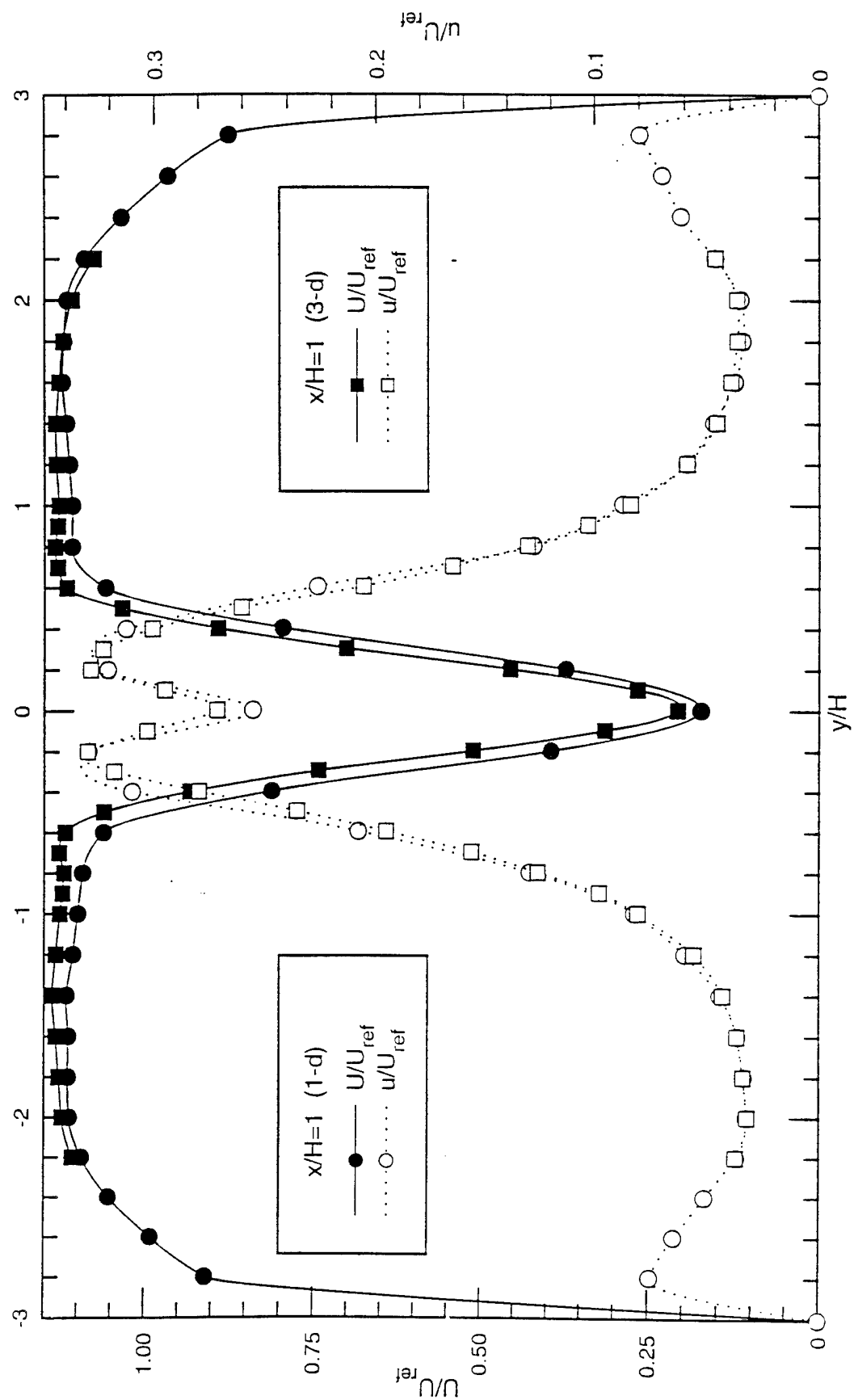


Figure 10. Comparison Between 1-D and 3-D LDV Measurements Shows Good Agreement

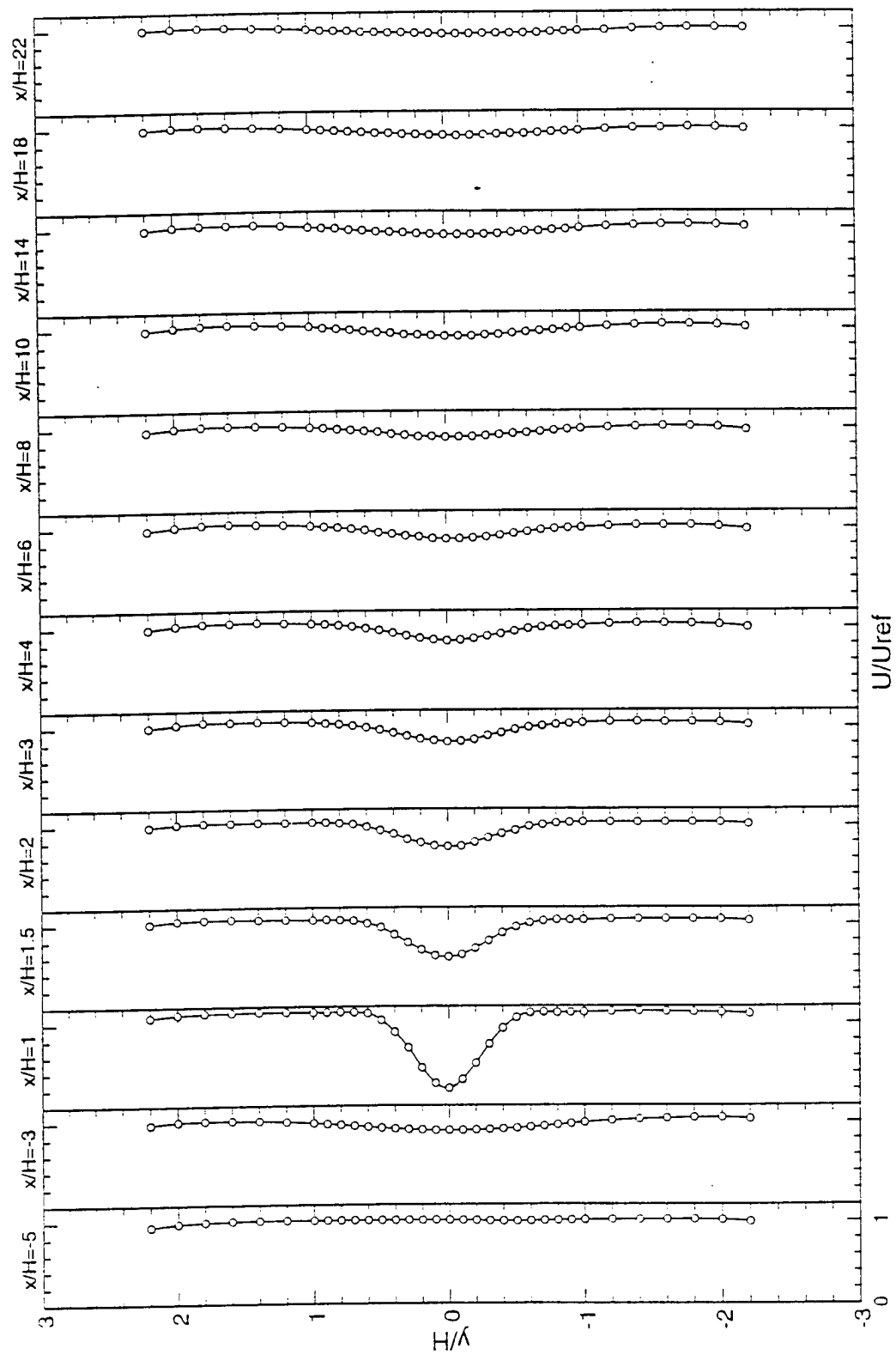


Figure 11. Normalized Mean Axial Velocity Profiles at Far Field Stations; 3-D LDV



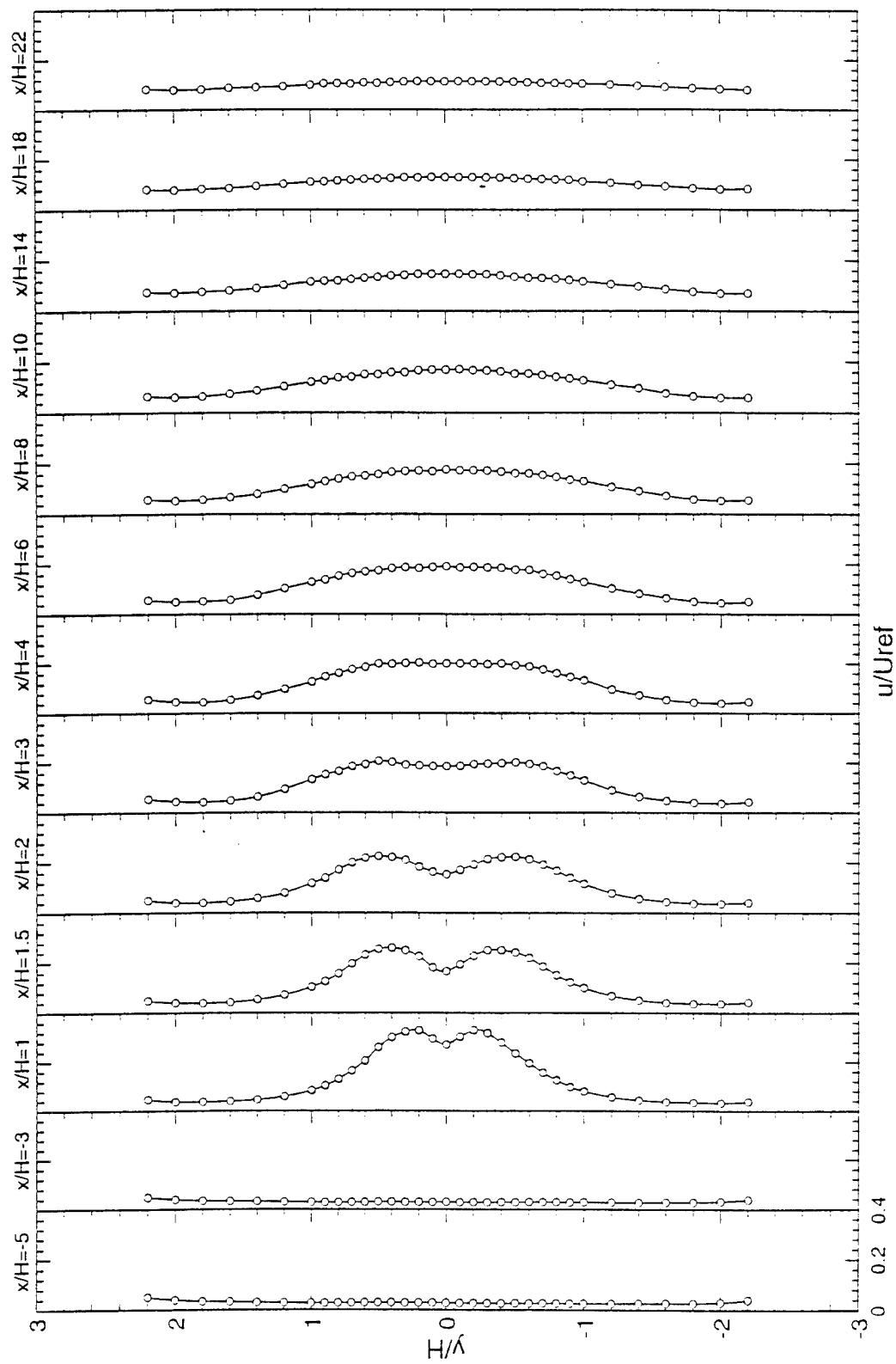


Figure 12. Normalized rms Axial Turbulent Velocity Profiles at Far Field Stations; 3-D LDV

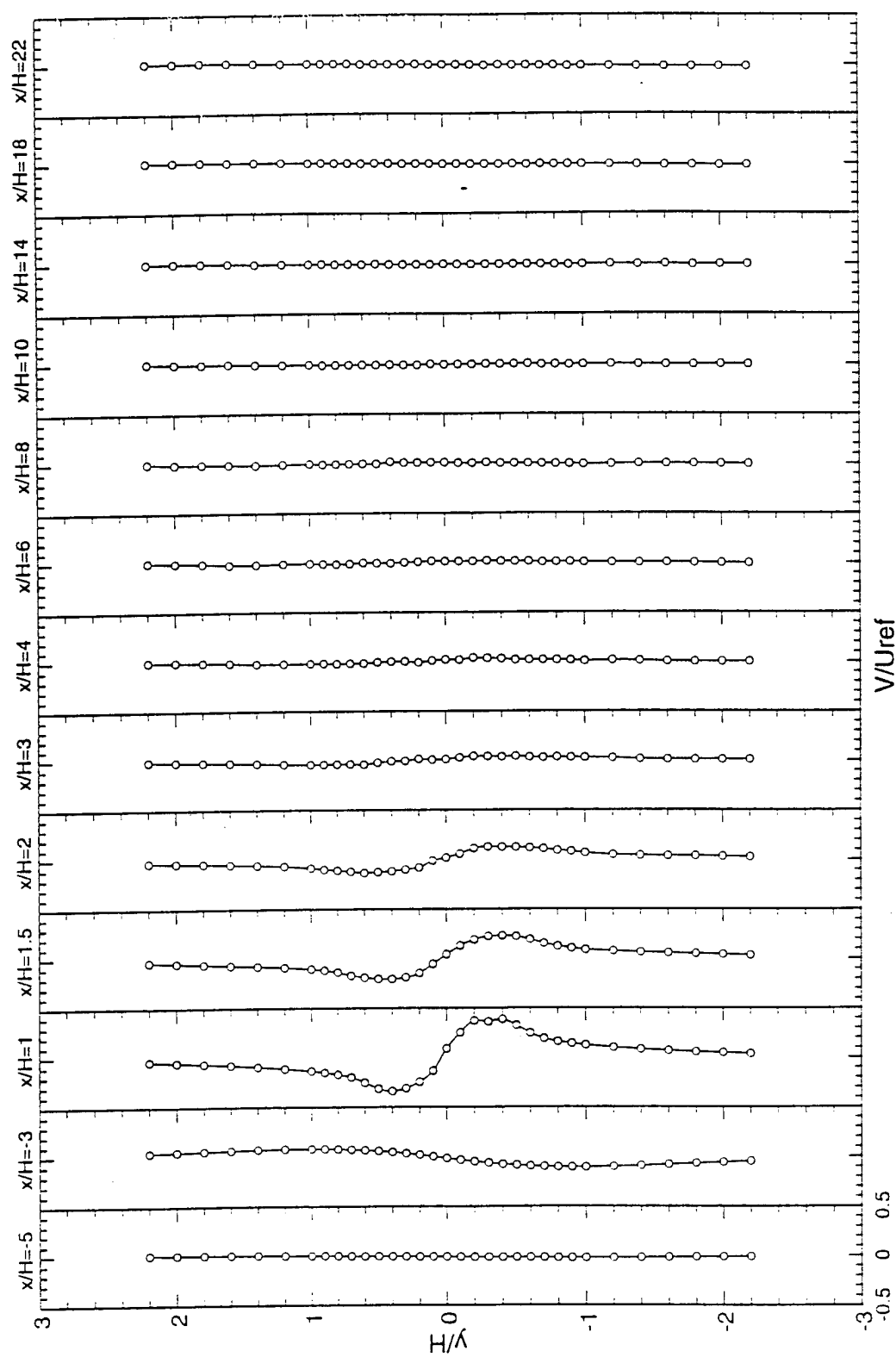


Figure 13. Normalized Mean Transverse Velocity Profiles at Far Field Stations; 3-D LDV

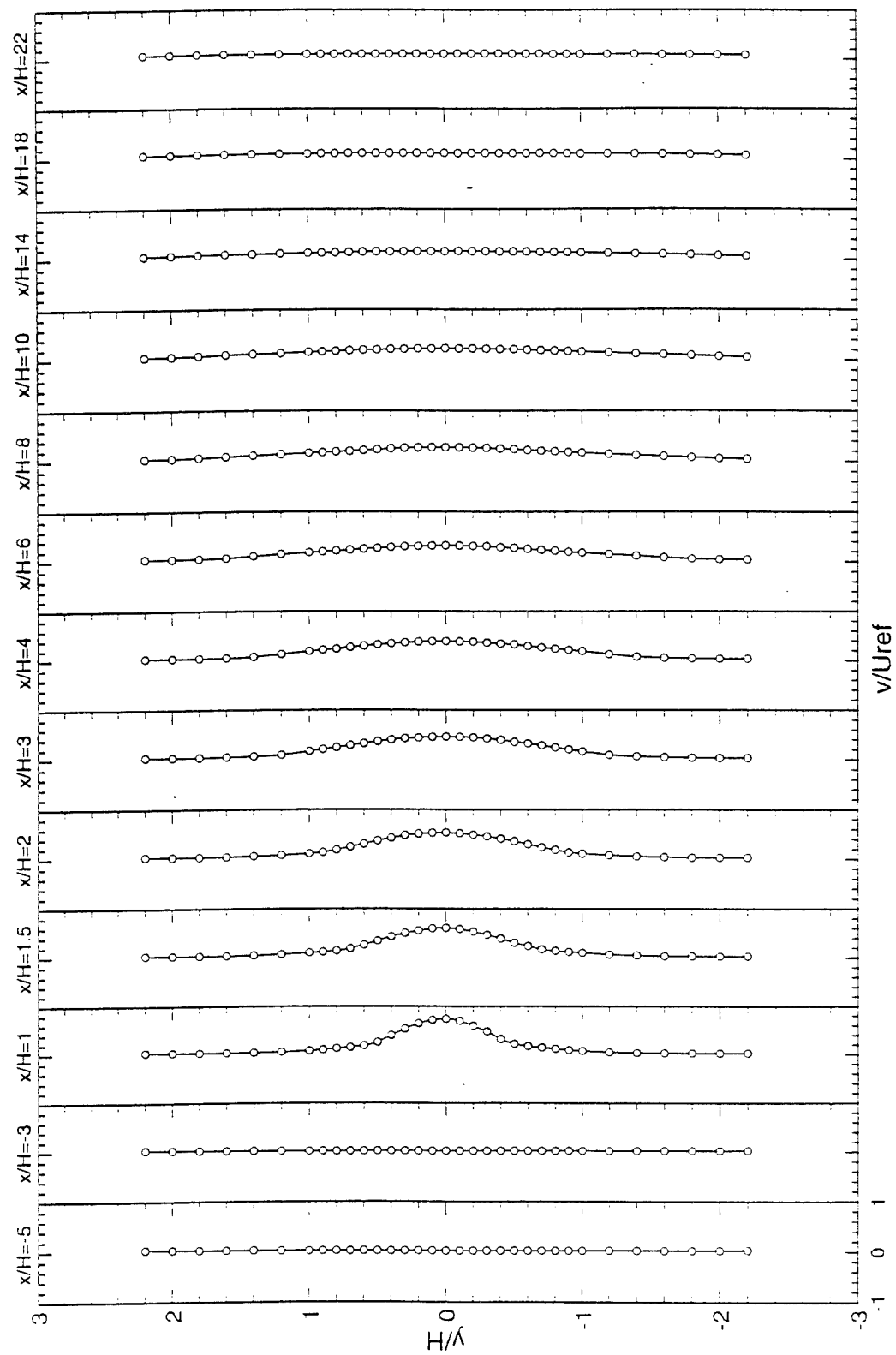


Figure 14. Normalized rms Transverse Turbulent Velocity Profiles at Far Field Stations; 3-D LDV

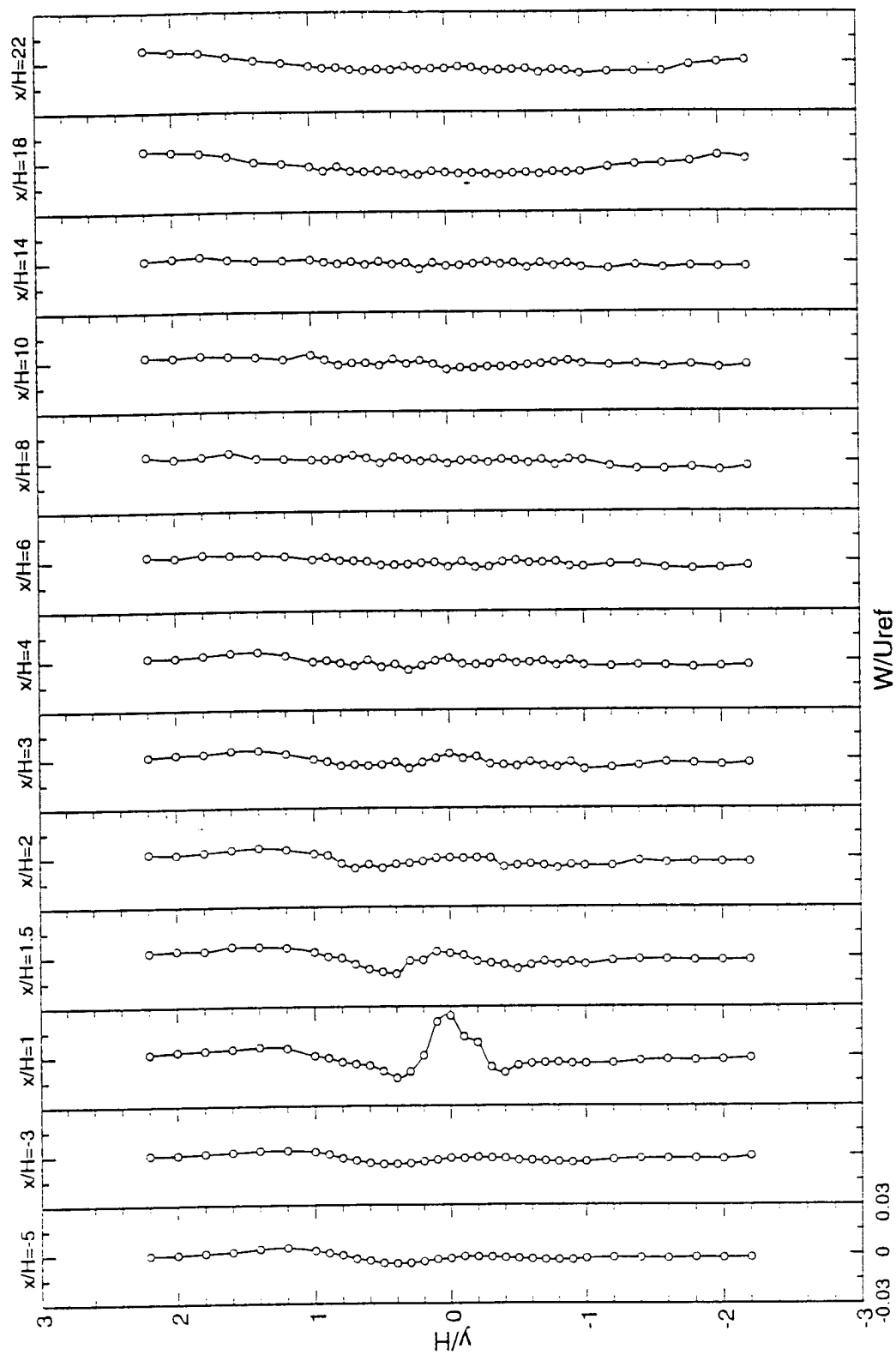


Figure 15. Normalized Mean Spanwise Velocity Profiles at Far Field Stations; 3-D LDV

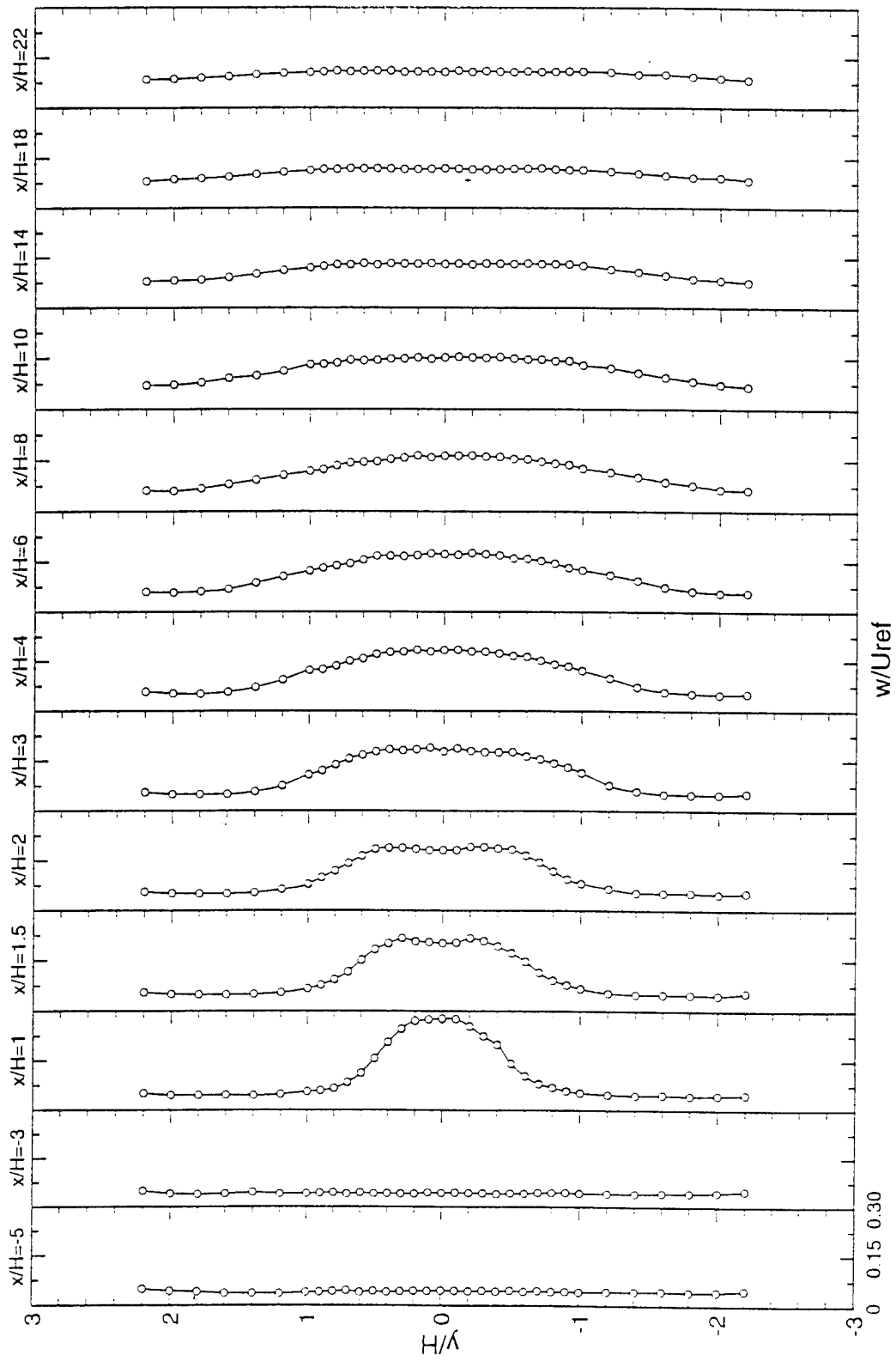


Figure 16. Normalized rms Spanwise Turbulent Velocity Profiles at Far Field Stations; 3-D LDV

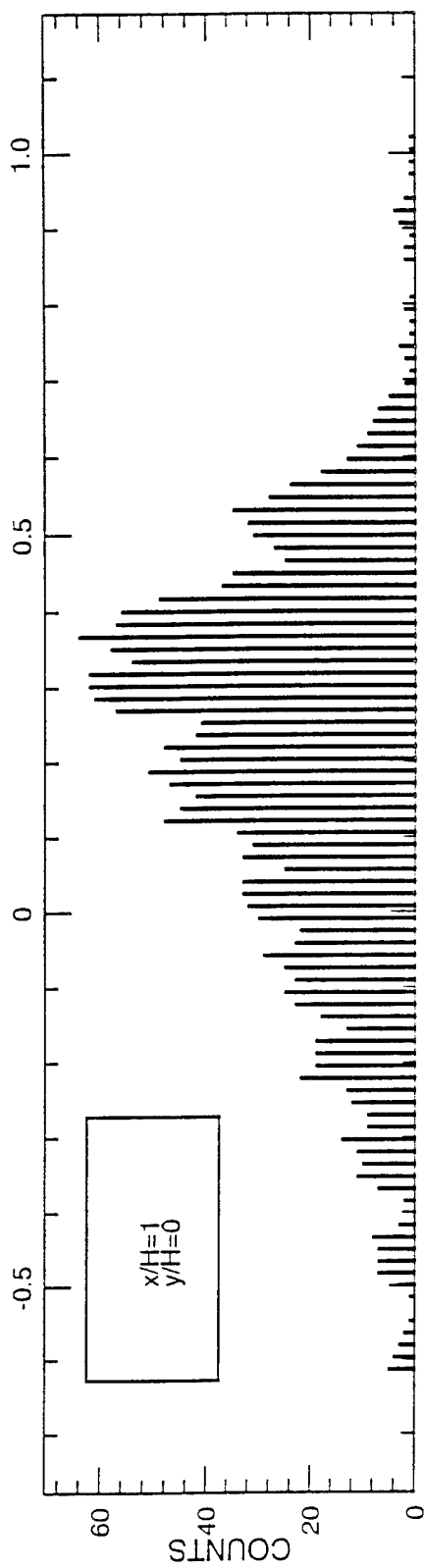
The reason the turbulence was not isotropic is due to the structure inherent in the turbulence. The turbulence in the IFF wake is dominated by large scale vortices shed alternately from the top and bottom corners of the IFF trailing edge. As each vortex is shed, they form a train of vortices of alternating directions moving downstream through the wake. The turbulence is now simply a measure of the velocity variations due to the vortices moving through a sampling point. If for example, the sampling point is on the centerline, there will be very little contribution to the axial component from the vortices, since the vortex cores are traveling near the centerline. However, there is a large contribution to the vertical velocity. The vertical velocity varies between  $\pm V_{\max}$  as each vortex passes the sampling point, leading to high turbulence at the centerline. This also leads to a bimodal PDF such as the one measured at  $x/H = 1$ ,  $y/H = 0$  (Figure 17). Likewise, the highest variation in the axial component occurs at the edges of the mean shear layer, where very little vertical velocity variation exists.

The spanwise velocity component ( $W$ ) was negligible throughout most of the test measurement domain, although a small mean flow was measured at  $x/H = 1$ . Two-dimensional geometries have been observed to produce three-dimensional flows due to the presence of the tunnel boundary layers. However, the spanwise centerline velocity should have no mean spanwise velocity component. The fact that there was spanwise flow measured at  $x/H = 1$  indicates one of two possibilities: 1) the flow and/or the geometry was not exactly symmetric, or 2) the  $z = 0$  station was not exactly centered with respect to the flow. The location of the reference point was accomplished by focusing the probe volume on each side wall and splitting the difference. The source of the spanwise flow was further investigated in the near field.

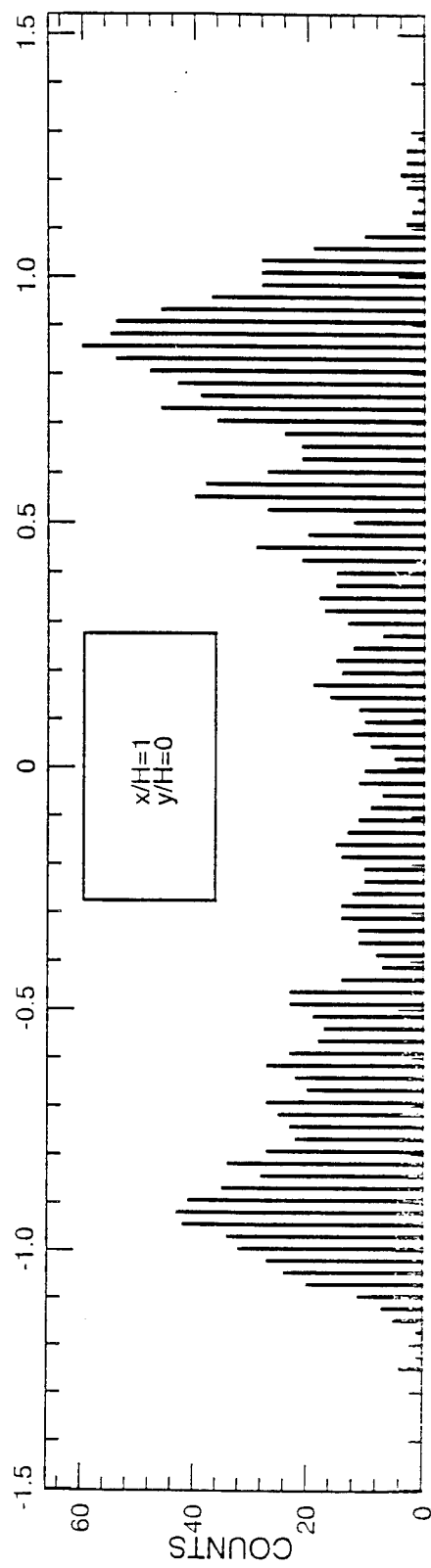
### 3.6.3 Three-Component Near Field Data

The near field three-component data are presented in Figures 18-26. The mean velocity profiles indicated that the measurement stations are within the recirculation zone, and that the recirculation zone extended to  $x/H = 0.9$ . The length of the recirculation zone is much smaller than that of a backward facing step, due to the instantaneous structure of the vortex shedding process that is not present with a backward facing step.

The profiles of the Reynolds normal stresses show that the peak intensities occurred at locations where the mean-velocity gradients were the highest. The normal stresses are also clearly not isotropic, as seen in a comparison of the stress ratios in Figures 27-29. The vertical normal stress ( $vv$ ) was found to be the dominate normal stress term. Reynolds shear stresses are also shown. The measurements indicated that the  $uv$  shear stress is the most significant of the three, and is five times higher than the other two shear stresses.



(a) Normalized Mean Axial Velocity PDF



(b) Normalized Mean Transverse Velocity PDF

Figure 17. Bimodal PDF Occurs at Centerline Position for Transverse Components

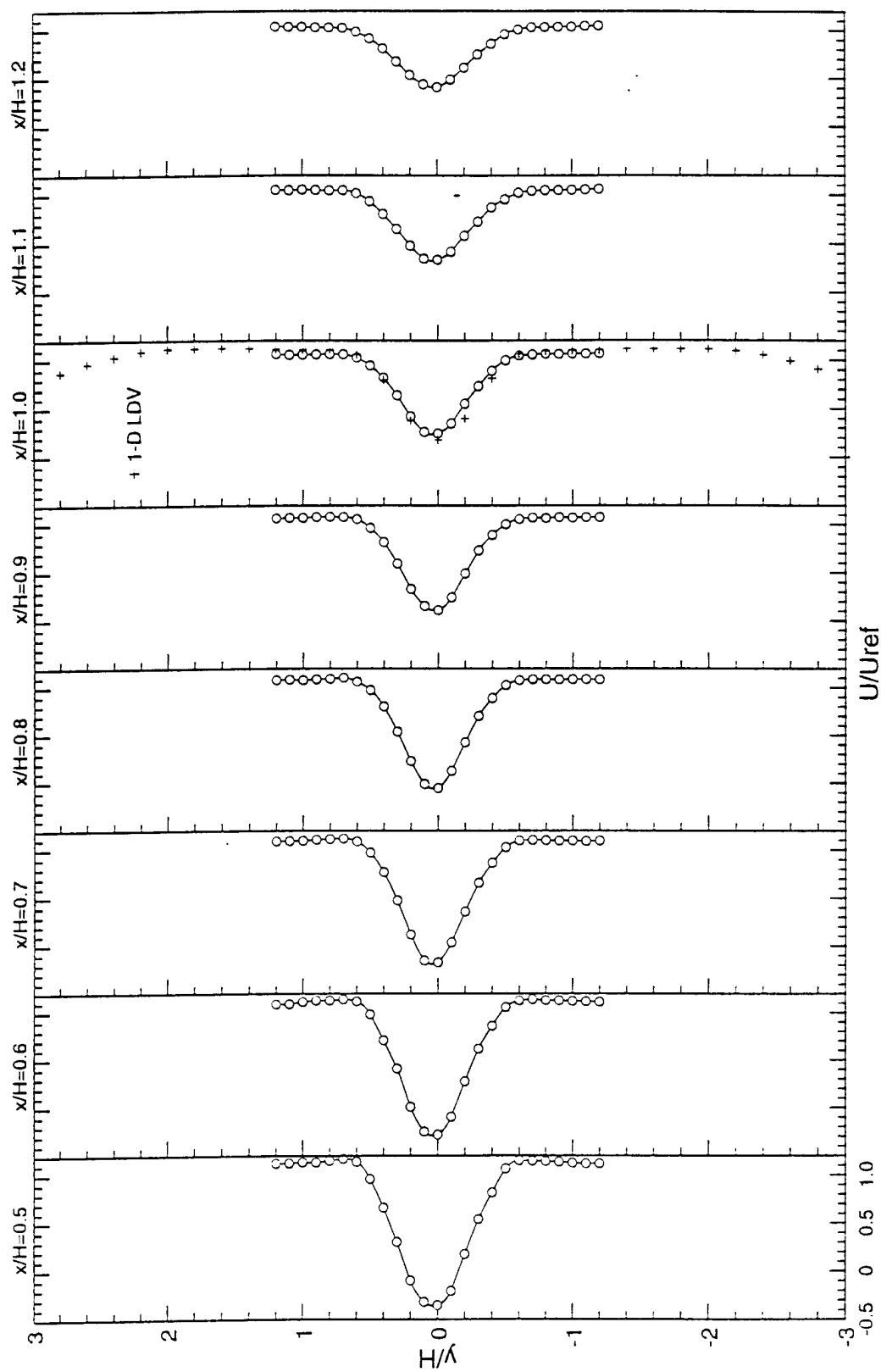


Figure 18. Normalized Mean Axial Velocity Profiles at Near Field Stations; 3-D LDV



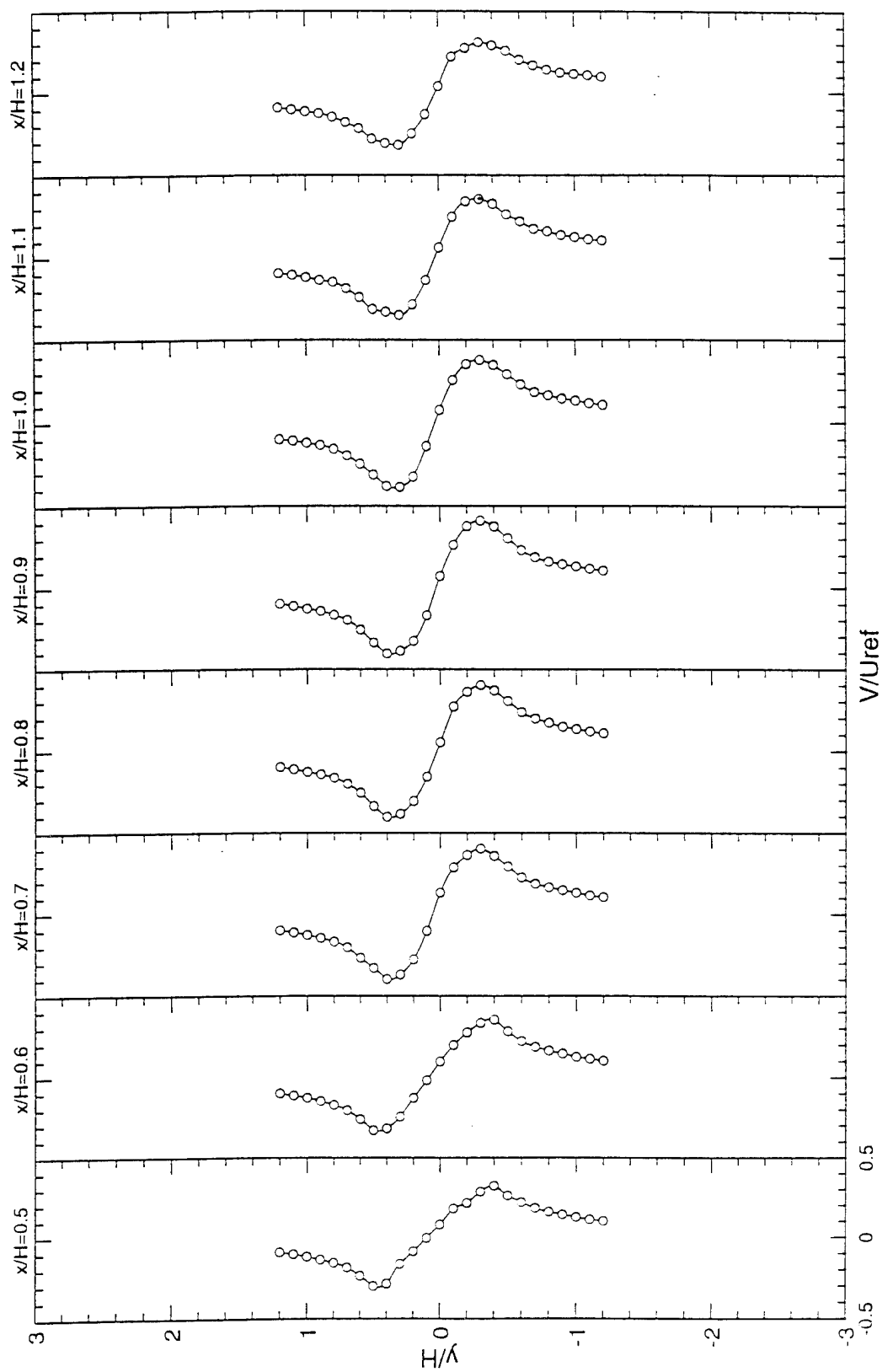


Figure 19. Normalized Mean Transverse Velocity Profiles at Near Field Stations; 3-D LDV

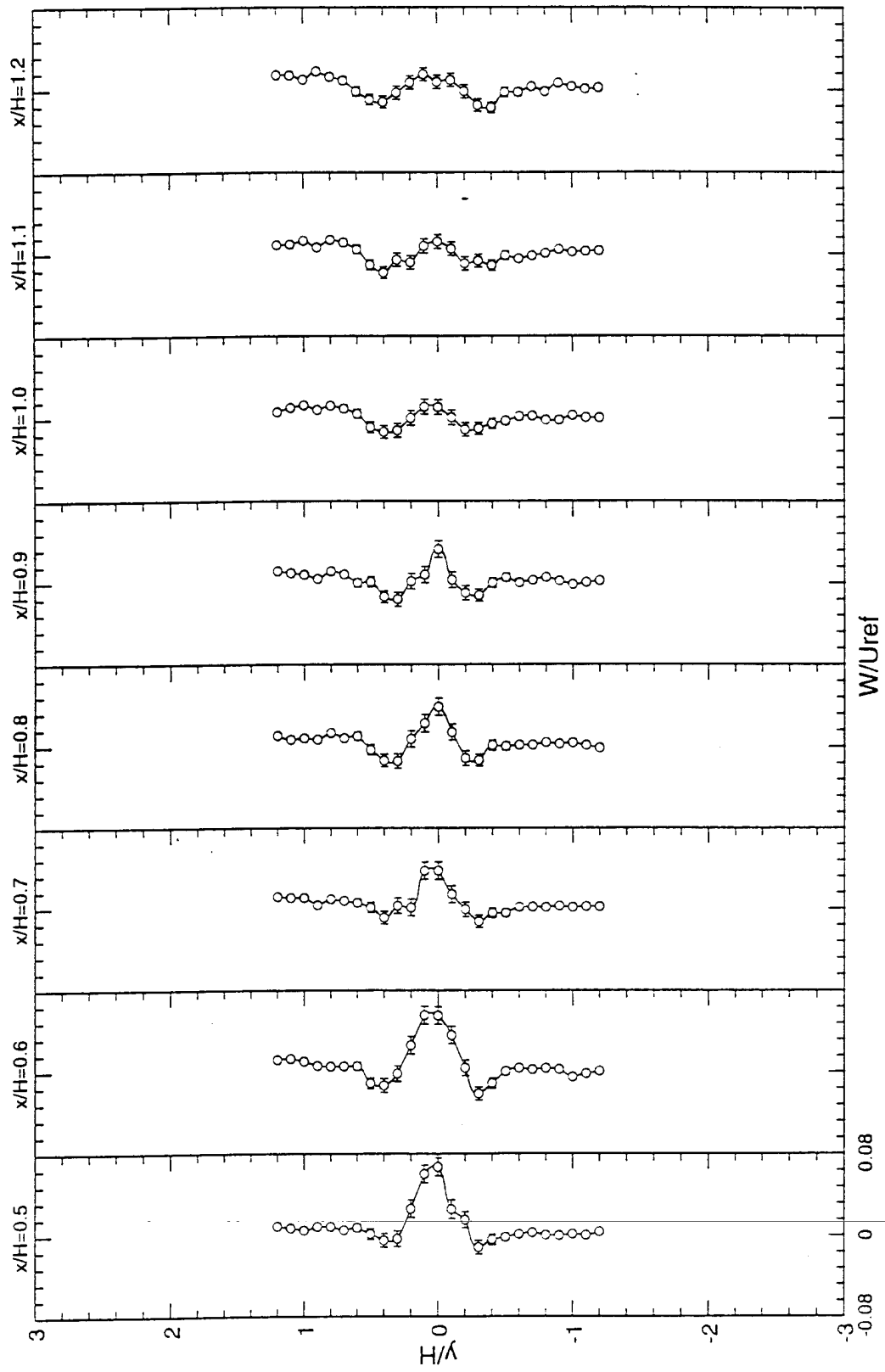


Figure 20. Normalized Mean Spanwise Velocity Profiles at Near Field Stations; 3-D LDV

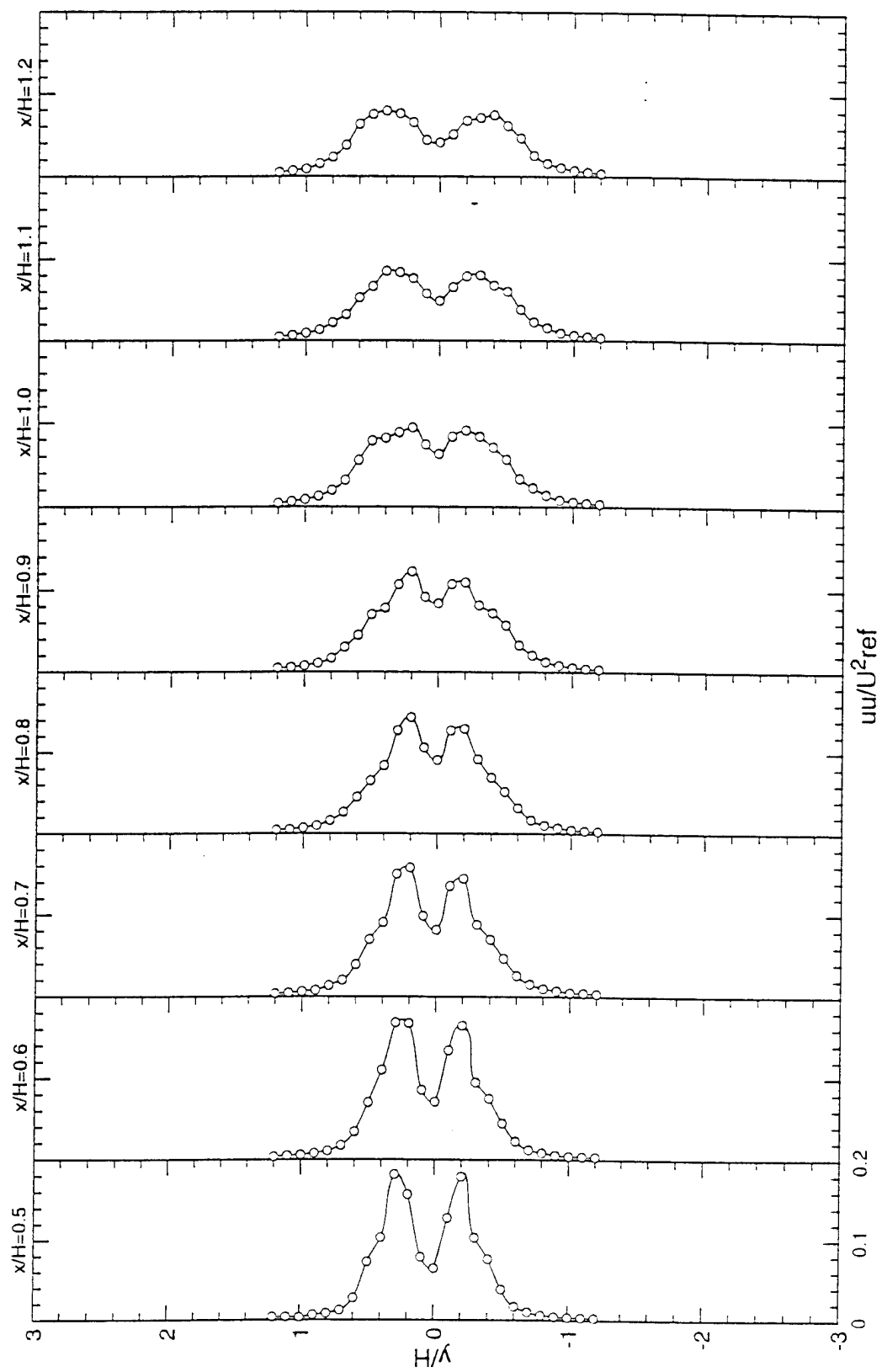


Figure 21. Normalized  $uu$  Turbulent Stress Distributions at Near Field Stations

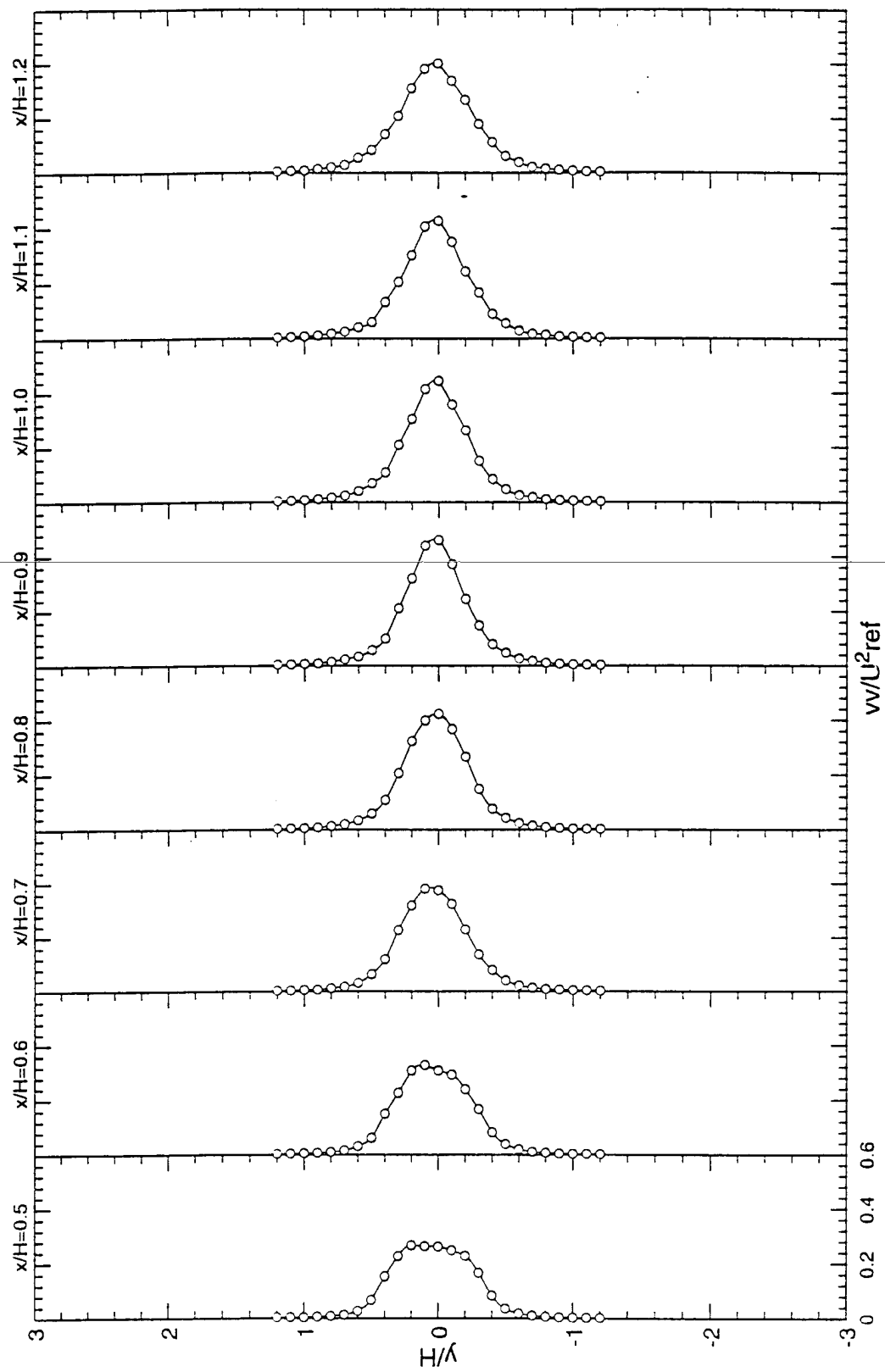


Figure 22. Normalized  $vv$  Turbulent Stress Distributions at Near Field Stations

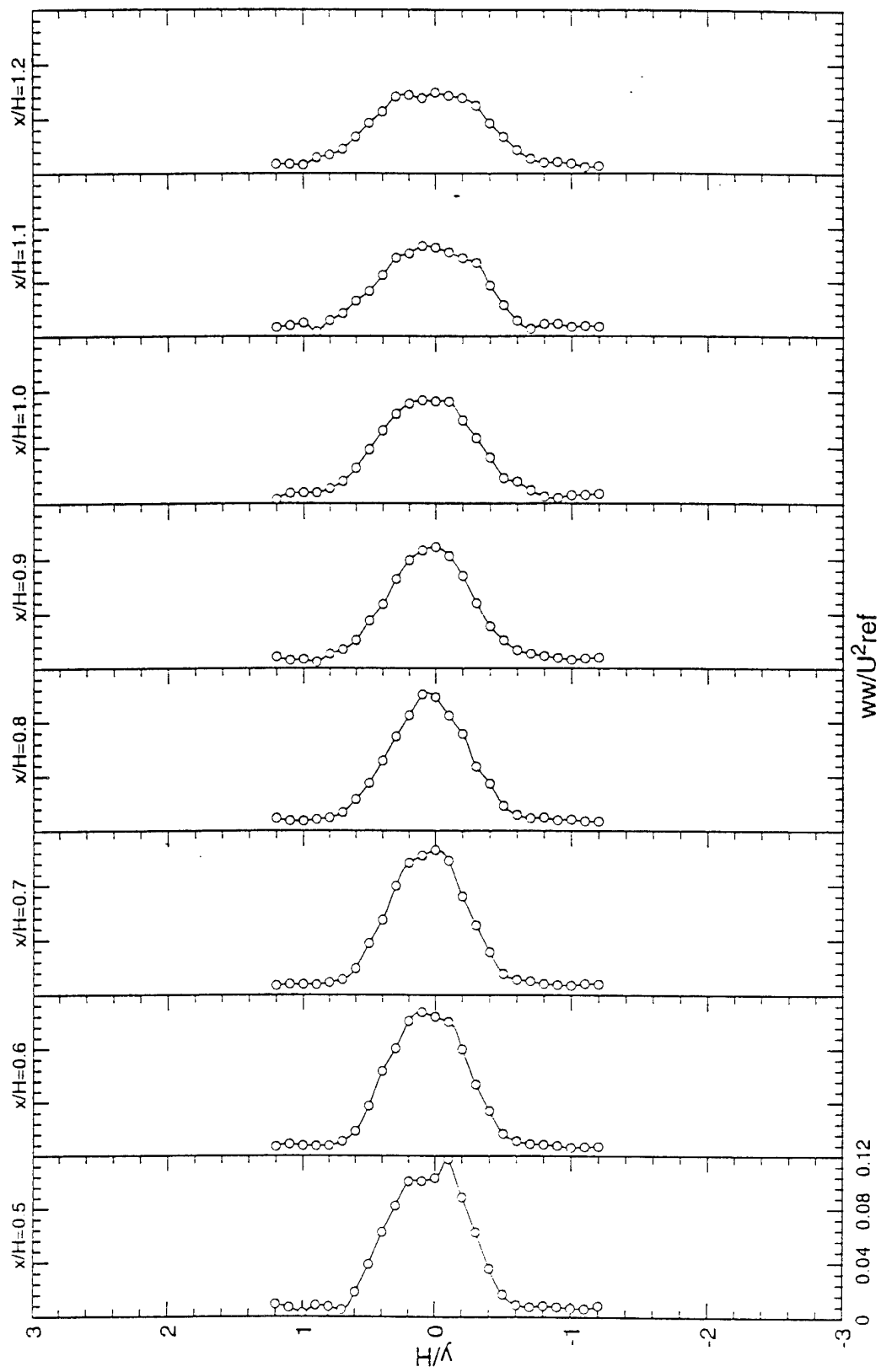


Figure 23. Normalized  $w w$  Turbulent Stress Distributions at Near Field Stations

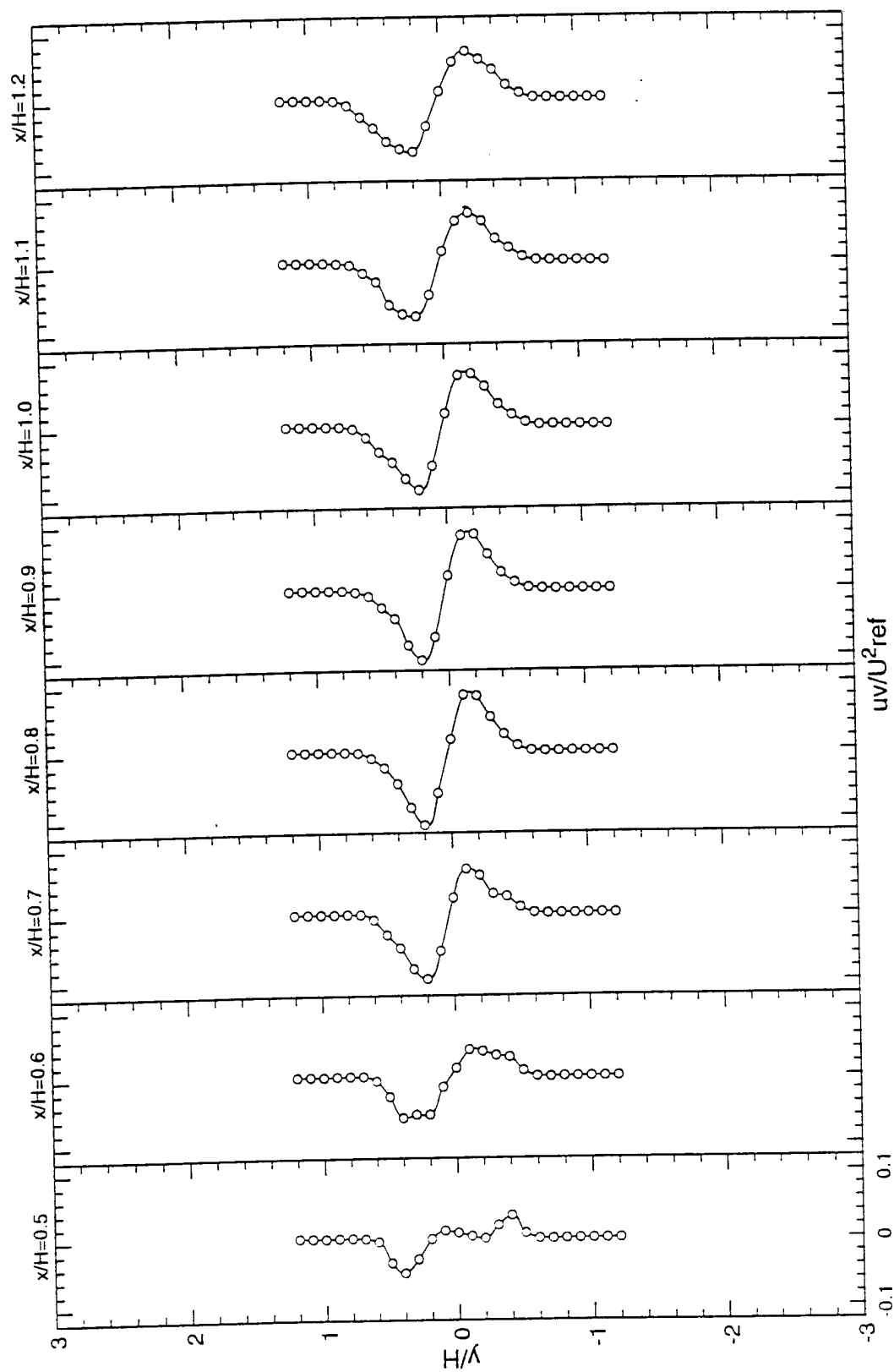


Figure 24. Normalized  $uv$  Turbulent Stress Distributions at Near Field Stations

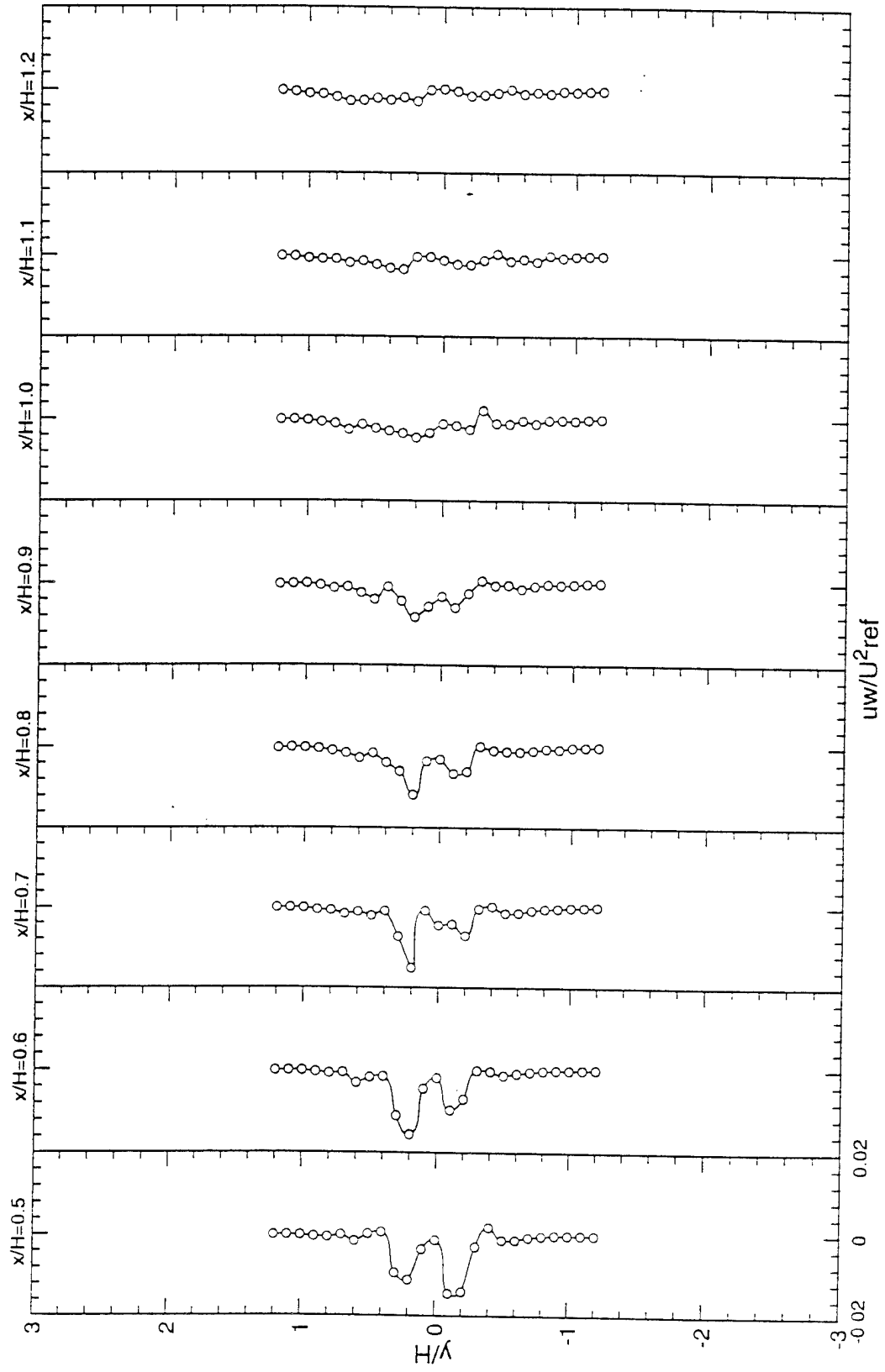


Figure 25. Normalized  $uw$  Turbulent Stress Distributions at Near Field Stations

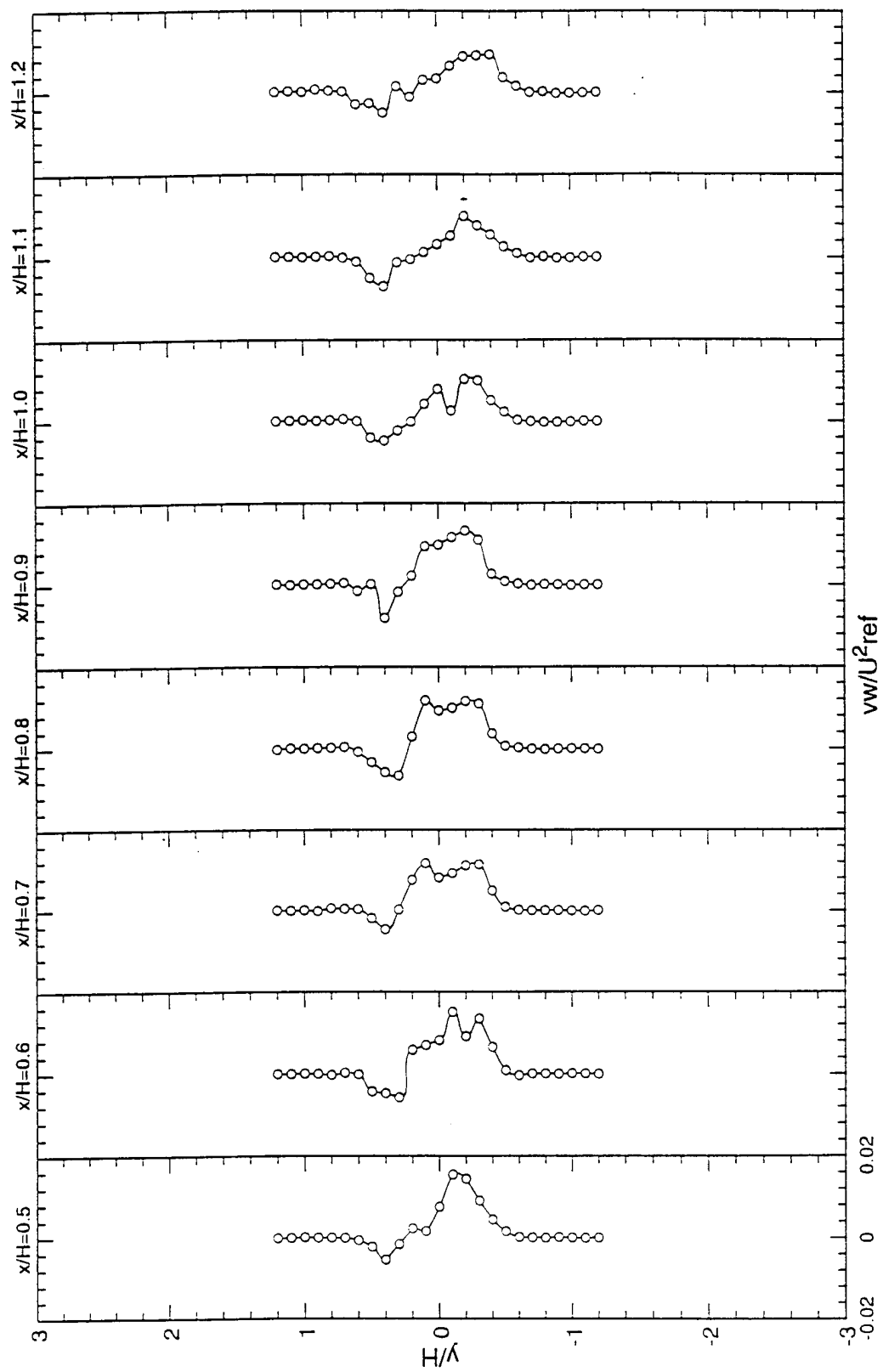


Figure 26. Normalized  $vw$  Turbulent Stress Distributions at Near Field Stations



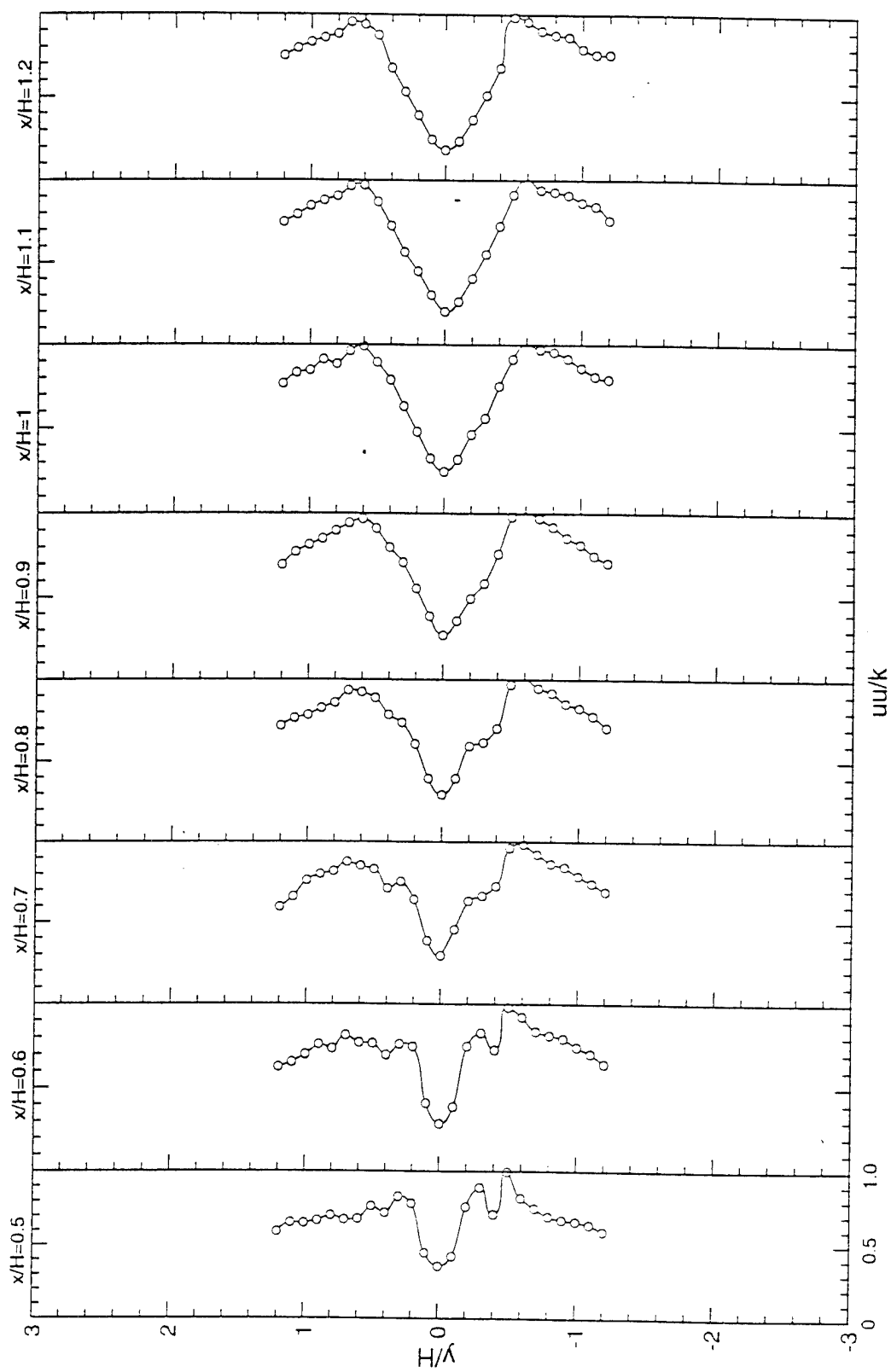


Figure 27. Axial Mean Normal Stresses - Isotropy Check (Isotropic  $uu/k = 2/3$ )

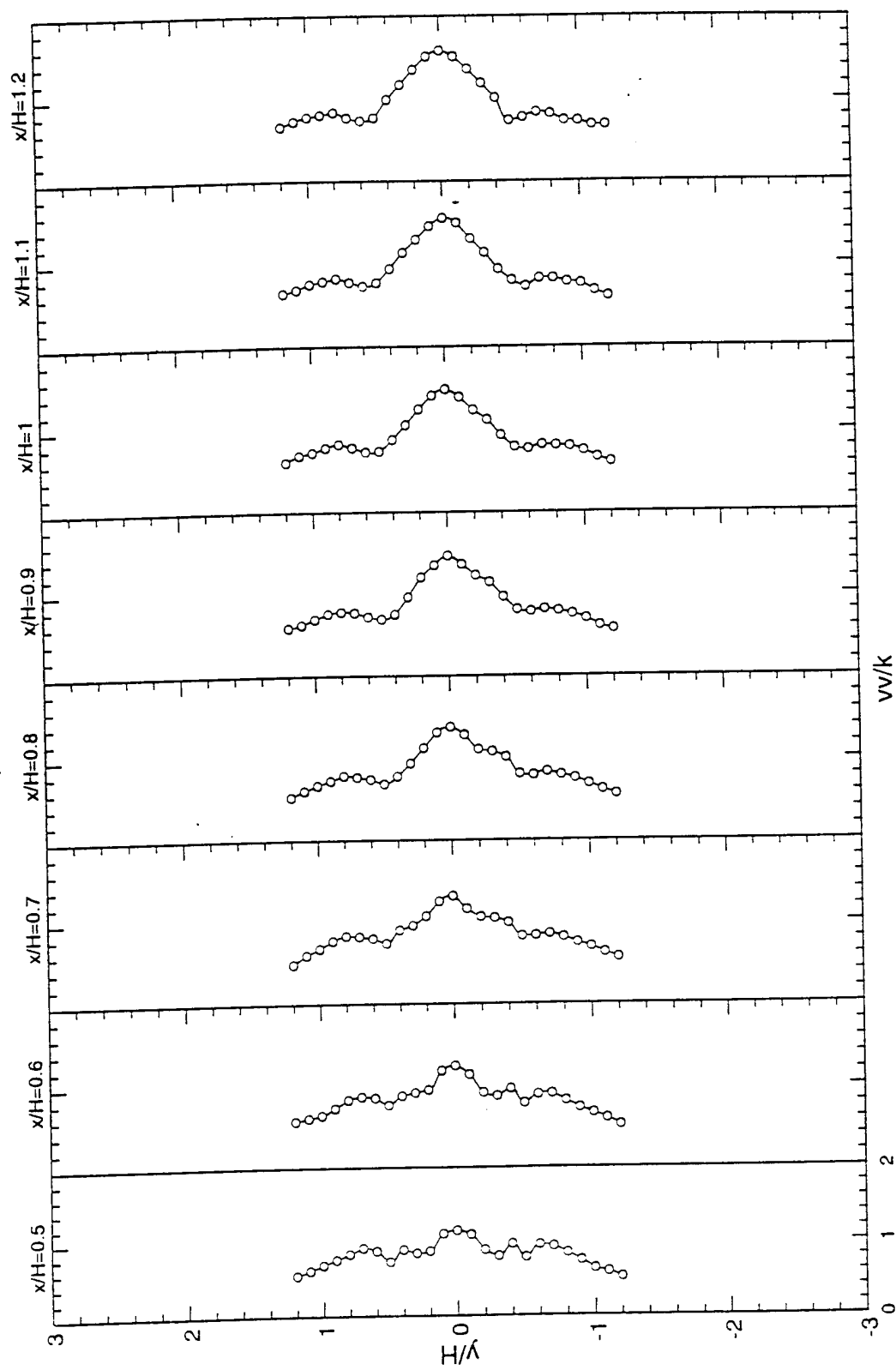


Figure 28. Transverse Mean Normal Stresses - Isotropy Check (Isotropic  $vv/k = 2/3$ )

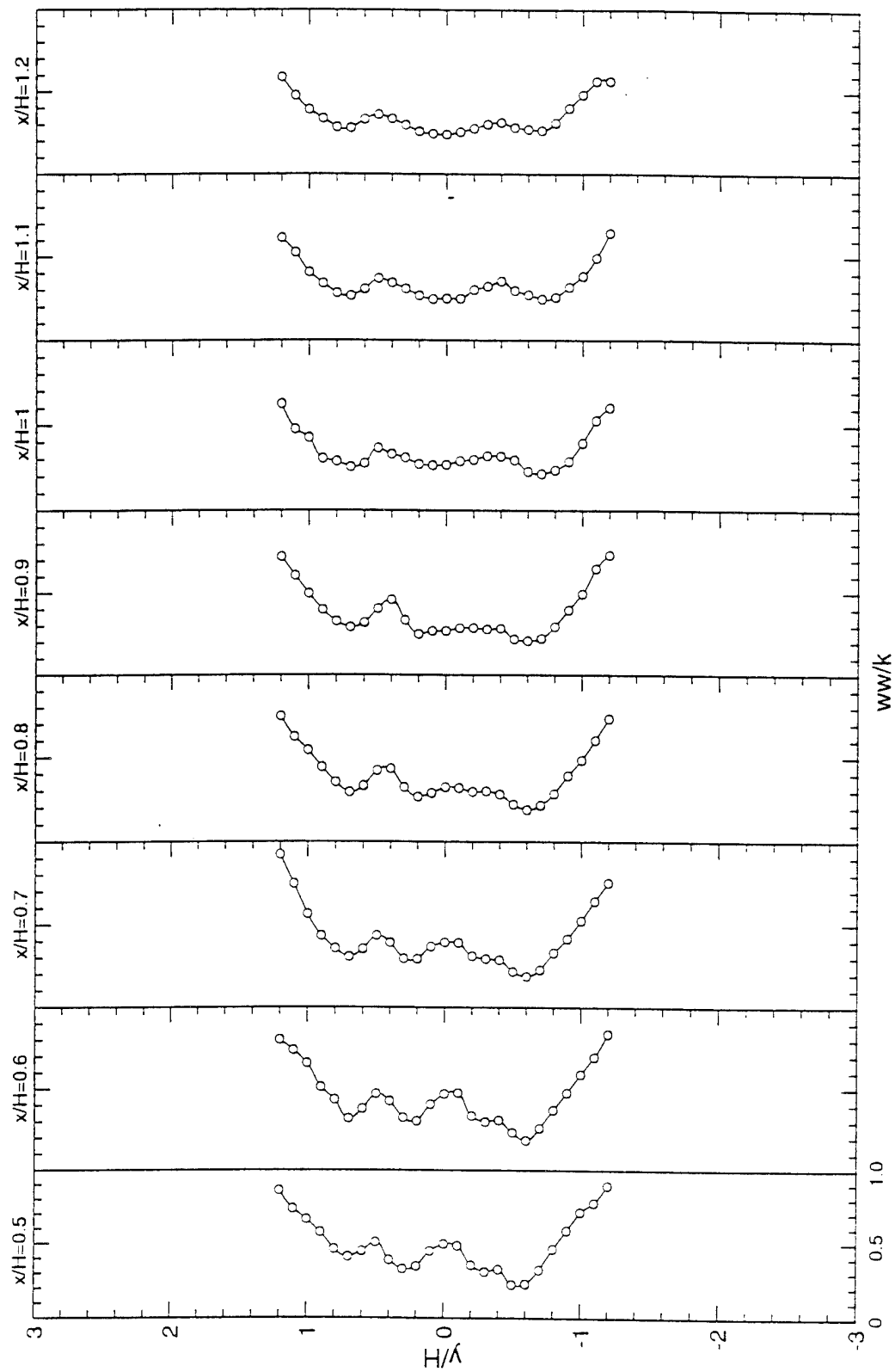


Figure 29. Spanwise Mean Normal Stresses - Isotropy Check (Isotropic  $ww/k = 2/3$ )

Also present in the near field data is the spanwise flow in the wake of the IFF. It was hypothesized that the presence of the tunnel boundary layers created a pressure force towards the center of the tunnel as the flow passed over the IFF. The flow reacts to the pressure force by forming four counter-rotating vortices on the back face of the IFF, as viewed from downstream. To test the hypothesis, several one-component (W) measurements were made in an attempt to capture the presence of the vortices (Figure 30). The flow can clearly be seen moving towards the centerline at the very near stations, and away from the centerline downstream of these stations, indicating the presence of at least two counter-rotating vortices, one on each side of the spanwise centerline. In addition, the vertical profiles show that there are two counter-rotating vortices in the vertical direction, with one on each side of the vertical centerline. Therefore, the original hypothesis is supported by the data.

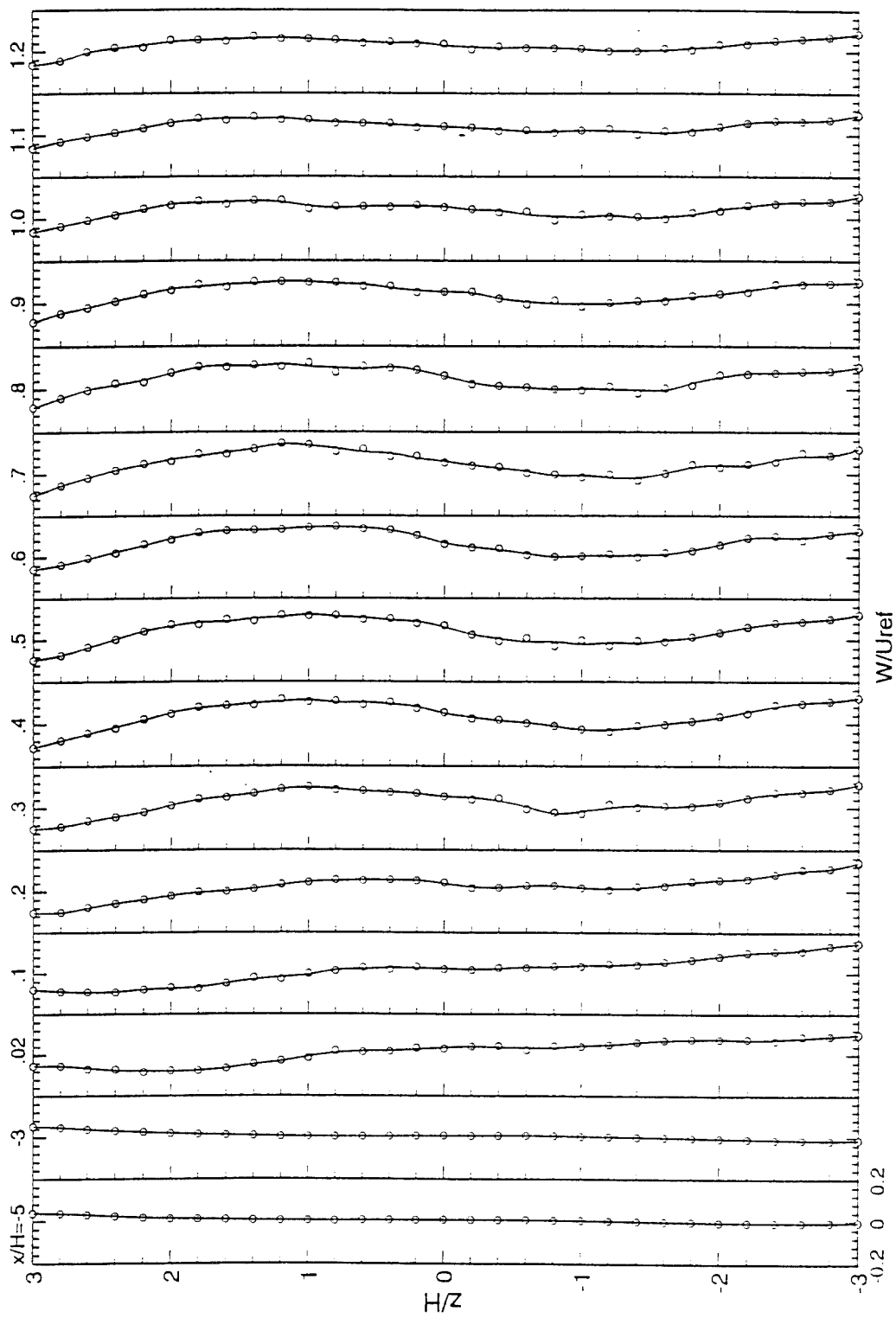


Figure 30. Normalized Mean Spanwise Velocity Profiles Indicate Presence of Vortex Flow; 1-D LDV

## 4.0 ISOTHERMAL NUMERICAL INVESTIGATION OF BASELINE IFF CONFIGURATION

The isothermal test matrix for the baseline IFF can be divided into seven incompressible cases. The first two cases were completed assuming that the flowfield was 2-D and symmetric; only the top half of the geometry was modeled and the solution was converged to steady state. The next three cases modeled the entire geometry in 2-D, and utilized time-accurate techniques to capture the unsteady flowfield behind the IFF. The last 2 cases were 3-D solutions. Table 1 summarizes the isothermal cases analyzed.

Table 1. Isothermal Numerical Test Cases

Case	Dimension	Grid	Turbulence Model	Time Integration
I	2-D	half-height	k- $\epsilon$	steady state
II	2-D	half-height	full Reynolds stress	steady state
III	2-D	full	laminar	time accurate
IV	2-D	full	k- $\epsilon$	time accurate
V	2-D	full	RNG k- $\epsilon$	time accurate
VI	3-D	full	RNG k- $\epsilon$	time accurate
VII	3-D	full	RNG k- $\epsilon$	time accurate

All solutions used 2nd order accurate central differencing, stabilized with upwind biasing. The time-accurate solutions were integrated through time using the Crank-Nicholson technique.

### 4.1 CFD Code

The numerical analyses for the current study was completed using a commercially available CFD code, CFD-ACE.<sup>24</sup> Developed by CFD Research Corporation, CFD-ACE includes the following features:

- solution of two- and three-dimensional Navier-Stokes equations for incompressible and compressible flows;
- cartesian and nonorthogonal curvilinear coordinates;
- single and multiblock grid topology;
- steady-state and time accurate solution algorithms;
- advanced turbulence modeling, including standard k- $\epsilon$ , RNG k- $\epsilon$ , and full Reynolds stress models;
- instantaneous, one-step, two-step and four-step combustion models with equilibrium products option, and prescribed and Monte Carlo PDF combustion models;

- g. first and second order upwind, central with damping, and Osher-Chakravarthy differencing schemes;
- h. co-located, fully implicit and strongly conservative finite volume formulation;
- i. pressure-based solution algorithms including SIMPLE and a variant of SIMPLER; and
- j. modified form of Stone's strongly implicit solver and conjugate gradient solver.

CFD-ACE has undergone a considerable amount of systematic quantitative validation for both incompressible and compressible flows. Over 50 validation cases have been performed to date, and good-to-excellent agreement has been shown between benchmark data and the numerical predictions.<sup>25,26</sup>

## 4.2 Computer

For all of the computations completed in the current study, a Silicon Graphics Indigo was used. The Indigo had a 100 MHz R4000 processor, and 96 MBytes of RAM, and 3 GBytes of hard drive disk space. Most of the steady-state analyses were completed overnight on the Indigo.

## 4.3 Geometry and Grid

The IFF configuration experimentally tested earlier by UTRC, and numerically by CFDRC in the Phase I effort of this study, was retained as the baseline configuration (Figure 31). The model has a 0.25 inch radius hemispherical nose with a 0.75-inch rectangular afterbody, for a total length of 1.00 inches, and a height of 0.5 inches. The total blockage was 17%, with the IFF installed in a 3 inch duct.

The computational domain started at a station of  $x/H = -5$ , and continued to  $x/H = 40$ . The time accurate grid consisted of four domains (Figure 32) with the following dimensions:

zone	dimensions	total
1	13 x 53	689
2	30 x 21	630
3	30 x 21	630
4	61 x 77	4697
		-----
		6646

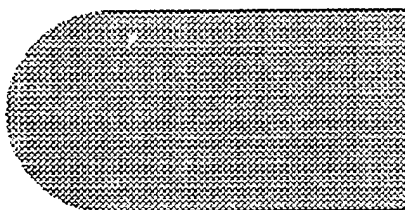
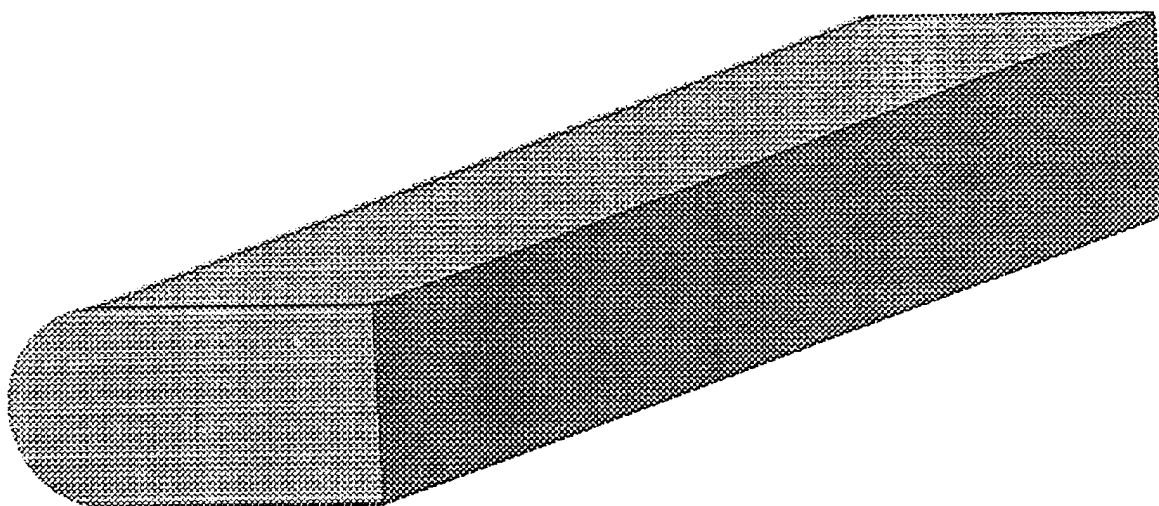


Figure 31. Baseline IFF Model used for Current Study



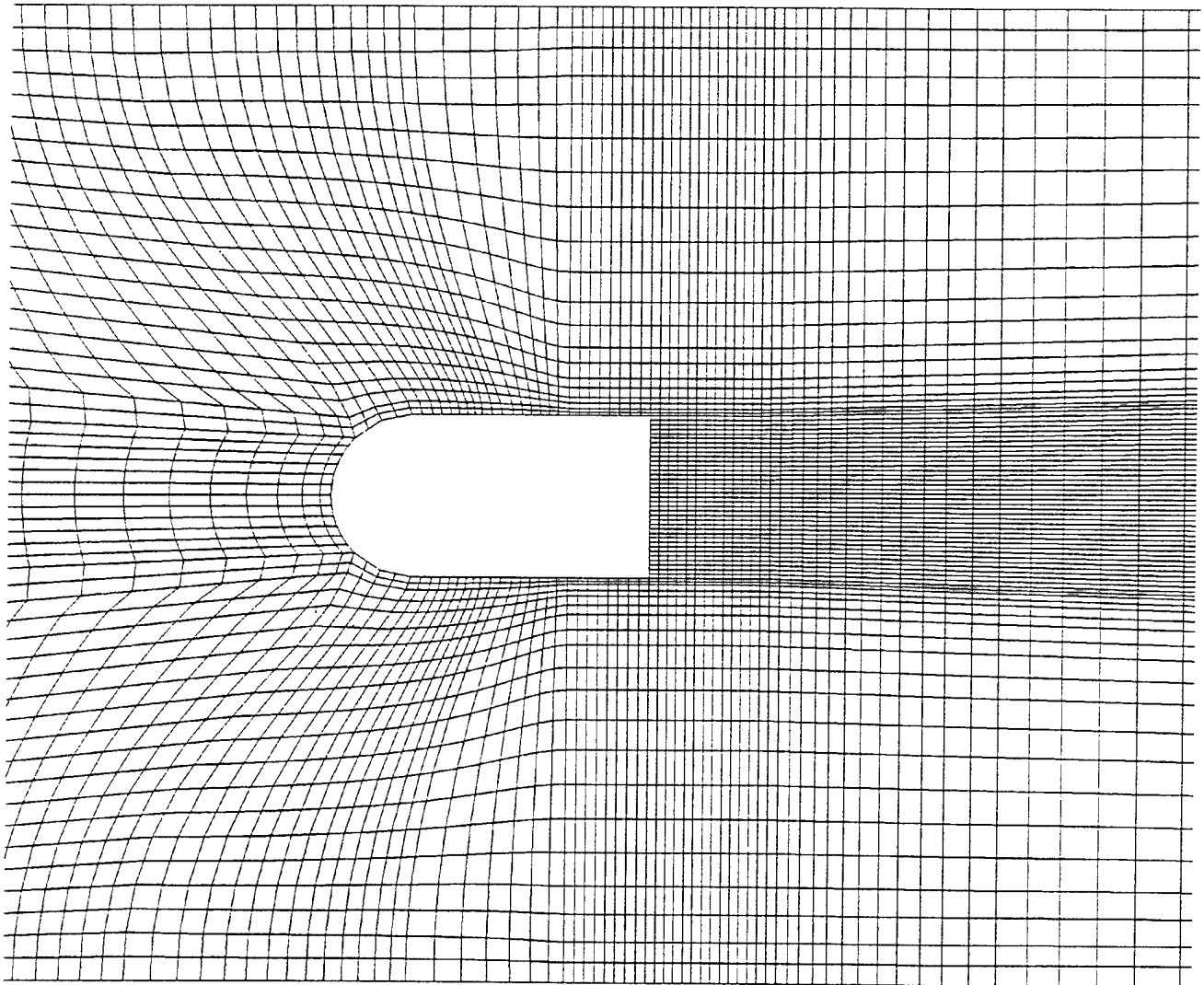
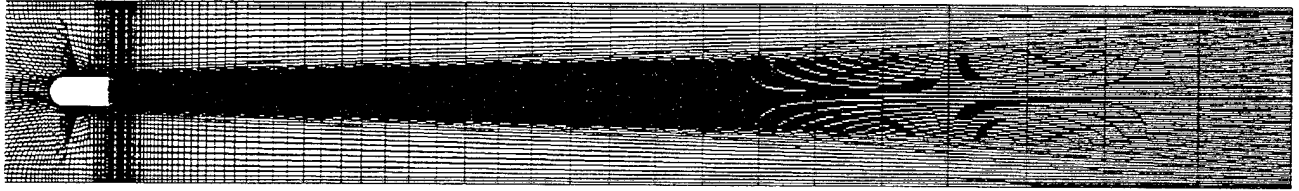


Figure 32. Computational Grid used for Numerical Study of Baseline IFF

The last zone contained the wake of the IFF and was the most densely packed, with 37 grid points across the back face of the IFF. For the steady-state solutions, the grid was cut in half at the centerline, and a symmetry plane was placed along the centerline.

All solutions used an inflow boundary condition set equal to the experimentally measured flow values at  $x/H = -5$ . The exit boundary condition was fixed at a constant pressure. The walls of the IFF and the walls of the tunnel were specified as no-slip boundaries. Freestream conditions were as follows:

$$\begin{aligned} U &= 24.5 \text{ m/s} \\ P &= 99257 \text{ Pa} \\ T &= 389 \text{ K} \\ u/U &= 0.04 \\ \mu_t &= 0.01 \end{aligned}$$

#### 4.4 Numerical Technique

##### Steady State Solutions

Cases I and II imposed a symmetry plane at the centerline of the geometry, preventing the asymmetric vortex shedding in the wake, and producing steady-state flow. The initial conditions were set to the freestream conditions, and the solution was converged 4 orders of magnitude for all variables. Convergence was typically completed within 1000 iterations, requiring 6 hours of CPU time.

After the solution was completed, the variables of interest were linearly interpolated to the experimental stations for comparison to the experimental data. The variables used in the data comparison were the mean velocity components ( $U$ ,  $V$ ), the mean Reynolds normal stresses ( $uu$ ,  $vv$ ), and the mean Reynolds shear stress ( $uv$ ). For the  $k$ - $\epsilon$  turbulence model, the modeled Reynolds stress components were extracted from the solution using the Boussinesq approximation:

$$\overline{u_i u_j} = \frac{\mu_t}{\rho} \left( \frac{\partial \bar{U}_i}{\partial x_j} + \frac{\partial \bar{U}_j}{\partial x_i} \right) - \frac{2}{3} k \delta_{ij}$$

where:  $\mu_t = 0.09 \rho \frac{k^2}{\epsilon}$

For Case II, the full Reynolds Stress Model (RSM) was added to CFD-ACE. The work was completed by Dr. Yong Lai of CFDRC, and included several validation cases. A summary of the Reynolds stress turbulence model employed, and a review of the validation cases is presented in Appendix A.

### Time-Accurate Solutions

Cases III-VII involved solving the time-accurate equations over the full grid. Since no symmetry plane was imposed on the centerline, the flow was free to oscillate about the centerline.

Solving the unsteady Navier-Stokes equations generates two contributions to the turbulence components. The first is the resolved contribution, and is generated by the large scale fluctuations in the velocity field the CFD solution computes. The fluctuations at a given point must be collected and analyzed with statistical methods in a manner analogous to collected LDV data. The second contribution to the turbulence comes from the turbulence model. The turbulence model contribution must also be computed at each time step (e.g. using the Boussineq approximation for the  $k$ - $\epsilon$  model) and averaged over time. The two contributions are added to obtain the full turbulence contribution.

Using turbulence modeling with the Reynolds averaged Navier-Stokes equations is valid only if the resolved mean flow fluctuations and the modeled turbulence perturbations are not correlated, i.e., there exists a spectral gap in the time scales of the two components.<sup>27</sup> If the two components are correlated, the assumptions made during the Reynolds averaging process are violated, and the more rigorous Large Eddy Simulation (LES) procedure must be used. The LES procedure formally separates the scales using a filtering technique, that restricts the turbulence model to scales smaller than the resolved scales.

The time scales for the Reynolds averaged approach can be compared to determine the validity of the application. For the current study, the resolved time scale can be assumed to be the inverse of the vortex shedding frequency. For the  $k$ - $\epsilon$  models, a representative turbulence time scale ( $\tau$ ) can be calculated by  $\tau = k/\epsilon$ .

For the unsteady cases, the solution procedure was started using the same method as the steady-state cases; the freestream conditions were used as the initial conditions, and the solution was run for 200 iterations in the steady-state mode. Since the inflow conditions were not exactly symmetric, the flow quickly began shedding alternating vortices in the wake. After 200 iterations, the solution was switched into the time-accurate mode to properly capture the vortex shedding process.

In the time accurate mode, the solution was progressed at time steps of  $5.0 \times 10^{-6}$  sec. During each time step, the variables were converged at least 3 orders of magnitude. The solution was advanced 4500 ( $\sim 9$  vortex shedding cycles) iterations in the time-accurate mode to allow any residuals from the initial start-up to exit the downstream boundary. The solution was then restarted and advanced approximately 2500 time steps to collect the turbulence statistics. Since only a few vortex shedding cycles were included in the collection sample ( $\sim 5$ ), care was taken to

ensure that the statistics were collected over a whole period of the vortex shedding cycle. During the statistics collection process, a sample was taken every 10 time steps and averaged with the existing sample set. At the completion of the run, the appropriate turbulence quantities were calculated in the same fashion as the experimental values (see Appendix B).

Case III provided a solution to the laminar Navier-Stokes equations, using an elevated laminar viscosity ( $1 \times 10^{-3} \text{ m}^2/\text{sec}$ ) as a simple model for the effect of turbulence. Such a solution resolves all velocity and Reynolds stresses to fidelity of the grid, without any actual modeling of the turbulence components.

Case IV employed the standard  $k$ - $\epsilon$  turbulence model with the time-accurate solver. An evaluation of the time scales will be presented with the data, to assess the presence of a spectral gap between the resolved and modeled turbulence scales.

Case V used a relatively new formulation of the  $k$ - $\epsilon$  turbulence model derived from the Renormalized Group theory (RNG). The RNG  $k$ - $\epsilon$  model is functionally very similar to the standard  $k$ - $\epsilon$  model. The major difference is that the ad-hoc constants used in the standard model are now derived from the RNG theory. The differences in the constants are as follows:

*Standard  $k$ - $\epsilon$  model*

$$C_\mu = 0.09, \quad C_{\epsilon 1} = 1.44, \quad C_{\epsilon 2} = 1.92 \\ \sigma_k = 1.0, \quad \sigma_\epsilon = 1.3$$

*RNG  $k$ - $\epsilon$  model*

$$C_\mu = 0.085, \quad C_{\epsilon 1} = 1.42 - \frac{\eta(1 - \eta/\eta_0)}{1 + \beta\eta^3} \\ C_{\epsilon 1} = 1.68, \quad \sigma_k = 0.7179, \quad \sigma_\epsilon = 0.7179 \\ \eta = \frac{Sk}{\epsilon} \quad S = \sqrt{2 S_{ij} S_{ij}} \quad \eta_0 = 4.38 \quad \beta = 0.015$$

The RNG  $k$ - $\epsilon$  model is derived by making an expansion about an equilibrium state with known Gaussian statistics, with the effects of mean strains being represented by a random force. The bands of the smallest scales are systematically removed and the remaining space is rescaled.<sup>28</sup> This process is continued until only the resolvable scales remain. Speziale and Thangam<sup>29</sup> have shown excellent results for a backward facing step using the RNG  $k$ - $\epsilon$  model. While the RNG model can easily be

integrated down to the wall without the use of wall functions, the method used in the current study still employed the standard wall functions.

Cases VI and VII were also unsteady and used the RNG  $k-\epsilon$  model, but solved the 3-D equations to provide an extra degree-of-freedom to the resolved turbulence component. Case VI used a relatively small spanwise domain ( $\sim 1H$ ) while Case VII covered a larger spanwise domain ( $\sim 6H$ ).

## 4.5 Numerical Results

### Steady State

The results for the two steady state cases are presented in Figures 33-37, and compared to the experimental data. The results are shown for the near wake region only, from  $x/H = 0.5$  to  $x/H = 1.2$ . The predicted mean velocities for Case I indicate that the numerical recirculation bubble for both cases extends to  $x/H=2$ , much further downstream than the experimentally determined bubble position. The numerical bubble length of two base heights, or four half bluff body heights, is similar to that of a backward-facing step. This is to be expected since the model resembles a backward-facing step with a slip wall at the centerline. The predicted Reynolds stresses are also comparable to those measured in backward-facing step flows. However, the experimentally measured Reynolds stresses for the IFF were found to be  $\sim 5$  times higher than those found in backward-facing step flows. Additionally, the turbulence values were clearly nonisotropic for the IFF flow, and the  $k-\epsilon$  model predicted isotropic turbulence.

The Reynolds stress model, while not restricted to isotropic turbulence, does not show a marked improvement over the standard  $k-\epsilon$  model. The RSM solves four more nonlinear partial differential equations than the  $k-\epsilon$  model and requires considerably more time to converge. In the case of the flameholder, the RSM model is not worth the increased computational effort. Since the model does not improve the solution by any significant amount, the error is probably not due to the nature of isotropic turbulence.

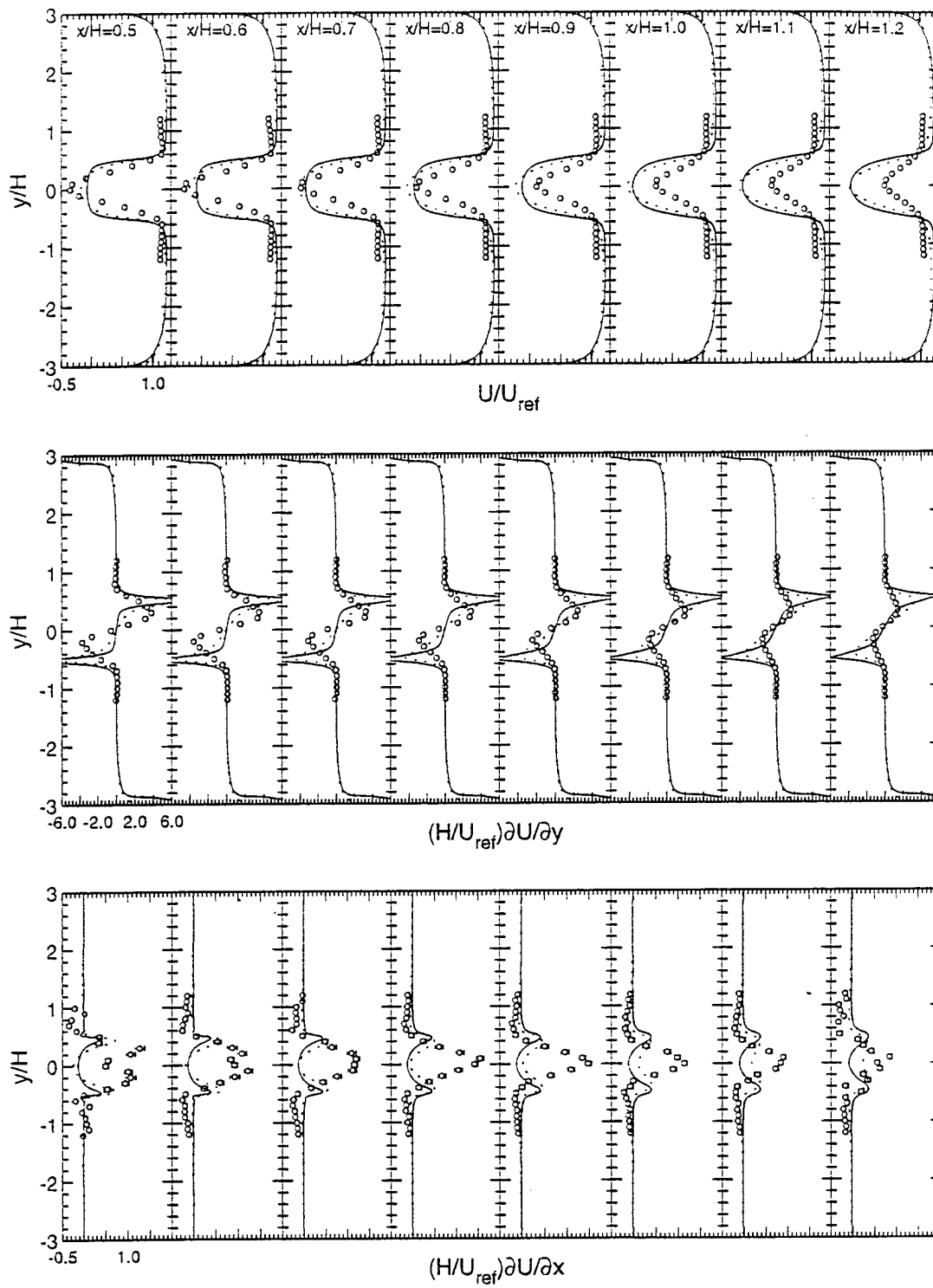


Figure 33. Normalized Mean Axial Velocity and Velocity Gradient Distributions  
 (○ data — RSM ···  $k-\epsilon$ )

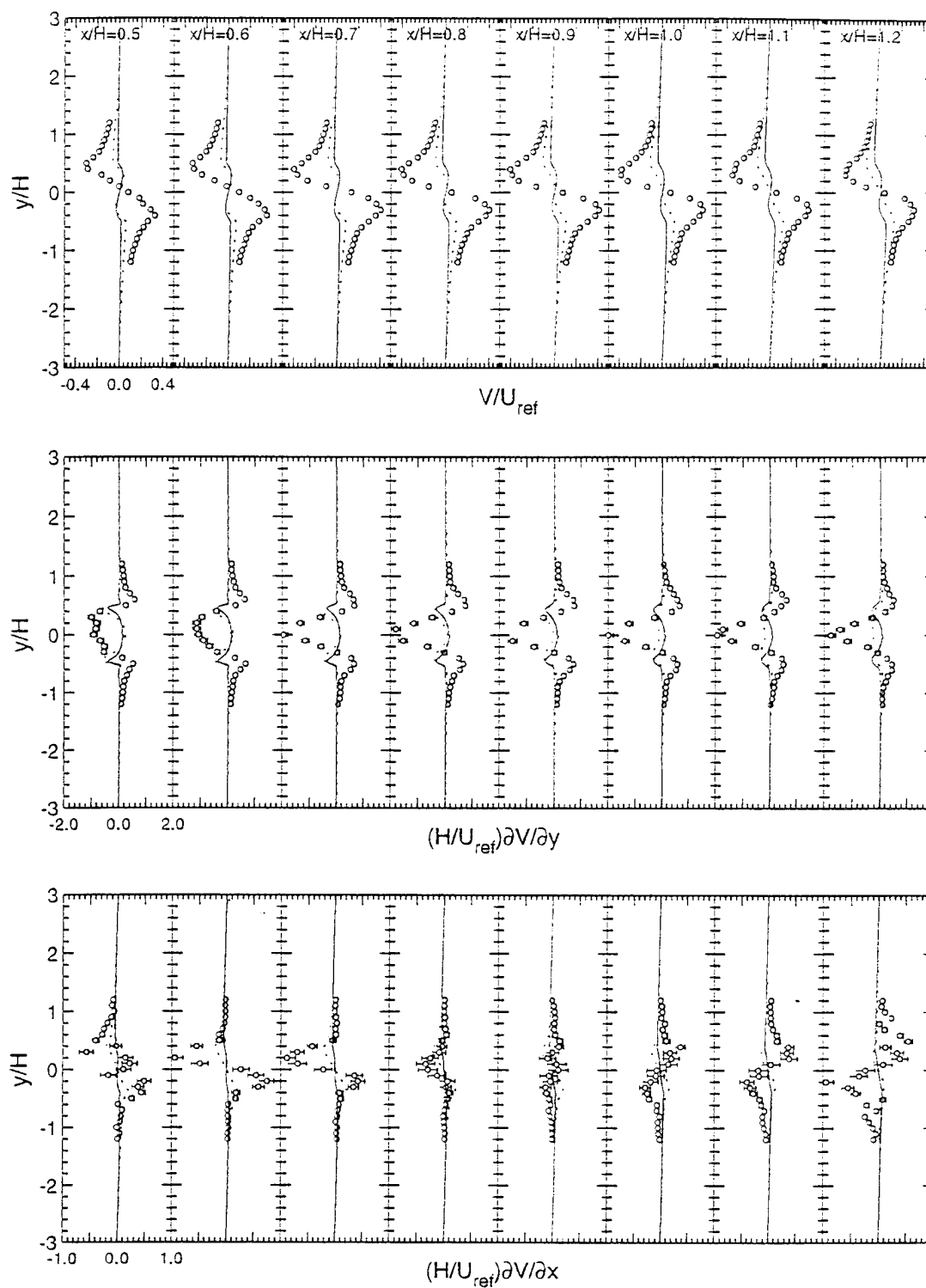


Figure 34. Normalized Mean Transverse Velocity and Velocity Gradient Distributions (○ data — RSM ···  $k-\epsilon$ )

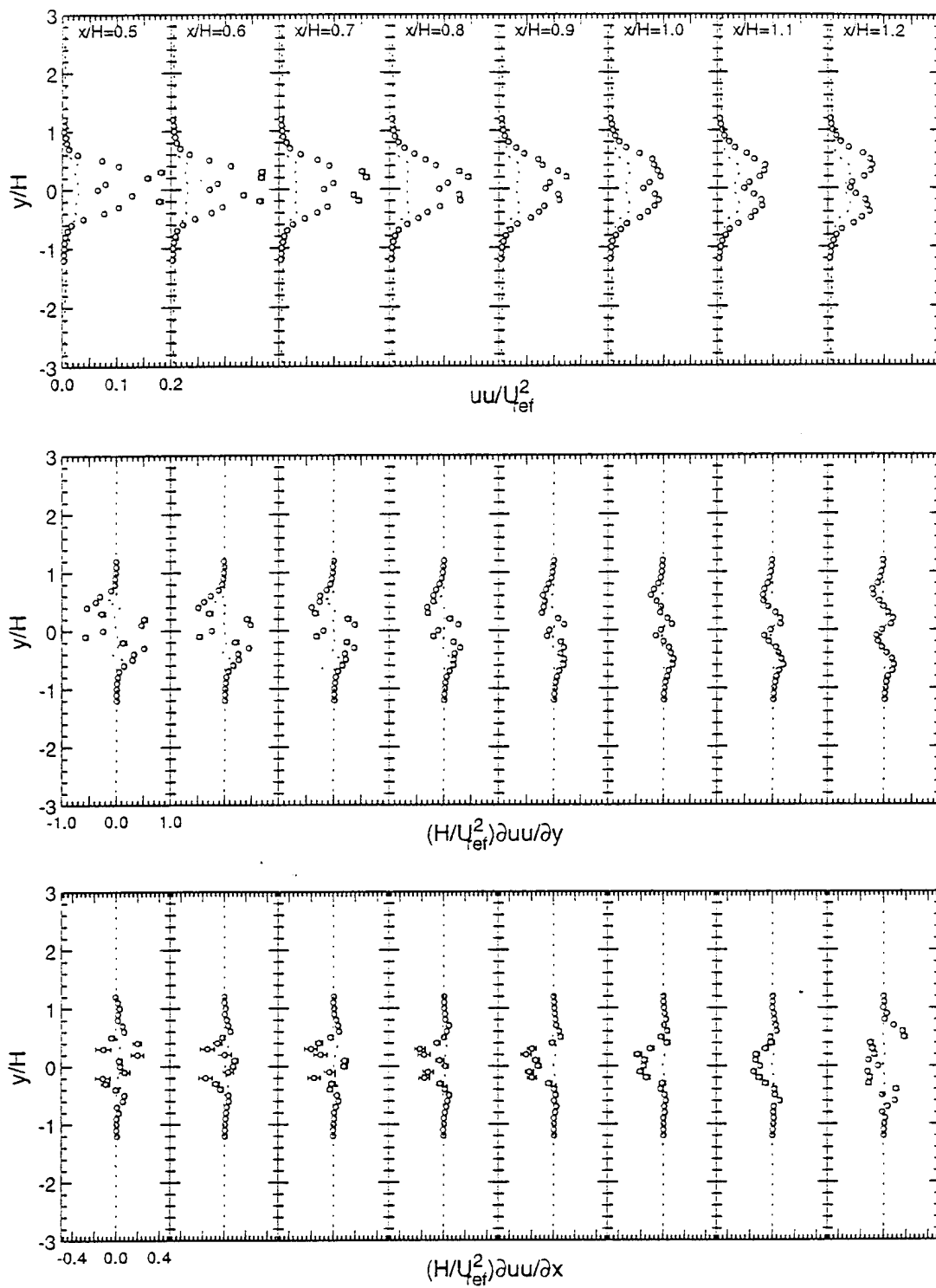


Figure 35. Normalized  $uu$  Turbulent Stress and Stress Gradient Distributions  
(O data ---  $k-\epsilon$ )



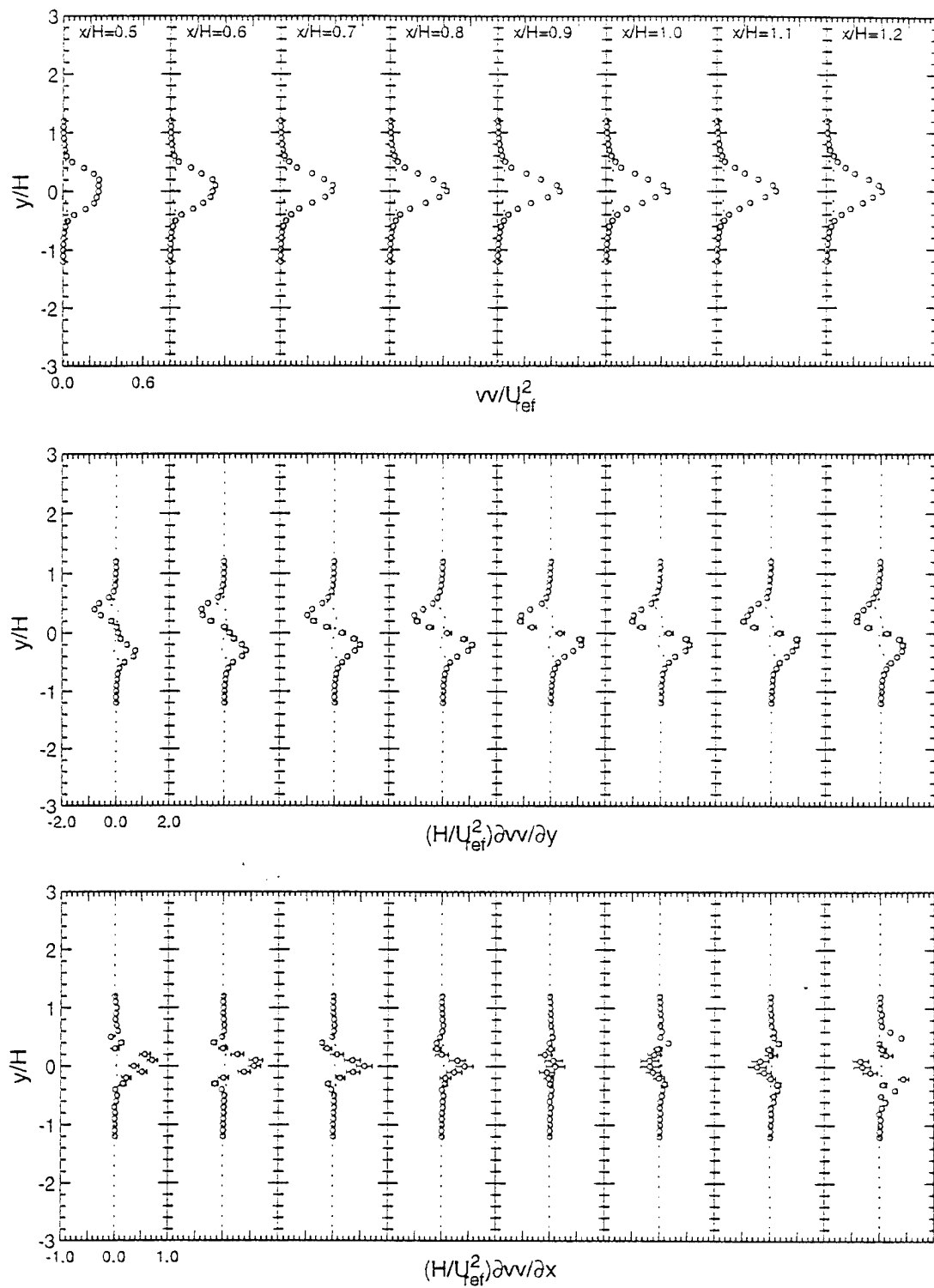


Figure 36. Normalized  $vv$  Turbulent Stress and Stress Gradient Distributions  
(o data ---  $k-\epsilon$ )

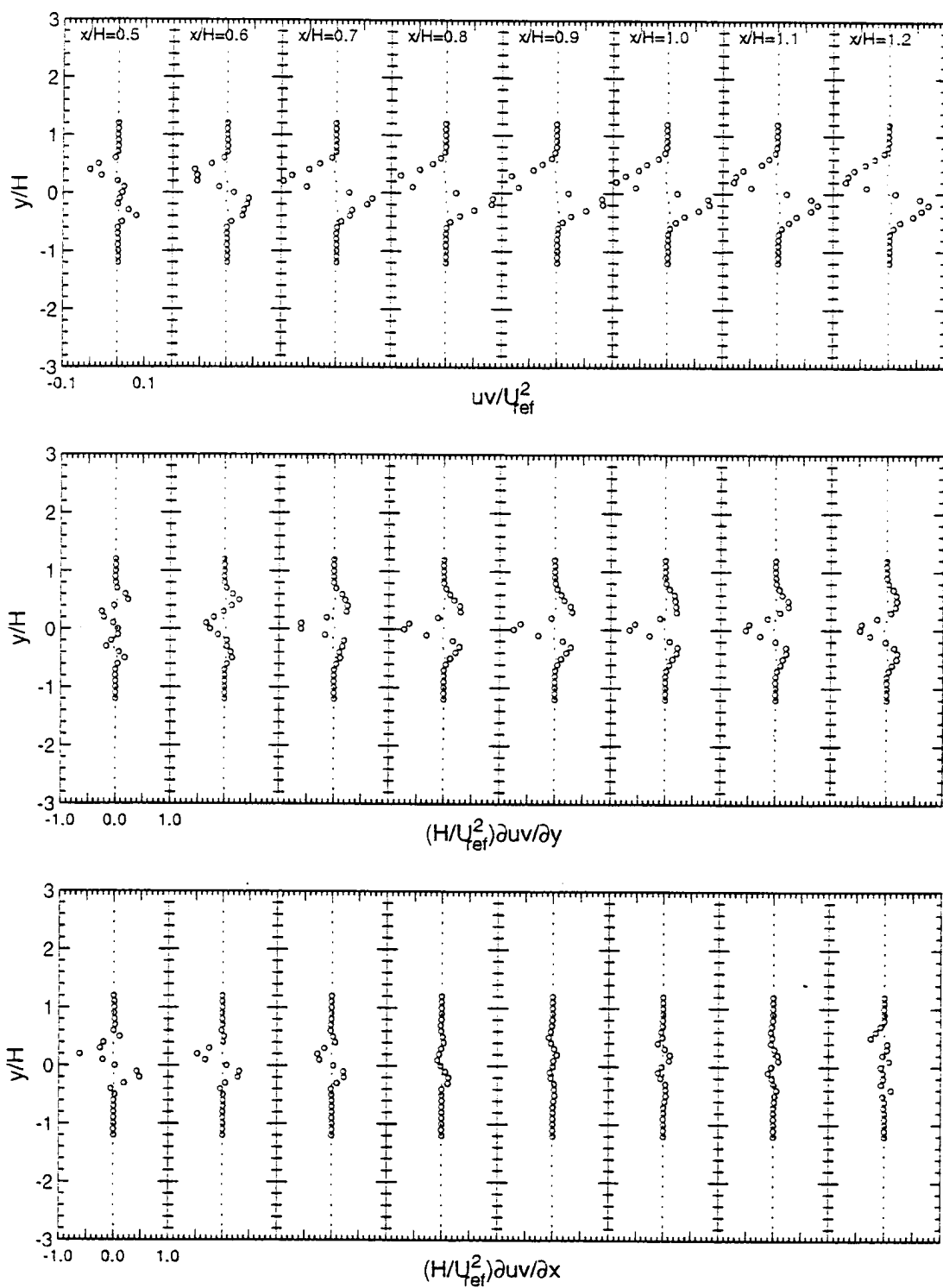


Figure 37. Normalized  $uv$  Turbulent Stress and Stress Gradient Distributions  
 (○ data    - - -  $k-\epsilon$ )

### Time Accurate

The time accurate solutions were initiated in an attempt to improve upon the steady-state computational results. Since the experimental results indicated that the IFF was shedding alternating large-scale vortices from the top and bottom corners of the IFF, significant turbulence must be generated from the vortices. Such turbulence would be beyond that generated by the backward-facing step. Therefore, in order to properly predict the higher turbulence, the unsteady nature of the flowfield must be taken into account. It is not reasonable to believe that a single turbulence model could properly predict a backward facing step and a bluff body, since the only geometrical difference is the boundary layer at the symmetry plane. A time-accurate simulation is necessary to properly capture the increased turbulence.

The three time-accurate calculations (Cases III, IV, and V) were able to predict the vortex shedding behind the IFF, and a sample result showing the instantaneous streamlines is presented in Figure 38. The structure of the vortex shedding is evident as the vortex from the lower surface has been shed downstream and the upper surface vortex is forming. The vortex pattern continues downstream, but as the vortex convective velocity accelerates to match the freestream velocity, the presence of the vortices in the streamlines is disguised.

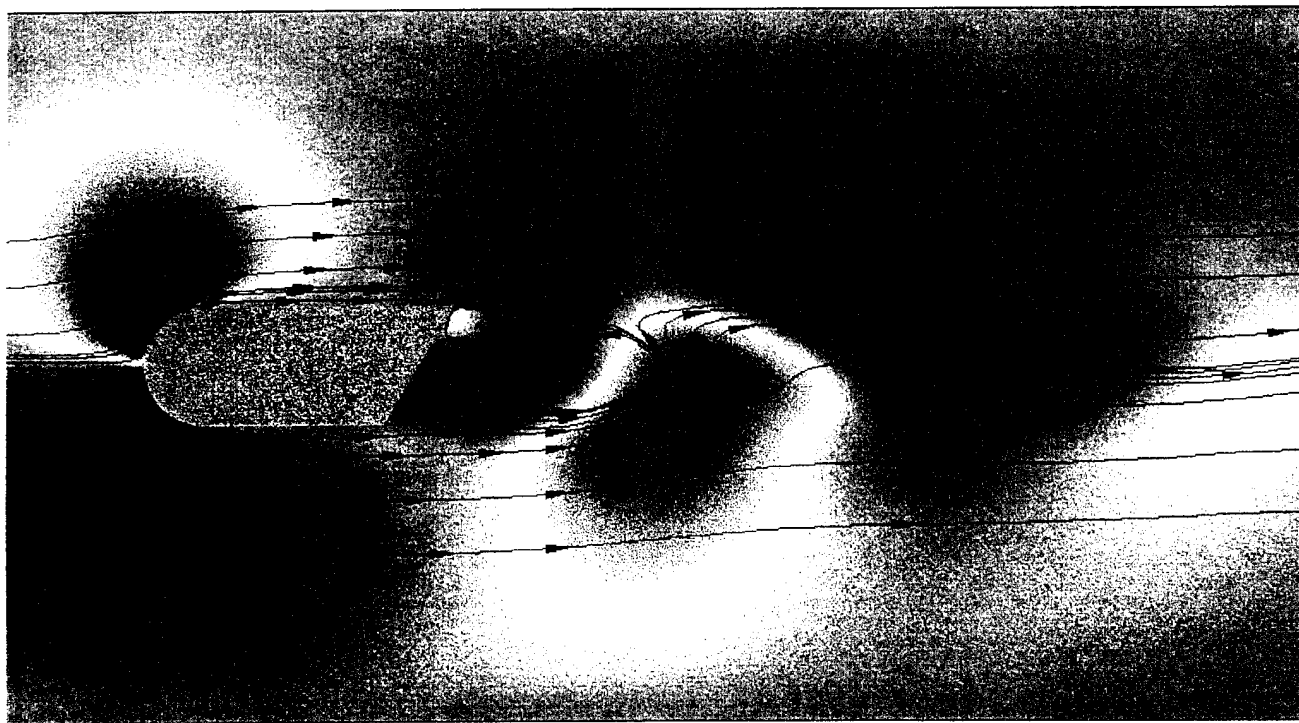


Figure 38. Streamlines Show Unsteady Vortex Motion Behind Example Bluff Body

Case III used a constant viscosity of  $1 \times 10^{-3} \text{ m}^2/\text{sec}$ , and predicted a Strouhal number of 0.271, 15% higher than the experimental value of 0.243. The mean and fluctuating velocity components are compared in Figures 5.9-5.13. The velocity data from the laminar unsteady solution showed much better agreement with the data than the steady state results. The predicted recirculation bubble length of 1.08 H was much closer to the experimental value of 0.9 H. In addition, the qualitative agreement of the turbulence profiles indicated that the vortex shedding is the dominant contributor to the turbulence in the experiment. A close examination of the data revealed that the strength of the shed vortices was probably too strong. To check the effect of the laminar viscosity on the solution, the run was repeated for two different values of viscosity,  $1 \times 10^{-2} \text{ m}^2/\text{sec}$  and  $1 \times 10^{-5} \text{ m}^2/\text{sec}$ . At the higher value of viscosity, the vortex shedding was damped and the solution returned to the steady-state results. At the lower viscosity, the vortex shedding frequency was increased slightly, but the strength of the vortices increased, significantly degrading the data comparison. Therefore, it was concluded that more accurate turbulence modeling was required to properly predict the flowfield.

Case IV addressed the issue of turbulence modeling by employing the standard k- $\epsilon$  turbulence model with the standard wall functions. The first attempt at using the k- $\epsilon$  turbulence model with the unsteady flow yielded a steady-state solution. Other researchers<sup>30</sup> have found similar results and have blamed the numerical formulation of the turbulence model. However, later studies found the damped behavior to be a function of the differencing scheme employed instead of the turbulence model.<sup>31</sup> The first attempt in the current study employed first order differencing in space. When central differencing was used, the vortex shedding was maintained. The k- $\epsilon$  model predicted the closest value for the Strouhal number at 0.240 (~1% low). The mean velocities and Reynolds stresses are shown in Figures 39-43. Examination of the mean axial velocities indicates that the k- $\epsilon$  solution is not much different from the laminar case, with the length of the recirculation zone about the same. However, the transverse velocity does show some differences. Very near the IFF, the k- $\epsilon$  model shows a better match to the data, with the inflection point at the centerline somewhat reduced. But further downstream, the laminar case maintains the higher transverse velocities reflected by the experimental data. This is due to the higher turbulent viscosity predicted in the wake by the k- $\epsilon$  model (0.004 vs 0.001 for the laminar case). The normal axial stress was also similar to the laminar case very near the IFF. But the axial trends were not correct for either the k- $\epsilon$  or laminar cases, showing increasing peak stresses with axial position, while the experiment showed a decreasing peak stress.

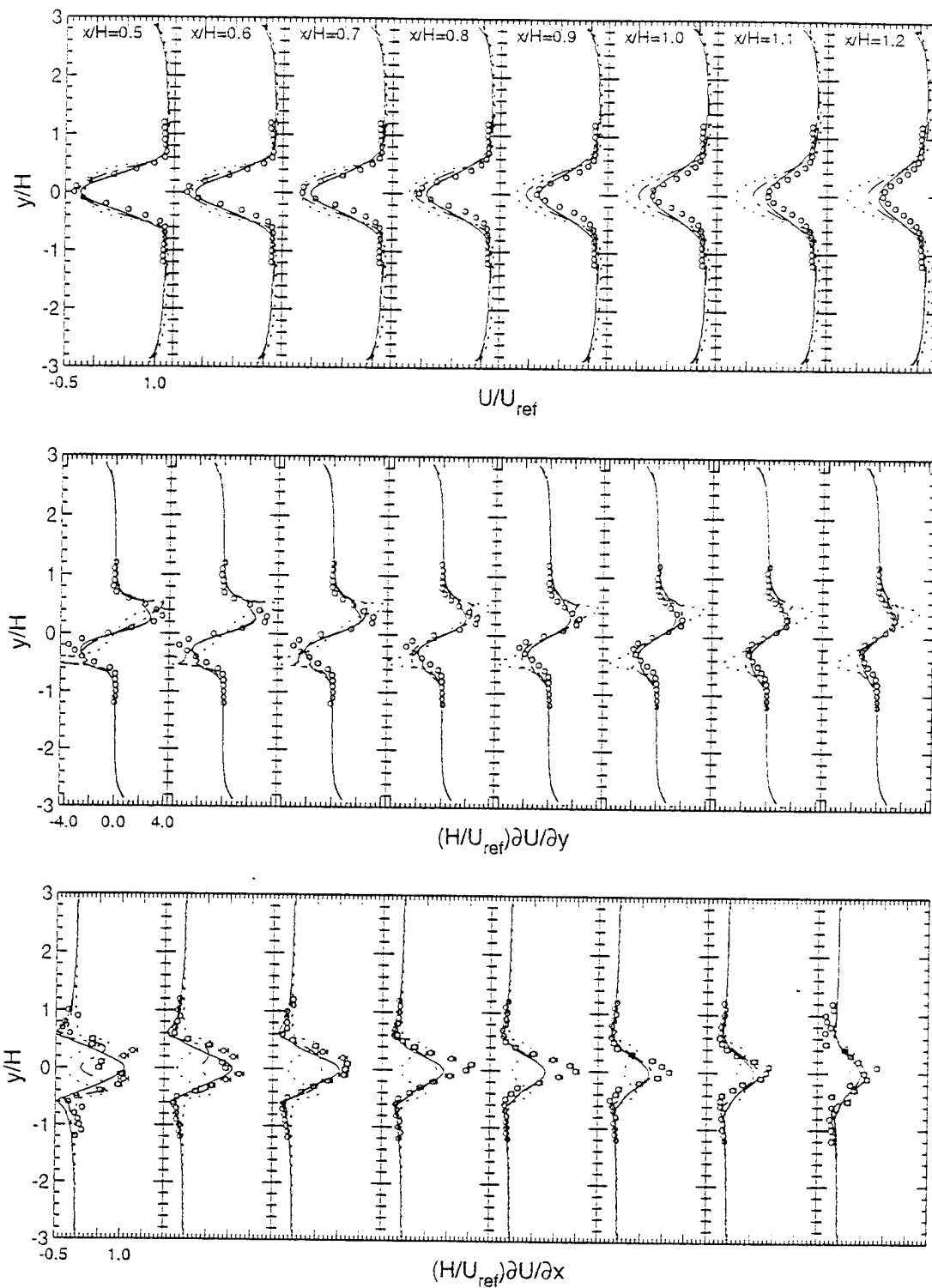


Figure 39. Normalized Mean Axial Velocity and Velocity Gradient Distributions  
 (○ data — RNG-2D ··· laminar — -  $k-\epsilon$ )

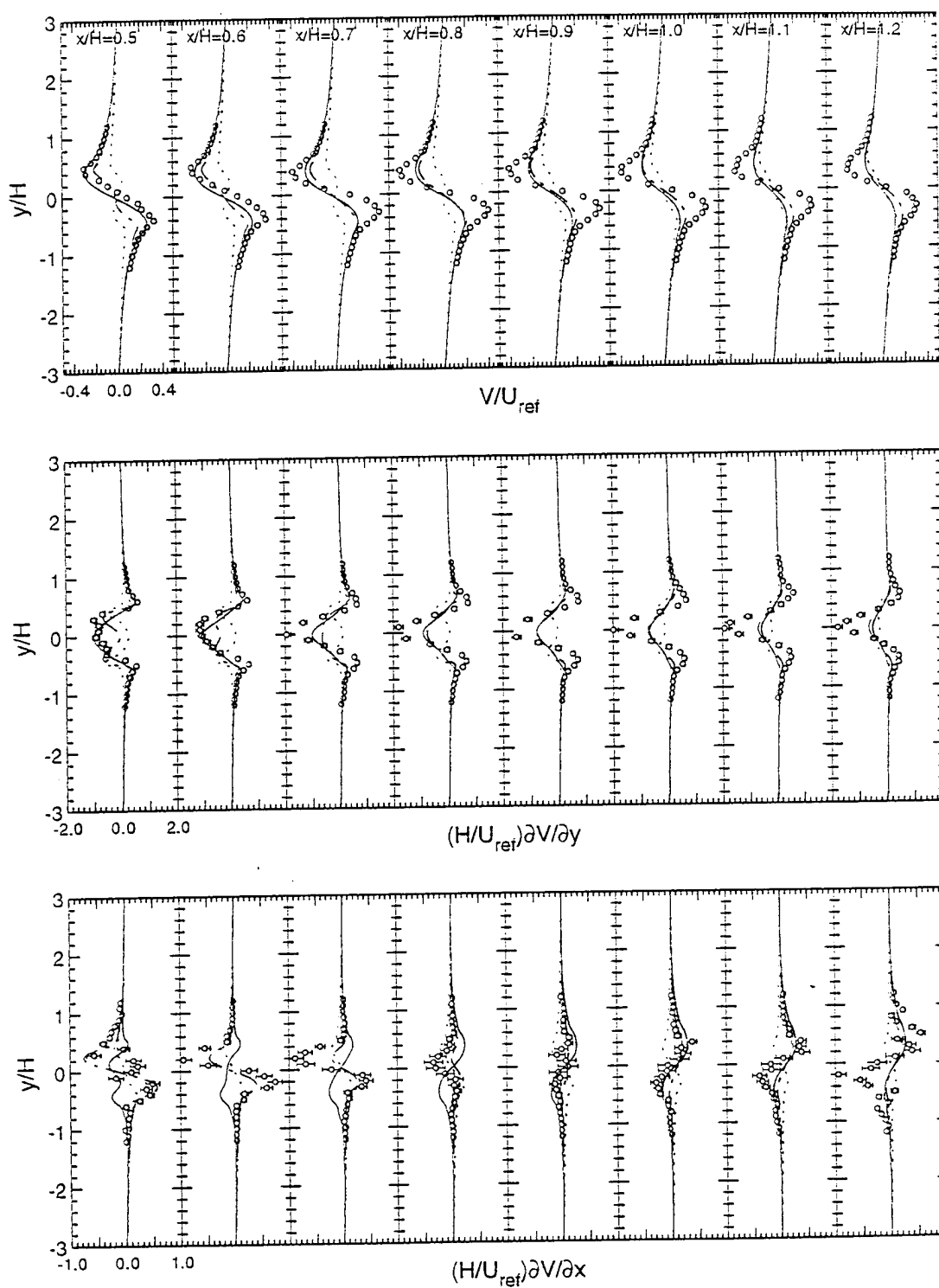


Figure 40. Normalized Mean Transverse Velocity and Velocity Gradient Distributions (○ data — RNG-2D ··· laminar — -  $k-\epsilon$ )

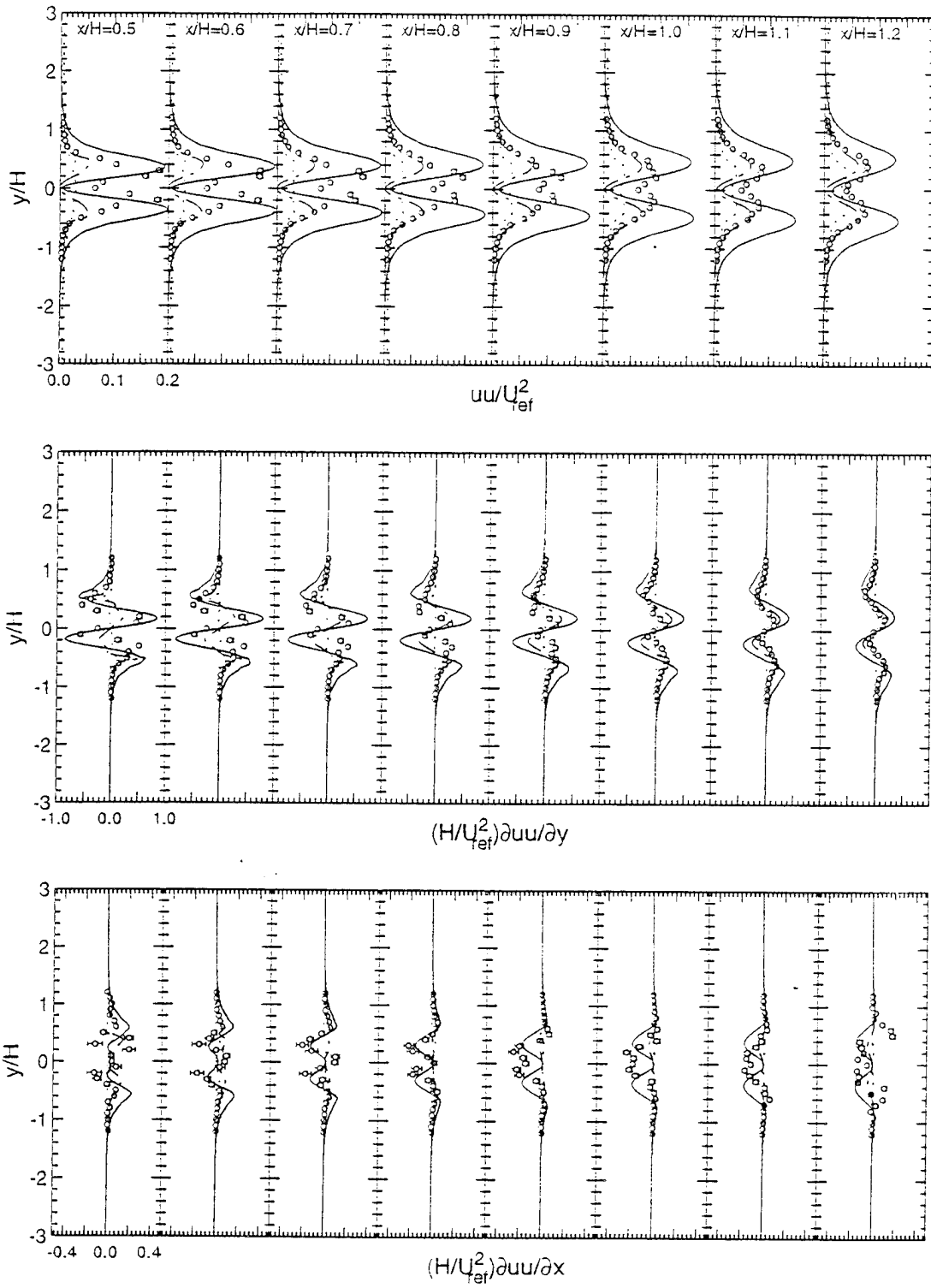


Figure 41. Normalized  $uu$  Turbulent Stress and Stress Gradient Distributions  
( $\circ$  data — RNG-2D  $\cdots$  laminar —  $k-\epsilon$ )

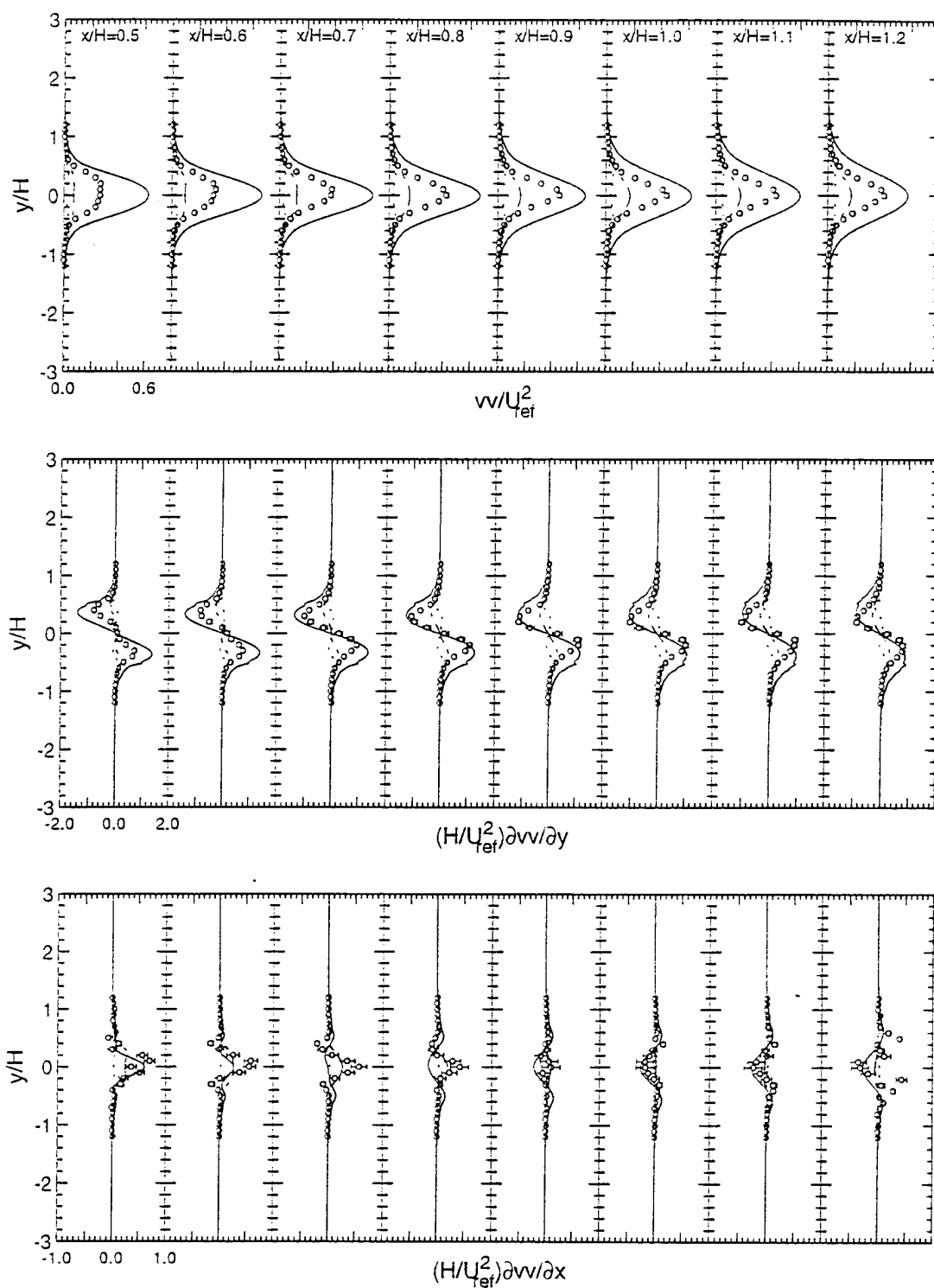


Figure 42. Normalized  $vv$  Turbulent Stress and Stress Gradient Distributions  
 ( $\circ$  data — RNG-2D ... laminar - - k- $\epsilon$ )



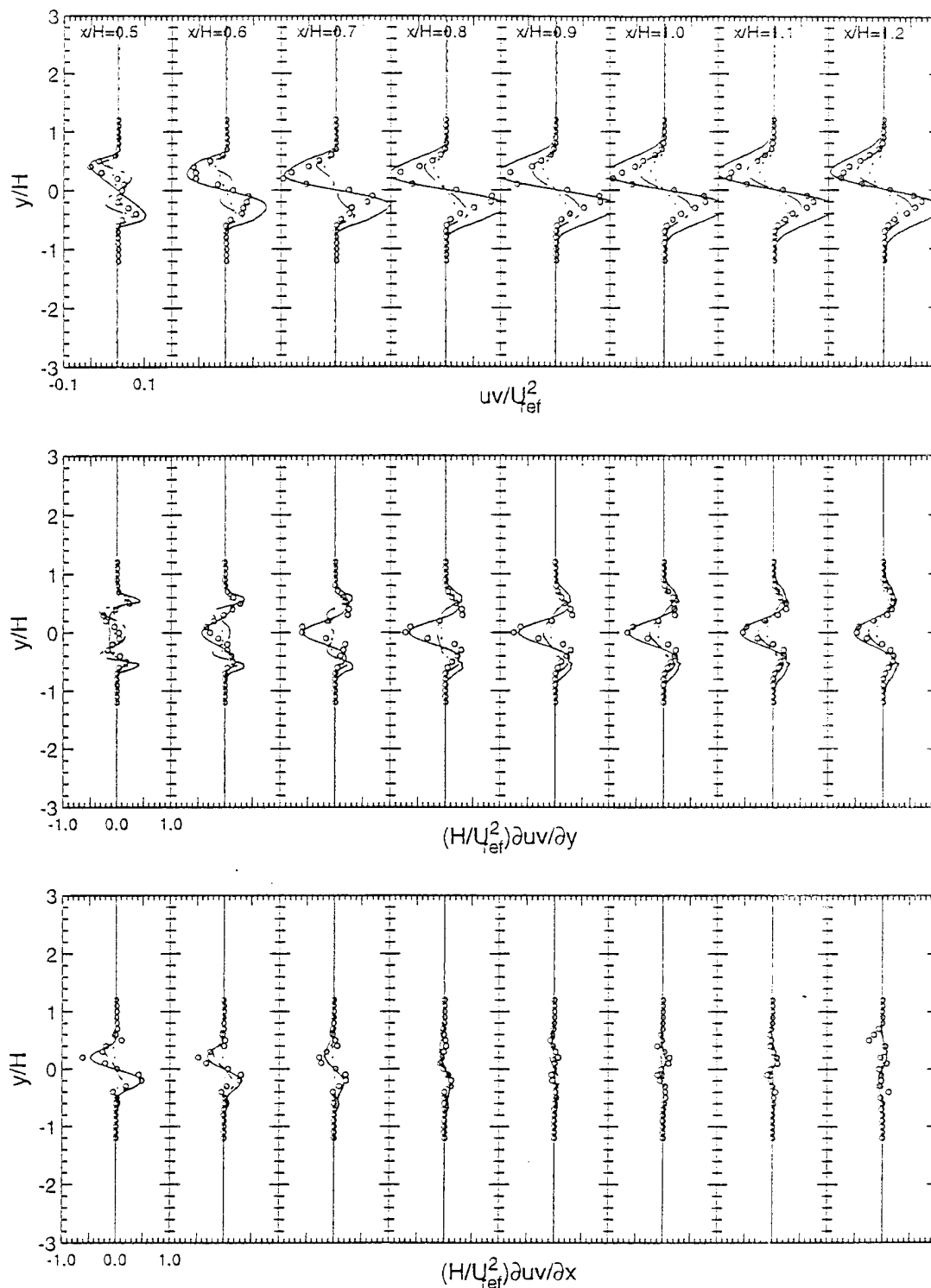


Figure 43. Normalized  $uv$  Turbulent Stress and Stress Gradient Distributions  
 (○ data — RNG-2D ··· laminar ---  $k-\epsilon$ )

In an effort to improve upon the predictions of the  $k-\epsilon$  turbulence model, a different derivation of the  $k-\epsilon$  model based on Renormalized Group theory (RNG), was tested (Case V). The RNG  $k-\epsilon$  model is functionally very similar to the standard  $k-\epsilon$  model, except that the constants are derived from the theory instead of being empirically correlated with experimental data. In addition, one of the constants,  $C_{\epsilon 1}$ , is no longer constant, but a function of local strain rates.

The results for Case V are also presented in Figures 39-43. The RNG  $k-\epsilon$  results were the best of the group, yielding very good results for the axial mean velocities. Although the transverse velocities compared well at the initial axial stations, the comparison degraded with increasing axial position, indicating that the vortex structures were dissipating too quickly in the numerical simulation. Both of the normal stresses were overpredicted by the RNG  $k-\epsilon$  model, but the axial trends were correct. The same can be said for the shear stress; the numerical values were slightly overpredicted, but the trends were correct. In both cases, the fact that the trends were correct is significant, since with the laminar and standard  $k-\epsilon$  cases, the trends were, in general, not correct. The RNG  $k-\epsilon$  model overpredicted the Strouhal number by 4% (0.253).

After the completion of the time-accurate solutions, an analysis of the relative time scales was possible. In all cases, the vortex shedding frequency was near 450 Hz, yielding a mean-flow time scale of  $\tau = 2 \times 10^{-3}$  sec. The standard  $k-\epsilon$  model produced a maximum time scale in the wake of  $\tau = 2 \times 10^{-3}$  sec. The fact that the time scales are the same indicates that a formal Large Eddy Simulation (LES) is required. However, the region within the recirculation zone had a much lower  $k-\epsilon$  time scale ( $2 \times 10^{-4}$  sec), indicating that the near field is probably accurate. The RNG  $k-\epsilon$  model generated similar time scales.

The results presented in the current study are not unlike that of other researchers. Martensson, et al.<sup>32</sup>, obtained similar results using a Large Eddy Simulation (LES) technique, and found that the transverse normal stress was reduced significantly when simulated with a 3-D analysis. Two 3-D analyses were completed as part of the present study, both using the RNG  $k-\epsilon$  turbulence model. The first analysis involved a narrow slice of the tunnel, spanning only one base height across the tunnel. The second solution utilized a larger spanwise section, covering 6 base heights across the tunnel.

For the purpose of the 3-D study, the grid was reduced in density to allow better resolution in the spanwise direction with the available computer resources. The new grid had the following dimensions and is shown in Figure 44.

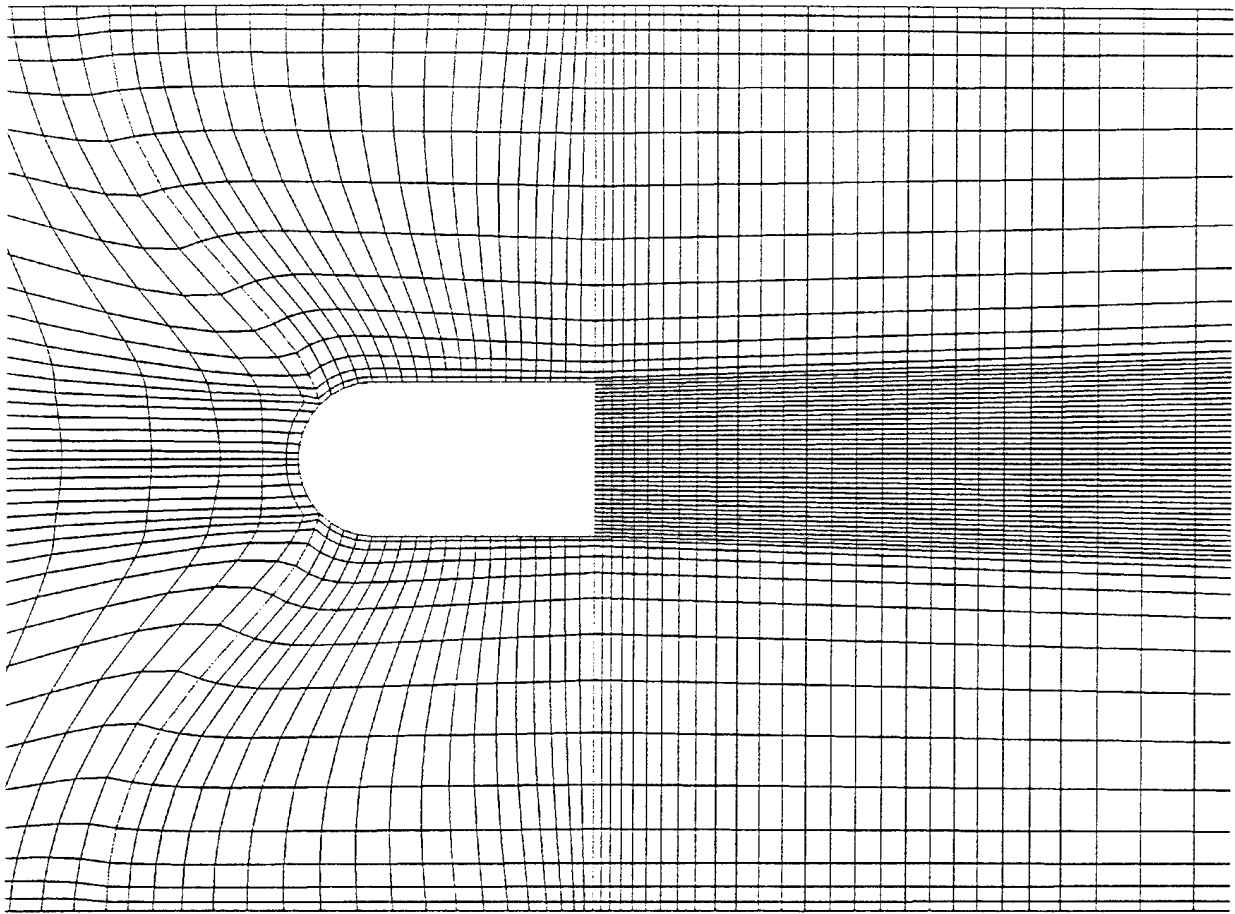


Figure 44. Coarse Grid used for 3-D Unsteady Analysis

zone	dimensions	total
1	9 x 41 x 25	9225
2	20 x 15 x 25	7500
3	20 x 15 x 25	7500
4	41 x 65 x 25	66625

-----  
90850

To test the effects of the new grid, a 2-D case was repeated for the coarse mesh and the results compared to the those from the original grid. At the near field stations, the results were virtually identical. But by 2 base heights downstream of the IFF, the comparison began to degrade at the centerline, producing a 5% error in U. Based on these results, the new coarse grid was considered sufficient to study the effects of the 3-D analysis on the near field solution only.

The first 3-D solution (Case VI) used periodic boundary conditions on the spanwise boundaries, and covered 1 base height with 25 planes in the spanwise direction. The

resulting time-averaged flowfield closely resembled that of the symmetric steady-state solution, with a long recirculation zone. Arnal and Freidrich<sup>33</sup> have reported similar difficulties with a backward facing step, indicating that spanwise extensions less than 4 step heights can artificially elongate the separation bubble. Why this happens is not clear.

As a result, a new solution (Case VII) was completed covering a larger spanwise domain. The new grid covered 6 base heights, also using 25 spanwise planes and periodic spanwise boundary conditions. One major difference was noted in the behavior of the 2-D and 3-D solutions. The 2-D solutions established a steady periodic motion very quickly, typically within 0.005 seconds. The 3-D solutions went through several different modes before settling down to what appeared to be a higher frequency mode (~500 Hz) superimposed on a lower frequency mode (~100 Hz). Therefore the 3-D solutions had to be run over a much longer period of time to establish the periodic motion. In addition, the amount of data collected to calculate accurate statistics increased dramatically, since the lowest frequency dictated the sampling window. The results from Case VII are shown in Figures 45-49. There is a slight improvement in the mean velocities at all stations as compared to the 2-D results. The predicted recirculation zone length matches the experimental results to within the fidelity of the experiments ( $x/H = 0.9$ ). However, the predicted Strouhal number is now 7% below the experimental value 0.226 vs. 0.243). The Reynolds stresses were reduced for all values, and compared very well with the experimental values. The exception was the transverse normal stress, which was reduced from the 2-D results, but was reduced well below the experimental results.

The effect of the added degree of freedom from the third axis of motion is several fold. First, the three dimensional vortex filament shed from the IFF is now free to distort in the spanwise direction. The low frequency made in the 3-D solution is evidence of such distortions. As a result of the spanwise distortions, the shed vortices will make a contribution to the spanwise stresses, dependant upon the magnitude of the spanwise distortion. Any contribution to the spanwise stresses will result in a likewise decrease to the axial and transverse stresses, dependant upon the local direction of the distortion. Such an idea was put forth by Perry and Steiner<sup>34</sup>, and is supported by the present results.

The second effect of the vortex filament distortion is to create a vortex stretching effect. As the vortex filament is distorted, the total length is increased. As a result, the vortex velocity increases to maintain the same angular momentum. Such vortex stretching could explain the consistent lack of agreement between the mean transverse velocity components moving downstream of the IFF.

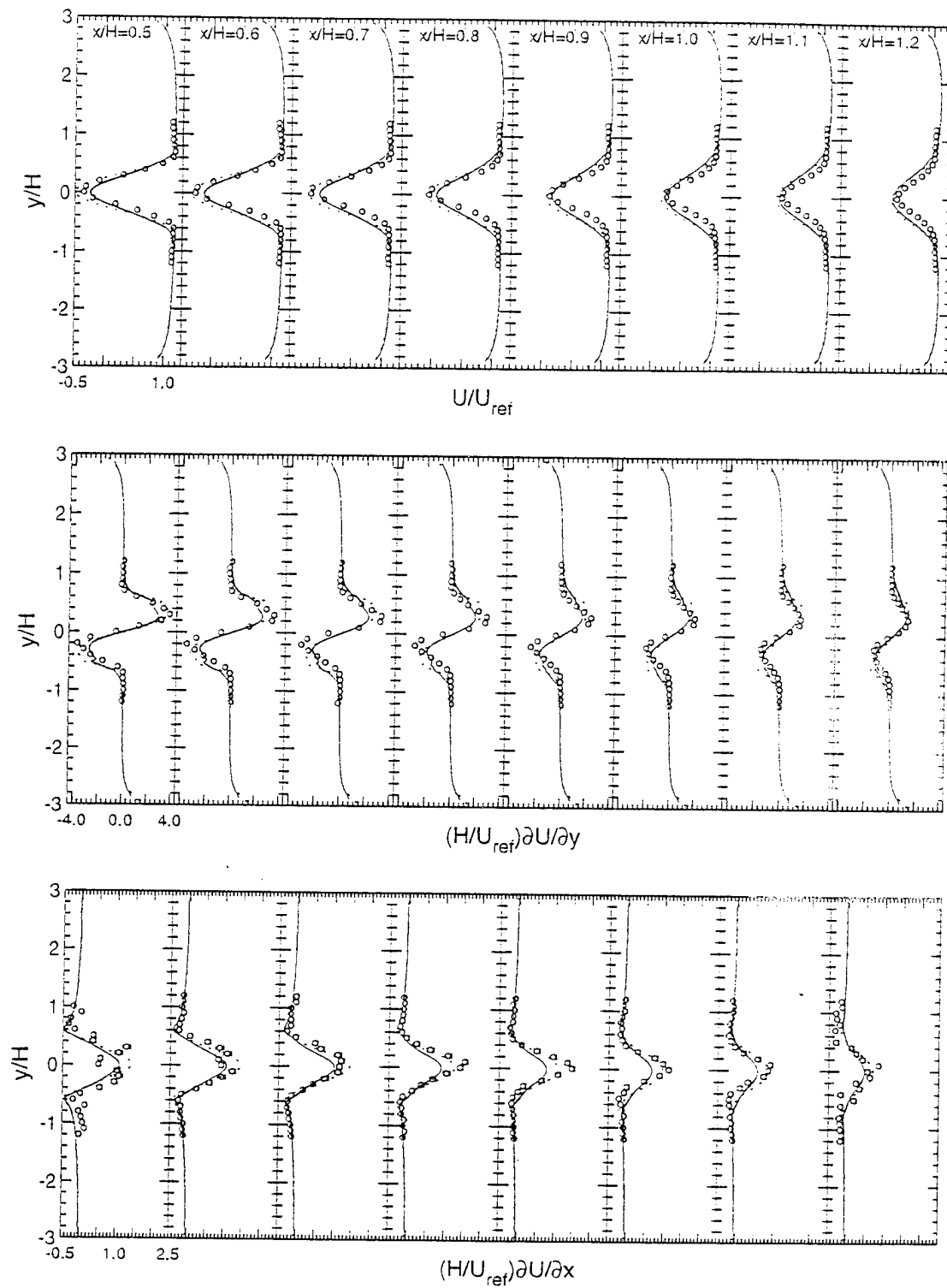


Figure 45. Normalized Mean Axial Velocity and Velocity Gradient Distributions  
 (○ data — RNG-2D ··· RNG-3D)

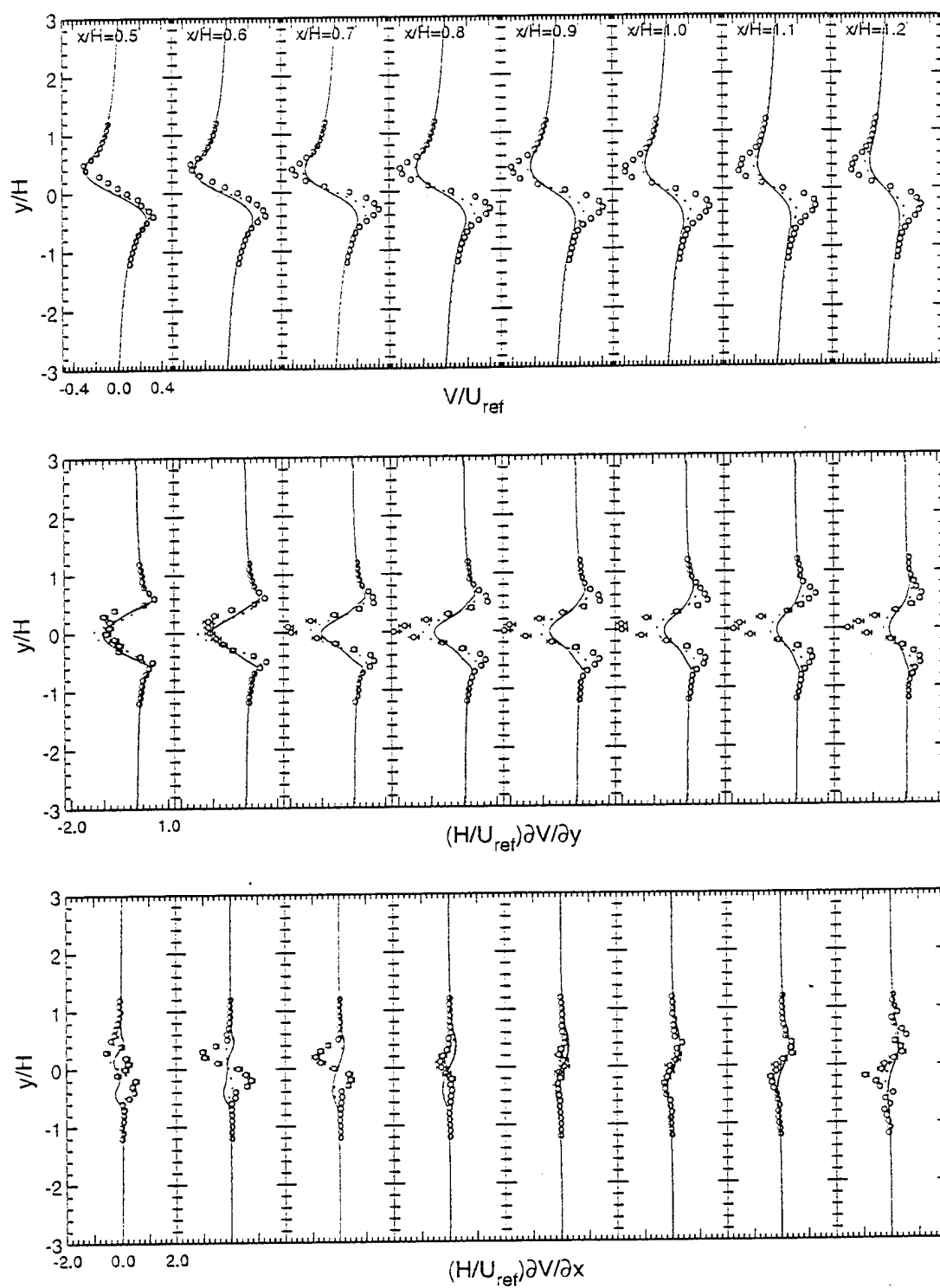


Figure 46. Normalized Mean Transverse Velocity and Velocity Gradient Distributions (○ data — RNG-2D ··· RNG-3D)

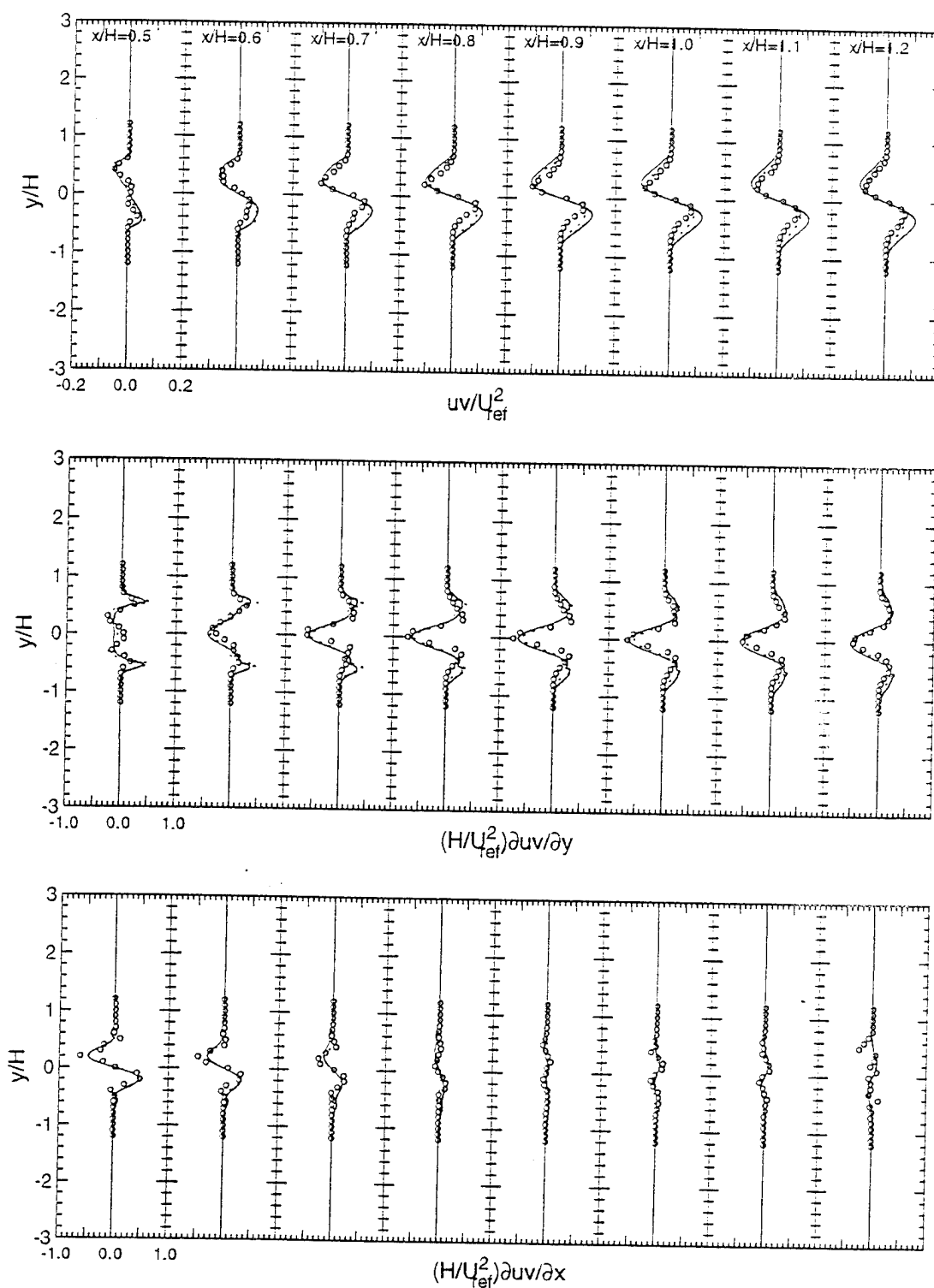


Figure 47. Normalized  $uv$  Turbulent Stress and Stress Gradient Distributions  
 (○ data — RNG-2D ··· RNG-3D)

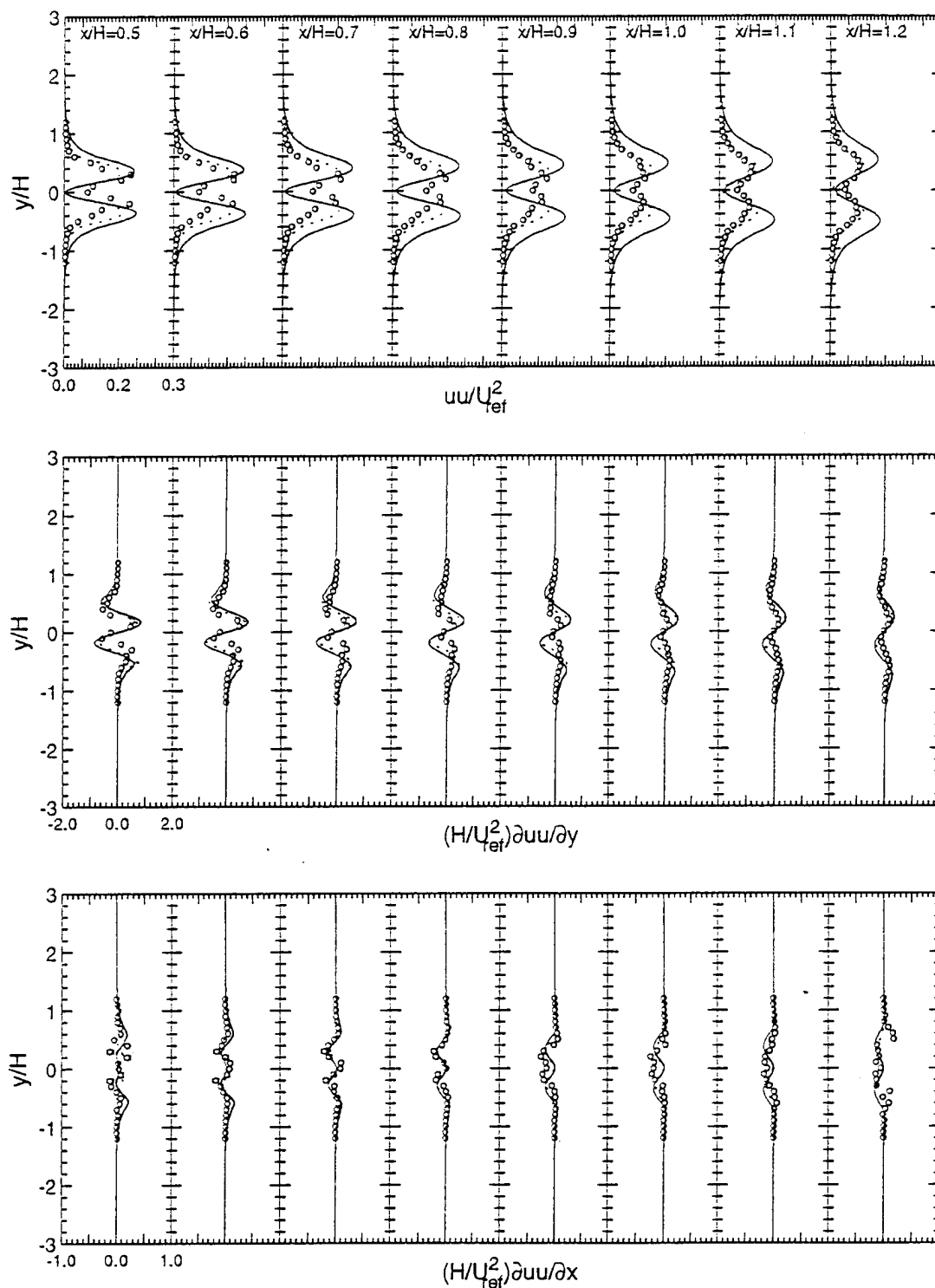


Figure 48. Normalized  $uu$  Turbulent Stress and Stress Gradient Distributions  
(o data — RNG-2D ··· RNG-3D)



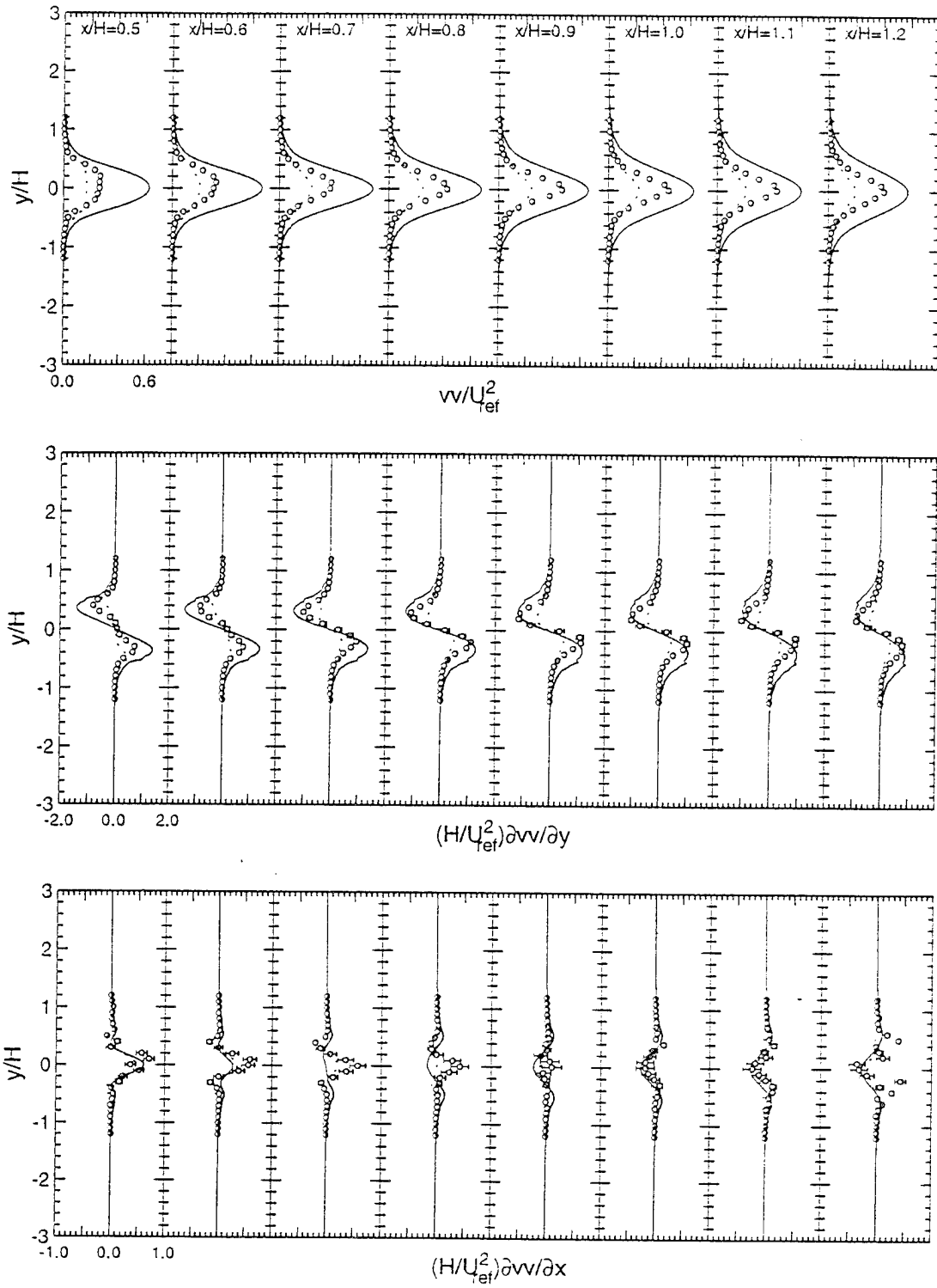


Figure 49. Normalized  $vv$  Turbulent Stress and Stress Gradient Distributions  
( $\circ$  data — RNG-2D ··· RNG-3D)

## 5.0 ADVANCED MODEL NUMERICAL TESTS

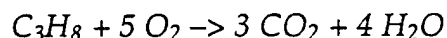
Running concurrently with the baseline tests was an effort to find a better design for the IFF. The goal was to create a flameholder with increased fuel/air mixing, without paying a high penalty in pressure loss. On some of the advanced models, simple combustion models were analyzed to establish the improvement to the combustion efficiency based on increased mixing. On all of the models, the cold pressure loss was calculated for comparison to the baseline.

A total of 27 different models were numerically tested in this phase of the study. A variety of different approaches were taken in an attempt to generate the large scale axial vortices. On the different models, 58 production CFD runs were completed, and countless smaller test cases were also completed. In the following sections, the computational methods used for the study will be reviewed. A summary of all the models tested will then be presented followed by a comparison of the data obtained from the numerical tests.

### 5.1 Computational Method

The same CFD code was used for the advanced model testing, that was used for the baseline isothermal tests (CFD-ACE, see Section 3.1). The major difference is that most of the solutions for the advanced models were completed using the steady state solver. While ignoring the unsteady contributions may have caused a small loss of accuracy, the trends were still evident between the different models.

Instantaneous reactions were used for all combustion calculations, based on the following stoichiometric equation:



It was felt that the simple model would identify the proper trends between the different models. For the rigorous combustion tests (presented in Section 8), more advanced combustion models were used.

The combustion efficiency, as used in the current study, is simply a function of the mixing occurring between the fuel and the air. Combustion efficiency is defined as:

$$\eta_{comb} = \frac{\text{heat released}}{\text{heat available in fuel}} = \frac{\text{fuel burned}}{\text{total fuel}}$$

For a mixing-controlled combustion model, combustion efficiency will always be 100% in any grid cell that is fuel lean. Efficiencies less than 100% will only occur in grid cells that are fuel rich, and represent the presence of unburned fuel. In the

current program, combustion efficiency was postprocessed by mass weighting and summing the combustion efficiencies in each cell in a specified axial plane.

The pressure losses for the flameholders models must be computed based on cold flow results. The heat release of combustion adds to the pressure loss, and complicates the comparison of different models. If one model has better combustion efficiency than another, it will also have more pressure loss due to heat release. Only cold flow pressure losses can be directly compared. Since the presence of the crossflow jet may also contribute to the pressure loss, all pressure loss calculations were completed with solutions that included the fuel injection, but did not allow combustion.

The total pressure loss associated with a bluff body can be computed in one of two ways. First, the mass weighted total pressures in each cell can be integrated across an axial plane to give a direct calculation of the total pressure. Or, the static pressure can simply be evaluated at the side wall of the duct downstream of the bluff body, and represents a good approximation to the total pressure loss when compared with the static pressure upstream. When using the second method, the static pressure must be evaluated far enough downstream, since the static pressure will partially recover in the wake of the bluff body.

The numerical solutions were completed using first order differencing in space on all variables. To model turbulence effects, the standard k- $\epsilon$  turbulence model was used along with the standard wall functions. All of the solutions were considered converged when all residuals were reduced by at least four orders of magnitude.

## 5.2 Inlet Conditions

The freestream inlet conditions were:

$U = 66 \text{ m/s}$   
 $M = 0.2$   
 $P = 20700 \text{ N/m}^2$   
 $T = 272 \text{ K}$   
 $u/U = 0.10$   
 $\mu_t = 0.01$   
working gas:     air

Uniform inlet conditions were used in all cases, and the inlet plane was approximately 20 base heights upstream of the IFF to allow a boundary layer to develop.

In the cases that included fuel injection, the following jet conditions were enforced:

$V = 114 \text{ m/s}$   
 $M = 0.42$   
 $P = 20700 \text{ N/m}^2$   
 $T = 272$   
 $u/U = 0.05$   
 $\mu_t = 0.01$   
working gas: propane

Unless otherwise noted, the jet conditions were set up to produce an equivalence ratio of 0.5 and a jet-to-freestream momentum flux ratio (J) of 4.4.

### 5.3 Advanced Flameholder Models

#### 5.3.1 Baseline Model

Before any advanced models were tested, a new baseline had to be established. The new baseline was different from the baseline tests presented in Section 4, due to several differences in the cases. First, the new baseline was three-dimensional since it included the fuel jets in the solution. Second, the inlet plane was set to a uniform velocity. Finally, the new baseline also needed to include combustion to determine the baseline combustion efficiency curve.

The grid for the new baseline case contained 36,465 grid points (55x39x17) and is shown in Figure 50. The grid covers only the top half of the domain, and spans from the midpoint of an injector to the midplane between injectors. Symmetry planes were used on both spanwise planes and at the tunnel centerline plane. Viscous boundaries were established on the top tunnel wall, as well as on the walls of the flameholder. The physical dimensions of the flameholder were the same as those in the isothermal tests (Section 4). The fuel injector measured 0.115 inches in diameter, and was modeled with a 4x4 round grid pattern. Injectors were vertically aligned and were spaced 0.5 inches apart. The baseline geometric blockage was 16.7%. The grid is recognized as being coarse, and a finer grid was run to ensure the coarse grid was sufficient to capture qualitative features of the flowfield. The fine grid solution compared well with the coarse grid solution; in order to reduce run times, the coarse grid was selected for parametric studies.

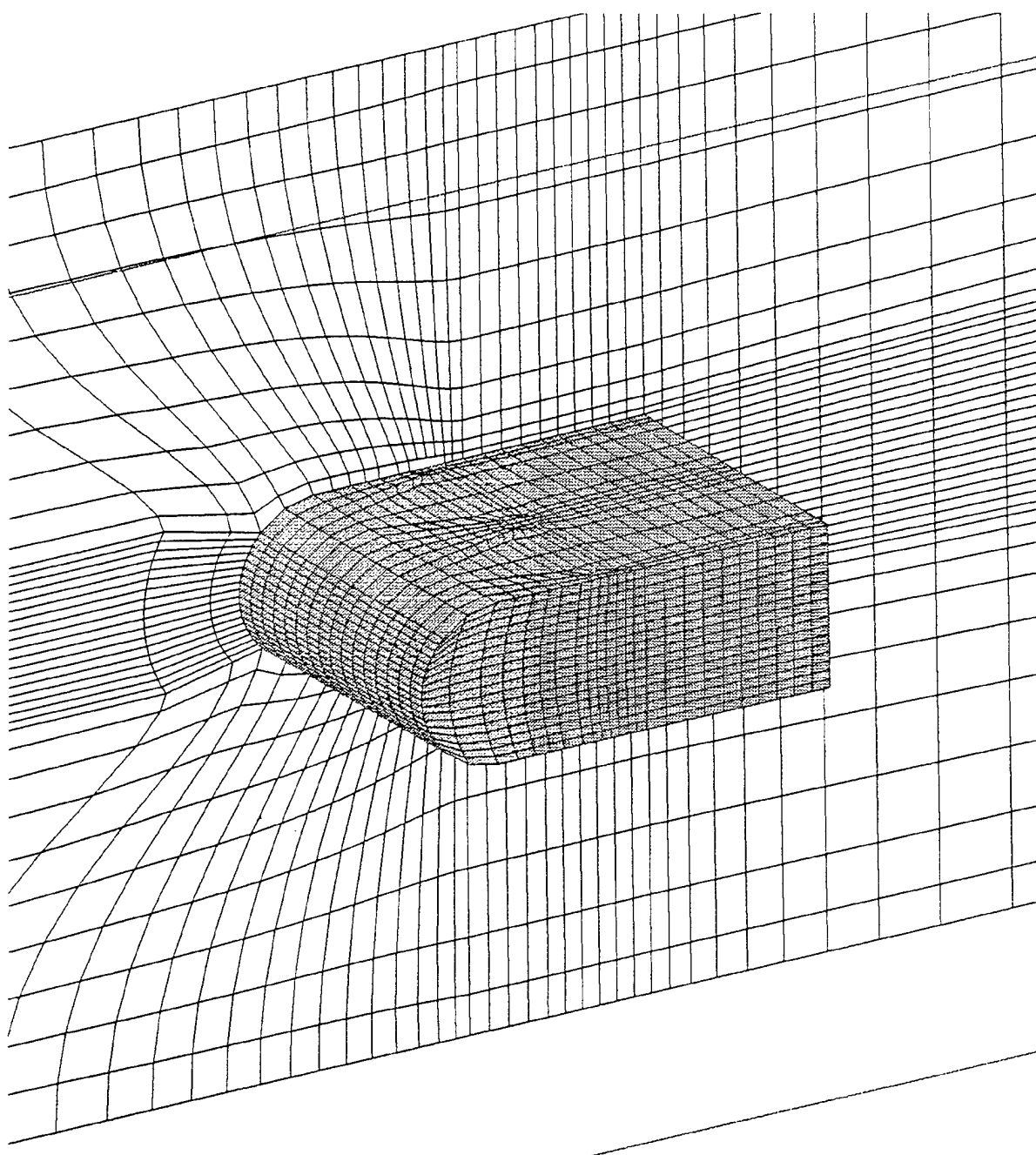


Figure 50. Computational Grid used for Baseline Performance Analysis

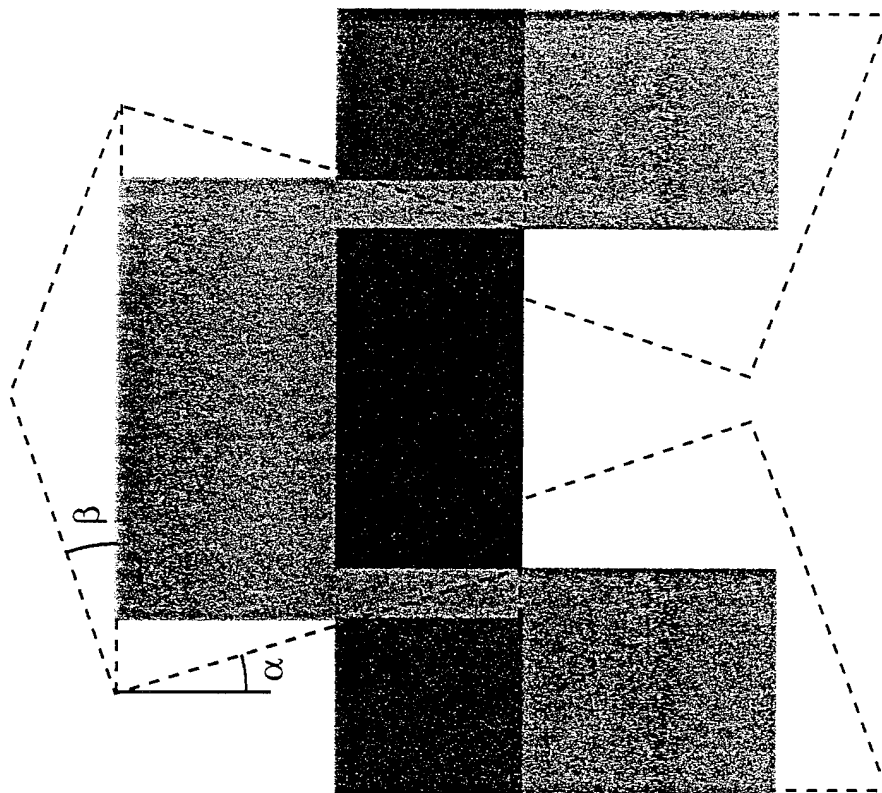
### 5.3.2 Advanced Model ADV2

The first advanced model tested was called ADV2. The name actually applied to an entire model group with several parametrics analyzed within the group. The first model tested was ADV2  $\alpha 0$ , and is shown in Figure 51. The total flameholder length was 1.34 inches with a maximum height of  $\pm 0.75$  inches. This model followed closely the Split-Notched IFF model from the Phase I study. It used square fingers that protruded into the flow from the trailing edge. The base area of each finger was equal to the original base area of the baseline model, therefore the total base area at the trailing edge (20.8%) was only increased by the extra material forming a web between the fingers. However, the geometric blockage created by the possible flow separating off of the ramps, was much larger at 35.4%. The CFD analysis was not set up to predict separation, due to the grid density and turbulence modeling, although the code did show some separation within the channel regions. The ramps were placed at 45 degrees on both top and bottom, and were expected to encounter some flow separation.

The second model from the ADV2 group was called  $\alpha 10$ , and was generated by slanting the web between the fingers at a 10 degree angle (Figure 52). The intent was to increase the axial vorticity by providing a sharper edge to generate the vortex. The most important effect of angling the web, was the increase in base area due to the stretching of the finger base areas. The new base area was 23.8%, with a geometric blockage of 38.4%. All other aspects of the flameholder were the same as the  $\alpha 0$  model.

The same idea of angling the web between the fingers was carried further with the next two models,  $\alpha 20$  and  $\alpha 30$  (Figures 53 and 54). The  $\alpha 20$  model had a base area/geometric blockage of 26.9%/41.5% while the  $\alpha 30$  model had 30.5%/45.0%.

The results from the combustion tests are shown in Figure 55. From the combustion efficiency curves, each advanced model can be seen to produce faster mixing than the baseline. This is due to the formation of a large axial vortex downstream of the flameholder, as can be seen in Figure 56. Of the four models tested, the  $\alpha 20$  model showed slightly better overall performance. Therefore, it was chosen for further parametric studies.



a) ADV2  $\alpha 0$

b) definition of  $\alpha$  and  $\beta$

Figure 51. 3-D Model of ADV2  $\alpha 0$ , and Definition of  $\alpha$ ,  $\beta$

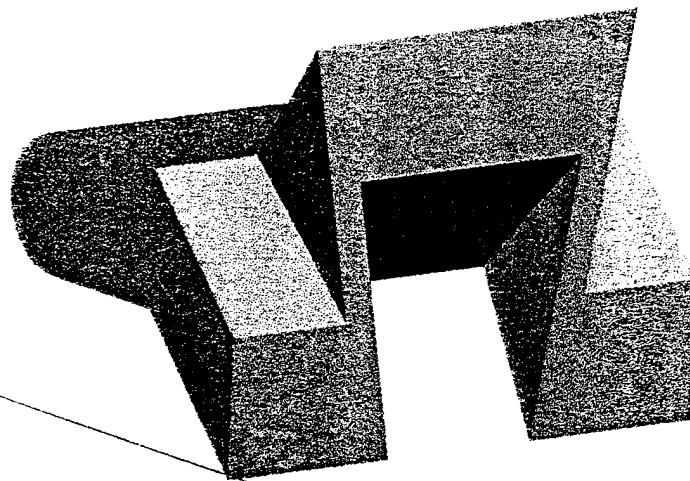


Figure 52. 3-D Model of ADV2  $\alpha_{10}$

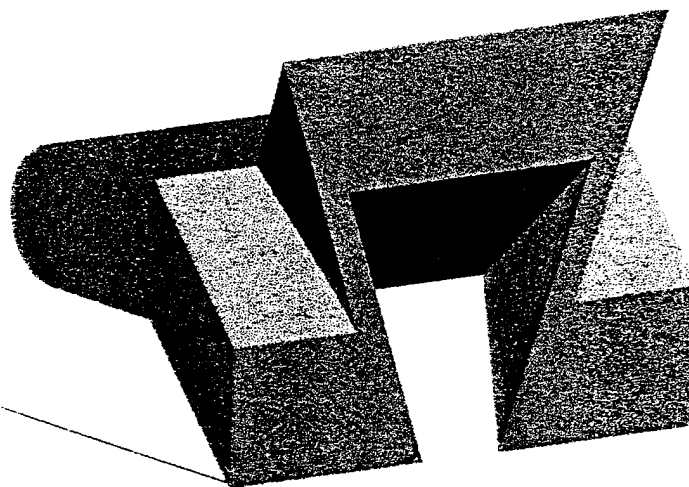


Figure 53. 3-D Model of ADV2  $\alpha_{20}$

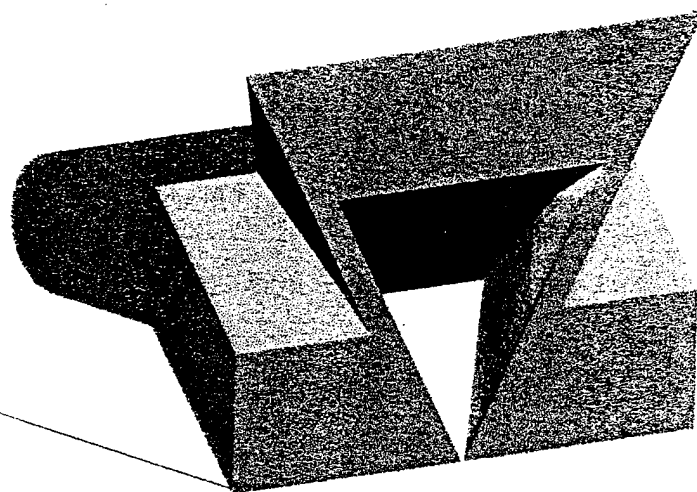


Figure 54. 3-D Model of ADV2  $\alpha_{30}$



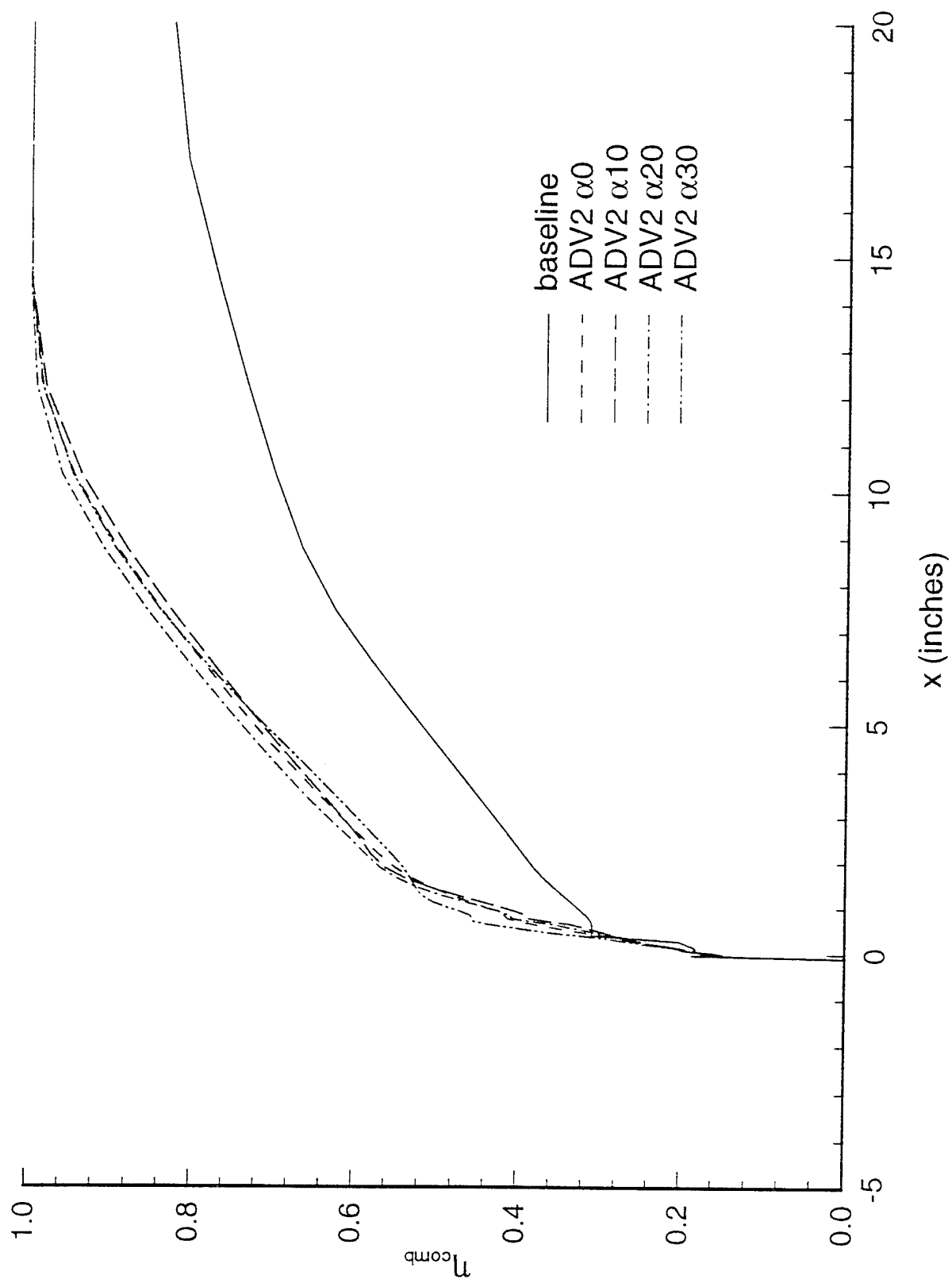


Figure 55. Combustion Efficiency for ADV2  $\alpha$  Models Shows  $\alpha 20$  Gives Superior Performance

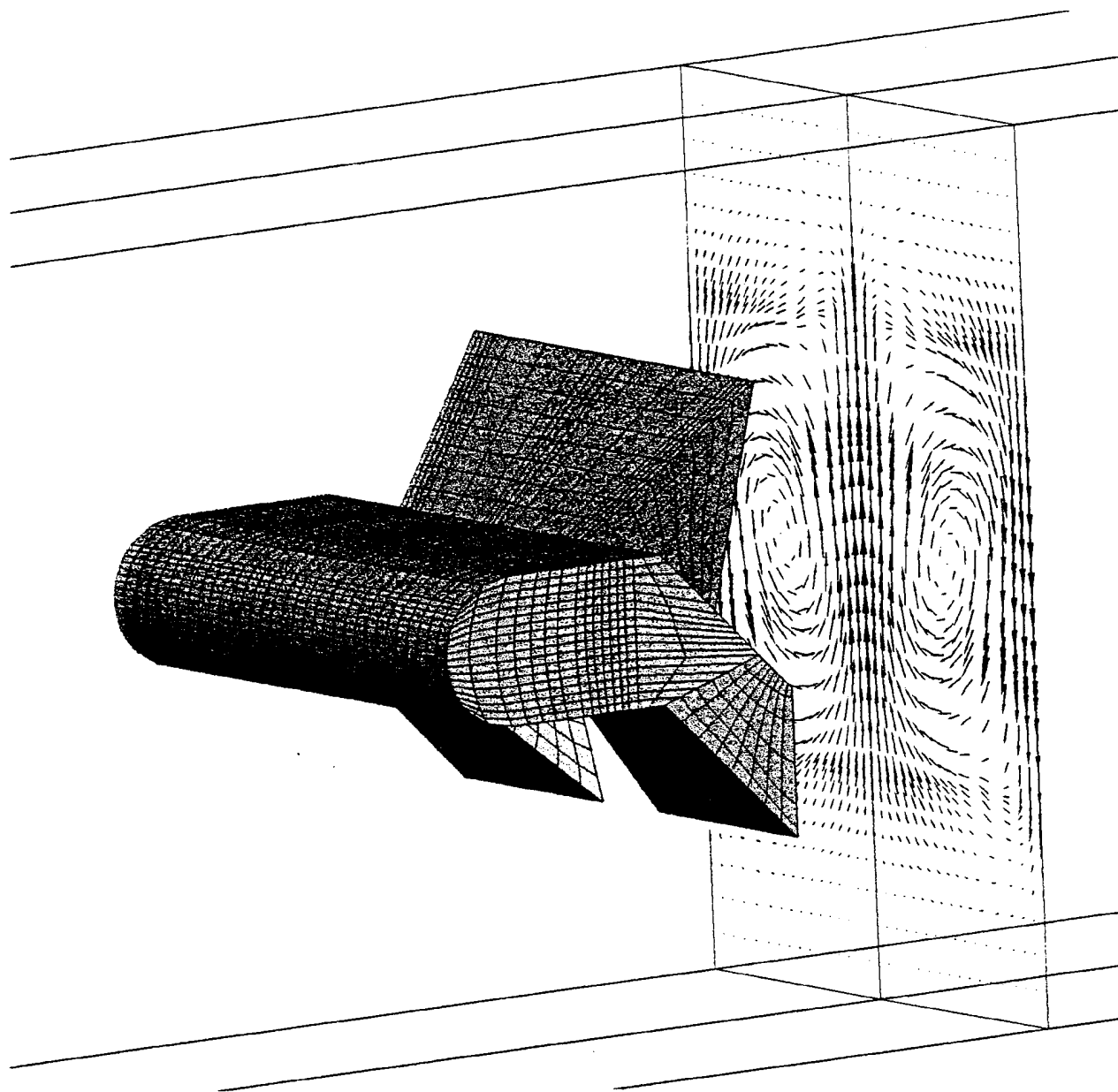


Figure 56. Large Scale Axial Vortices Enhance Fuel-Air Mixing;  $ADV2 \propto 20$

From Figure 57, the presence of a strong fuel core can be seen above the ramp. The fuel is from the injector directly in front of the ramp. Possible performance gains were recognized if the fuel core could be better distributed. The first trial at redistributing the fuel core was to change the angle on the top of the ramp. Two different angles were tested:  $\beta 20$  and  $\beta -20$  shown in Figures 58 and 59. The intent was to create a secondary vortex located near the top of the ramp. However, no vortex was formed and the fuel distribution was not significantly changed. The new combustion efficiency curves are shown in Figure 60, and show that the  $\beta 20$  model does not change the performance much, even though the blockage is considerably higher (32.8%/47.4%). The  $\beta -20$  model shows reduced performance with blockages of (19.8%/34.4%).

The next attempt to redistribute the fuel core was to eliminate the fuel jet directly in front of each ramp, thereby eliminating the fuel core (model JETMOD). The fuel lost to the removed injectors is replaced by additional fuel introduced through the remaining injectors. To keep the momentum flux ratio the same, the increased fuel flow was introduced by increasing the size of the remaining injectors to a diameter of 0.133 inches. The trial was modeled on the ADV2  $\alpha 20$  model only. The fuel distribution is shown in Figure 61 for the two cases. Although the fuel core has been removed, the remaining fuel is slightly more concentrated in the center of the flow. The resulting combustion efficiency curves are shown in Figure 62, where the modification is seen to have little if not a detrimental effect. The ramps clearly serve two purposes. Not only do they provide for the strong axial vorticity, but they also direct the fuel to the outer regions of the flow above and below the flameholder.

Of all the models tested in the preceding series, ADV2  $\alpha 20$  showed the best combustion performance. However, the pressure loss associated with the mixing enhancement must also be considered. Figure 63 shows the cold pressure loss of all the models tested. Clearly the pressure losses were much higher than the baseline IFF. Even a double base IFF (two IFF's placed vertically in tandem) had a much lower pressure loss, while providing the most flame stability, based on the base area.

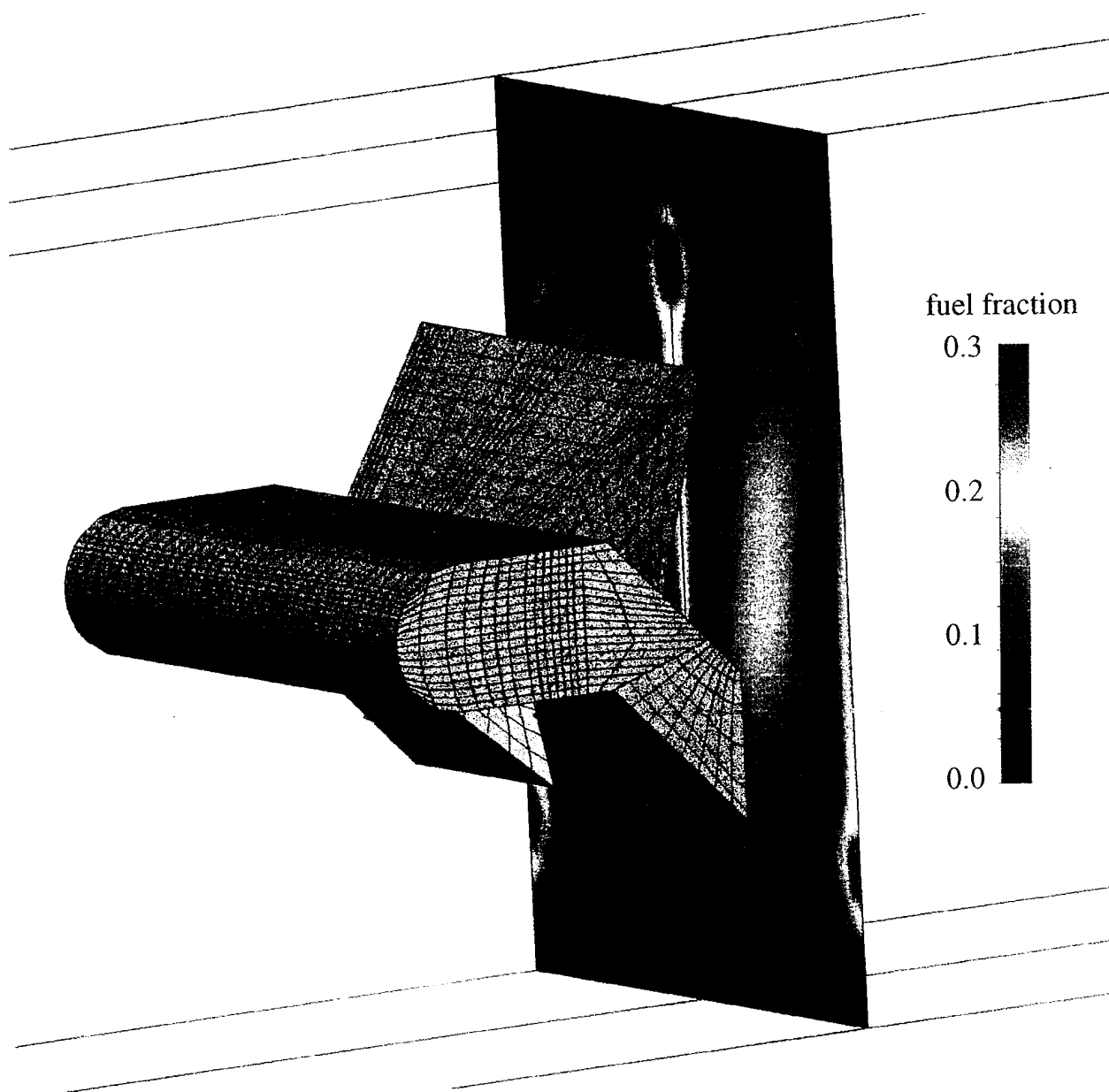


Figure 57. Strong Fuel Core Forms Above Ramp; ADV2  $\alpha 20$

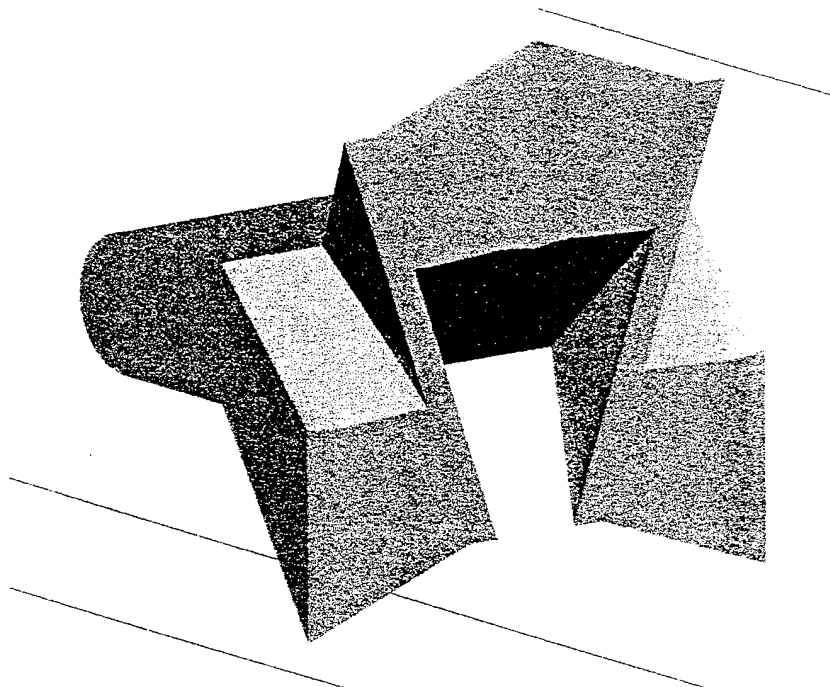


Figure 58. 3-D Model of ADV2  $\beta$ 20

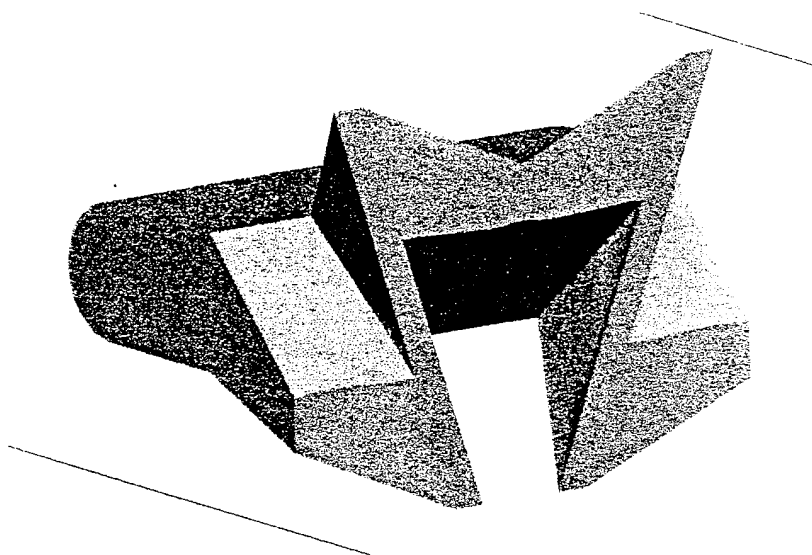


Figure 59. 3-D Model of ADV2  $\beta$ -20

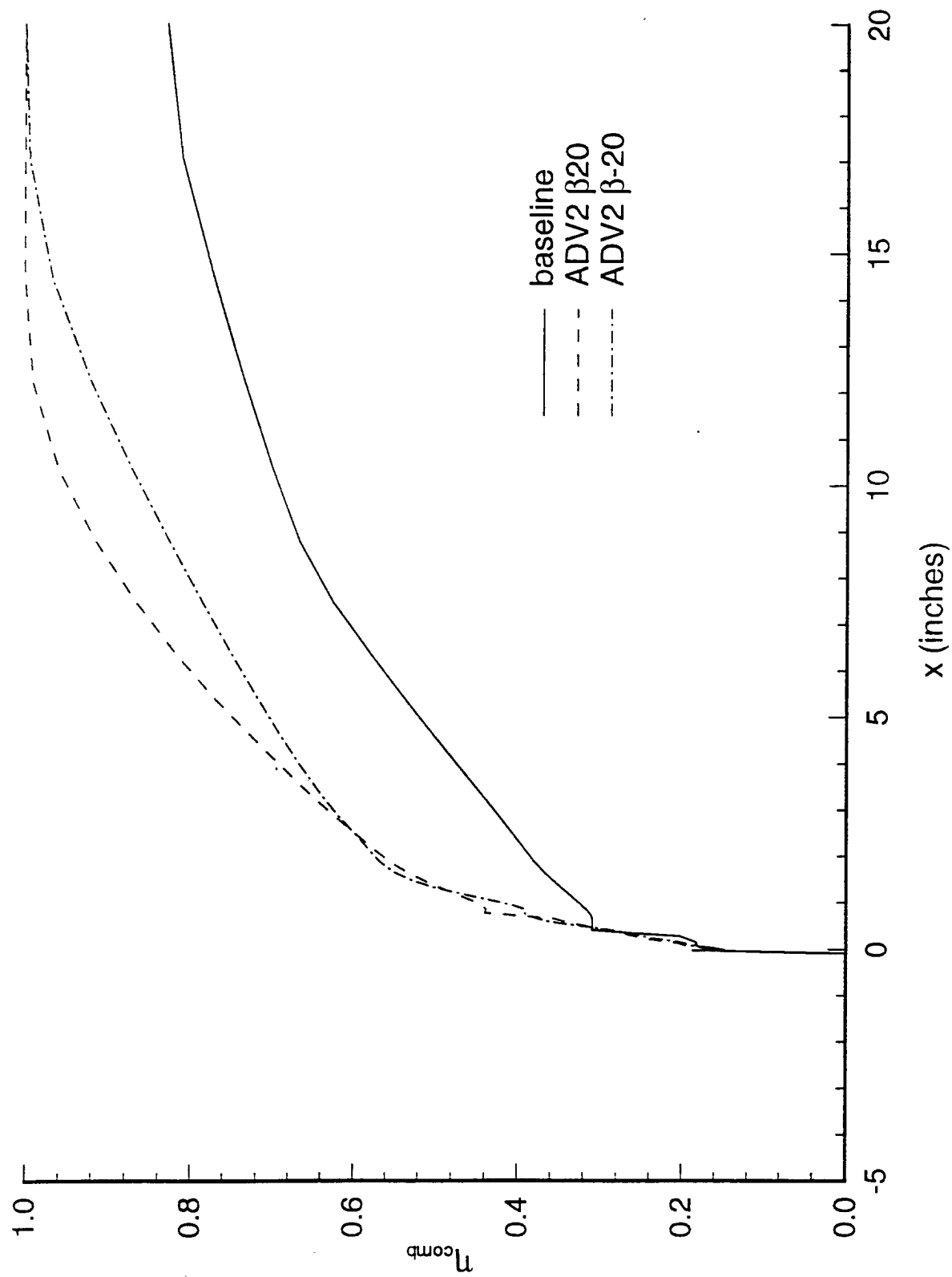
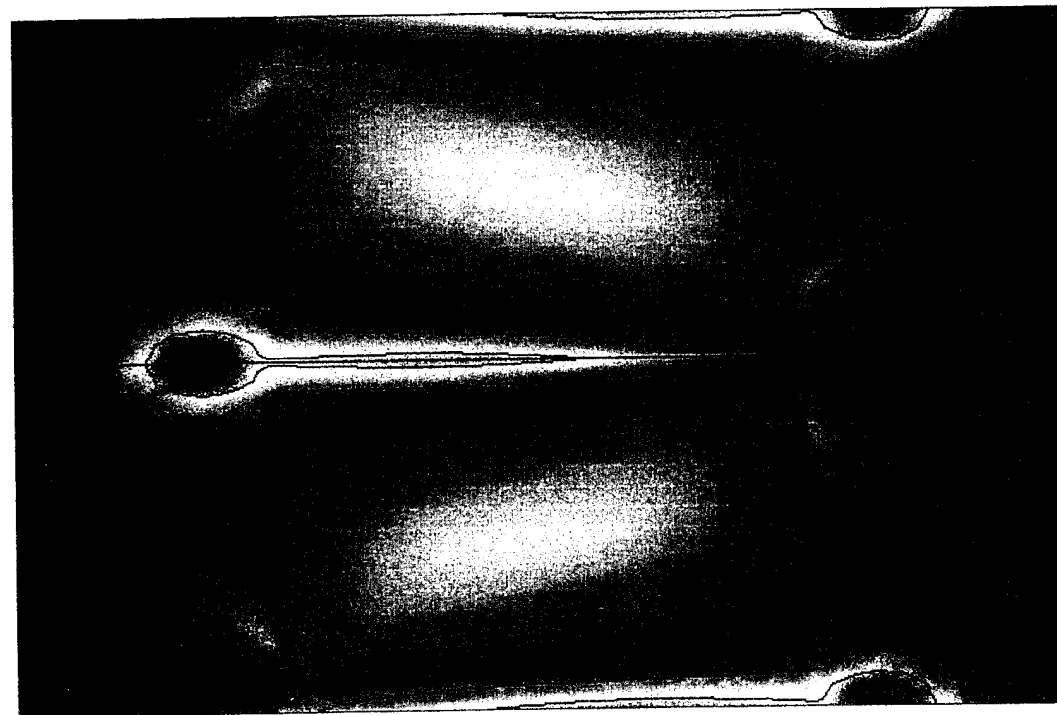
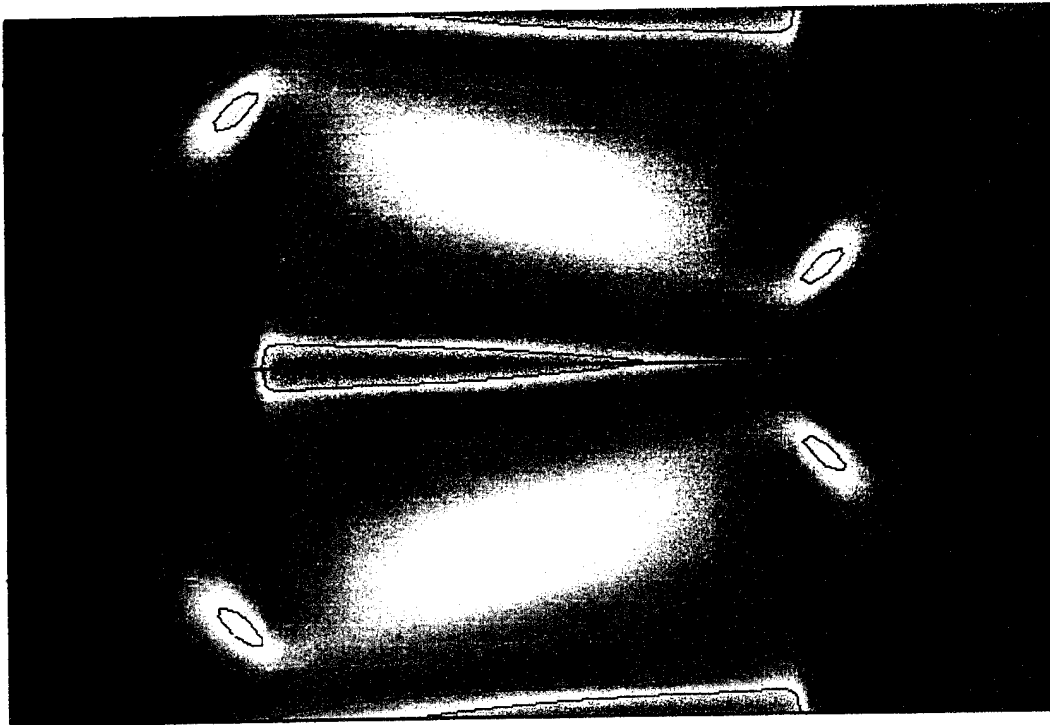


Figure 60. Combustion Efficiency for ADV2  $\beta$  Models



a) original ADV2  $\alpha 20$



b) center jet turned off

Figure 61. Model JETMOD Reduces Presence of Fuel Core

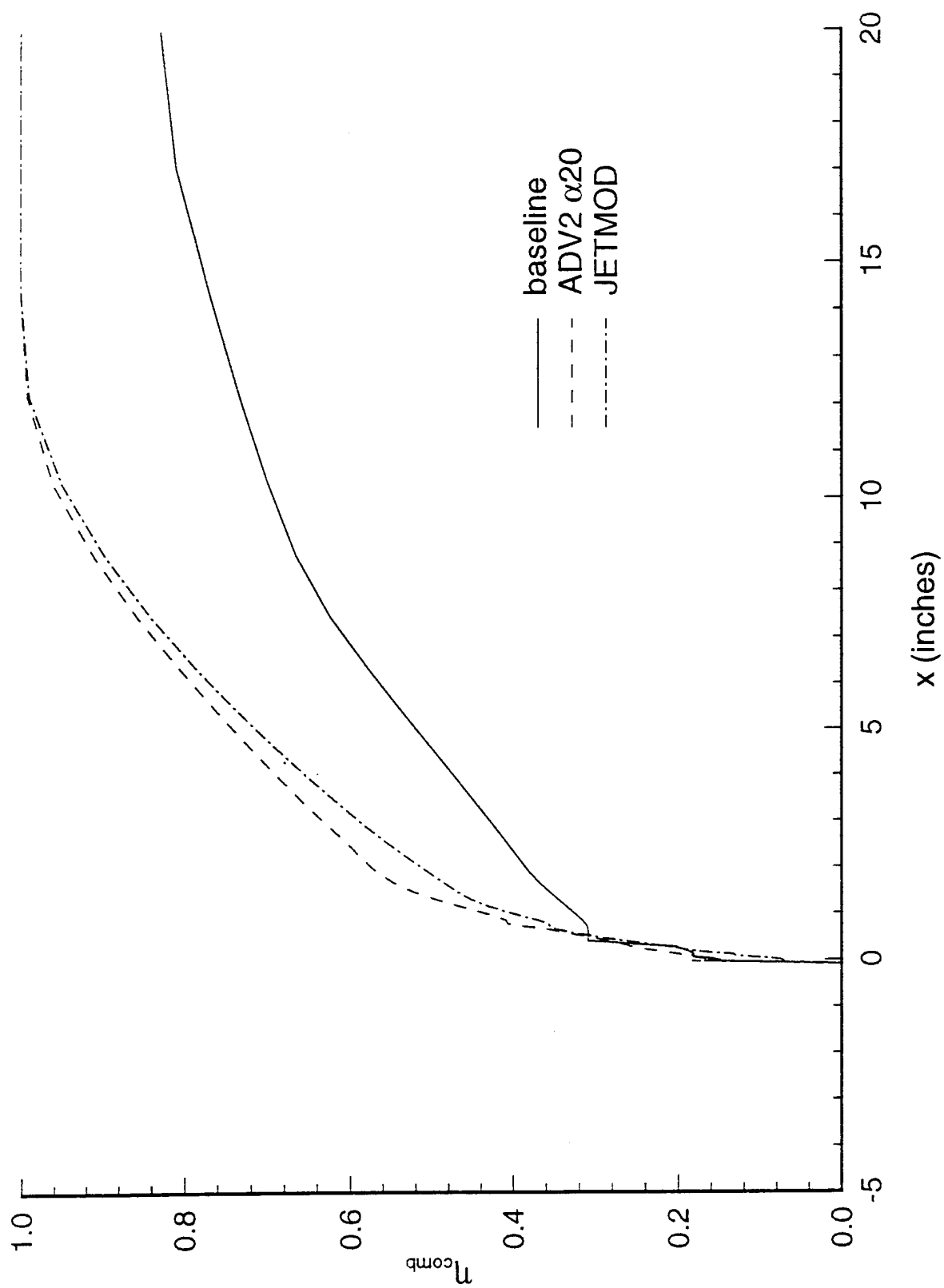


Figure 62. Model JETMOD does not Improve Combustion Efficiency



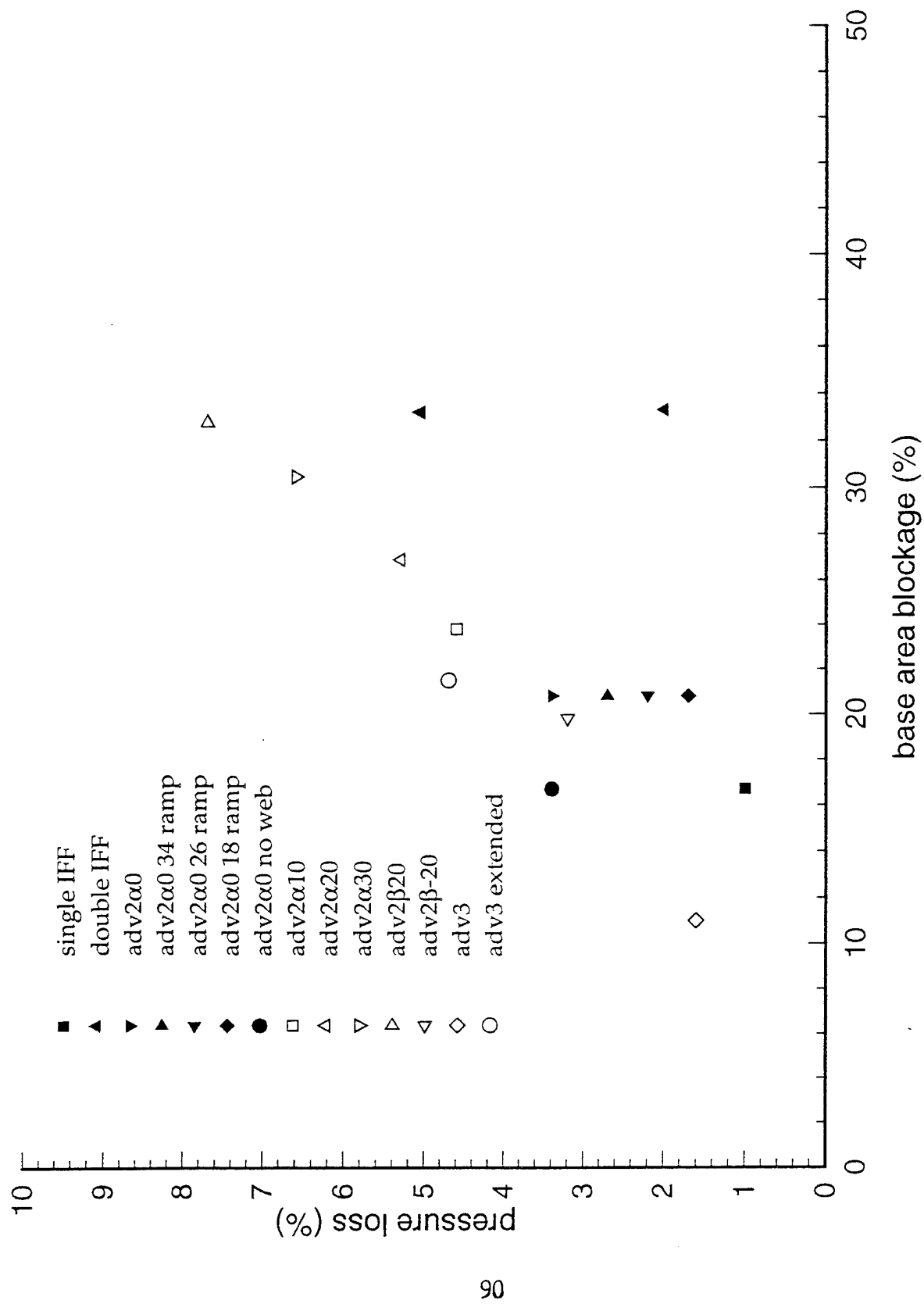


Figure 63a. Pressure Loss for All Models Analyzed

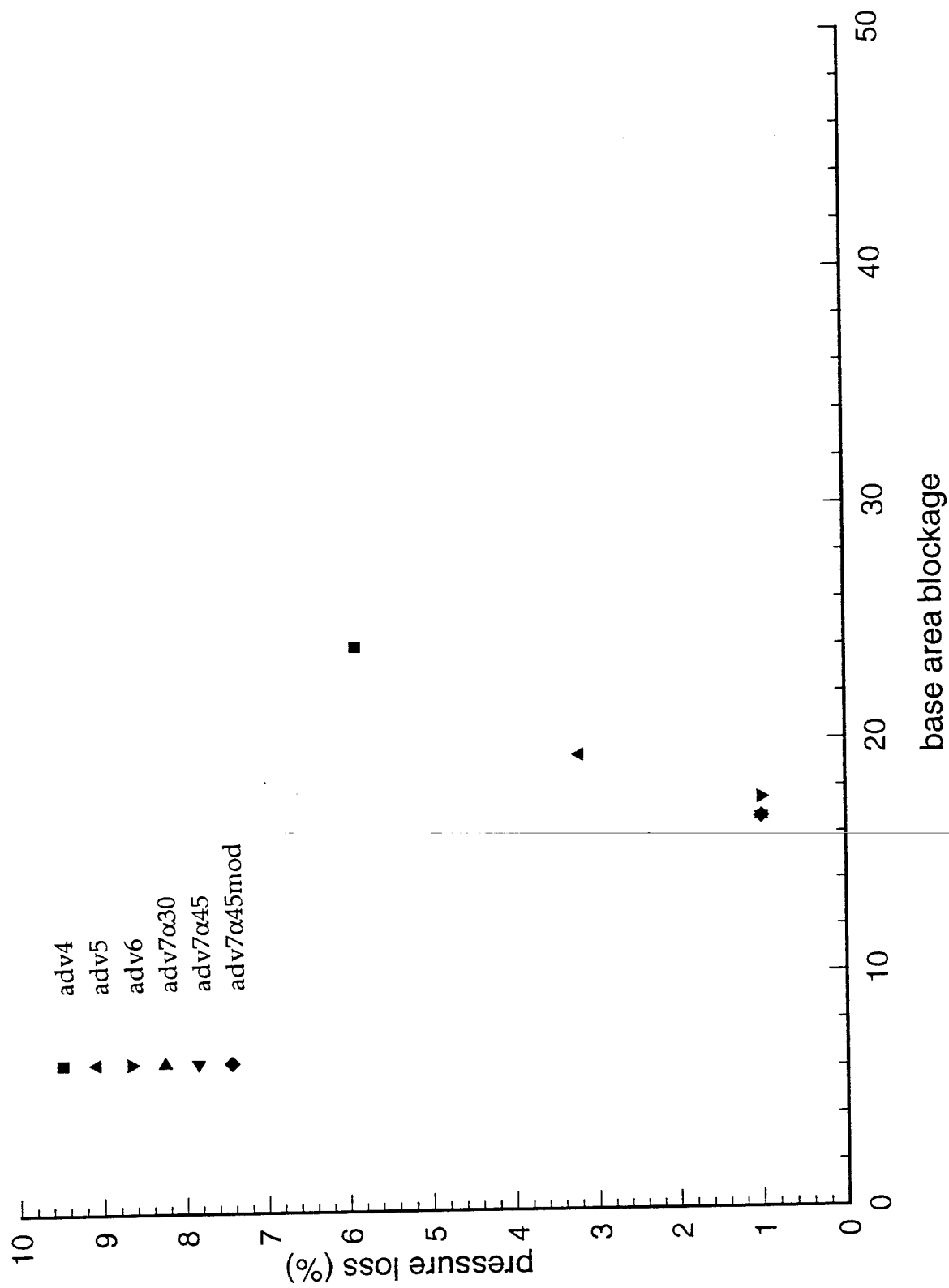


Figure 63b. Pressure Loss for All Models Analyzed

In an effort to reduce the pressure loss, a parametric study was completed on the effect of reducing the ramp angle. To keep the base area constant, the tail of the flameholder was axially stretched until the desired angle was attained. Four different tail lengths were tested, using the  $\alpha 0$  model as a baseline (see Figure 64). In this study, the maximum crossflow velocity at a given station during nonreacting tests, instead of the combustion efficiency, was used to judge the mixing ability of the different designs. The results are shown in Figure 63, where the pressure loss is seen to be directly related to the ramp angle; the lower the angle, the lower the pressure loss. However, the crossflow velocity does not follow the same trend. The 34 degree ramp provides the highest crossflow velocity, but still a lower pressure loss than the 45 degree baseline. As the ramp angle decreases further, the crossflow velocity declines. Based on these comparisons, the best choice based on both criteria would be the 26 degree ramp, having a substantial crossflow component and a relatively low pressure loss.

As a final check with the ADV2 series, the  $\alpha 0$  model was tested with and without a web between the fingers. The results showed a small decrease in pressure loss (0.4%) and virtually no difference in the crossflow profile. Therefore, there was a slight performance gain by not providing a web between the fingers. Removing the web also removed an area that is difficult to cool, due to the relative thickness of the web. However, removing the web removes any connection between the base faces of individual fingers. Such connectivity may be necessary for proper ignition propagation across the flameholder.

### 5.3.3 Advanced Model ADV3

The next advanced model, ADV3, took a slightly different approach. The previous models incorporated large base areas at the end of each finger with a thin web connecting the fingers. ADV3 took the opposite approach by providing a thick web, with thin connecting regions at the ends of each finger (see Figure 65). By removing much of the material from the end of the fingers, the fingers did not protrude as far into the freestream, and thus reduced the frontal area of the flameholder. The side angle of  $\alpha 20$  was retained from the previous tests, and the inward ramps were kept at 45 degrees, and had the same possible separation problems as the ADV2 models.

The results from ADV3 are shown in Figures 66 and 63. The pressure losses were greatly reduced compared to the other models, due to the reduced blockage. However, the combustion efficiency was considerably less than the ADV2  $\alpha 20$  model. In addition, the characteristic dimension of the flameholder face was only 0.25 inches - half that of ADV2 - and therefore would provide less flame stability.

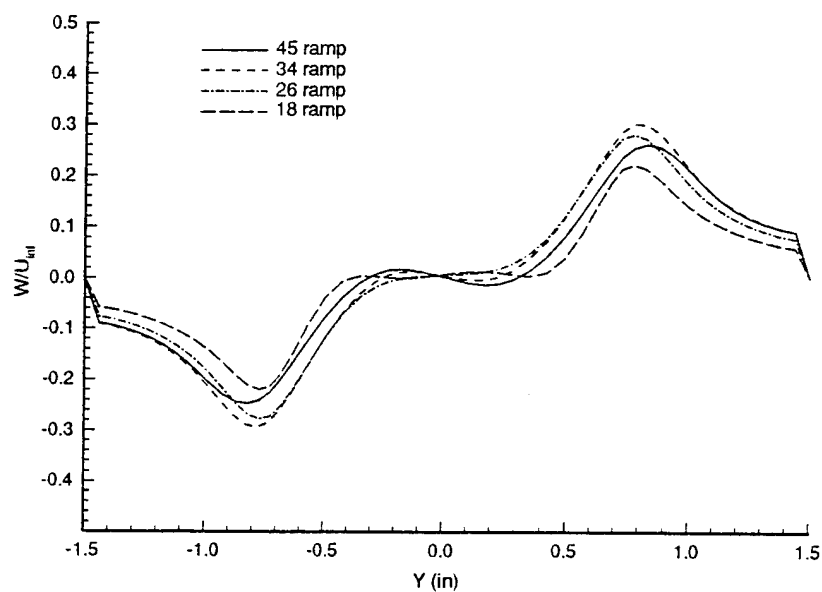
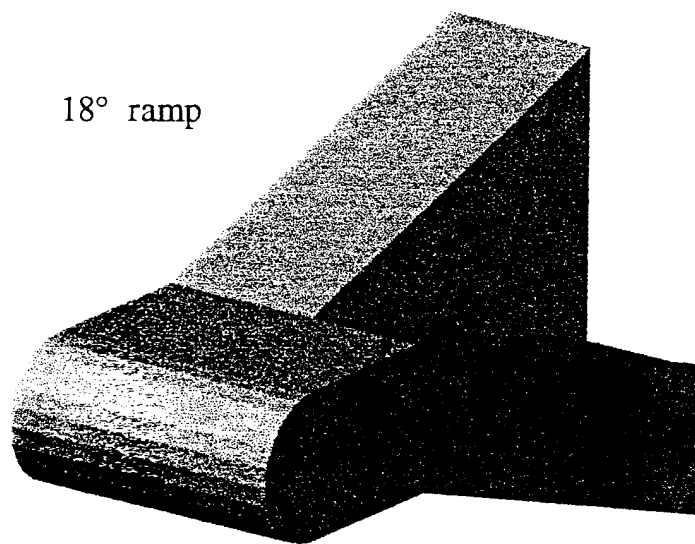
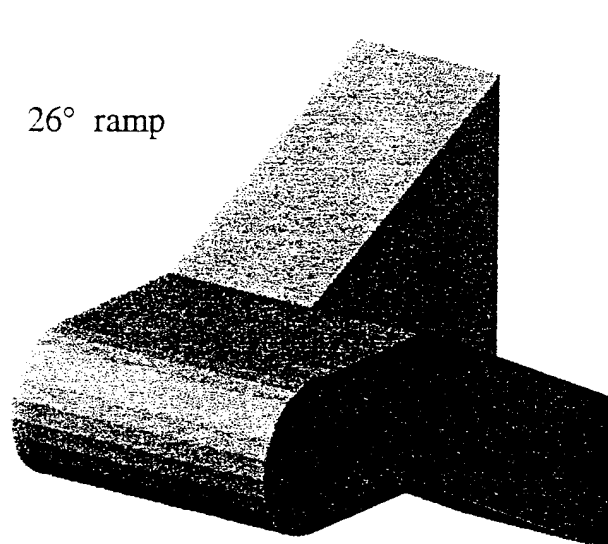
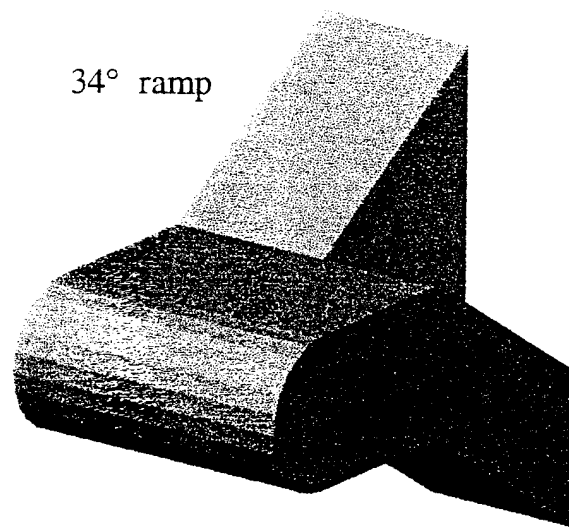
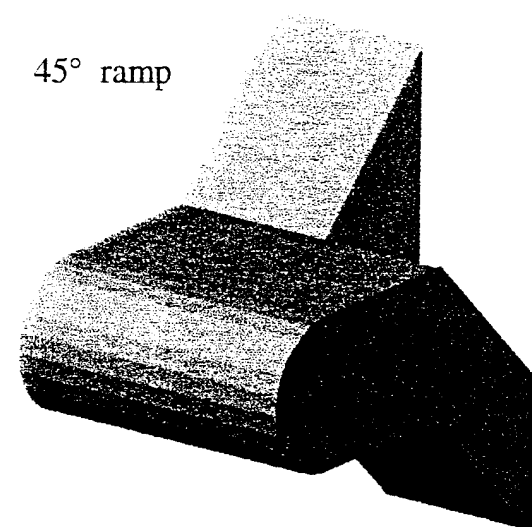


Figure 64. Parametric Study on Ramp Angle, by Varying Tail Length

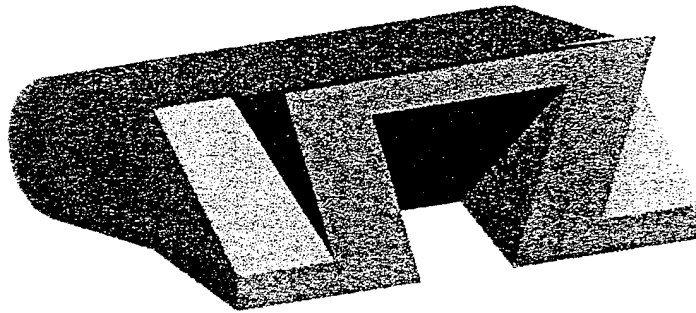


Figure 65. 3-D Model of ADV3

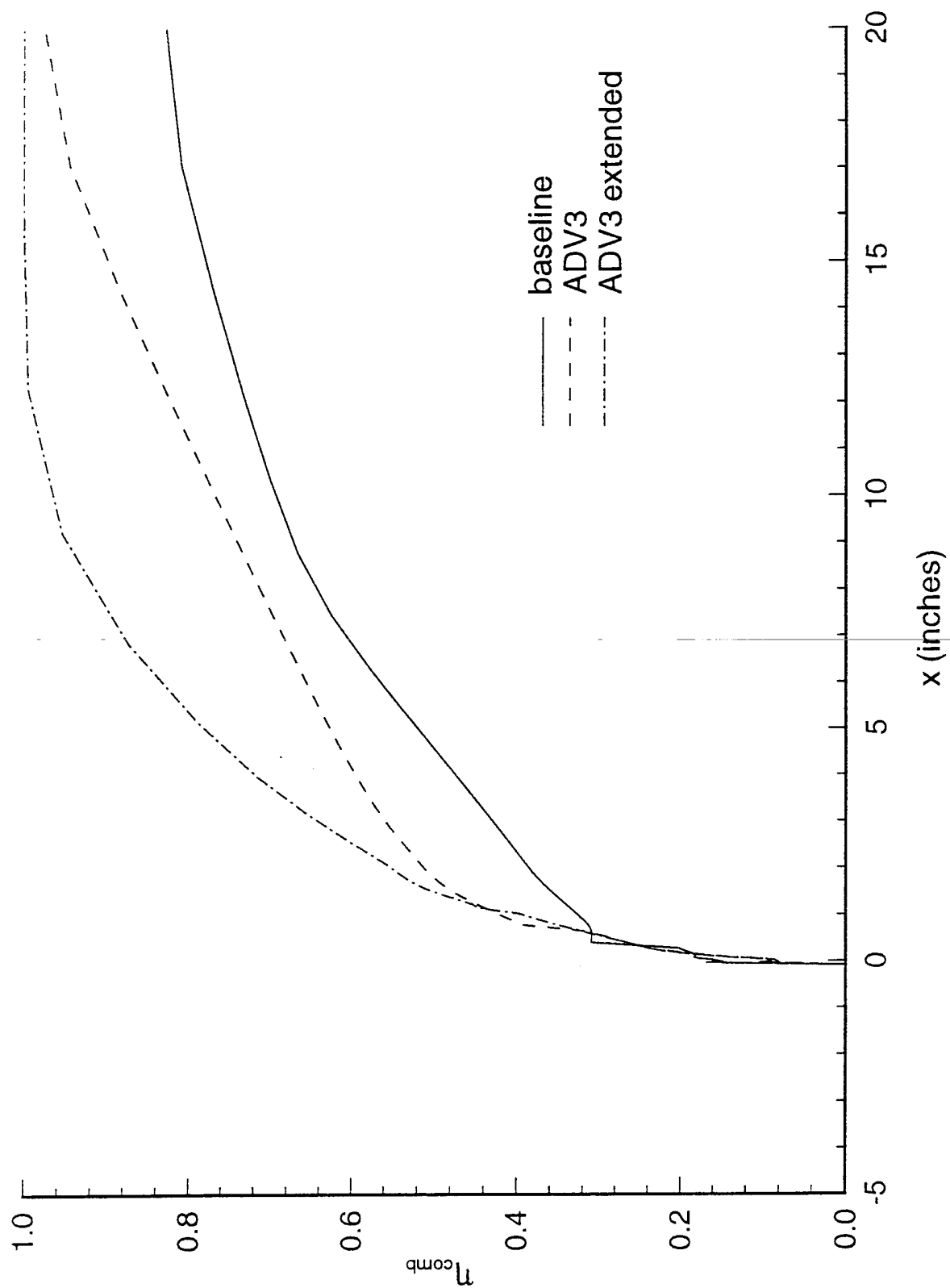


Figure 66. Combustion Efficiency for ADV3 Models

A second variant of ADV3 was tested, and was generated by extending the trailing edge downstream another 0.375 inches, while holding the inner ramp angle constant at 45 degrees (Figure 67). The outer web thickness was also held constant at 0.125 inches, providing a 30 degree outward facing ramp. The results are also shown in Figures 66 and 63. The combustion efficiency was very close to that of the ADV2  $\alpha$ 20 model. But the geometric blockage is comparable to that of ADV2  $\alpha$ 20, and the pressure loss reflects that fact, matching the ADV2  $\alpha$ 20 results.

#### 5.3.4 Advanced Model ADV4

The advanced model ADV4 was the first of two exotic models intended to explore different ways of using the momentum of the fuel to help create the axial vortices. ADV4 is shown in Figure 68 and was designed from the extended version of ADV3, by joining the tips of the adjacent fingers together with a fuel bar. The fuel was then injected through the fuel bar instead of through the injectors located in the mid-section of the IFF. The goal was to use the fuel to enhance attached flow passing through the channels between the fingers (see Figure 69). With the attached flow, the axial vortex would be strengthened. The results shown in Figures 70 and 63 show that the design performed poorly in all aspects. Having the highest geometric blockage (47%), the pressure losses are high. In addition, the fuel is injected from below the centerline, degrading fuel penetration. As a result, the mixing performance, and combustion efficiency, is very low.

#### 5.3.5 Advanced Model ADV5

The next advanced model, ADV5, was also an exotic approach. ADV5 relied on the principles of the Coanda effect and slotted flap technology to increase the mixing performance. The Coanda effect has been demonstrated to reduce the drag of bluff bodies.<sup>35</sup> Shown in Figure 71, ADV5 injects the fuel tangentially with the freestream, using the Coanda effect to pull the flow around the curved surface of the finger. The remaining surface of the finger was energized with the high momentum flow coming through the slotted flap located below the fuel injector.

A two-dimensional model was first tested to verify the validity of the design. Figure 72 shows the velocity vectors that resulted from the 2-D analysis. It can be seen that the model operates as expected, with the injector and slotted flap providing attached flow.

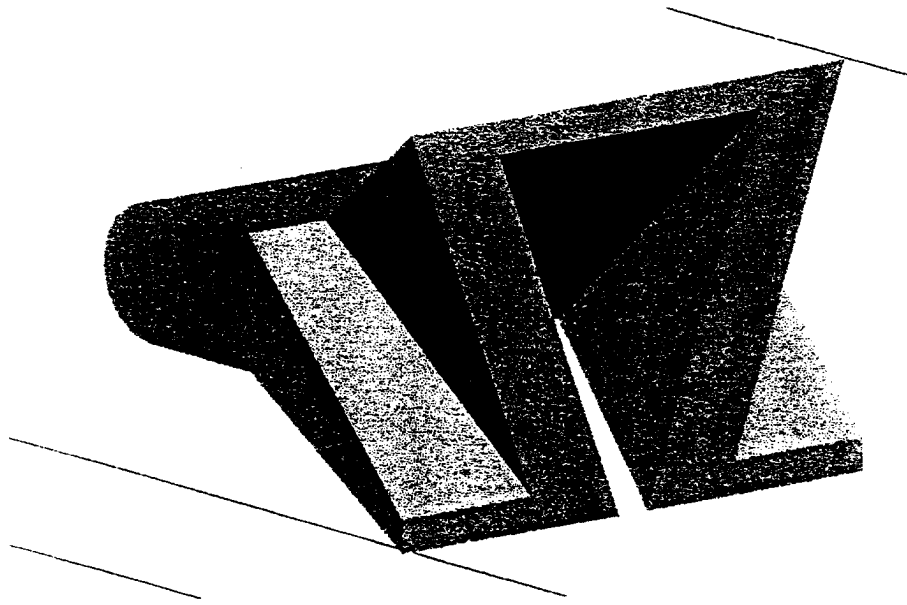


Figure 67. 3-D Model of ADV3 Extended

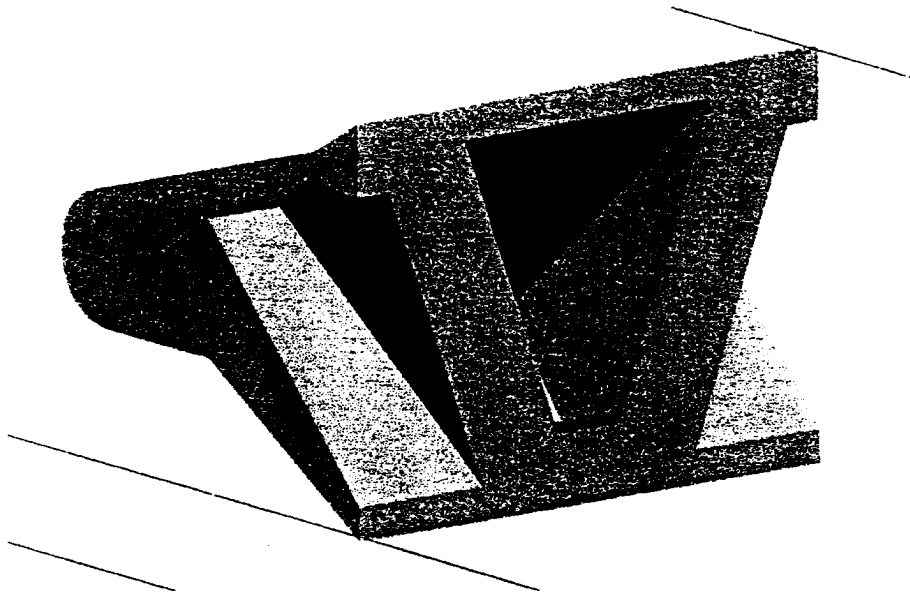


Figure 68. 3-D Model of ADV4



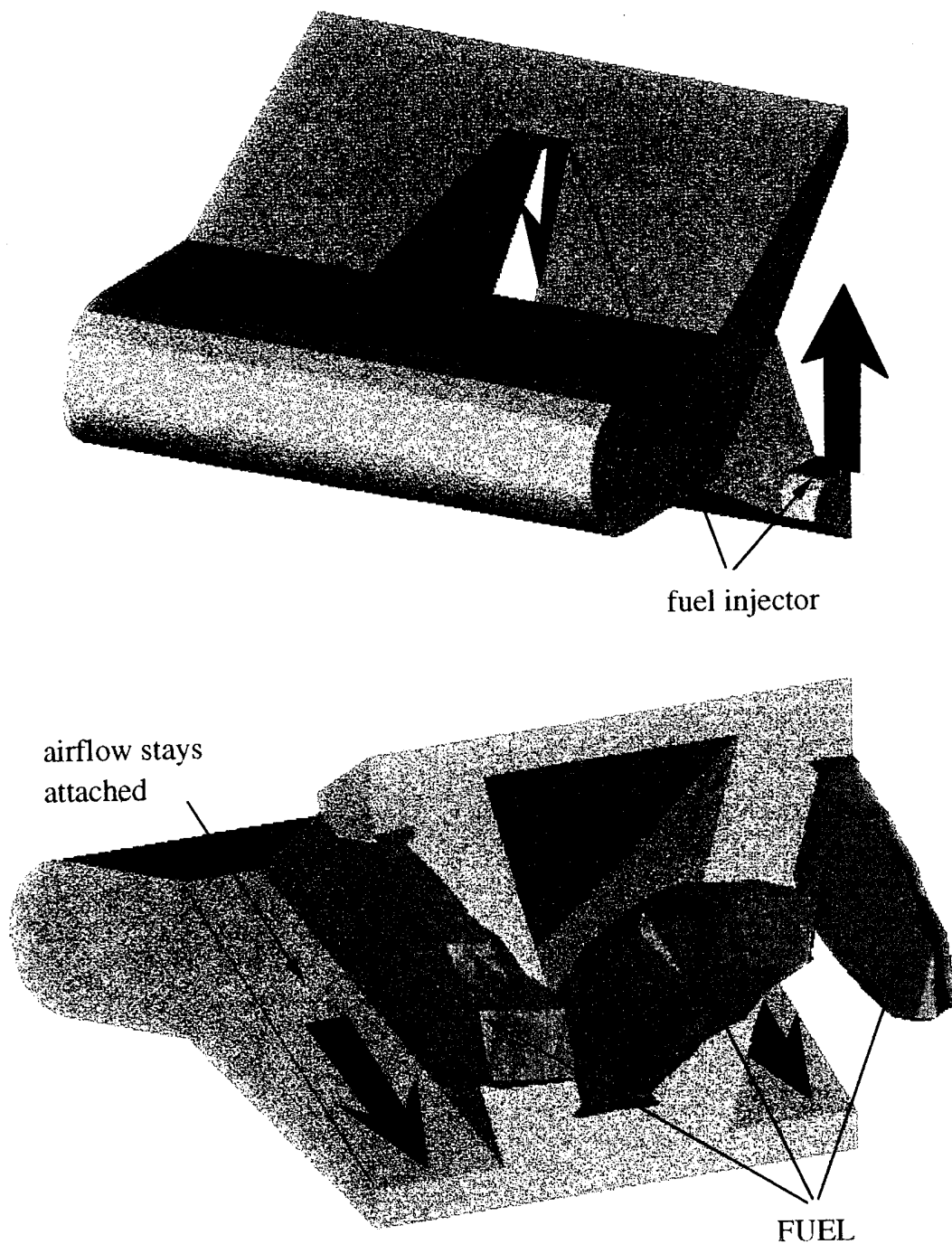


Figure 69. ADV4 with Fuel Injected Near the Inlet

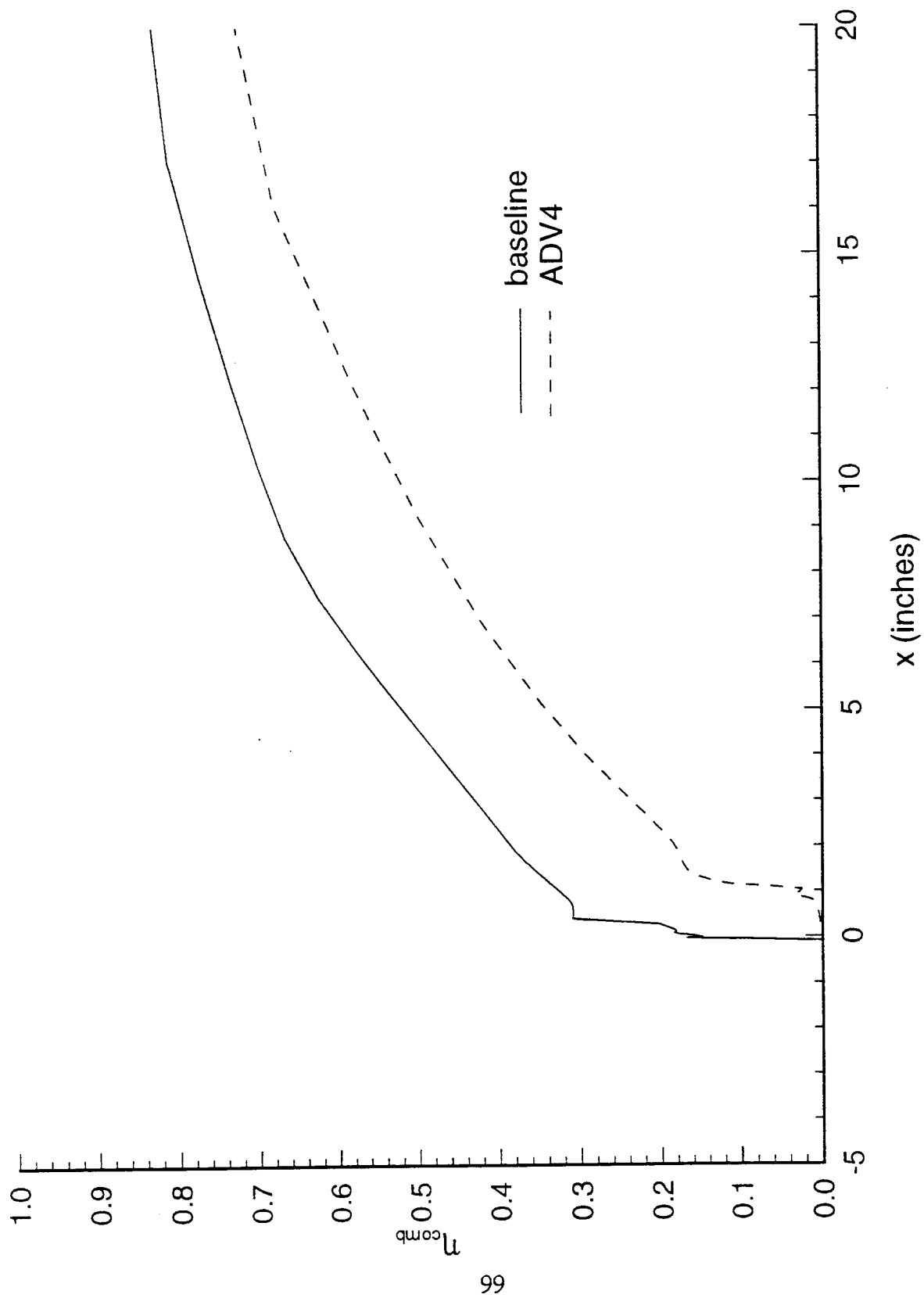


Figure 70. Combustion Efficiency for ADV4 Models

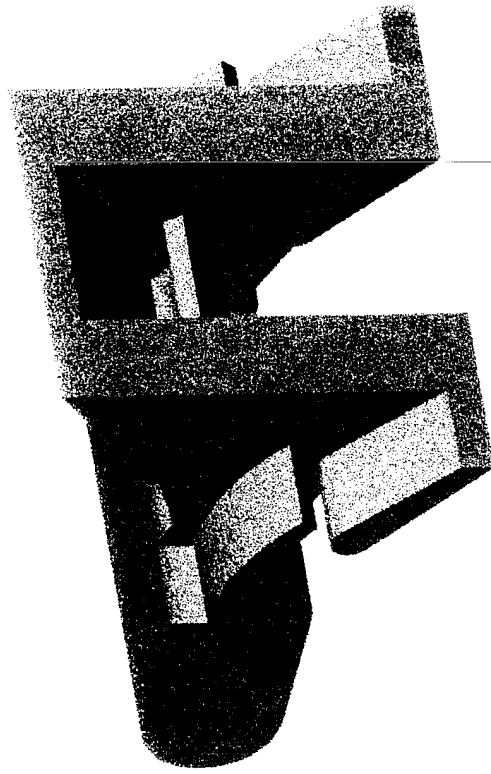
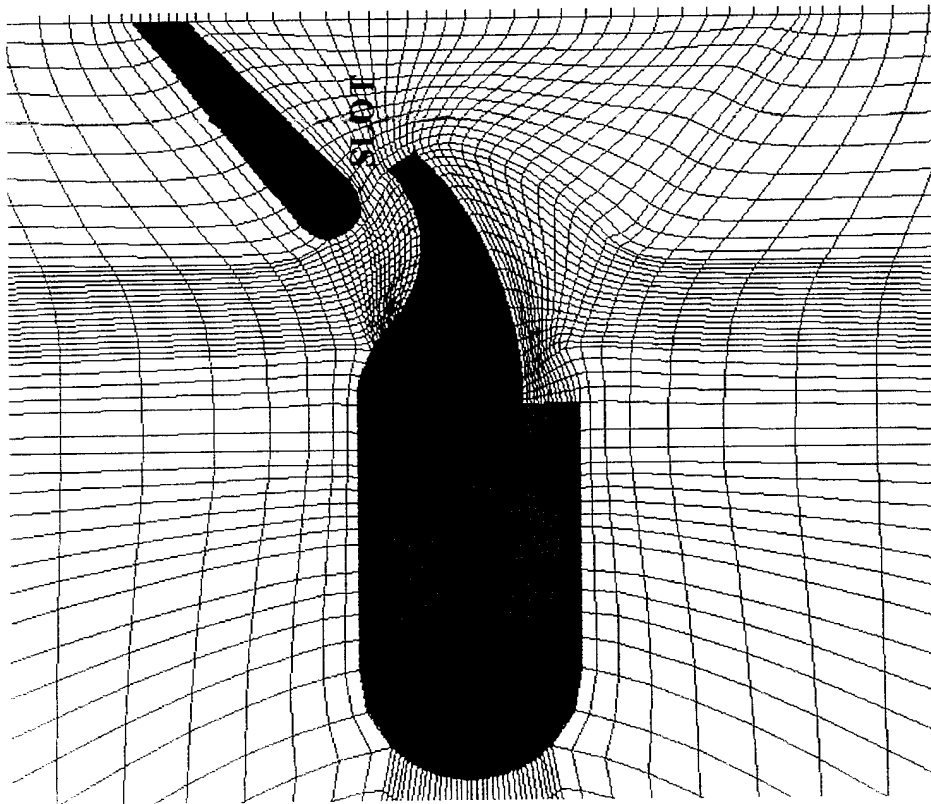


Figure 71. 3-D Model of ADV5

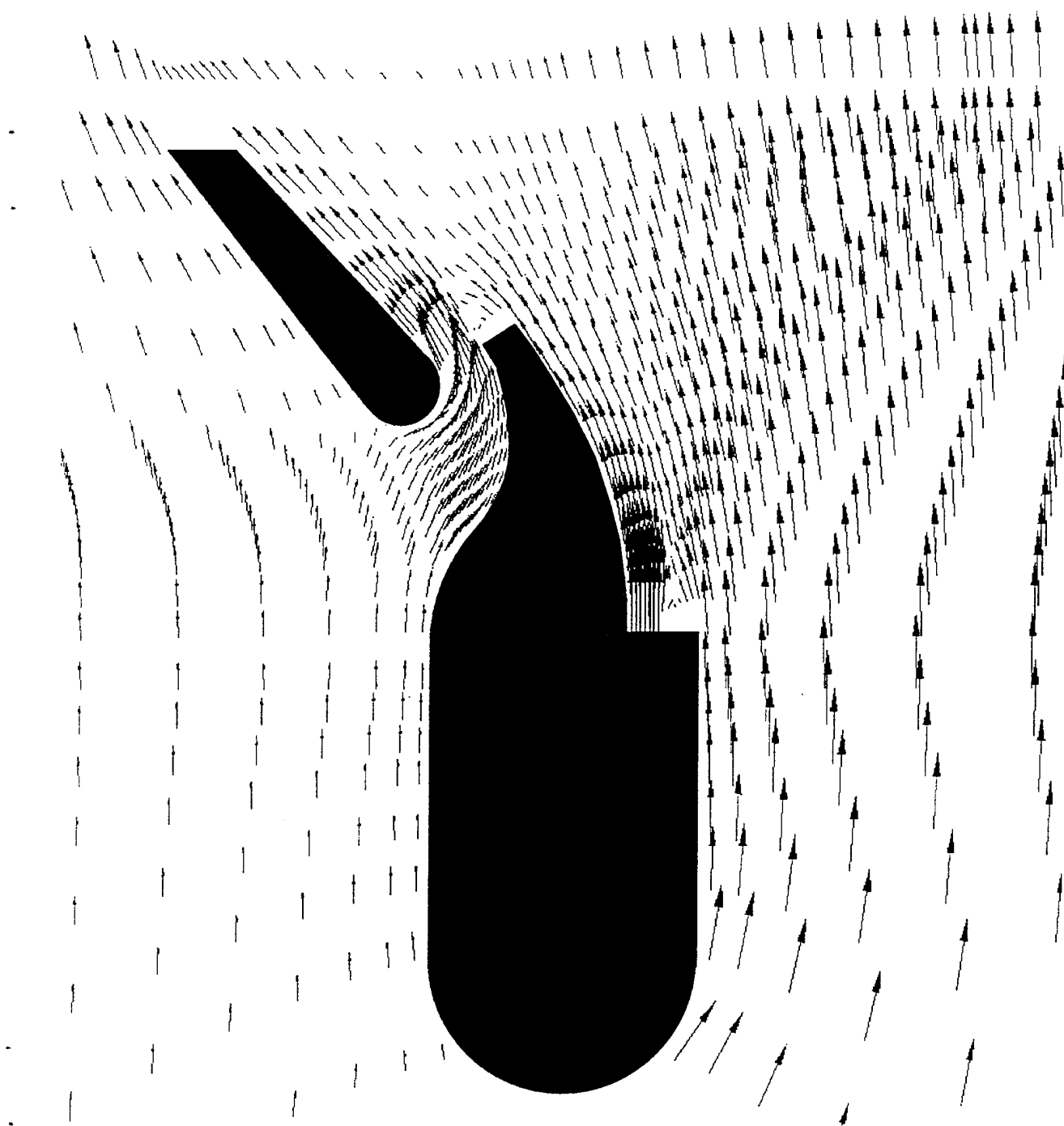


Figure 72. Velocity Vectors from 2-D Analysis of ADV5 Show Attached Flow

The three-dimensional model was analyzed next, and the results are shown in Figures 73 and 63. The mixing performance was the best, by far, of any of the models tested, reaching 100% combustion by nearly 1/3 the distance of the ADV2  $\alpha$ 20 model. The pressure loss was better than for other models of similar blockage, due to the net gain in total pressure from the tangential fuel injection. The pressure loss is still substantially higher than the baseline IFF pressure loss (by a factor of 3), and the combustion efficiency gains would probably not overcome the pressure losses.

#### 5.3.6 Advanced Model 6

Since all of the previously tested models had substantially higher pressure losses than the baseline, attention turned to testing models with smaller base areas in an effort to make smaller mixing gains, with little increase in pressure loss. The first attempt employed a small triangular fin on the top surface of the IFF near the injector. The fin measured 0.25 inches high and 0.4 inches long, and was placed at a 30 degree angle to the flow. The leading edge was placed 0.25 inches outboard of the injector centerline, which is approximately halfway between injectors. ADV6 is shown in Figure 74, with the crossflow vectors plotted just downstream of the flameholder. The analysis showed that the vortex generator produced a smaller, tighter vortex than the other models, but has a pressure comparable to the baseline IFF pressure loss (Figure 63). The numerical test was isothermal without fuel injection, to examine only the effects of the fin. To judge the mixing ability of ADV6, an analysis determined that a fluid element passing near the vortex generator would make one complete turn at 2.7 inches downstream, as compared to 5 inches downstream for ADV2  $\alpha$ 20. However, the vertical extent of the effect seemed to be limited. At the midpoint between the IFF surface and the top wall, there was very little influence from the vortex generator. But the vortex generator did improve the lateral fuel distribution along the base of the flameholder.

A parametric test was initiated to determine the effect of the lateral placement of the fin, on pressure loss. However, when the fin was placed near either symmetry plane, numerical instabilities resulted, possibly from unsteady separation from the underside of the fin.

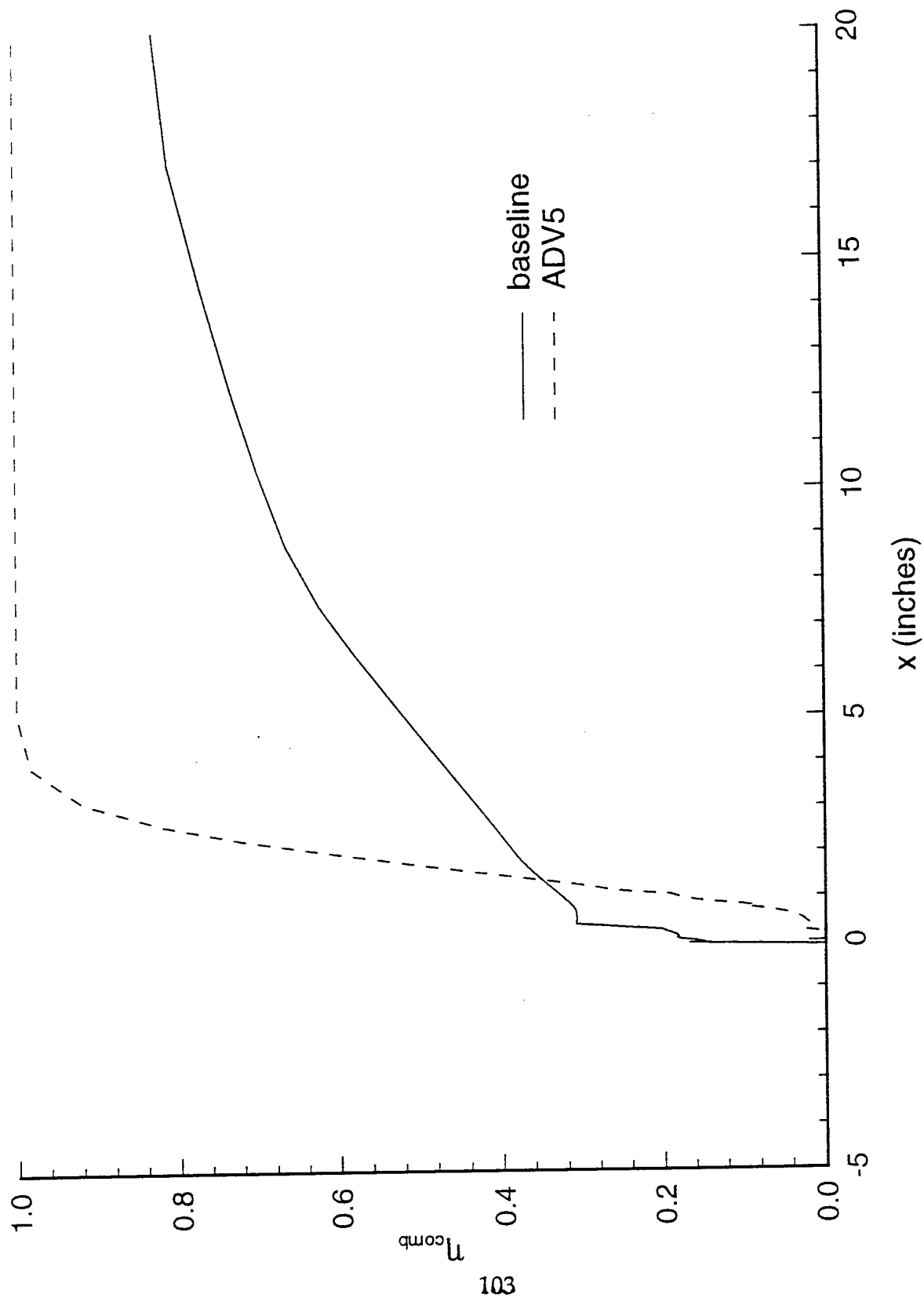


Figure 73. Combustion Efficiency for ADV5 Models

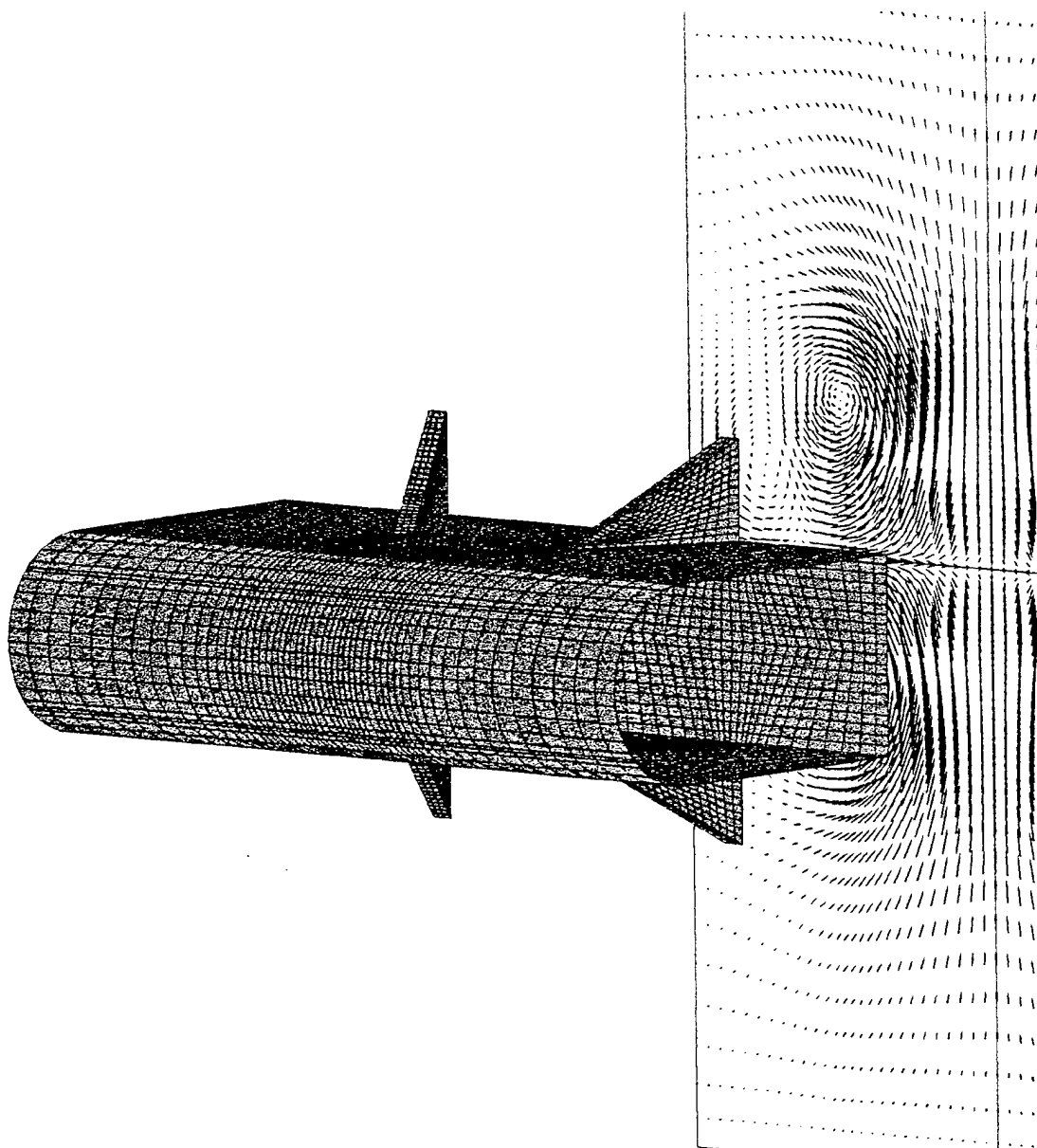


Figure 74. 3-D Model of ADV6 with Velocity Vectors Downstream of Flameholder

### 5.3.7 Advanced Model 7

Another approach to improving the performance of the IFF, was to take advantage of the unsteady vortices that were shed from the base of the IFF during the isothermal tests (see Section 4). Advanced model ADV7 was an attempt to modify the paths of the shed vortices. Then, by altering the effect laterally, a wave could be imposed on the wake, creating a larger shear surface for increased mixing. The new design had a simple slant cut into the back face of the IFF (Figure 75), in an attempt to skew the wake. A parametric study was run with three different backface angles. The analysis was completed in two-dimensions using the unsteady solution algorithm. While each geometry produced a slightly different wake pattern, the vortices simply filled any voids created on the back face of the IFF, with no change in the wake overall. Therefore, the design was not successful. Subsequent experimental testing verified the results.



(a) 2-D Model of ADV7  $\alpha 30$



(b) 2-D Model of ADV7  $\alpha 45$



(c) 2-D Model of ADV7  $\alpha 45\text{mod}$



(d) 3-D Model of ADV7  $\alpha 30$

Figure 75. 2-D and 3-D Models of ADV7



### 5.3.8 Advanced Model 8

The final advanced model tested (ADV8) again used the momentum of the fuel to try to control the motion of the wake. Shown in Figure 76, ADV8 followed the baseline IFF shape, but injected the fuel directly into the wake at the top edge of the base of the IFF. Two different fuel injection angles were tested: 45 degrees, and 67 degrees from horizontal. Again, the tests were conducted in two-dimensions using the unsteady flow solver.

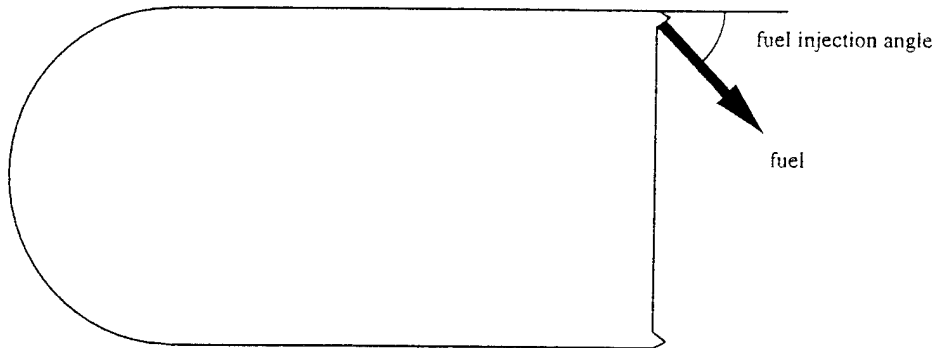
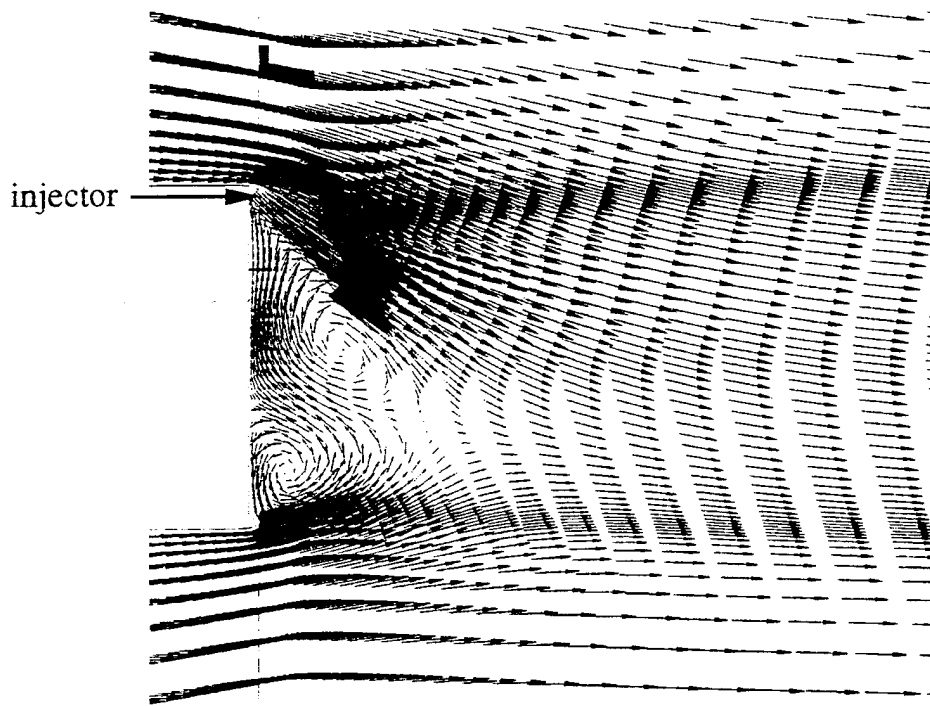


Figure 76. Schematic of ADV8

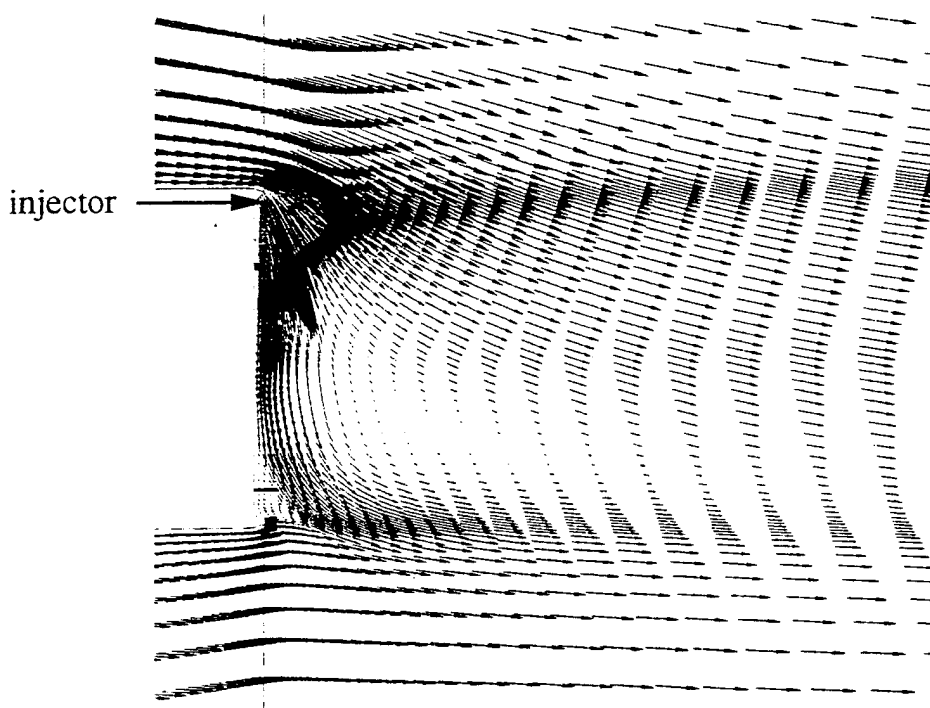
The time-averaged velocity fields are shown in Figure 77 for both fuel injection angles. The 45 degree case did exhibit some unsteady vortex motion with stronger perturbations to the mean flow than the baseline IFF. However, the mean recirculation zone behind the IFF was considerably smaller, which would result in short residence times and poor flame stability characteristics. The 67 degree case did not show any signs of vortex shedding, and therefore offers much less mixing than the baseline IFF. Since the fuel is injected directly into the wake, the mixing of the fuel with the outer regions of air would be very poor.

## 5.4 Discussion

Through the numerical testing of the many different flameholder shapes, anchoring the flame on the center region, as opposed to the ends of the fingers, appears preferable. This was demonstrated between the ADV2  $\alpha 20$  and the ADV3 extended model. The primary difference was the location of the flameholder base. ADV3 actually had more geometric blockage, but performed better in terms of combustion efficiency and pressure loss. The center anchor position also anchors the flame in the center of the vortex. At lean combustion conditions, with the onset of vortex shedding, the vortex anchored flame may prove to be more stable, reducing the lean blowout limit of the combustor. The only difficulty with the center flameholder comes during ignition. Without a continuous flameholder surface, ignition may not propagate across the flameholder. However, the fire may travel along the webs. This question would need to be addressed through experimental testing.



a) fuel jet at  $45^\circ$  from horizontal yields unsteady solution



b) fuel jet at  $67^\circ$  from horizontal yields steady-state solution

Figure 77. Velocity Fields for ADV8 Model, with Two Fuel Injection Angles

The best design, based on combustion efficiency and pressure loss, was the ADV5 model. ADV5 provided excellent combustion performance, but still had three times the pressure loss of the baseline. Further study needs to be completed to determine the possible tradeoffs between the pressure loss and the mixing performance. Possible design modifications include extending the Coanda surface and eliminating the flap. The vertical extent of the flameholding surface could also be reduced. The blockage will then be reduced, but the fuel will still be providing a net gain to the total pressure while maintaining a strong vortex. Finally, the flameholding surface could be reshaped by rounding the corners and allowing it to follow the rounded shape of the vortex core.

ADV5 has another problem that should be addressed. The design relies on the fuel to provide attached flow on the body. The combustor would not perform as well when operating under liquid fuel conditions, or under low power conditions. The extent of this problem has not been determined.

Design ADV6 also shows some promise, with the use of simple vortex generators mounted on the IFF surface. This design shows the best promise of introducing some performance gain with very little additional pressure loss. However, the vortex generators would be in immediate danger of melting, since they would be immersed in an auto-ignition flame. One solution may be to inject the fuel through the trailing edge of the vortex generators. The fuel could then be used to cool the fins, while injecting the fuel directly into the vortex core. The flameholder and the fins would then be out of the fire, with a corresponding longer operational life. In addition, the fuel would be providing a gain in total pressure due to the tangential injection. This can be a detriment, however, as the fuel may not penetrate sufficiently into the airstream. The vortex generated by the fins is not as large as the other designs (ADV2, ADV5), and may not provide enough mixing to offset the loss of fuel penetration.

## 6.0 ISOTHERMAL EXPERIMENTAL TESTS: ADVANCED MODELS

Four advanced models were fabricated for testing. The advanced model, ADV2, consisted of an attachment that replaced the existing 0.125 inch dump plate on the baseline IFF (Figure 78). The attachments consisted of three identical wedges that created 45 degree ramps on the trailing edge of the IFF. Each wedge was 0.5 inches long and extended into the freestream flow by 0.5 inches. The separate parts were assembled onto a 0.125 inch plate that was then fastened to the baseline IFF, making the total length of the ADV2 model equal to 1.5 inches. Three ramps were fabricated, with the center ramp facing down, and the two outboard ramps facing up. Only three ramps were included in the tests in an effort to simplify the numerical comparisons.

Three other advanced models were quickly tested: ADV7/mod1, ADV7/mod2, and ADV7/mod3 (see Figure 79). ADV7/mod1 was fabricated by taking simple trailing edge extension blocks and cutting the trailing edge back at a 30 degree angle to the vertical. The model consisted of two extension blocks, one cut 30 degrees facing up, the other cut 30 degrees facing down. The hope was that each piece would skew the wake in a favored direction, resulting in a spanwise pressure gradient that would induce a vortex. ADV7/mod2 attempted to further enhance the mixing by alternating the face directions across the span of the model. Finally, ADV7/mod3 took the mod2 extensions and mounted them on the leading edge of the baseline IFF, replacing the hemispherical nose.

### 6.1 Test Results

The only advanced model extensively tested was ADV2, with three ramps. The presence of an axial vortex pair was evident in the data, with a peak crossflow velocity of  $0.22 U_{inf}$ , at  $x/H = 4.0$ . A parcel of air crossing near this point would require at least 10 base heights to make one full revolution. It was felt by the program monitor that this was not sufficient to substantially enhance the fuel air mixing.

Another model tested, ADV7/mod1, was an attempt to make smaller gains at fuel-air mixing, but at much lower pressure losses. However, ADV7/mod1 and mod2 both produced results that were not significantly different from the baseline results, in terms of both the velocities, and pressure losses. The conclusion was that the trailing edge can be modified in an arbitrary manner with no effect on the flowfield, as long as no protrusions are introduced beyond the vertical extent of the baseline geometry.

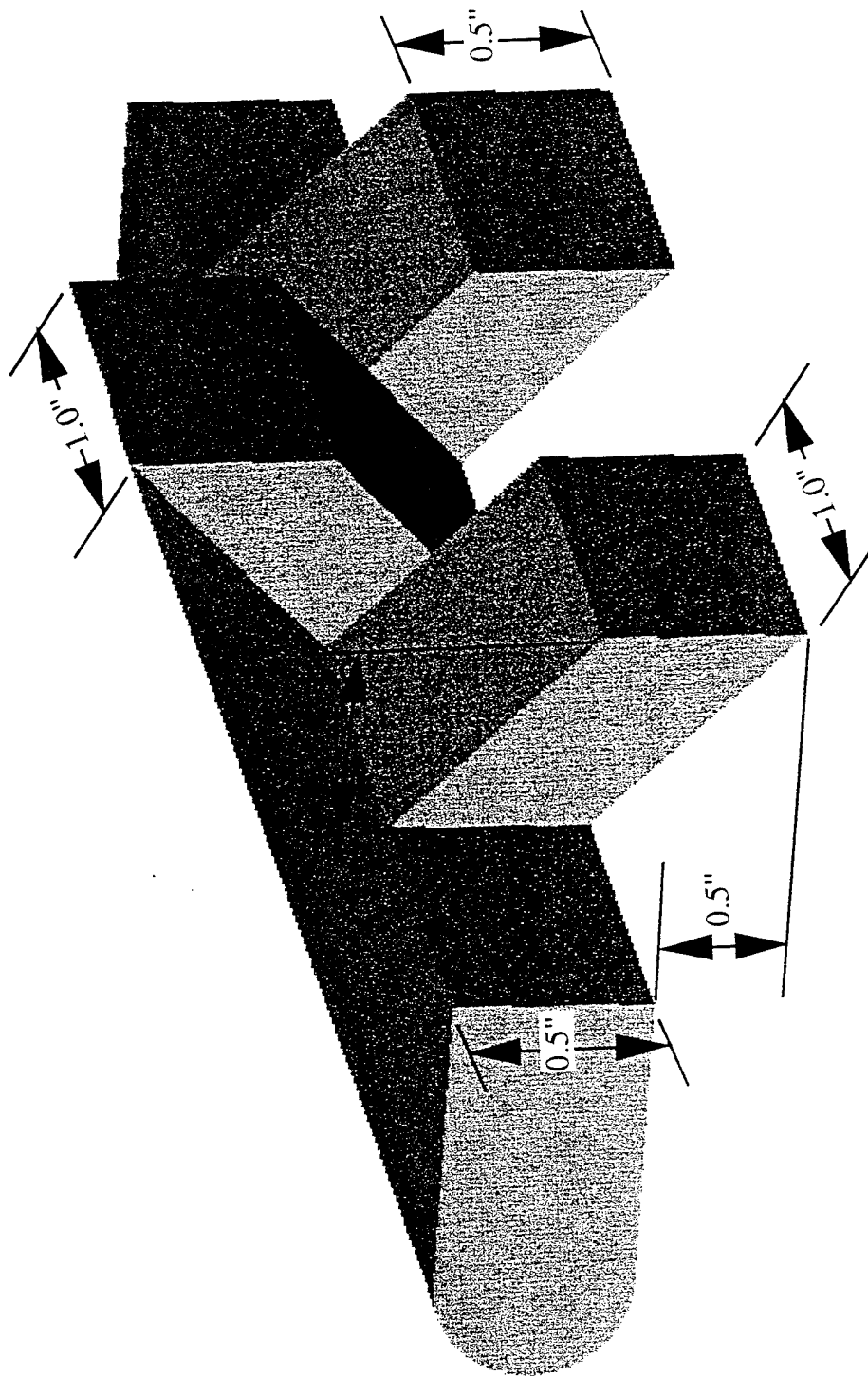
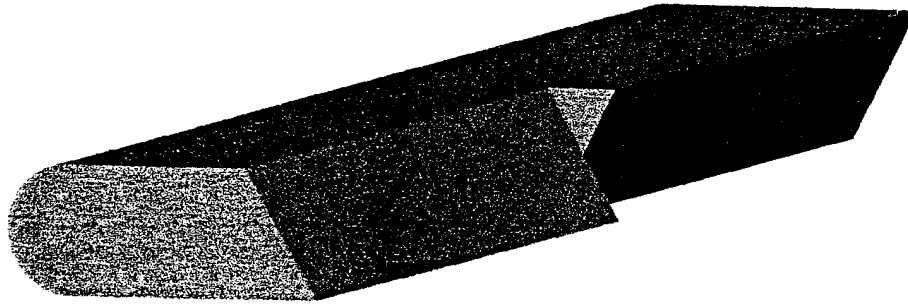
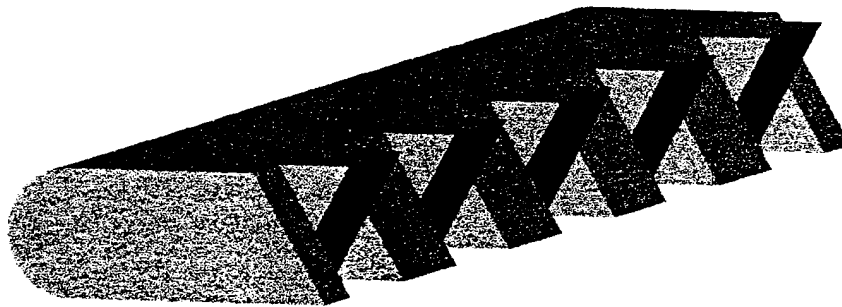


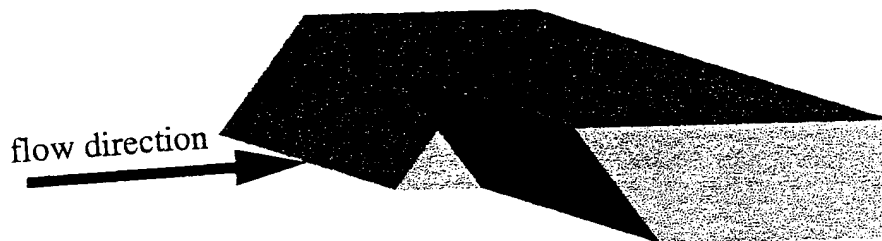
Figure 78. Advanced Model ADV2, as Tested with Three Ramps



a) ADV7/mod 1 ; two spanwise cuts



b) ADV7/mod 2 ; multiple spanwise cuts



c) ADV7/mod 3 ; two spanwise cuts on leading edge

Figure 79. ADV7 Models as Tested

ADV7/mod3 did produce some different results. The goal was to produce leading edge vortices from the corners of the leading edge extensions as the flow passed around the IFF. Unfortunately, no corner vortices were found, although a large single vortex was formed through the entire test section as a result of the opposite direction of each leading edge extension. This large vortex had very low velocities and would not significantly enhance mixing.

## 6.2 Pressure Losses

The static pressure losses were measured for all models based on the difference between the static pressure at  $x/H = -24$ , and  $x/H = 48$ . Both pressure ports were connected to the opposite sides of a micromanometer. The pressure losses were low due to the low air velocities measuring 0.08% for the baseline IFF. The advanced model ADV2 had over three times the baseline pressure loss at 0.29%. This value cannot be directly compared to the numerical results, since the fingers did not extend to the walls. Based on these results, it was felt that the ADV2 pressure losses would offset any gains made from enhanced fuel/air mixing created by the vortex formation. All of the ADV7 models had the same pressure loss as the baseline, since they all had the same base areas and geometric blockages as the baseline.

## 7.0 EXPERIMENTAL COMBUSTION TESTS

The original Phase I plans called for the design and fabrication of a water-cooled combustion test section for installation into Test Cell 19. The tunnel design placed the IFF model spanning the tunnel in the vertical direction, providing a top view of the IFF through the side window. The overall design included full view windows on the top and bottom of the test section, and partial view windows on the sides. The test section was 42 inches long and the optical quality quartz windows were 14 inches long. The window retainers could be reversed to change the window viewing area from upstream to downstream, providing a total viewing area of 26 inches in the axial direction.

LDV velocity data and CARS temperature data were to be taken throughout the test section for the baseline and one advanced model, at one equivalence ratio. The isothermal tests were also to be repeated on the baseline model. Test Cell 19 included support for providing clean nonvitiated air up to temperatures of 1000 F, and had a full settling chamber and transition section for high quality inlet flow. In addition to a new test section, a new Mach control section was needed for the subsonic tests.

The design for both the test section and Mach control section was completed on schedule. Most of the mechanical design and drafting work was completed by Mr. Gary Haines of Cincinnati Control Dynamics, Inc. Mr. Steven Green of Wright Laboratory completed many of the heat transfer and cooling requirement calculations for the test section. However, the sections were never installed and the tests were canceled due to scheduling difficulties.

For documentation purposes, the basic component design criteria are presented in the next sections for each component, followed by a list of uncompleted items for future reference.

### 7.1 Test Section Design

The conceptual design of the test section (see Figure 80) was 48 inches long with a 6x6 inch internal cross section. The reversible window panels provided access from 6 inches upstream of the model trailing edge to 20 inches downstream, on three sides. The bottom window was limited to view from the trailing edge to 8.5 inches downstream. All solid walls of the tunnel were constructed from a copper/stainless steel sandwich with cooling channels cut into the copper. The outer stainless jacket sealed against the copper to close the water channels. Water channels were also provided along the side window frames to provide some cooling to the copper frame, to reduce the linear thermal growth of the copper wall.



# Combustion Test Facility

## Cooling Water System

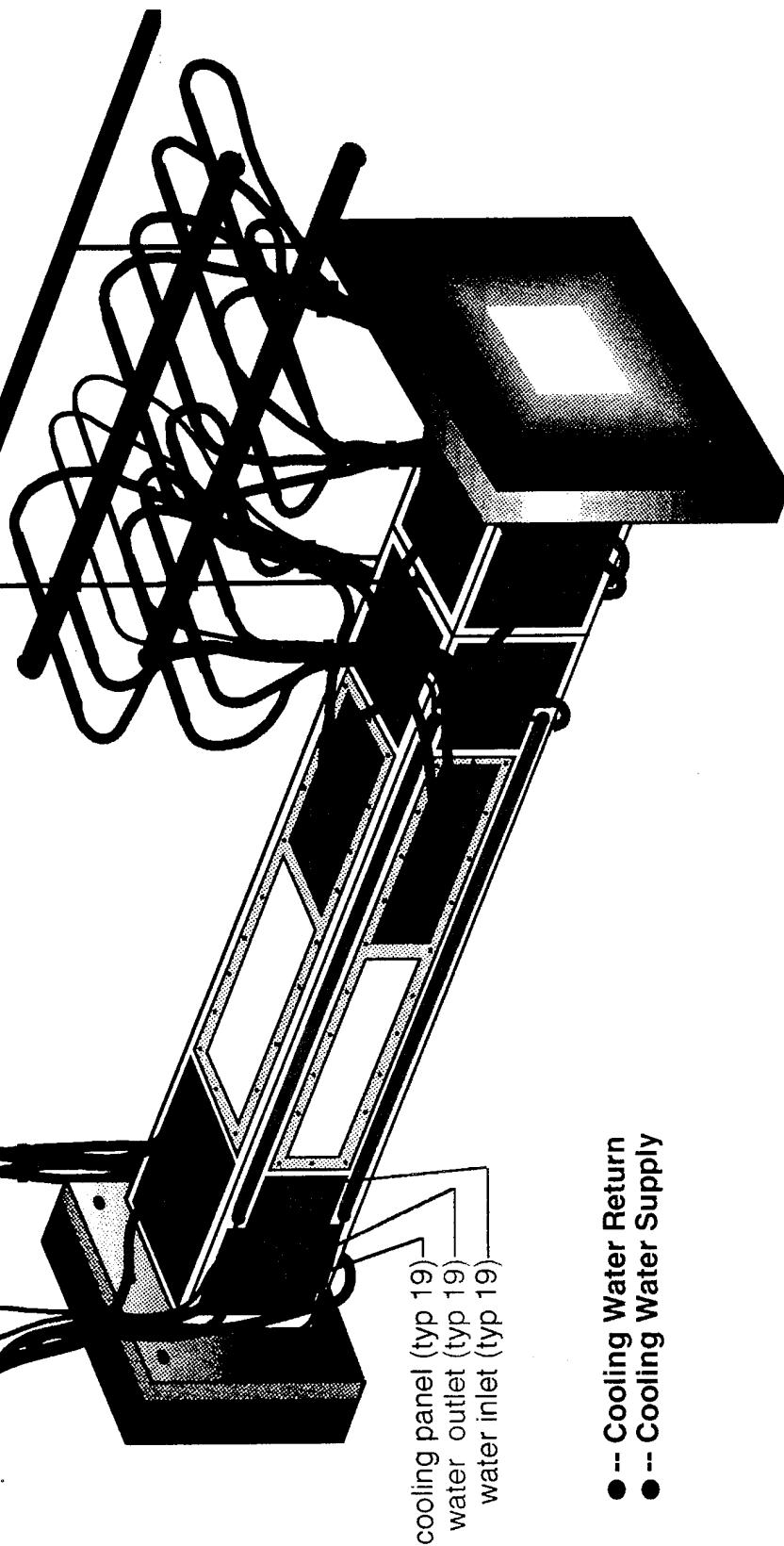


Figure 80. Schematic of Combustion Test Section

The quartz windows, being uncooled, were the limiting structural components. The maximum overall equivalence ratio was limited to  $\phi=0.2$  to keep the window temperatures below 1300 K. Window growth with temperature was not considered a problem ( $<0.005$  inch) and was neglected. A window thickness of 0.75 inches was chosen for all windows. Table 3 shows the window dimensions and factor of safety for all windows at a 2 atmosphere pressure differential.

Table 3. Factor of Safety for Tunnel Windows at 30 psig

window	size (inches)	factor of safety
top	14x6.75	4
sides	14x3	17
bottom	8.5x6.75	7

The side windows were held in place by retaining strips. The side windows become part of the side wall window retainer unit when installed. The top and bottom windows do not become part of their respective wall units, but the windows are trapped between the stainless steel outer jacket and the edges of the copper side walls. Therefore, if the top wall window retainer is removed, the window will remain resting on top of the test section, supported by the side walls.

To facilitate the acquisition of tunnel temperatures and pressures, taps were drilled in several places down the midline of each wall section. The ports open up to a larger threaded chamber in the stainless steel, and should be sealed with a pipe plug when not in use.

The test section was fabricated at Sydney Tool and Die in Sydney, Ohio. The components were shipped to Wright Patterson AFB, and inspected. Each wall was assembled and pressure checked to 100 psi. The windows were cut and polished by Glass Fab, Inc, located in Rochester, N.Y. The specifications on the windows required an 80/50 scratch/dig polish, a flatness of 1 fringe per inch, and a homogeneity of  $5 \times 10^{-6}$  or better.

## 7.2 Transition Section Design

When the tests were rescheduled for Test Cell 18, a new transition had to be designed to fit the new facility. The transition had one main purpose - to smoothly transition from the round pipe of the tunnel air supply, to the square test section. To reduce costs, standard hardware was utilized as much as possible.

The critical component of the entire section was the transition liner, and was custom made. The liner internal geometry was designed using a purely mathematical function to transition from a round cross section to a square cross section with zero axial slope at each end.<sup>36</sup> The transition function had no physical

basis. The liner shape was then electronically delivered to the Air Force Machine Shop at Wright Laboratory, where stereo lithography was used to fabricate the liner. Typically used to fabricate manufacturing prototypes, stereo lithography uses an ultra violet laser to paint a given cross section of the design in a thin layer of liquid polymer. The liquid polymer hardens when struck with the laser. The liquid polymer level is then raised slightly in the tank, and the next cross section is painted. The process is repeated, building up one cross section on top of the other until the article is completed. There is no constraint to the complexity of the article that can be produced with stereo lithography.

The transition liner was actually fabricated in three sections, to make the most efficient use of the stereo lithography machine. When finished, the pieces were sanded and glued together to form the finished product. Although the process is typically used to construct prototypes or mold casts, the plastic transition liner was the actual part used in the tunnel. The liner acted only to provide a flow path, and did not carry any loads or contain any pressure. To contain the pressure, the liner was fit inside of a 12-inch nominal pipe, that was welded closed at one end, and fitted with an open flange at the other. The closed end was machined with a round hole to hold the round end of the liner, and machined with threaded holes to mate to the existing tunnel supply pipe. The flange end was fit with a blank flange that had been machined with a square hole to fit the square end of the liner. The blank flange also had threaded holes to connect to the test section. To protect the liner from vibrational stress, and to provide additional support, expanding foam filler was purchased to fill the space between the pipe and the outside of the liner. However, this step was never completed.

### 7.3 Choke Block Design

The design for the choke block section did not change when the tests were moved from Test Cell 19 to Test Cell 18. Several designs were considered, including a water cooled cone that moved axially to change the blockage at the test section exit. While the cone provides the easiest method of tunnel operation, simple 2-D flaps were selected due to the ease of design and fabrication.

The choke blocks were designed with a different approach than the test section. Instead of a copper cooling wall covered by a stainless steel jacket, the choke blocks used single plate stainless steel walls with straight axial cooling tubes drilled through the ends of the top and bottom walls. The water flowed from the front of the section and dumped out the rear of the walls directly into the tunnel exhaust section. The side walls were not cooled since they were protected by the flappers. The copper flappers were cooled by water sprayed on the leading edge from holes in the side walls, just upstream of the flappers. The Mach number was controlled by setting the position of each flapper with a threaded plunger mounted near the trailing edge of each flapper. Care must be taken to set each flapper symmetrically,

or flow asymmetries could develop in the test section. The section was fabricated by Sydney Tool and Die.

#### 7.4 Baseline Model Design

The baseline model designed for the combustion tests was less complex than the isothermal model design. For the isothermal model, several tail pieces were designed to fit on the centerbody in a modular fashion, and without any screw heads exposed on the back face. The combustion model design was not as modular. The model was machined from a solid piece of stainless steel to the shape of the IFF, with an additional tail piece that screwed directly onto the base of the primary piece. The screw heads were countersunk to provide minimum flow interference. The 1.0-inch base height of the model provided the same blockage as in the isothermal tests. A pair of holes were drilled through the span of the model to serve as fuel manifolds. Stainless steel, thick-walled tubes were threaded into each hole, passing through the floor of the tunnel, and acted as two pins to maintain the model's orientation in the tunnel. To hold the model firmly against the tunnel floor, two snap rings were installed near the midpoint of the length of the fuel tubes, capturing a small steel plate between the rings and the outside of the tunnel floor (Figure 81). Four bolts threaded through the plate and pressed against the outside floor of the tunnel. By uniformly tightening the bolts, the plate exerted a uniform pressure against the snap rings, firmly holding the IFF model in place. The opposite end of the model was fit with an o-ring to provide a cushion against the upper window. The Model was fabricated by Tipp Machine & Tool, Inc, in Tipp City, Ohio.

#### 7.5 Miscellaneous Information

While many of the parts have been assembled, the entire system has never been assembled, and no leak checks have been completed on the air circuit. Several sub-components need to be obtained or fabricated to complete the system. These include:

- 1) leveling bolts;
- 2) gaskets between components;
- 3) choke block set screws;
- 4) retaining snap rings for IFF model; and
- 5) installation of foam filler in transition section.

For the leveling bolts, two 1/2 inch bolts should be sufficient on each end of the test section. The bolts will be threaded through the floor of the mounting structure and rest against the bottom of the tunnel.

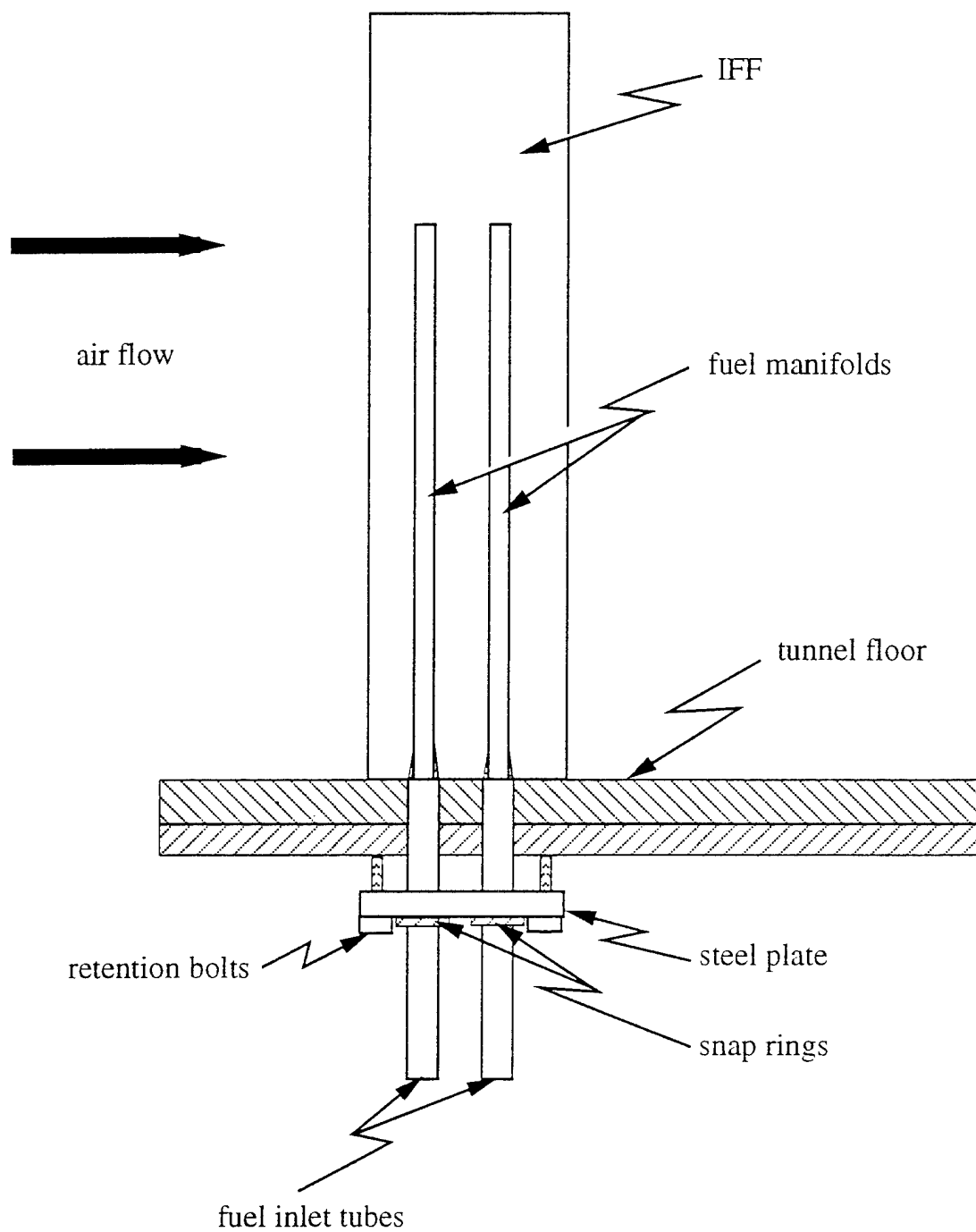


Figure 81. Schematic of IFF Mounting System for Combustion Tests

Gaskets will need to be fit between the following components:

- a) air supply pipe;
- b) transition section;
- c) mounting flange;
- d) test section;
- e) choke block section;
- f) downstream mounting flange; and
- g) tunnel exhaust.

The choke block set screws will have to be made from 1/2 inch fine thread all-thread, and should be at least 4 inches long. A nut tack-welded on the end of the all-thread should provide as a suitable bolt head. During the design process, it was suggested that the set screws be fabricated with a micrometer-type scale to provide precise settings on both sides of the tunnel. It was decided that such accuracy was not necessary. A built-in device to measure the distance from the side of the tunnel with an accuracy of 0.050 inch should be sufficient.

The snap rings used to hold the IFF model in place still need to be acquired. The snap rings are an odd size and may have to be special ordered (Truarc external series 5100-40, 13/38)

The tunnel design was carefully considered and well constructed. However, there were some lessons learned during the fabrication process that should be considered for future modifications. The top window retainer should be held in by positive locking latches to make removal of the window easier. Only one window needs easy removal, to provide access to the model and the other windows for cleaning. In addition, all window retainers need handles installed for easier handling. The retainers fit with tight tolerances and are difficult to remove. Without handles, the chances are increased that a section will be dropped during installation or removal.

## 7.6 Test Cancellation

The combustion tests were originally scheduled to be completed in Test Cell 19, and were to use the clean heated air system available in that facility. Scheduling overruns of other tests operating in Cell 19 at the time forced the current project to be rescheduled for Test Cell 18. The rescheduling had two major implications: 1) there was no heated air system available in Cell 18, and 2) the new test section would have to be retrofitted to fit the new facility, including the fabrication of the transition section. Both were deemed acceptable to keep the tests on-line. Unfortunately, there were also other tests being conducted in Test Cell 18. The current tests were postponed a number of times, and were eventually canceled when the program ran out of time.

## 8.0 NUMERICAL COMBUSTION TESTS

Since no experimental combustion data were produced in this program, another data set was selected for the numerical study. The data set selected for study was that of Sjunnesson, et al.<sup>37</sup> This data set was selected because it was a recent experiment that included detailed CARS, LDV, and gas analyses for a simple geometry. The data set had been the focus of several earlier numerical studies, and was judged to be a good data base for CFD comparisons.

### 8.1 Experimental Data Set

The flameholder model tested by Sjunnesson was cylindrical with an equilateral triangular cross section measuring 40 mm on a side (see Figure 82). The tunnel cross section was 12 cm high by 24 cm wide. A premixed air/propane mixture was introduced to the tunnel at equivalence ratios varying from 0 to 1.1. Inlet Mach numbers ranged from 0 to 0.2, at a Reynolds number of  $5.5 \times 10^5$ , based on the hydraulic diameter of the combustor. Inlet temperature was 288 K, and the pressure was ambient.

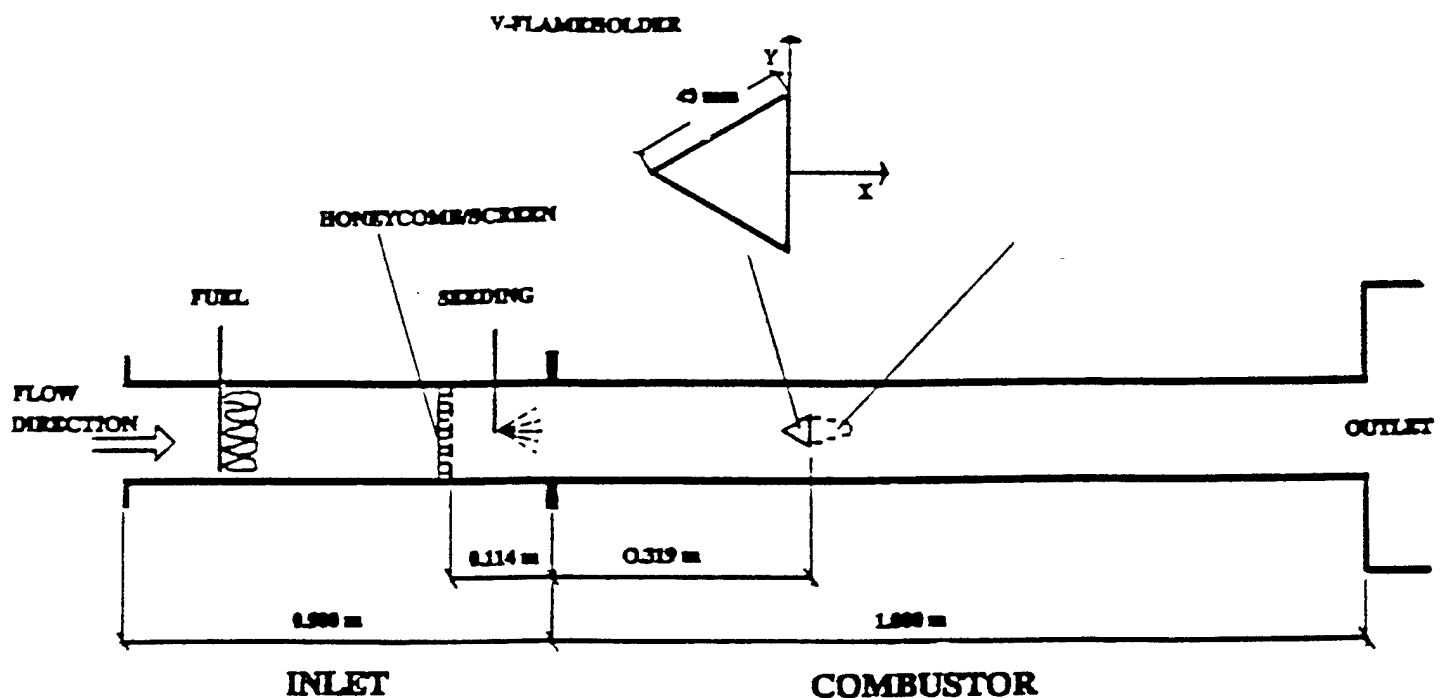


Figure 82. A Schematic Drawing of the Validation Rig

The isothermal tests showed expected results. Vortices were shed behind the flameholder in a regular pattern. At the combustor conditions, no vortex shedding was indicated, even at the lowest equivalence ratio ( $\phi=0.58$ ). Tunnel acoustics are known to play an important role in ducted burners, and the experimentalists noticed three instabilities during their tests. A screech mode (1400 Hz) was found at  $\phi=0.72$ , a longitudinal mode (100 Hz) was found at  $\phi = 0.95$ , and a combination of the two modes was found at the same conditions as the screech mode. The low frequency mode can cause numerical difficulties, since it is of the same frequency range as the vortex shedding, and can have significant amplitudes. Sjunnesson found that the low frequency mode created large changes in the structure of the wake near the flameholder. At one point in the periodic cycle, the wake bulged out and became much thicker than the base height of the flameholder.

## 8.2 Numerical Details

The CFD code tested with the triangular flameholder was the same code used for the isothermal tests: CFD-ACE. CFD-ACE has several combustion models, including simple instantaneous chemistry, equilibrium chemistry, and finite-rate chemistry using one, two, or four step models. The finite-rate methods can be made to react to equilibrium conditions using an efficient table look-up routine. Several advanced methods are also available in CFD-ACE, such as the prescribed PDF and Monte Carlo PDF models.

The numerical tests were completed using the single step propane model with the reaction rate constants taken from Westbrook and Dryer<sup>38</sup>:

$$A T^n e^{(-E_a/RT)} [C_3H_8]^a [O_2]^b$$

$$A = 8.6 \times 10^{11}$$

$$a = 0.1$$

$$n = 0$$

$$b = 1.65$$

$$E_a = 30.0$$

The simulations were performed at the following freestream conditions:

$$U_\infty = 17.3 \text{ m/sec}$$

$$P_\infty = 100 \text{ kPa}$$

$$T_\infty = 288 \text{ K}$$

$$\phi = 0.61$$

The grid is shown in Figure 83. Two different grids were used, with the difference coming in the location of the inlet plane. The first grid started at 200 mm upstream,



and used the first plane of experimental data for the inflow conditions. However, due to interactions with the tunnel acoustics, it was felt that the entire tunnel length had to be modeled, and the grid was started at 819 mm upstream of the flameholder, with a uniform inlet condition. No-slip walls were maintained on both walls of the tunnel and on the walls of the flameholder. The downstream grid exited into a dump diffuser with an equivalent 2-D area as the experimental axisymmetric dump chamber. The exit plane of the dump chamber was held at a constant pressure condition.

The numerical tests were completed using the same methodology as used for the isothermal unsteady analyses. Therefore, any vortex shedding, or lack of vortex shedding, along with other instabilities, would be accounted for in the solution.

### 8.3 Numerical Results

The case selected for study was at  $\phi = 0.61$ , corresponding to case 1 from Sjunnesson et al.<sup>37</sup> The objective of the calculation was to compare numerical results with experimental measurements. The experimental study did not show any combustion instabilities at this equivalence ratio. High speed photographs indicated the heat release occurred in the simultaneous roll-up of the two shear layers behind the flameholder. The high strain rate reduced the heat release immediately behind the flameholder. Temperature measurements on the combustor centerline showed unburned fluid was entrained behind the recirculation zone.

The numerical results showed strong pressure oscillations, which were not expected at this equivalence ratio. These pressure oscillations appeared to be an axial "organ-pipe" mode with a frequency of approximately 200 Hz. This mode is similar to the combustion instability observed experimentally at a higher equivalence ratio. The pressure history at a point on the combustor centerline, behind the flameholder, is shown in Figure 84. The pressure throughout the combustor oscillated in phase, with the maximum amplitude at the inlet.

The flame shape in the region immediately behind the flameholder is shown at a sequence of different times in Figure 85. The difference in time between plots is 0.4 ms. The pressure at the base of the flameholder is at a maximum at time  $t_1$ . Shortly after the pressure reaches the peak, a pair of counter-rotating vortices are shed simultaneously from the corners of the flameholder and the flame front bulges out. The pressure peaks again at  $t_5$ , triggering the shedding of another vortex pair. As the vortices are convected downstream, cold fluid is entrained into the wake region. The flow becomes asymmetrical further downstream, as the vortices interact. This flow did not reach a regular periodic state.

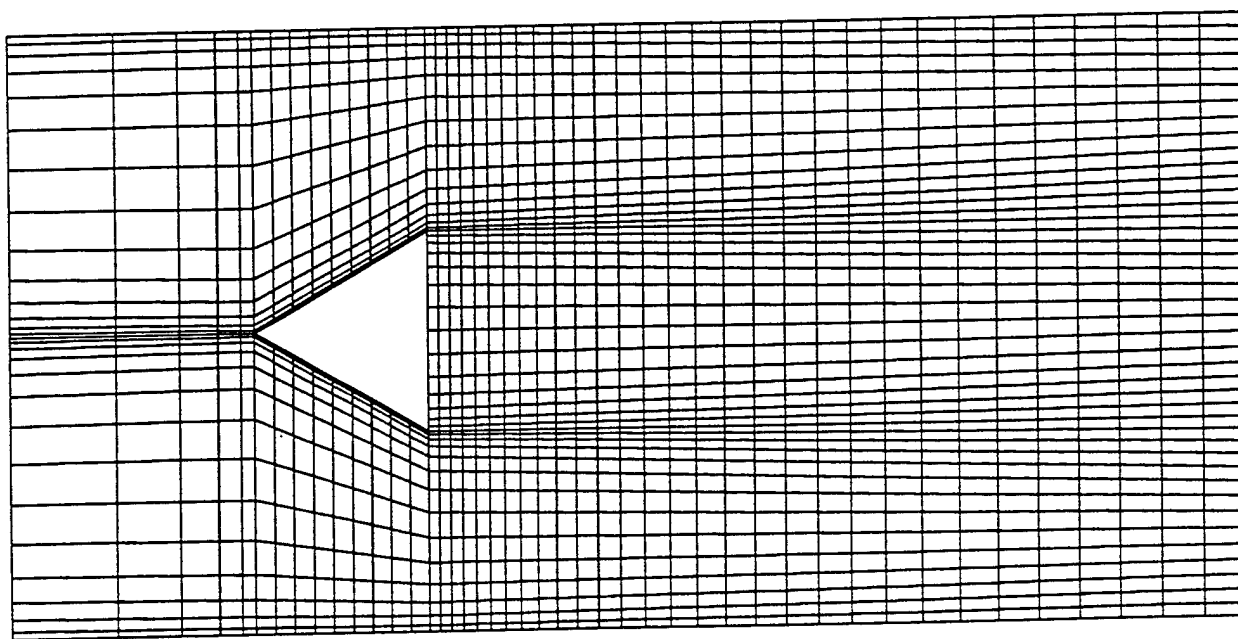
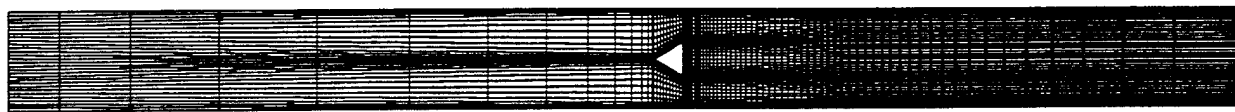


Figure 83. Grid for Reacting-Flow Case Modeling Sjunnesson Experiment

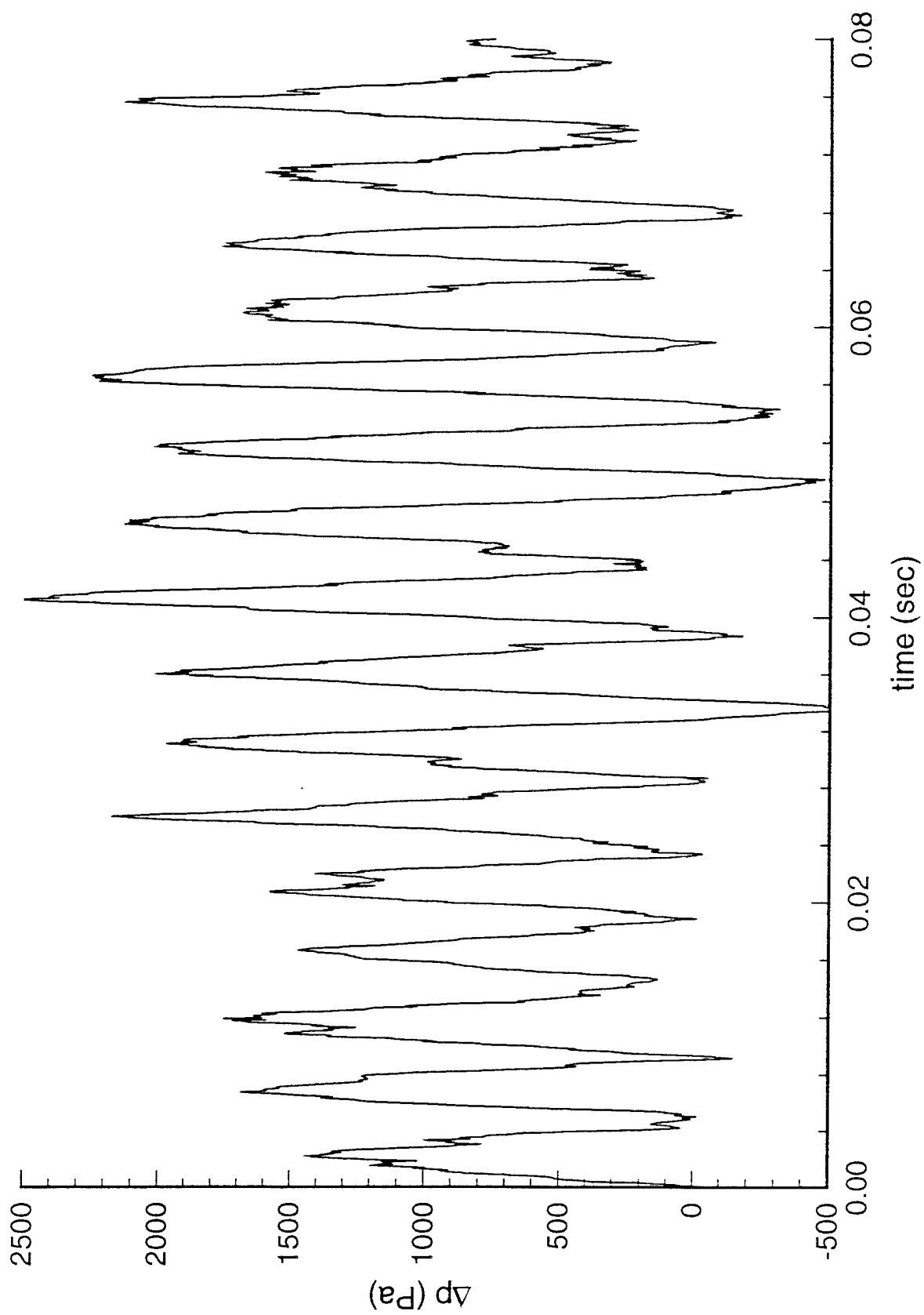


Figure 84. Pressure History at Centerline,  $x/H = 1$ , Demonstrates Acoustic Pressure Waves in Tunnel

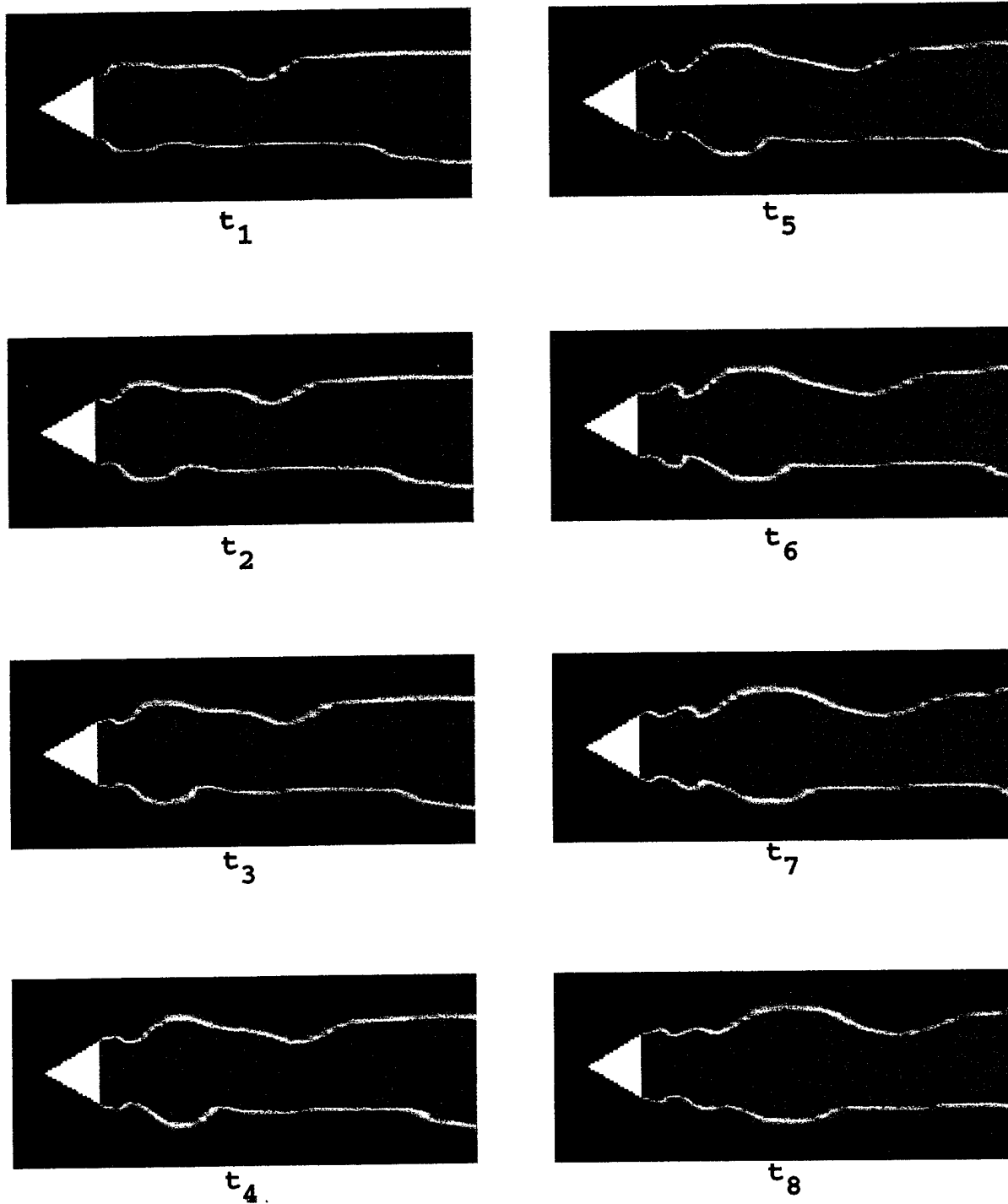


Figure 85. Sequence of Flame Shapes for Triangular Flameholder with  $\phi = 0.61$ ; Color Denotes Temperature (Blue = 288 K, Red = 1710 K)

### Effects of Initial and Boundary Conditions

The pressure oscillations that dominated the flow were created by the initial conditions used for the transient combustion simulation, and then sustained by interactions with the heat release from combustion during the simulation. The initial conditions for the flow were uniform and the same as the upstream boundary, except for the region behind the flameholder. A high temperature was specified behind the flameholder to start the finite-rate reaction. This is the same methodology used for the nonreacting calculations, except for the elevated temperature. These conditions are artificial and do not satisfy conservation of mass, momentum, or energy. After a transition period, the initial conditions are not expected to be important. The flow rate at the inlet and the pressure at the exit are fixed, so that unsteady flow patterns should be caused only by instabilities in the flow.

Integration of the continuity equation shows the local rate of change of density is proportional to the mass imbalance for each control volume. The continuity equation is used to derive a pressure correction equation for the numerical method used in this study. The mass imbalance for each cell is part of the source term for the pressure correction equation. The mass imbalances caused by the initial flow field not satisfying continuity create large initial changes in pressure. These changes were expected to decay to a much lower level.

The boundary conditions for this simulation reflect some of the pressure wave that is generated by the initial conditions. The pressure at the exit boundary was fixed, while the pressure at the inlet boundary had a zero gradient. As a result, a standing quarter-wave was set up in the combustor. Changes in pressure led, in turn, to changes in enthalpy, which affected the local reaction rate and changed the flame shape. The flame shape was also altered by changes in the local flow patterns caused by pressure oscillations. Unsteady heat release causes combustion instability when the fluctuating pressure is in phase with the fluctuating pressure field. The unsteady heat release appeared to resonate with the pressure field in this simulation and sustain the pressure oscillations.

One method used to reduce the transition period at the beginning of the transient simulation and the disturbance in the pressure field was to first perform a steady-state calculation. The steady state results would be used as the initial conditions for the transient case. This procedure was used in this study. The residuals for each variable could only be reduced two to three orders of magnitude before the solution began to oscillate. The solution was not symmetric and had the appearance of the alternate vortex shedding seen in the nonreacting simulations. The partially-converged steady-state solution was then used as the initial value for the transient calculation. Errors in mass conservation were reduced, but not eliminated, by the steady-state calculation. The mass conservation errors were still large enough to

create large pressure oscillations. There was no substantial difference in the flow patterns in simulations started from steady state results or from the initial conditions discussed above.

### Flat Plate Flameholder

The flow for this case was expected to show vortex shedding patterns similar to the nonreacting cases, although the volumetric expansion caused by heat release from the reaction reduces the vorticity of the fluid and is expected to stabilize the shear layers. An earlier study of unsteady combustion<sup>39</sup> showed the transition process as the equivalence ratio was reduced for a flame stabilized by a flat plate. The operating conditions for the earlier study used a higher inlet temperature (800K) and lower pressure (30 kPa), but the same fuel and reaction mechanism. The flow field was steady as the equivalence ratio was reduced from 1.0 to 0.8. As the equivalence ratio was further reduced to 0.4, low-amplitude, high-frequency oscillations were observed in the pressure field but the flow field remained steady. As the equivalence ratio was reduced even further, vortices were shed from the top and bottom of the flameholder in an alternating fashion. Low-frequency pressure oscillations were observed upon each change in the inlet fuel/air ratio. These oscillations died out after several cycles. A regular, periodic flow was observed for the lower equivalence ratios.

There was some concern that the difference in flow patterns observed in this study and the earlier study with the flat plate were due to changes in the solution algorithms during the development of the computer code. Significant changes had been made to the code, including the addition of multiblock capability and major changes to the solution of the energy equation. In an effort to determine if code changes were responsible for the unexpected flow patterns, one of the flow conditions that produced vortex shedding in the earlier study was reproduced. The previous results were successfully reproduced with the computer code used in this study, indicating the differences in the observed flow patterns were due to physical differences in the flows.

One significant difference between this and the earlier study, besides the operating conditions, was that the earlier study used a constant turbulent viscosity, instead of the two-equation model used here. In order to determine that the different flow pattern was caused by physics, and not modeling, a calculation was made with a flat plate flameholder, constant turbulent viscosity, and the operating conditions for the triangular flameholder. The plate height was the same as the flameholder base and the tunnel dimensions were the same as used for the triangular flameholder.

Results with the flat plate were consistent with the triangular flameholder case. The flow was nearly symmetrical and dominated by axial pressure oscillations. Instantaneous velocity vectors and temperature contours are shown for the region immediately behind the flameholder in Figure 86. The pair of vortices are periodically shed and convected downstream. Unburnt gas is entrained by the vortex shedding and intermittently reaches the centerline. Pressure and temperature histories on the centerline are shown in Figure 87. The temperature drop when unreacted fluid reaches the centerline is strongly correlated with peaks in the pressure field, although the cold fluid does not reach the centerline on every cycle. The similarity between the results with both flameholder shape shows the flow patterns are not an artifact of the turbulence modeling or multiblock solution.

Because the experimental instabilities were only observed for higher equivalence ratios, the calculation was repeated with the equivalence ratio reduced to 0.55. Instantaneous velocity vectors and temperature contours are shown in Figure 88 for the same region shown above. The vortices are now shed alternately from the top and bottom of the flameholder. Pressure oscillations are an order of magnitude smaller than with  $\phi = 0.61$ . The reduced amount of heat released at this equivalence ratio is not sufficient to sustain the pressure oscillations, and the flow is controlled by the instability of the shear layers behind the flameholder.

#### Reduced Equivalence Ratio

Because the flat plate results showed reduced pressure oscillations at a lower equivalence ratio, the triangular flameholder calculation was repeated with an equivalence ratio of 0.55. All conditions except the equivalence ratio were unchanged. This calculation did not show the alternate vortex shedding observed for the flat plate flameholder with the same conditions. Figure 89 shows velocity vectors and temperature contours in the vicinity of the flameholder. The flow pattern is symmetric. There is a small oscillation of the wake region, but no evidence of large-scale vortex shedding.

The simulation was started with the RNG  $k$ - $\epsilon$  turbulence model. The final 5000 time steps were made with a constant effective viscosity, to check the sensitivity of the solution to the turbulence modeling. The history of pressure behind the flameholder is shown in Figure 90, with time  $t = 0.0$  corresponding to the change in turbulence model. The amplitude of the pressure oscillations decays, indicating the reduced heat release does not sustain the axial instability mode. The amount of heat release appears to be enough to prevent the alternating vortex shedding. The difference in flow patterns between the flat plate and triangular flameholders must be attributed to the change in the shape of the flameholder.

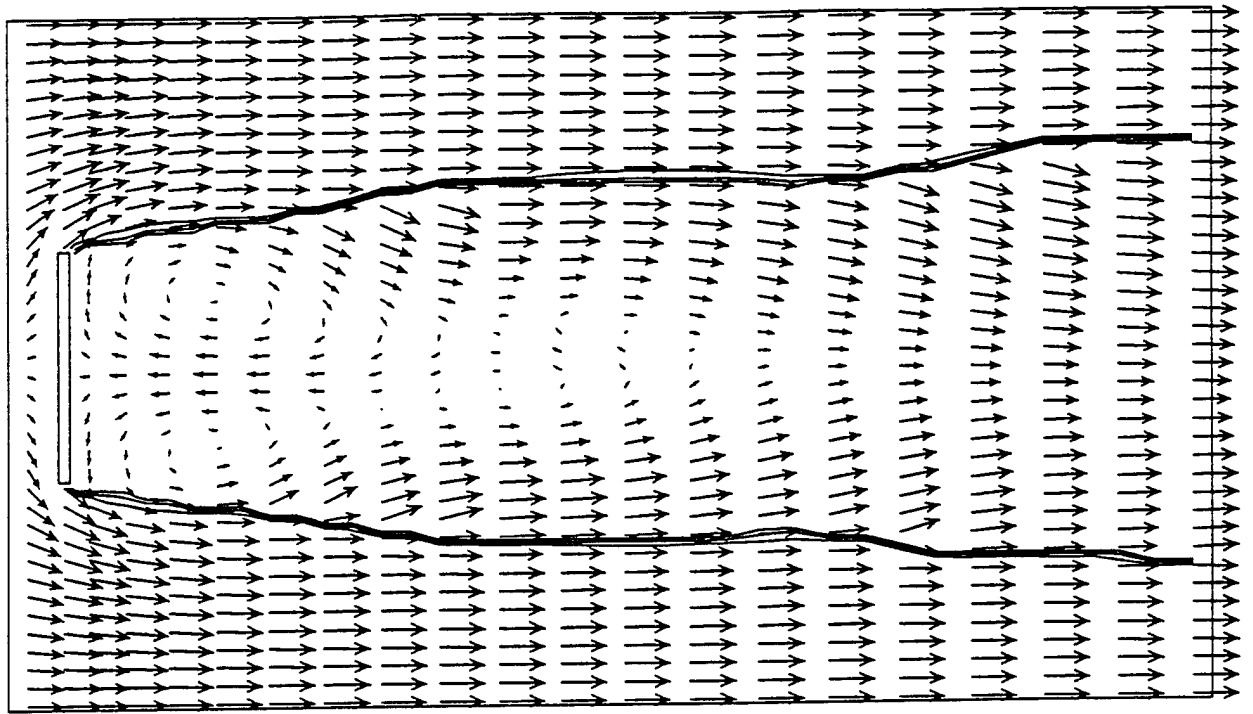


Figure 86. Instantaneous Velocity Vectors and Temperature Contours for the Flat Plate Flameholder with  $\phi = 0.61$

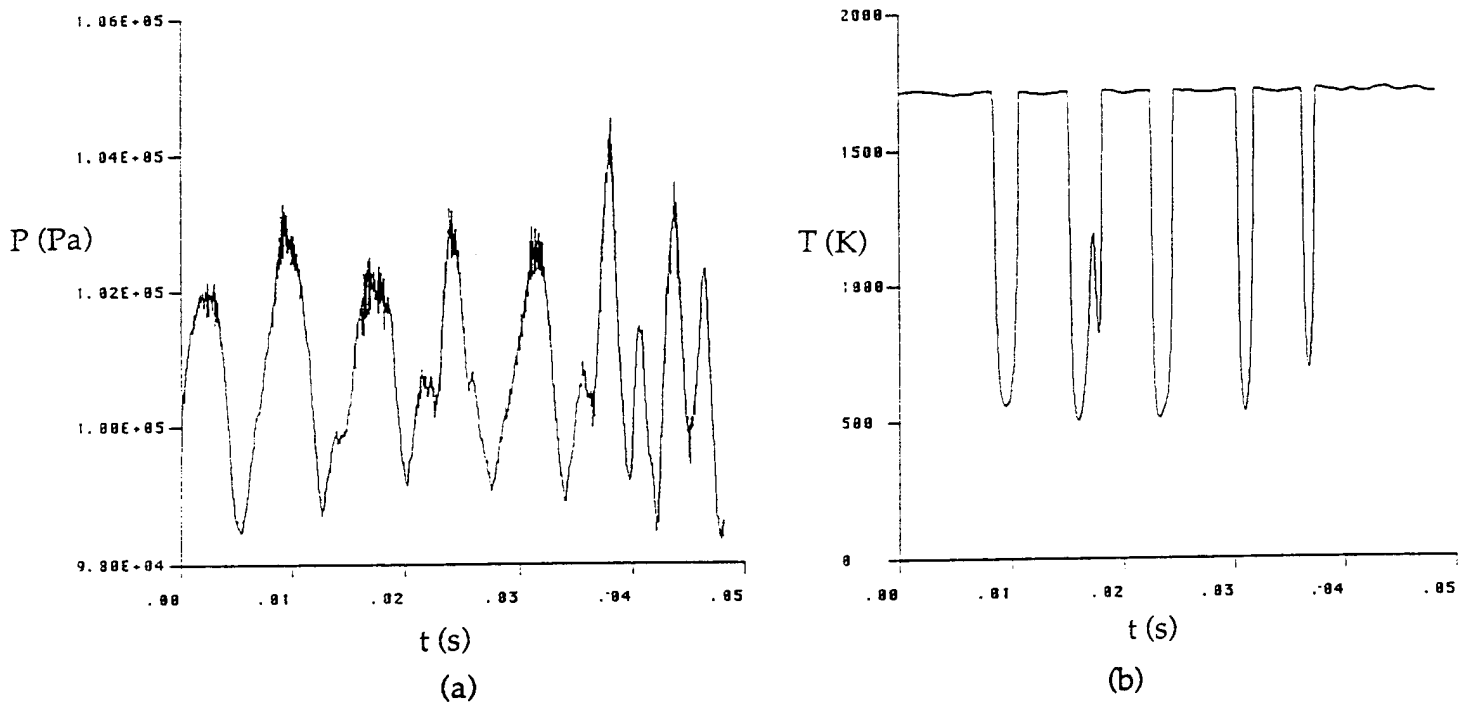


Figure 87. Time Histories of Pressure and Temperature Behind the Flat Plate Flameholder ( $\phi = 0.61$ )



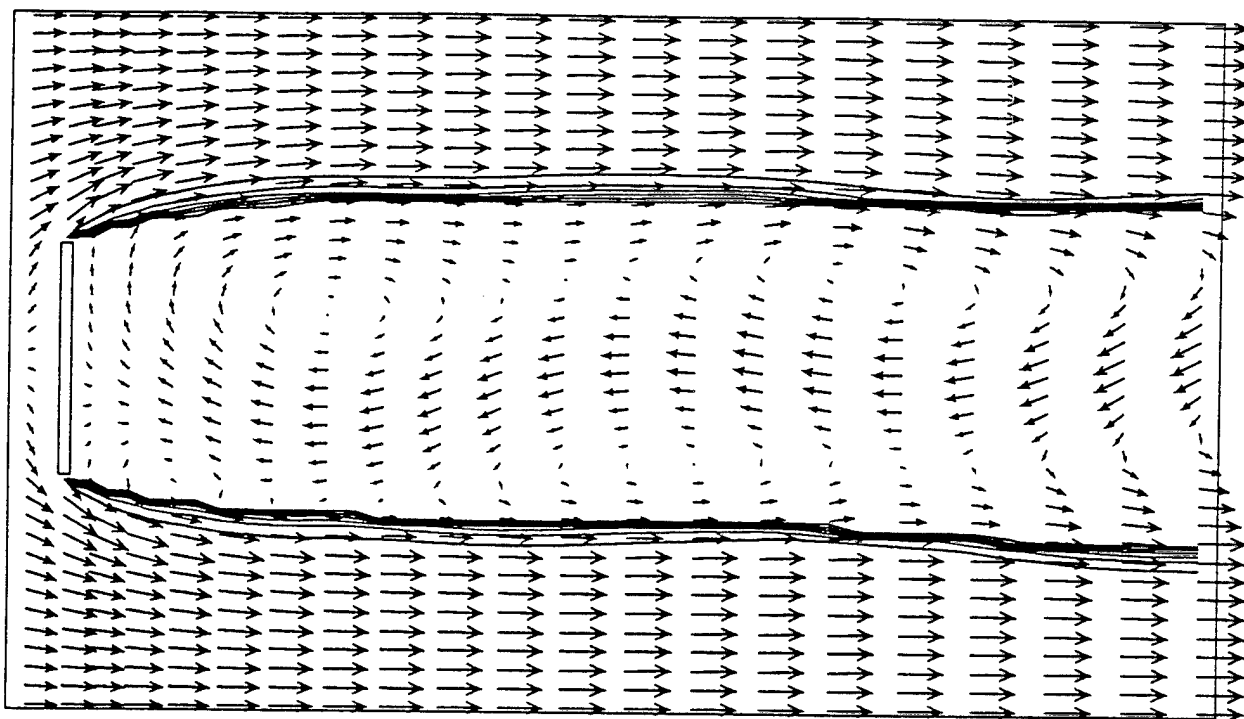


Figure 88. Instantaneous Velocity Vectors and Temperature Contours for Flat Plate Flameholder with  $\phi = 0.55$

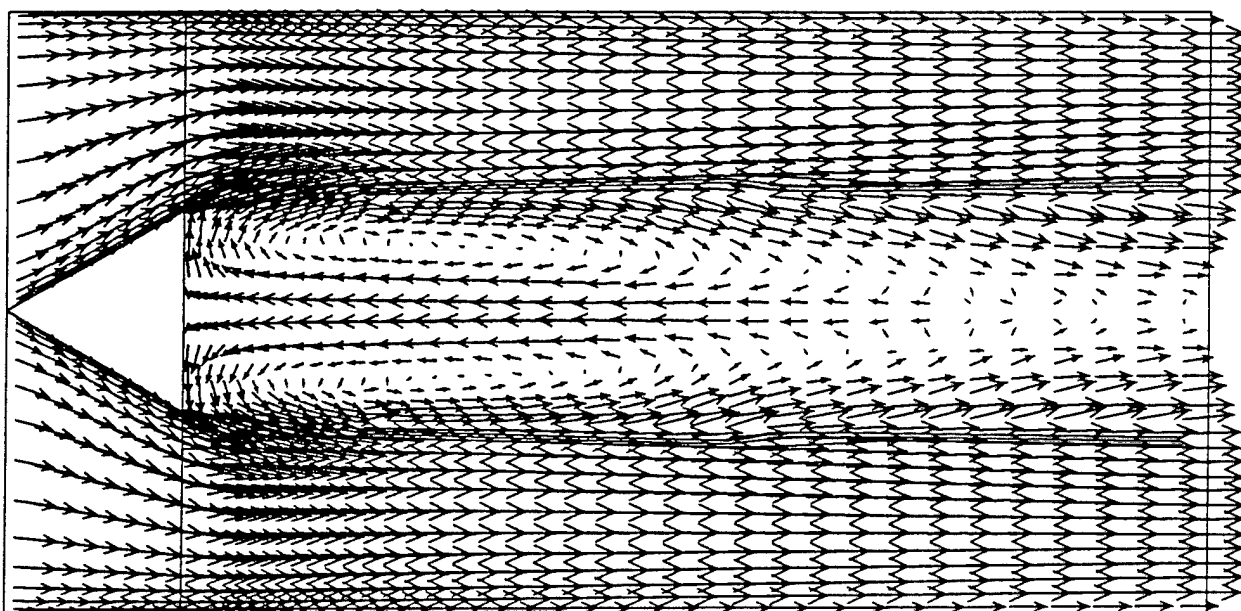


Figure 89. Instantaneous Velocity Vectors and Temperature Contours for Triangular Flameholder with  $\phi = 0.55$

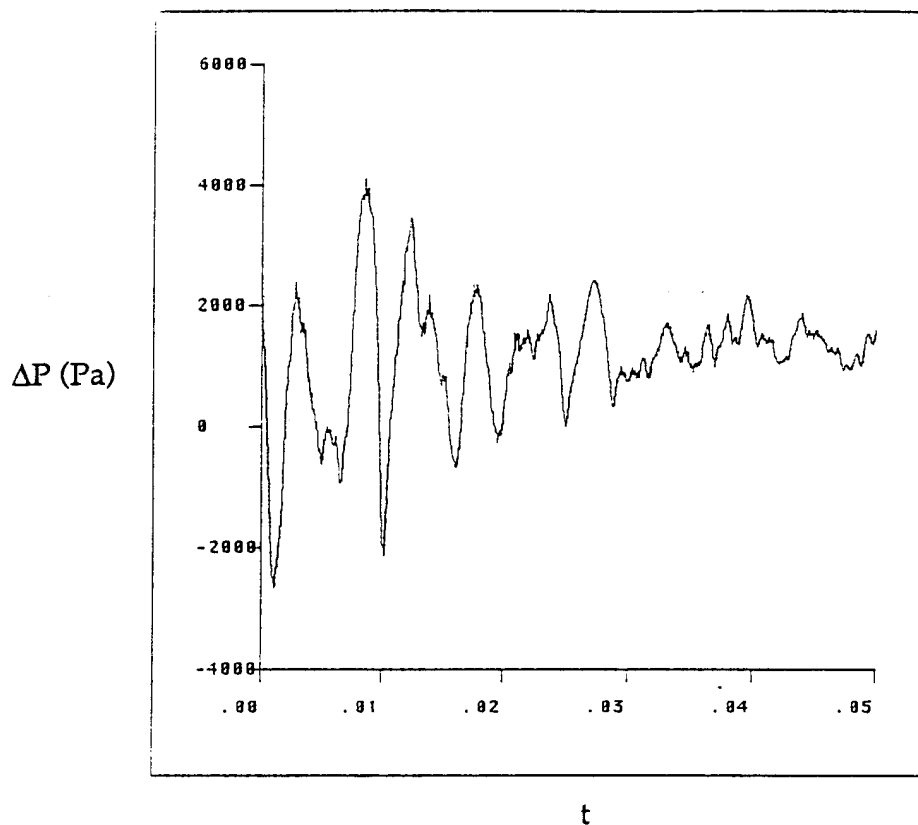


Figure 90. Pressure History Behind Triangular Flameholder with  $\phi = 0.55$

### Summary

No comparison has been made to experimental results because the flow regime does not appear to be the same at the equivalence ratio considered. The occurrence of an axial combustion instability mode at a lower equivalence ratio than was seen experimentally could be due to several factors. First, the boundary conditions in the simulation may be artificially reflecting pressure waves back into the computational domain. Care was taken to locate the boundaries at the combustor inlet and exit planes, but information is transferred into the computational domain at the exit by a characteristic wave moving upstream.

A second factor in the prediction of combustion instability is the combustion model. A single-step model was used in this study. While this model was successful in earlier studies and with simpler geometry, the immediate conversion of fuel into products could alter the way heat release from the reaction interacts with the fluctuating pressure field. A more realistic model would have multiple steps and the heat would not be released all at once.

A third factor is the interaction between turbulence and combustion. The combustion model used in this study is "quasi-laminar", in that the production rate is calculated from the mean species concentrations. The experimental results showed the heat release was controlled by mixing in the shear layers. In the

numerical study, the reaction rate was fast enough for the fuel to completely react at the base of the flameholder.

More work needs to be done on the transient combustion simulations to distinguish between numerical and physical instabilities. The initial and boundary conditions must be as physically correct as possible. The combustion simulations should be performed with more realistic chemistry models that account for the effect of turbulence on combustion.

## 9.0 CONCLUSIONS

Numerical analyses using 2-D and 3-D steady-state and time accurate methods, under reacting and nonreacting conditions, were performed on the baseline IFF geometry and 28 advanced designs. Many of the advanced designs showed improved mixing and combustion efficiency, but they also significantly increased the cold flow pressure loss of the flameholder. The best advanced model was ADV5, which used the axially injected fuel stream to reduce the pressure loss while maintaining discrete flame kernels at the center of each vortex. Possible design improvements consist of lengthening the tail to reduce the turning angles of the ramp, and reducing the maximum vertical extent of the flameholder. Such modifications will reduce the effectiveness of the vortex, but should make a larger reduction to the pressure loss.

Detailed combustion analyses of the triangular flameholder were performed at equivalence ratios of 0.61 and 0.55. Coupling between acoustics and combustion caused the flow to be dominated by axial pressure waves. The flow patterns were irregular and characterized by the simultaneous shedding of vortices from the top and bottom of the base of the flameholder. Simulations of a simpler flat plate flameholder at the same equivalence ratios showed the acoustic-combustion interactions were reduced at the lower equivalence ratio, but the influence of flameholder geometry was not investigated further.

The isothermal experimental tests were completed for the baseline IFF with no injection. Regular alternating vortices were shed from the trailing edge with a Strouhal number of 0.243, yielding a mean recirculation bubble with a length of 0.9 H. The turbulence in the wake was not isotropic, with the  $uv$  and  $vv$  components of the Reynolds stresses making the largest contribution. Comparisons with the numerical data showed that the use of a steady-state symmetric solution will generate a solution similar to a backward facing step flow, with much lower Reynolds stresses than the bluff body flow. The use of 3-D time-accurate schemes were necessary to properly capture the vortex shedding of the flowfield. Such algorithms are not practical for use as design tools at the present time.

A water-cooled combustion test section was designed and fabricated. No tests were completed due to the lack of availability of test facilities at Wright Laboratory.

## 10.0 REFERENCES

1. Wotel, G. J., and Maurice, L. Q., "High Speed Turboramjet Ramburner Technology Development," 1989 JANNAF Propulsion Meeting, Cleveland, OH, May, 1989.
2. Hautman, D. J., and Rosfjord, T. J., "High Speed Turboramjet Cold Flow and Combustion Measurements," 1989 JANNAF Propulsion Meeting, Cleveland, OH, May, 1989.
3. Hautman, D. J., and Rosfjord, T. J., "Inlet Flow Documentation and Combustion Measurements in a Ramjet Test Combustor," 26th JANNAF Combustion Meeting, Pasadena, CA, October, 1989.
4. Hautman, D. J., and Rosfjord, T. J., "Transverse Liquid Injection Studies," 26th Joint Propulsion Conference, AIAA 90-1965, July 16-18, 1990.
5. Hautman, D. J., and Rosfjord, T. J., "Transverse Gaseous Injection into Subsonic Air Streams," AIAA 29th Aerospace Sciences Meeting, January 7-10, 1991.
6. Anderson, T. J. and Eckbreth, A. C., "CARS Temperature/Multi Species Measurements for High Speed Airbreathing and Rocket Propulsion Testing," 23rd Combustion Symposium, Orleans, France, July 23-27, 1990.
7. Caron, S. D., and Gallagher, K. E., "High Speed Turboramjet Ramburner Component Test Program," 1989 JANNAF Propulsion Meeting, Cleveland, OH, May, 1989.
8. Caron, S. D., and Gallagher, K. E., "High Speed Turboramjet Ramburner Component Test Results," 1990 JANNAF Propulsion Meeting, 1990.
9. Hautman, D. J., Pfau, D. J., and Anderson, T. J., "Combustion Tests in a Ramjet Test Combustor," 27th JANNAF Combustion Meeting, Cheyenne, WY, November, 1990.
10. Hanna, M., Bardon, M., and Rao, V., "Flame Stabilization Behind Bluff Bodies," AIAA 89-2801, July 1989.
11. Williams, G. C., Woo, P. T., and Shipman, C. W., "Boundary Layer Effects on Stability Characteristics of Bluff Body Flameholders," 6th Symposium (International) on Combustion, The Combustion Institute, Pittsburgh, PA, 1965, pp. 427-438.
12. Nicholson, H. M., and Field, J. P., "Some Experimental Techniques for the Investigation of the Mechanism of Flame Stabilization in the Wakes of Bluff-Bodies," 3rd Symposium on Combustion, Flame, and Explosion Phenomena, Williams and Wilkins, Baltimore, MD, 1949, pp. 44-68.
13. Mansingh, V., and Oosthuizen, P., "Effects of Splitter Plates on the Wake behind a Bluff Body," AIAA Journal, May, 1990, pp. 778-783.
14. Fail, R., "An Experimental Investigation of Flow Past Flat Plates of Various Shapes Normal to the Wind Stream," 9th International Congress of Applied Mechanics, Paper 1-76, June, 1956.

15. Stwalley, R. M., and Lefebvre, A. H., "Flame Stabilization Using Large Flameholders of Irregular Shape," *Journal of Propulsion*, vol 4, no. 1, Jan-Feb, 1988.
16. Rizk, N. K., and Lefebvre, A. H., "On the Relationship Between Flame Stability and Drag of Bluff-Body Flameholders," 7th International Symposium on Air Breathing Engines, Beijing, China, September, 1985.
17. McCormick, D. C., and Bennet, J.C., "Vortical and Turbulent Structure of a Lobed Mixer Free-Shear Layer," AIAA 93-0219, 31st Aerospace Sciences Meeting, Reno, NV, Jan, 1993.
18. Abolfadl, M. A., and Sehra, A. K., "Experimental Investigation of Exhaust System Mixers for a High Bypass Turbofan Engine," AIAA 93-0022, 31st Aerospace Sciences Meeting, Reno, NV, Jan, 1993.
19. Peschke, W. T., and McVey, J. B., "Study of Streamwise Vorticity-Stirred Combustion," UTRC Report R93-958160-1, December, 1993.
20. Malecki, R., and Lord, W., "Navier-Stokes Analysis of a Lobed Mixer and Nozzle," AIAA 93-0453, 28th Aerospace Sciences Meeting, Reno, NV, Jan, 1990.
21. Elliot, J. K., Manning, T. A., Qiu, Y. J., Greitzer, E. M., and Tan, C. S., "Computational and Experimental Studies of Flow in Multi-Lobed Forced Mixers," AIAA 92-3568, 28th Aerospace Sciences Meeting, Reno, NV, Jan, 1990.
22. Craig, R. R., Nejad, A. S., Hahn, E. Y., and Schwartzkopf, K. G., "Approach for Obtaining Unbiased Laser Doppler Velocimetry Data in Highly Turbulent Flows," *J. Propulsion and Power*, vol. 2, no. 6, pp. 541-545, Nov-Dec, 1986.
23. Rabe, D., and Sabroske, K., "Laskin Nozzle Performance for Laser Flow Measurement Seeding," AIAA 94-0044, 32nd Aerospace Sciences Meeting, Reno, NV, 1994.
24. Avva, R., "CFD-ACE Theory Manual," CFDRC Report, GR-93-1.
25. Smith, C. E., Ratcliff, M. L., Przekwas, A. J., and Habchi, S. D., "Validation of an Advanced Turbulent Combustion Code: REFLEQS," 7th SSME CFD Workshop, NASA MSFC, 1989.
26. Avva, R. K., Smith, C. E., and Singhal, A. K., "Comparative Study of High and Low Reynolds Number Versions of k-e Models," AIAA-90-0246, 28th Aerospace Sciences Meeting, Reno, NV, Jan, 1990.
27. Wilcox, D. C., "Turbulence Modeling for CFD," DCW Industries, Inc., La Canada, CA, 91011, Chpt 2.
28. Yakhor, V., Orszag, S., Thangan, S., Gatski, T., and Speziale, C., "Development of Turbulence Models for Shear Flows by a Double Expansion Techniques," *Phys Fluids*, A.4 (7), 1992.
29. Speziale, C., and Thangam, S., "Analysis of an RNG Based Turbulence Model for Separated Flows," NASA CR 189600.
30. Franke, R., and Rodi, W., "Calculation of Vortex Shedding Past a Square Cylinder with Various Turbulence Models," *Turbulent Shear Flows* 8, Springer-Verlag, 1991.

31. Przulj, V., and Younis, B., "Some Aspects of the Prediction of Turbulent Vortex Shedding," Fluids Engineering Division, Vol. 149, Separated Flows, ASME, 1993.
32. Martensson, H., Eriksson, L. and Albraten, P., "Numerical Simulations of Unsteady Wakeflow," 10th International Symposium on Air-Breathing Engines (ISABE), Vol. 2, Nottingham, England.
33. Arnal, M., and Friedrich, R., "Large-Eddy Simulation of a Turbulent Flow with Separation," Turbulent Shear Flows 8, Springer-Verlag, 1991.
34. Perry, A., and Steiner, T., "Large-Scale Vortex Structures in Turbulent Wakes Behind Bluff Bodies: Part I. Vortex Formation Processes," J. Fluid Mech., vol 174, pp. 233-270.
35. Freund, J. and Mungal, M., "Drag Modification and Wake Control of an Axisymmetric Bluff Body Using the Coanda Effect," AIAA 92-2705-CP, 1992.
36. Chen, T. H., and Nejad, A. S., "Design of Round-to-Square Transition Section; Analysis and Computer Code," WL-TR-93-2054, Jan, 1993.
37. Sjunnesson, A., and Henrikson, P., "CARS Measurements and Visualization of Reacting Flows in a Bluff Body Stabilized Flame," AIAA 92-3650, 28th Joint Propulsion Conference, Nashville, TN, 1992.
38. Westbrook, C. K., and Dryer, F. L., "Simplified Reaction Mechanisms for the Oxidation of Hydrocarbon Fuels in Flames," *Combustion Science and Technology*, Vol. 27, pp. 31-43, 1981.
39. Leonard, A. D., Smith, C. E., and Van Erp, C., "Large Eddy Simulation of Blowout of a Bluff-Body Stabilized Flame in a Duct," AIAA 91-1862, 1991.
40. Gibson, M. M. and Launder, B. E., "Ground Effects on Pressure Fluctuations in the Atmospheric Boundary Layer," J. Fluid Mech., Vol. 86, pp. 491-511, 1978.
41. Obi, S., Peric, M., and Scheuerer, G., "Second-Moment Calculation Procedure for Turbulent Flows with Colocated Variable Arrangement," AIAA Journal, Vol. 29, pp. 585-590, 1991.
42. Naot, D., Shavit, A., and Wolfshtein, M., "Numerical Calculation of Reynolds Stresses in a Squire Duct with Secondary Flow," *Warme und Stoffubertragung*, Vol. 7, pp. 151-161, 1974.
43. Eaton, J. K., and Johnston, J. P., "Turbulent Flow Reattachment: An Experimental Study of the Flow and Structure Behind a Backward-Facing Step," Themosci Div. Rept MD-39, Stanford Univ., Stanford, CA, 1980.
44. Stevens, S. J. and Fry, P., "Measurements of the Boundary-Layer Growth in Annular Diffusers," J. Aircraft, Vol. 10, pp. 73-80, 1973.
45. Nejad, A. S., Favaloro, S. C., Vanka, S. P., Samimy, M. and Langenfeld, C., "Application of Laser Velocimetry for Characteristics of Confined Swirling Flows," J. Engr. for Gas Turbines and Power, Vol. 111, pp. 36-45, 1989.
46. Hogg, S. and Leschziner, M. A., "Computation of Highly Swirling Confined Flow with a Reynolds Stress Turbulence Model," AIAA Journal, Vol. 27, pp. 57-63, 1989.

47. Favaloro, S., Nejad, A., Ahmed, S., Miller, T., and Vanka, S., "An Experimental and Computational Investigation of Isothermal Swirling Flow in an Axisymmetric Dump Combustor," AIAA Paper 89-0620, 1989.
48. Jones, W. P. and Pascau, A., "Calculation of Confined Swirling Flows with a Second Moment Closure," *Journal of Fluids Engineering*, Vol. 111, pp. 248-255, 1989.
49. Shih, T-H., Shabbir, A., and Lumley, J. L., "Advances in Modeling the Pressure Correlation Terms in the Second Moment Equations," NASA TM-104413, 1991.
50. Speziale, C. G., Sarkar, S., and Gatski, T. B., "Modeling the Pressure-Strain Correlation of Turbulence: An Invariant Dynamical Systems Approach," *J. Fluid Mech.*, Vol. 227, pp. 245-272, 1991.
51. Durst, F., and Rastogi, A. K., "Theoretical and Experimental Investigations of Turbulent Flows with Separation," *Turbulent Shear Flows I*, Springer-Verlag, pp. 208-219, 1977.



**APPENDIX A.**

**A NUMERICAL METHOD FOR THE SECOND-MOMENT  
TURBULENCE CLOSURE WITH APPLICATIONS**

## A.1 INTRODUCTION

In the last two decades, a large number of turbulent flow cases have been compiled demonstrating that the widely used isotropic eddy-viscosity closures is inaccurate. Most of these flow can be classified as "complex" since extra significant rate-of-strain components are present due to rotation, streamline curvature, separation, three-dimensionality, *etc.* As a result, we have witnessed the development of many "improved" eddy-viscosity models to take a particular extra strain rate into account by modifying the model constants or adding extra terms. Unfortunately, this approach often finds limited use due to the lack of generality and its ad hoc nature. A potentially more rewarding approach is to go beyond the eddy-viscosity assumption and to develop higher moment turbulence closures. The second-moment closure is the lowest level of closures which has the potential to retain many important physical mechanisms and thereby is likely to account for different extra-strain rates automatically. It is precisely this reason that the second-moment closure has been the subject of extensive studies in the last two decades. The validation and further refinement of newly developed second-moment turbulence closures that heavily rely on the use of an accurate and robust computational approach. However, the incorporation of the second-moment closure into the existing eddy-viscosity turbulence model based numerical approach is not a trivial task. One of the prominent issues is the treatment of the Reynolds stress terms in the momentum equations. This treatment has a lot to do with the stability and efficiency of the computational procedure.

The major objective of the present study is to address several numerical issues related to the incorporation of the second-moment turbulence closure into a colocated grid approach on non-orthogonal grids. To demonstrate the robustness of the numerical method, the Gibson-Launder model<sup>40</sup> is incorporated and used to calculate three turbulent flows: backward facing step flow; faired diffuser flow; and confined swirling flow.

## A.2 GOVERNING EQUATIONS

This study deals with stationary and incompressible turbulent flows. The Reynolds-averaged mass and momentum conservation equations can be concisely written in Cartesian tensor form as:

$$\frac{\partial(\rho U_j)}{\partial x_j} = 0 \quad (1)$$

$$\frac{\partial(\rho U_i U_j)}{\partial x_j} = -\frac{\partial P}{\partial x_i} + \frac{\partial}{\partial x_j} \left( \mu \frac{\partial U_i}{\partial x_j} - \rho \overline{u_i u_j} \right) \quad (2)$$

where  $U_j$  and  $u_j$  are the  $j$ th components of the mean and fluctuating velocity,  $P$  is the mean pressure,  $\rho$  and  $\mu$  are the fluid density and viscosity. With a second-moment closure, the transport equations for the Reynolds stresses are solved and can be written as:

$$\begin{aligned} \frac{\partial \rho U_k \overline{u_i u_j}}{\partial x_k} = & \frac{\partial}{\partial x_k} \left( \mu \frac{\partial \overline{u_i u_j}}{\partial x_k} \right) - \frac{\partial}{\partial x_k} (\rho \overline{u_i u_j u_k} + \overline{p u_i} \delta_{jk} + \overline{p u_j} \delta_{ik}) \\ & - \left( \rho \overline{u_i u_k} \frac{\partial U_j}{\partial x_k} + \rho \overline{u_j u_k} \frac{\partial U_i}{\partial x_k} \right) + p \left( \frac{\partial u_i}{\partial x_j} + \frac{\partial u_j}{\partial x_i} \right) - 2\mu \frac{\partial u_i}{\partial x_k} \frac{\partial u_j}{\partial x_k} \end{aligned} \quad (3)$$

or symbolically as:

$$C_{ij} = D_{ij}^H + D_{ij}^T + P_{ij} + \Phi_{ij} - \epsilon_{ij} \quad (4)$$

where the terms on the right hand side (RHS) represent the viscous diffusion, turbulent diffusion, production, redistribution, and dissipation of  $\overline{u_i u_j}$ . Of the five terms on the RHS of Equation (3),  $D_{ij}^H$  and  $P_{ij}$  are exact and require no modeling. The remaining terms either involve higher-order correlation of  $u_i$ , correlations with the fluctuating pressure or correlations with the velocity gradient  $\partial u_i / \partial x_j$ . Therefore, models are needed for  $D_{ij}^T$ ,  $\Phi_{ij}$  and  $\epsilon_{ij}$  to form a closed set of governing equations.

In this study, the second-moment closure follows closely the model of Gibson-Launder.<sup>40</sup> This selection is based on the fact that the Gibson-Launder model is one of the most popular models and there exists a large number of validated cases available for comparison.

The models for  $D_{ij}^T$ ,  $\Phi_{ij}$  and  $\epsilon_{ij}$  are give as:

$$D_{ij}^T = \frac{\partial}{\partial x_k} \left[ C_s \rho \frac{k}{\varepsilon} \overline{u_k u_l} \frac{\partial \overline{u_i u_j}}{\partial x_l} \right] \quad (5)$$

$$\Phi_{ij} = \Phi_{ij,1} + \Phi_{ij,2} + \Phi_{ijw} \quad (6)$$

$$\Phi_{ij,1} = -C_1 \rho \frac{\varepsilon}{k} \left( \overline{u_i u_j} - \frac{2}{3} k \delta_{ij} \right) \quad (7)$$

$$\Phi_{ij,2} = -C_2 \left( P_{ij} - \frac{1}{3} P_{kk} \delta_{ij} \right) \quad (8)$$

$$\begin{aligned} \Phi_{ijw} = & C_{1w} \rho \frac{\varepsilon}{k} \left( \overline{u_k u_m} n_k n_m \delta_{ij} - \frac{3}{2} \overline{u_k u_i} n_k n_j - \frac{3}{2} \overline{u_k u_j} n_k n_i \right) f_w \\ & + C_{2w} \left( \Phi_{km,2} n_k n_m \delta_{ij} - \frac{3}{2} \Phi_{ik,2} n_k n_j - \frac{3}{2} \Phi_{jk,2} n_k n_i \right) f_w \end{aligned} \quad (9)$$

$$\varepsilon_{ij} = \frac{2}{3} \rho \varepsilon \delta_{ij} \quad (10)$$

where  $n_i$  is the  $i$ th component of the unit normal to a wall and

$$f_w = \frac{C_\mu^{3/4}}{\kappa} \frac{k^{1.5}}{\varepsilon y_w} \quad (11)$$

with  $y_w$  being the distance normal to a wall.

Finally, a transport equation for the turbulent dissipation rate,  $\varepsilon$  is needed for the closure and is modeled as:

$$\begin{aligned} \frac{\partial(\rho U_j \varepsilon)}{\partial x_j} = & \frac{\partial}{\partial x_j} \left( \mu \frac{\partial \varepsilon}{\partial x_j} \right) + \frac{\partial}{\partial x_j} \left( C_\varepsilon \rho \frac{k}{\varepsilon} \overline{u_j u_k} \frac{\partial \varepsilon}{\partial x_k} \right) \\ & + C_{\varepsilon 1} \frac{\varepsilon}{2k} P_{kk} - C_{\varepsilon 2} \rho \frac{\varepsilon^2}{k} \end{aligned} \quad (12)$$

The model constants are chosen according to Gibson-Lauder<sup>40</sup> as:

$$\{C_1, C_2, C_{1w}, C_{2w}, C_s, C_\varepsilon, C_{\varepsilon 1}, C_{\varepsilon 2}, C_\mu, \kappa\} = \{1.8, 0.6, 0.5, 0.3, 0.22, 0.18, 1.44, 1.92, 0.09, 0.41\}$$

### A.3 NUMERICAL METHOD

As mentioned in the introduction, the Reynolds stress force,  $\partial \overline{u_i u_j} / \partial x_j$ , appears explicitly in the momentum equations for the second-moment closure. A major portion of this force acts as a diffusive force. The numerical treatment of this force needs special attention.

In the past, most researchers adopted the apparent anisotropic eddy viscosity approach. The full Reynolds stress force is taken as a diffusive contribution by introducing an anisotropic eddy-viscosity  $\mu_{ij}$  as:

$$\mu_{ij} = \frac{\frac{2}{3} \rho k \delta_{ij} - \rho \overline{u_i u_j}}{\frac{\partial U_i}{\partial x_j} + \frac{\partial U_j}{\partial x_i}} \quad (13)$$

This way, the positive  $\mu_{ij}$  will serve as an anisotropic eddy viscosity and negative  $\mu_{ij}$  will be treated explicitly. Despite its benefit of being able to account for the anisotropic turbulent diffusion, and ease of implementation, this approach may find numerical problems associated with the possible huge value of  $\mu_{ij}$ . Therefore, some limits have to be applied to  $\mu_{ij}$  in the iterative procedure of a computational method. Consequently, the overall numerical procedure may be degraded tremendously. In this study, a different approach is used. The approach follows the work of Obi *et al.*<sup>41</sup> by using a special evaluation of the cell face Reynolds stresses to eliminate the possible decoupling between velocities and Reynolds stresses on a colocated grid. The proposed special interpolation technique resulted in an explicit relation between the Reynolds stresses and the strain rates. This feature naturally leads to the semicoupled treatment of the Reynolds stress force thereby promoting the stability and robustness of the numerical method. The numerical method is described below.

#### A.3.1 Discretization

All the governing equations except the continuity can be expressed in Cartesian coordinates as:

$$\begin{aligned} \frac{\partial \rho U_k \phi}{\partial x_k} &= \frac{\partial}{\partial x_1} \left[ \Gamma_{11} \frac{\partial \phi}{\partial x_1} \right] + \frac{\partial}{\partial x_2} \left[ \Gamma_{22} \frac{\partial \phi}{\partial x_2} \right] + \frac{\partial}{\partial x_3} \left[ \Gamma_{33} \frac{\partial \phi}{\partial x_3} \right] + S_\phi \\ &= \frac{\partial}{\partial x_k} \left[ \Gamma_{kk} \frac{\partial \phi}{\partial x_k} \right] + S_\phi \end{aligned} \quad (14)$$

Note that  $\Gamma_{kk}$  is not a tensor and no summation on  $\Gamma_{kk}$  is implied.

Equation (14) can be transformed into a body-fitted coordinate ( $\xi_1, \xi_2, \xi_3$ ) as:

$$\frac{\partial}{\partial \xi_k} [\rho(U, \xi_{k,j})\phi] = \frac{\partial}{\partial \xi_k} \left[ J \Gamma_{kj}^* g^{kj} \frac{\partial \phi}{\partial \xi_j} \right] + S_\phi \quad (15)$$

where  $\Gamma_{kj}^*$  is not a tensor and is defined as:

$$\Gamma_{jk}^* = \frac{\Gamma_{ll} \xi_{k,l} \xi_{j,l}}{|\xi_{k,l} \xi_{j,l}|} ; (k, j = 1, 2, 3) \quad (16)$$

and

$$g^{kj} = |\xi_{k,l} \xi_{j,l}| ; J = \frac{\partial(x_1, x_2, x_3)}{\partial(\xi_1, \xi_2, \xi_3)} \quad (17)$$

In the above,  $\xi_{k,l}$  e.g. means  $\partial \xi_k / \partial x_l$ .

The discretization of Equation (15) is carried out using a finite-volume approach. First, the solution domain is divided into a finite number of discrete volumes or cells, where all variables are stored at their geometric centers. The equation is then integrated over all the cells by using the Gaussian Theorem. A detailed discretization process was described before and is not reported here. It is sufficient to point out that the final discretized equation for  $\phi$  at a control volume P can be written in a linear equation form as:

$$\begin{aligned} A_p \phi_p = & A_W \phi_W + A_E \phi_E + A_S \phi_S + A_N \phi_N + A_L \phi_L + A_H \phi_H \\ & + A_{SW} \phi_{SW} + A_{SE} \phi_{SE} + A_{NW} \phi_{NW} + A_{NE} \phi_{NE} \\ & + A_{LS} \phi_{LS} + A_{LN} \phi_{LN} + A_{HS} \phi_{HS} + A_{HN} \phi_{HN} \\ & + A_{WL} \phi_{WL} + A_{WH} \phi_{WH} + A_{EL} \phi_{EL} + A_{EH} \phi_{EH} + S^\phi \end{aligned} \quad (18)$$

or

$$A_p \phi_p = \sum_{nb} A_{nb} \phi_{nb} + S_\phi \quad (19)$$

In the above, subscripts W, E, S, N, L, H denote the cells located West, East, South, North, Low, High side of cell P, and nb refers to all the neighboring cells.

### A.3.2 Evaluation of the Cell Face Stresses

In a discretized form, the cell face stresses are needed to obtain the Reynolds stress force in the momentum equation. To avoid the decoupling of the velocities and the stresses and to extract the necessary diffusive contribution of the stress force, a special technique is needed and presented next.

First, the discretized Reynolds stress transport equation is organized as follows:

$$A_p(\overline{u_i u_j})_p = \sum_{nb} A_{nb}(\overline{u_i u_j})_{nb} - \left[ \omega_{ij} \frac{\partial U_i}{\partial x_j} + \omega_{ji} \frac{\partial U_j}{\partial x_i} \right] \cdot \nabla + S_{ij} \quad (20)$$

In the above,  $\nabla$  is the cell volume and  $\omega_{ij}$  is not a tensor and no summation on  $i$  or  $j$  is implied. For the Gibson-Launder model without the inclusion of the wall reflection term, the coefficients,  $\omega_{ij}$  can be listed as:

$$\begin{cases} \omega_{ij} = \left(1 - \frac{2}{3}C_2\right) \rho \overline{u_i^2} & (\text{if } i = j) \\ \omega_{ij} = (1 - C_2) \rho \overline{u_i^2} & (\text{if } i \neq j) \end{cases} \quad (21)$$

Note that the above coefficients are always positive since  $C_2 = 0.6$  is used by the Gibson-Launder model. Therefore, the cell center stress  $\overline{u_i u_j}$  can be calculated from Equation (20) as:

$$\overline{u_i u_j} = \left[ \frac{\sum_{nb} A_{nb}(\overline{u_i u_j})_{nb} + S_{ij}}{A_p} \right] - \left[ \beta_{ij} \frac{\partial U_i}{\partial x_j} + \beta_{ji} \frac{\partial U_j}{\partial x_i} \right] \quad (22)$$

with

$$\beta_{ij} = \frac{\omega_{ij} \cdot \nabla}{A_p} \quad (23)$$

Now, the cell face Reynolds stress can be obtained by linearly interpolating all terms in Equation (22) except for the velocity gradient, *i.e.*

$$(\overline{u_i u_j})_f = \left\langle \frac{\sum_{nb} A_{nb}(\overline{u_i u_j})_{nb} + S_{ij}}{A_p} \right\rangle - \left\{ \langle \beta_{ij} \rangle \left( \frac{\partial U_i}{\partial x_j} \right)_f + \langle \beta_{ji} \rangle \left( \frac{\partial U_j}{\partial x_i} \right)_f \right\} \quad (24)$$

where  $\langle \rangle$  denotes linear interpolation from cell centers to the cell face. Equation (24) was used by Obi *et al.* to calculate the cell face stresses. However, Equation (24) can be simplified by noting that:

$$\langle \overline{u_i u_j} \rangle = \left\langle \frac{\sum_{nb} A_{nb} \langle \overline{u_i u_j} \rangle_{nb} + S_{ij}}{A_p} \right\rangle - \left\langle \left( \beta_{ij} \frac{\partial U_i}{\partial x_j} + \beta_{ji} \frac{\partial U_j}{\partial x_i} \right) \right\rangle \quad (25)$$

Substitution of Equation (25) into Equation (24) yields:

$$(\overline{u_i u_j})_f = \langle \overline{u_i u_j} \rangle + \left\langle \beta_{ij} \frac{\partial U_i}{\partial x_j} \right\rangle - \langle \beta_{ij} \rangle \left( \frac{\partial U_i}{\partial x_j} \right)_f + \left\langle \beta_{ji} \frac{\partial U_j}{\partial x_i} \right\rangle - \langle \beta_{ji} \rangle \left( \frac{\partial U_j}{\partial x_i} \right)_f \quad (26)$$

For practical purposes, it is more convenient to use the following interpolation:

$$(\overline{u_i u_j})_f = \langle \overline{u_i u_j} \rangle + \langle \beta_{ij} \rangle \left[ \left\langle \frac{\partial U_i}{\partial x_j} \right\rangle - \left( \frac{\partial U_i}{\partial x_j} \right)_f \right] + \langle \beta_{ji} \rangle \left[ \left\langle \frac{\partial U_j}{\partial x_i} \right\rangle - \left( \frac{\partial U_j}{\partial x_i} \right)_f \right] \quad (27)$$

It is seen from Equation (27) that the cell face stress is obtained with linear average of the cell center stresses plus a third derivative velocity term. The above interpolation formula is not only much simpler to implement but it also has a clear physical meaning. The third-derivative velocity term serves as a high order damping to suppress the oscillatory mode. This Reynolds stress force in the momentum equation has been transformed into a new form which gives an explicit diffusive contribution.

In Body-Fitted Coordinates, the Reynolds stress force can be expressed as:

$$f_i = - \frac{\partial}{\partial x_j} (\rho \overline{u_i u_j}) = - \frac{1}{J} \frac{\partial}{\partial \xi_k} (\rho J \xi_{k,j} \overline{u_i u_j}) \quad (28)$$

Integration over a control volume gives:

$$F_i = \int f_i dV = - \frac{\delta}{\delta \xi_k} (\rho J \xi_{k,j} \overline{u_i u_j}) \quad (29)$$

where  $\delta$  denotes a central difference operator.

Substitution of (27) into (29) yields:

$$F_i = F_{i1} + F_{i2} \quad (30)$$

$$F_{i1} = - \frac{\delta}{\delta \xi_k} [\rho J \xi_{k,j} \langle \overline{u_i u_j} \rangle] - \frac{\delta}{\delta \xi_k} \left[ \rho J \xi_{k,j} \left( \langle \beta_{ij} \rangle \left\langle \frac{\partial U_i}{\partial x_j} \right\rangle + \langle \beta_{ji} \rangle \left\langle \frac{\partial U_j}{\partial x_i} \right\rangle - \langle \beta_{ji} \rangle \left( \frac{\partial U_j}{\partial x_i} \right)_f \right) \right] \quad (31)$$



$$F_{2i} = \frac{\delta}{\delta \xi_{kl}} \left[ \rho J \langle \beta_{ij} \rangle \xi_{k,j} \xi_{l,j} \frac{\partial U_i}{\partial \xi_l} \right] \quad (32)$$

It is seen by comparing Equation (32) with (15) that  $F_{2i}$  term is exactly the diffusion term needed to promote the stability of the numerical method by defining  $\Gamma_{kl}^*$  for  $U_i$ -momentum equation as:

$$\Gamma_{kl}^{*i} = \frac{\rho \langle \beta_{ij} \rangle \xi_{k,j} \xi_{l,j}}{|\xi_{k,j} \xi_{l,j}|} \quad (33)$$

where the superscript,  $i$ , is added to  $\Gamma_{kl}^*$  to represent  $U_i$ -momentum equation. The remaining force term  $F_{1i}$  will be calculated explicitly.

### A.3.3 Boundary Conditions

Most boundary conditions can be imposed without any difficulty except at a wall and at a symmetry in a body-fitted coordinate grid. At a solid wall, the wall function approach of Launder and Spalding is used for the momentum equations. The application of the wall functions to the Reynolds stress equations is not trivial in a BFC grid. In this study, fixed Reynolds stress values near a wall are used.

Naot *et al.*<sup>42</sup> derived the following near wall stress relations based on the equilibrium assumptions and by comparing the experimental data.

$$\frac{\overline{uu}}{\frac{2}{3}k} = 1.95 ; \quad \frac{\overline{vv}}{\frac{2}{3}k} = 0.375 ; \quad \frac{\overline{ww}}{\frac{2}{3}k} = 0.675 ; \quad -\frac{\overline{uv}}{k} = 0.2 \quad (34)$$

To apply the boundary condition to a BFC grid, let us define a local coordinate system  $(x,y,z)$  at the wall such that  $y$  is normal to the wall;  $x$  is along the flow direction; and  $z$  is normal to the  $xy$  plane. Then, the Reynolds stresses defined on the  $xyz$  system can be obtained by Equation (34). However, a global cartesian coordinate system  $(x_1, x_2, x_3)$  is used in this study and the Reynolds stresses  $\overline{u_i u_j}$  are represented in  $(x_1, x_2, x_3)$  system. Therefore, a transformation needs to be established and it can be expressed as:

$$\overline{u_i u_j} = \alpha_{1i} \alpha_{1j} \overline{u^2} + \alpha_{2i} \alpha_{2j} \overline{v^2} + \alpha_{3i} \alpha_{3j} \overline{w^2} + (\alpha_{1i} \alpha_{2j} + \alpha_{2i} \alpha_{1j}) \overline{uv} \quad (35)$$

where  $\alpha_{ij}$  is the directional cosine representing the projection of the  $i$ th unit base of  $(x,y,z)$  system to the  $j$ th base of the  $(x_1, x_2, x_3)$  system. With Equation (35), the wall boundary conditions can be easily applied to the stress equations in a general coordinate system.

On a symmetry surface, a similar transformation is applied. The Reynolds stresses on a symmetry surface can be obtained as:

$$(\overline{u_i u_j})_{symm} = \alpha_{1i} \alpha_{1j} \tau_{11} + \alpha_{2i} \alpha_{2j} \tau_{22} + \alpha_{3i} \alpha_{3j} \tau_{33} + (\alpha_{1i} \alpha_{3j} + \alpha_{3i} \alpha_{1j}) \tau_{13} \quad (36)$$

with

$$\tau_{lm} = \alpha_{li} \alpha_{mj} \overline{u_i u_j} \quad (37)$$

where  $\overline{u_i u_j}$  is the stress at the cell center.

## A.4 APPLICATIONS

Three turbulent flows are calculated to demonstrate the numerical method. The first is the backward facing step flow investigated by Eaton and Johnston.<sup>43</sup> This case is used to make sure the BFC formulation recovers to the cartesian grids as required. The second case is a turbulent flow over a faired annular diffuser measured by Stevens and Fry.<sup>44</sup> This case is chosen to demonstrate the BFC capability. The third case is the confined swirling flow measured by Nejad *et al.*<sup>45</sup> and is used to demonstrate the solution of all six Reynolds stress equations. The second-moment calculation results will be compared to the standard k- $\epsilon$  model to show the strength of the second-moment closure.

### A.4.1 Backward-Facing Step Flow

The computational domain is shown in Figure A-1. The inlet U-velocity and the turbulent kinetic energy are obtained from the experimental data. The V-velocity component and the Reynolds shear stresses are set to zero and the normal Reynolds stresses are obtained assuming isotropy. The dissipation rate at the inlet is estimated from  $K^{1.5}/(0.05H)$ . Computations are performed on a nonuniform grid consisting of  $140 \times 70$  cells with 40 streamwise cells located between  $x/H = (-1.5, 1.0)$  and another 60 between  $x/H = (1.0, 12.0)$ . This grid should be sufficient to generate a grid-independent solution based on the previous results. The measure of the computational time indicated that the second-moment closure took about 4 to 5 more total CPU time than the k- $\epsilon$  model.

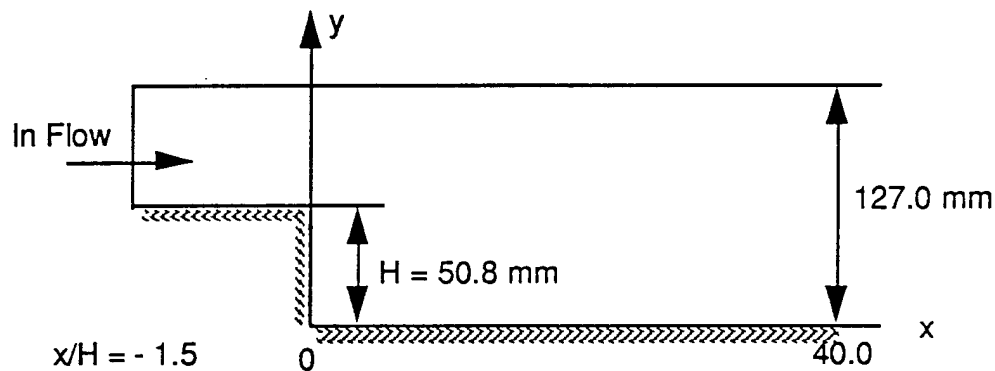


Figure A-1. The Computational Domain of the Backward-Facing Step

The mean streamwise velocity profiles are presented in Figure A-2 comparing the second-moment closure and the k- $\epsilon$  model with the experimental data. Similar to the finding of Obi *et al.* where a different backward facing step was calculated, the second-moment closure is able to predict the experimentally observed monotonic

increase in the reverse velocity away from the bottom wall (see  $x/H = 1.0$  in Figure A-2), whereas the  $k-\epsilon$  model behaves in an opposite trend. This different behavior is due to the fact that the second-moment closure predicts the existence of a secondary recirculation at the corner while the  $k-\epsilon$  model fails to predict it. This can be seen clearly in Figure A-3 where the computed streamlines are displayed. The predicted size of the secondary recirculation is about  $0.93H$  which is quite consistent with the experimental data of  $1.0H$ . Overall, it is seen that the second-moment closure gives better mean velocity agreement with the experimental data. Despite quite different predictions of the secondary recirculation, the calculated sizes of the primary recirculation are similar between the two models. The second-moment model predicts the reattachment length of  $7.06H$  while the  $k-\epsilon$  model is  $6.91H$ . The experimentally determined reattachment length is  $8.0H$ . Therefore, both models underpredict the reattachment length by 12~14%.

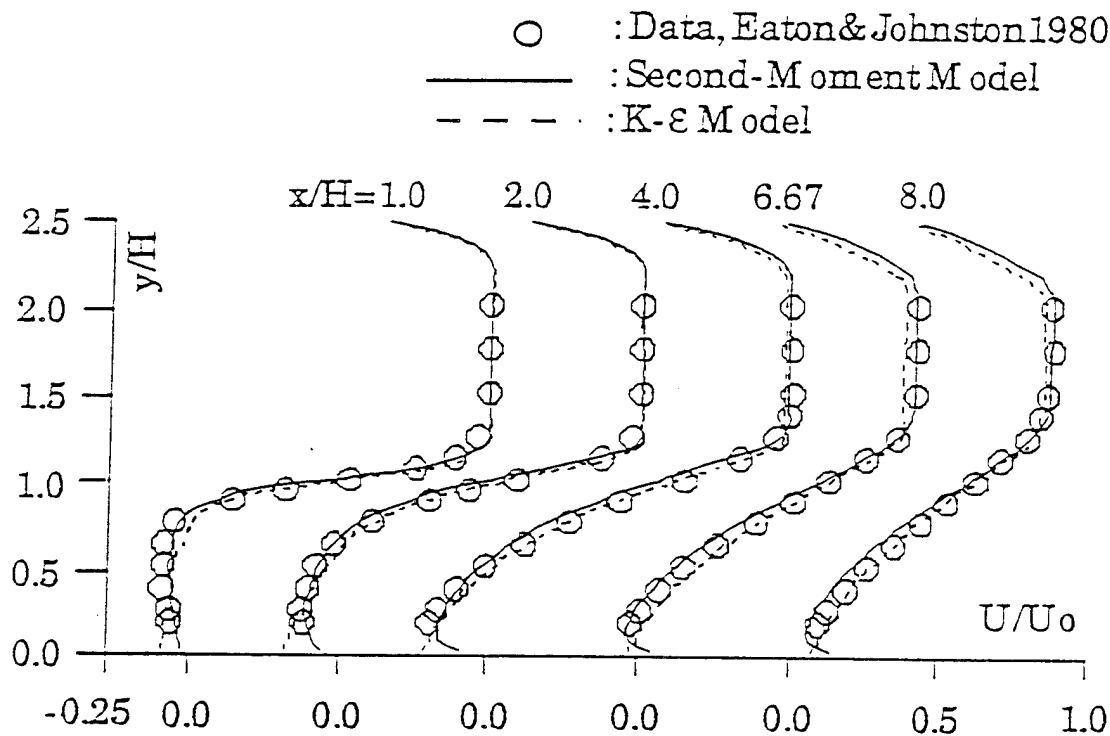


Figure A-2. The Comparison of the Mean Streamwise Velocity

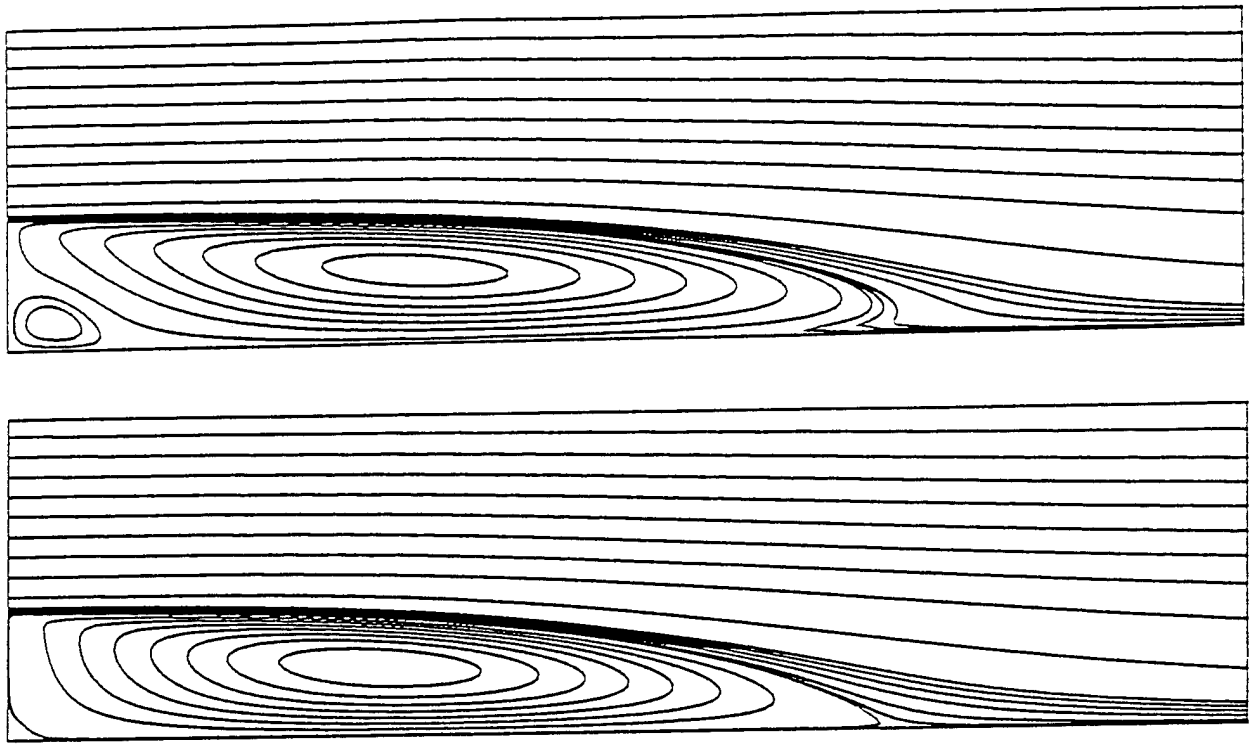


Figure A-3. The Calculated Streamlines -Top: the second-moment closure  
Bottom: the k- $\epsilon$  model

Figures A-4 and A-5 present the turbulent normal stress  $\overline{u^2}$  and the shear stress  $\overline{uv}$ . Both stresses are predicted well by the second-moment closure at  $x/H = 1.0$  and  $2.0$ , but greater discrepancies show up further downstream. As expected, the normal stress is severely underpredicted by the k- $\epsilon$  model due to its isotropic eddy-viscosity assumption. However, the shear stress is calculated unexpectedly well by the k- $\epsilon$  model as seen in Figure A-5.

#### A.4.2 An Axisymmetric Faired Diffuser Flow

The turbulent flow through an axisymmetric faired diffuser as shown in Figure A-6 is calculated to demonstrate the calculation method on a body-fitted-coordinate grid. The diffuser consists of an entry annular pipe, an inlet bend, a straight diffuser, an outlet bend, and an exit annular pipe. The experimental test was carried out by Stevens and Fry and a numerical study was reported by Jones & Manners. The inlet of the computational domain is located at  $0.0762$  m upstream of the inlet bend. (Note that the width of the entry annular pipe is  $0.0254$  m.) All main variables at the inlet are obtained from the fully-developed annulus solutions to minimize the inlet condition uncertainty. This is possible since a long entry length (about  $50.0$  hydraulic diameter of the entry annulus) was used in the experiment and the data suggested that the fully developed conditions have been established.

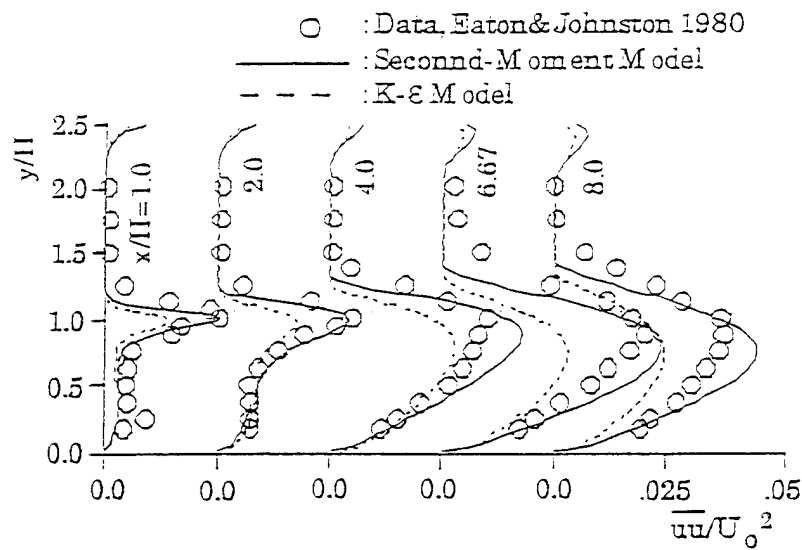


Figure A-4. The Comparison of the Turbulent Normal Stress Component

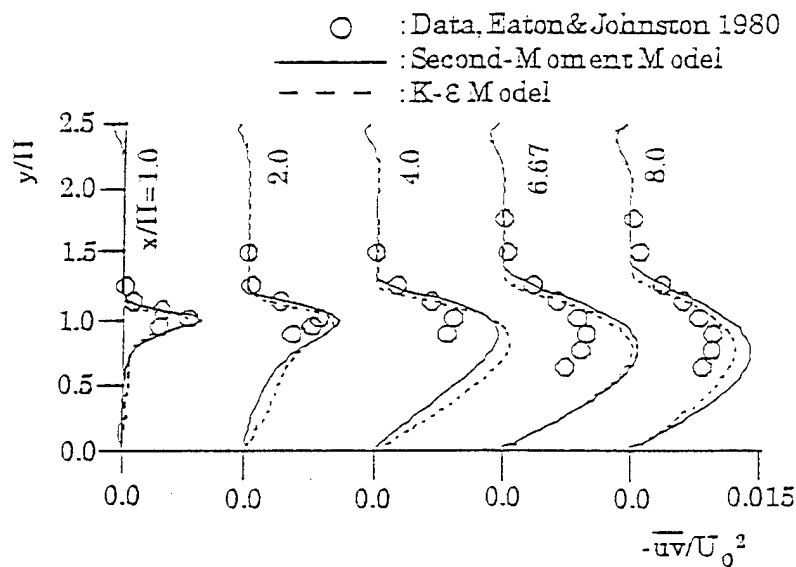


Figure A-5. The Comparison of the Turbulent Shear Stress Component

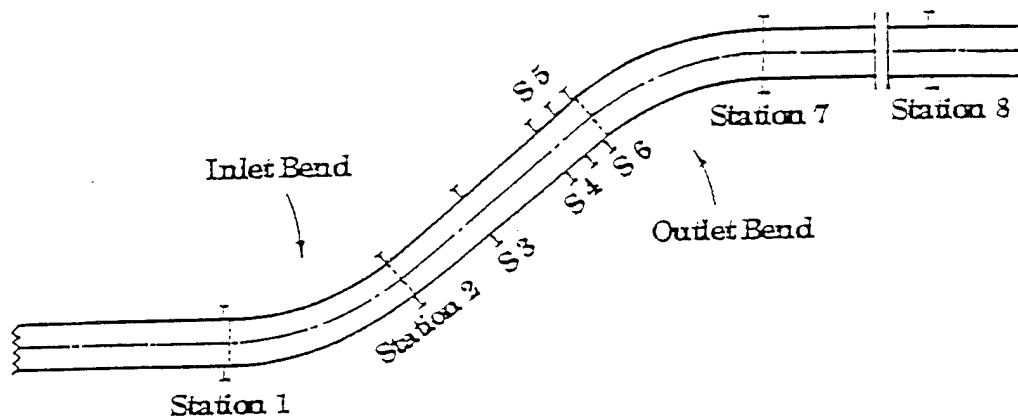


Figure A-6. The Geometry of the Axisymmetric Faired Diffuser

The exit of the computational domain is placed 0.508 m downstream of the outlet bend and all the variables are extrapolated except the pressure. A fixed pressure condition is applied at the exit. The long length of the exit annulus is used to minimize the influence of the Newman type exit boundary conditions.

Both the second-moment turbulence model of Gibson-Lauder and the standard k- $\epsilon$  model are used for the calculation. The computational mesh is chosen as 100x50 in the streamwise and cross-stream directions, respectively, based on the grid-independence study of Jones and Manners. The second-moment model took about twice the total CPU time of the k- $\epsilon$  model calculation. Both computations will reach the convergence criterion in 600 to 800 iterations.

Figures A-7 and A-8 present the radial distribution of the mean axial velocity and Reynolds shear stress at several streamwise locations, respectively. The station numbers correspond to the selected measurement stations as indicated in Figure A-6.  $\eta$  is the local nondimensional distance coordinate approximately normal to the inner and outer annular walls with  $\eta = 0$  at the outer wall. As can be seen, from Figure A-7, the second-moment closure prediction of the mean streamwise velocity is in good agreement with the measured data, whereas the k- $\epsilon$  model results are not. In the straight diffuser section, the mean streamwise velocity is overpredicted near the outer wall and underpredicted at the inner wall by the k- $\epsilon$  model. This trend of the results by the k- $\epsilon$  model is not surprising since the streamline is strongly curved for the flow. The flow streamline curvature tends to invalidate the standard k- $\epsilon$  model. Therefore, the calculated result prove that the second-moment closure has naturally taken the extra-strain effect, induced by streamline curvature, into account. The most remarkable result is the comparison of the streamwise velocity at station 8 in Figure A-7. The experimental data suggest that the maximum velocity location is switched from the outer wall to the inner wall after the fluid is coming out of the outlet bend. This unusual feature is well captured by the second-moment closure. However, the k- $\epsilon$  model will keep the maximum velocity location near the outer wall, and totally missed this experimentally observed feature.

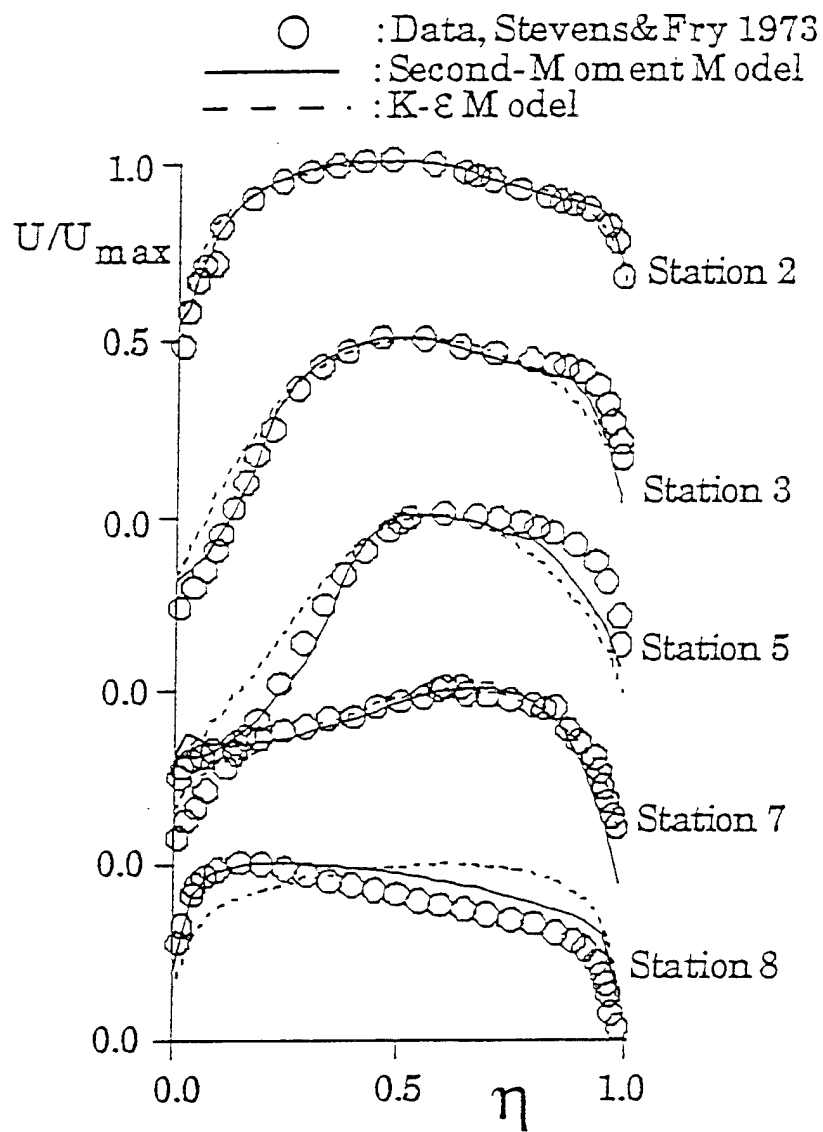


Figure A-7. The Comparison of the Mean Streamwise Velocity



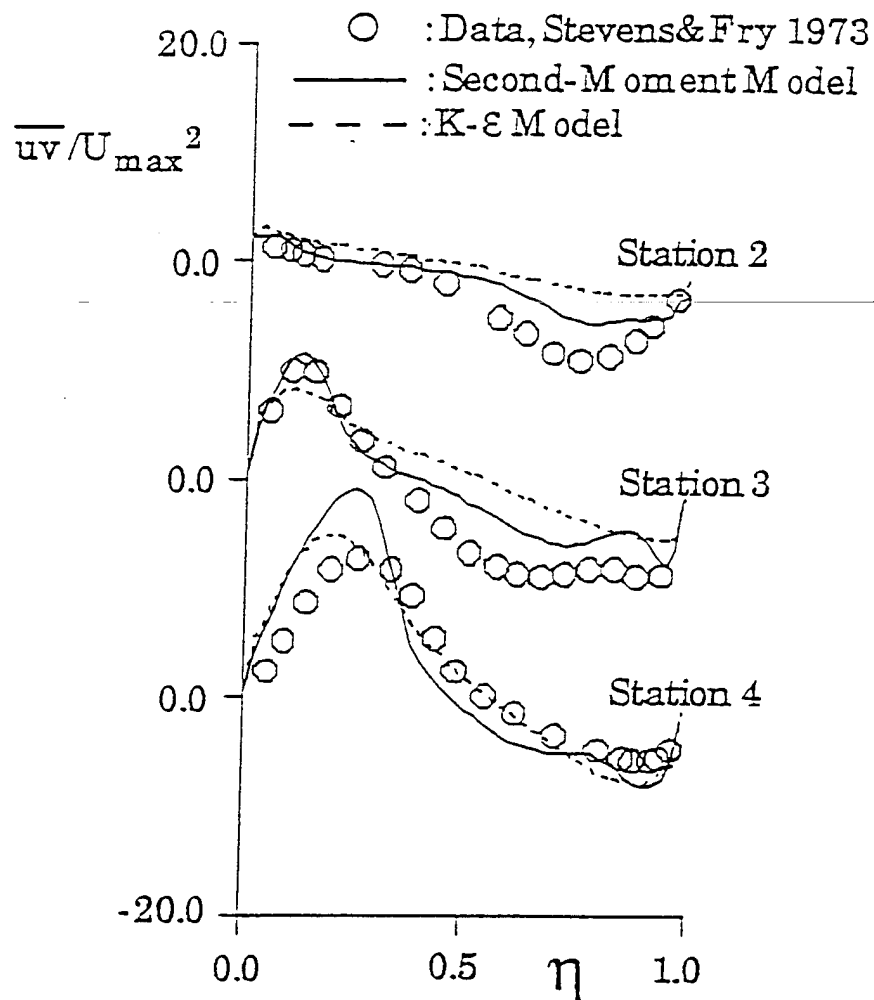


Figure A-8. The Comparison of the Turbulent Shear Stress Component

#### A.4.3 Confined Swirling Flow

The confined swirling flow calculated in this study was experimentally studied by Nejad et al.<sup>45</sup> and is shown schematically in Figure A-9. It is seen that the dump combustor consists of two sections: the inlet pipe and the combustion chamber. The inlet pipe has an inner diameter of 101.6 mm and a cylindrical teflon swirler is located 50.8 mm upstream of the dump plane. The combustor chamber is 1850 mm in length and has a 152.4 mm I.D. Air is the working fluid and the inlet centerline velocity is measured 360 mm upstream of the swirler housing and is kept at 19.2 m/s. This corresponds to a Reynolds number of 125,000 based on the combustor inlet diameter. The computation corresponds to the case with a swirl number of 0.5. The experimental data showed that this swirl number is just strong enough to lead to flow reversal near the chamber centerline after the dump plane.

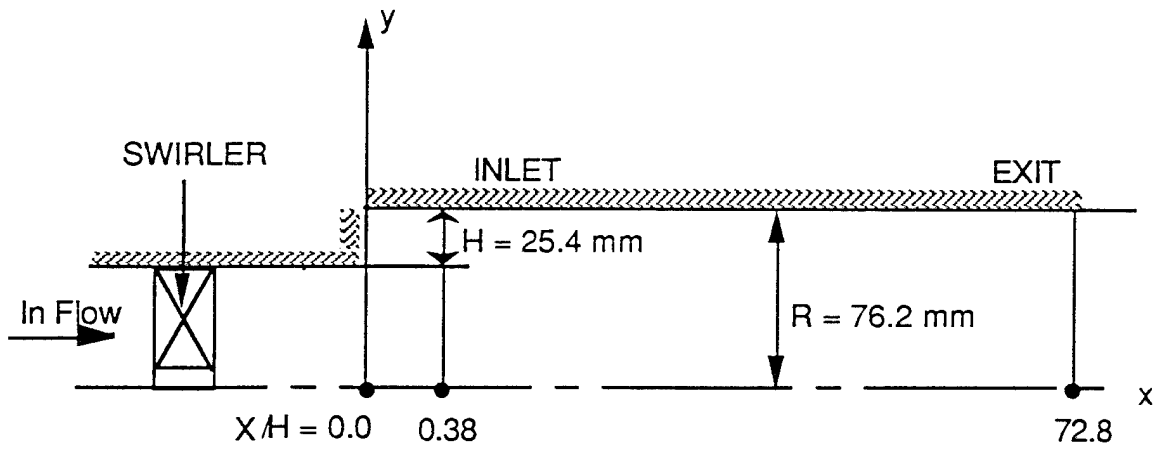


Figure A-9. The Geometry of the Swirling Flow Studied

For all the computations, the inlet is located 0.38 step height downstream of the dump plane. This is the closest location to the swirler where detailed experimental data are available for the mean velocity components and the Reynolds stresses except  $\epsilon$ . It is known that swirling flow computations are very sensitive to the inlet conditions. Therefore, complete availability of the experimental data at the inlet makes this set of data valuable to assess turbulence model performance. The only uncertainty at the inlet, therefore, is the specification of the turbulent dissipation rate  $\epsilon$  and it will be discussed shortly.

The outlet boundary is placed 72.8 step heights downstream of the dump plane. This outlet is far enough from the inlet to minimize the influence of the exit boundary conditions. At the outlet, all main variables are extrapolated.

At the solid walls, the standard wall function approach is adopted. Finally, at the centerline symmetry, the derivatives of all variables are set to zero except  $\bar{u}\bar{v}$  and  $\bar{v}\bar{w}$ ;  $\bar{u}\bar{v} = \bar{v}\bar{w} = 0$  at symmetry instead.

The turbulent dissipation rate must be specified by the modeler. One of the most used approaches is based on the turbulence-energy equilibrium and  $\epsilon$  is estimated as

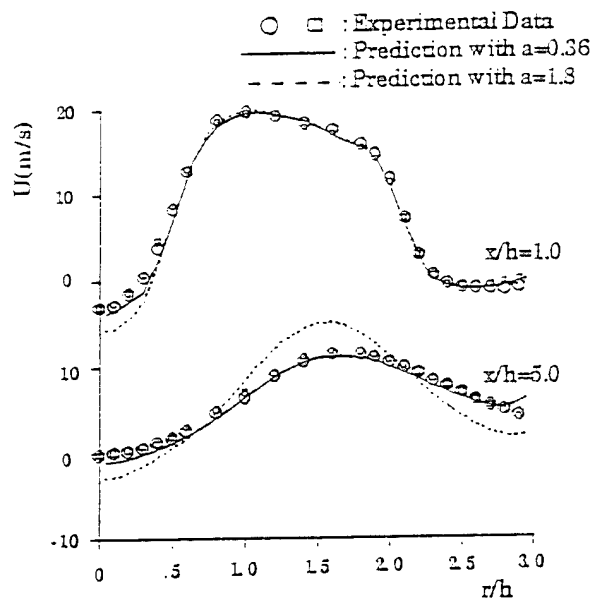
$$\epsilon = \frac{K^{1.5}}{aR} \quad (38)$$

where  $R$  is the radius of the chamber and  $a$  is a constant to be determined. In the RSTM calculation of strongly swirling flows by Hogg and Leschziner<sup>46</sup>,  $a$  of 0.36 was used based on numerical optimization. In another  $k$ - $\epsilon$  computation of the Nejad et al.<sup>45</sup> swirling flow,  $a=0.3$  was used by Favaloro et al.<sup>47</sup> since it gave the best compromise for several swirl numbers calculated. In this study, an independent calculation was carried out to investigate the sensitivity of the solution to  $a$ . Two  $a$ -

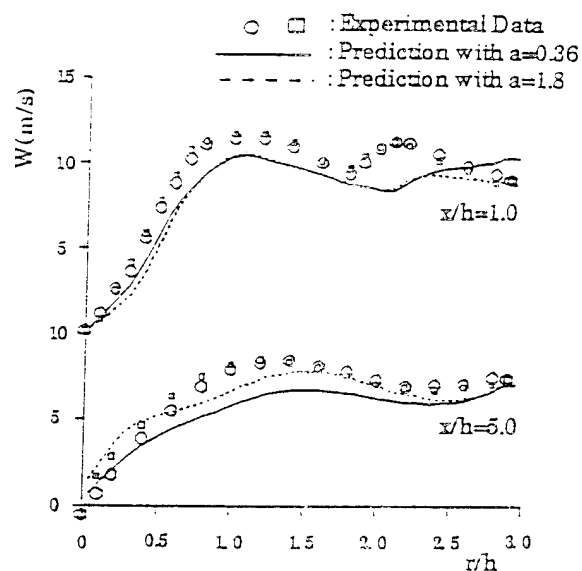
values, 0.36 and 1.8, were used to calculate the swirling flow using the RST model. The calculated radial distributions of the mean axial velocity, swirl velocity, and the turbulent kinetic energy are shown in Figure A-10 at two axial locations. It is seen that the calculated results are quite sensitive to the inlet  $\epsilon$ . It is suggested that the inlet  $\epsilon$  should be chosen such that the predicted resultant turbulent kinetic energy matches the experimental data as close to the inlet as possible. The above criterion is based on two observations: (1)  $k$  directly responds to the inlet  $\epsilon$  and is heavily influenced by  $\epsilon$ . Besides,  $k$  is readily measurable and is available from most turbulent flow data sets. (2) Theoretically,  $\epsilon$  should be chosen such that all the measured data satisfy the governing equations at the inlet. This is obviously impractical. Therefore, the nearest data to the inlet could be used to determine the proper inlet  $\epsilon$ . In this study, the above criterion results in the choice of a of 0.36 as used by Hogg and Leschziner.<sup>46</sup> It should be pointed out in passing that the same inlet  $\epsilon$  also resulted in close agreement with the experimental data at  $x/h=1.0$  for the  $k$ - $\epsilon$  model.

In this study, effort has been spent to use the grid which provides essentially a grid-independent solution. Two highly nonuniform grids are selected: a 70x35 grid (designated as coarse grid) and a 120x60 grid (designated as fine grid). Most of the axial grid is clustered within the central and behind-step separated zones. For the fine grid, 30 cells are used between the inlet and  $x/h$  of 4, and 60 cells are non-uniformly distributed between  $x/h$  of 4 and  $x/h$  of 26. The RSTM predicted radial variations of the mean axial velocity, swirl velocity, and the turbulence kinetic energy are displayed in Figure A-11 at two axial locations. It is seen that increasing grid from 75x35 to 120x60 produced only marginal differences. Therefore, it is believed that the solutions obtained using the 120x60 grid are essentially grid independent. It is worthy to mention that a 48x48 grid was selected by Hogg and Leschziner<sup>46</sup> and a 100x66 grid was used by Jones and Pascau<sup>48</sup> based on their grid-independence study.

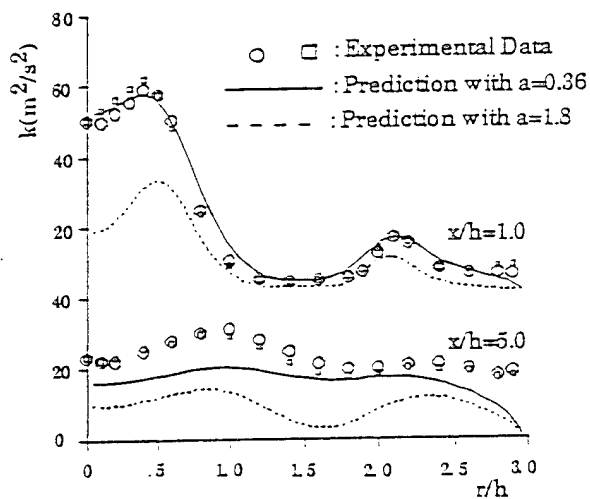
The Reynolds stress transport model, the standard  $k$ - $\epsilon$  model, and the RNG-based  $k$ - $\epsilon$  model are used to calculate the swirling flow of Nejad et al.<sup>45</sup> All the results presented below are obtained using the fine grid (120x60). The results are considered to be converged only if the total absolute sum of the residuals for each governing equation, normalized by the inlet flux, is reduced four orders of magnitude. Further decrease in the residuals did not change the final solution more than 0.1 percent.



(a) Mean Axial Velocity

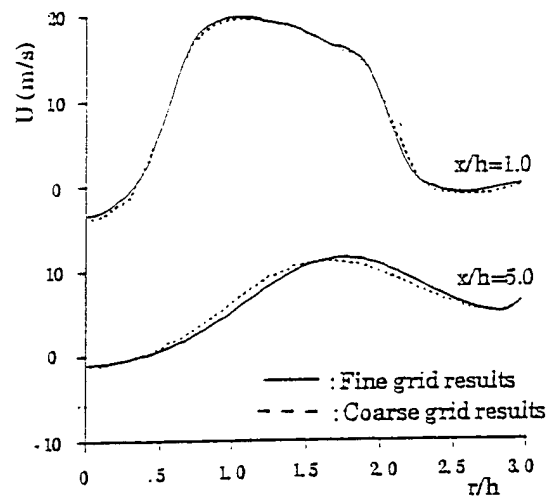


(b) Mean Swirl Velocity

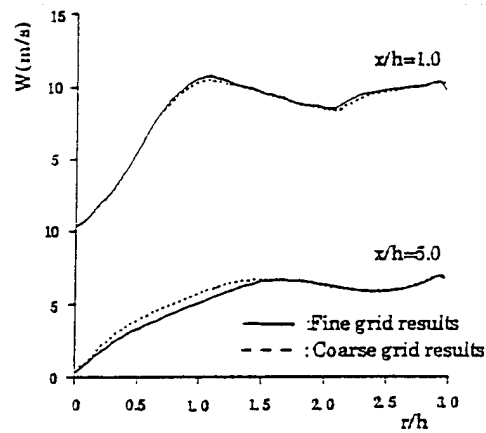


(c) Turbulent Kinetic Energy

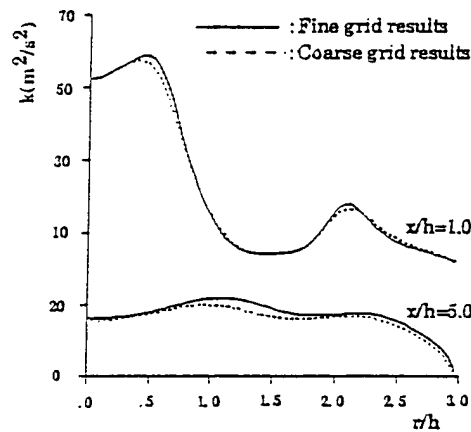
Figure A-10. Sensitivity of the Computed Solution to the Inlet  $\epsilon$



(a) Mean Axial Velocity



(b) Mean Swirl Velocity



(c) Turbulent Kinetic Energy

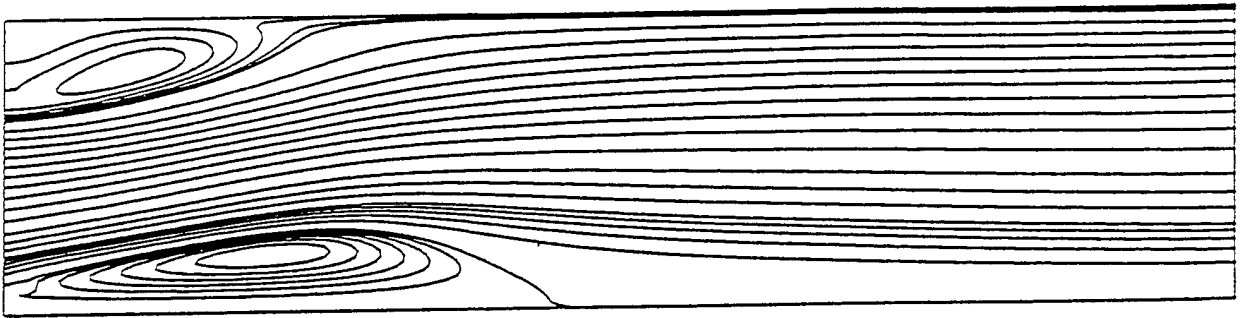
Figure A-11. Sensitivity of the Computed Solution to the Grid

The calculated streamline patterns of the three turbulence models are displayed in Figure A-12 and the predicted size of the central separation zone ( $L_c$ ) and the corner reattachment length ( $L_t$ ) are compared to the experimental data in Table A-1. It is seen from Figure A-12 and Table A-1 that both the standard k- $\epsilon$  model and the RNG-based k- $\epsilon$  model failed to predict the existence of the central reversed zone. On the other hand, the RST model was capable of predicting the occurrence of the central reversed zone although there was an over-prediction of the size. It is believed that the failure of the two-equation type models is resulted from the isotropic eddy-viscosity assumption. This isotropy leads to a too-high turbulent viscosity for the swirling flow and consequently suppresses the central reversed zone.

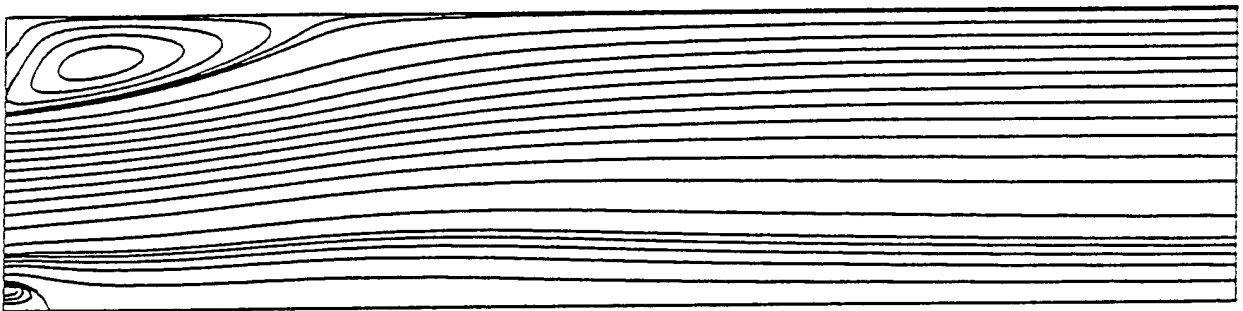
Table A-1. Comparison of the Central Separation Size ( $L_c$ ) and the Corner Reattachment Length ( $L_t$ )

	Computational Results		Experimental Data	
	$L_c/H$	$L_t/H$	$L_c/H$	$L_t/H$
RST Model	5.96	3.15	4.4	3.2
Standard k- $\epsilon$ Model	0.84	3.53	4.4	3.2
RNG-Based k- $\epsilon$ Model	0.89	4.36	4.4	3.2

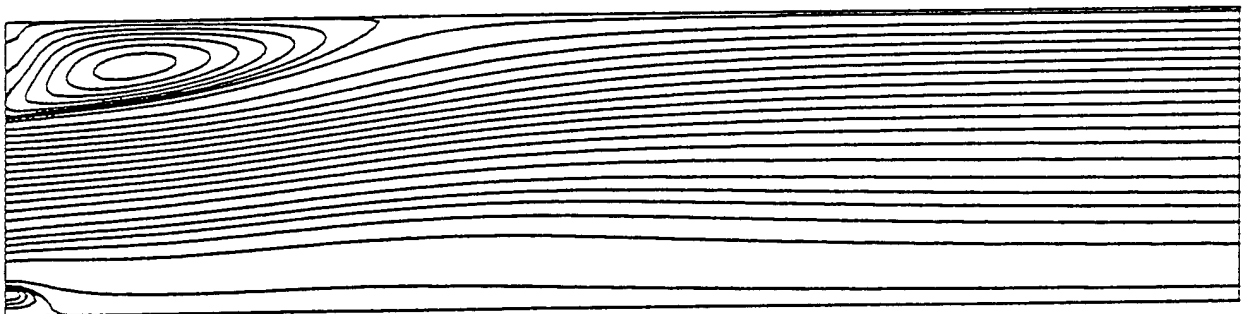
To substantiate the above argument, the flow was also calculated using the k- $\epsilon$  model with much lower inlet  $\mu_T$ . This could be achieved by increasing the inlet turbulence dissipation rate  $\epsilon$ . It was found that the central reversed flow would appear if inlet  $\epsilon$  was several times larger. As expected, however, the calculated turbulence quantities such as the turbulent kinetic energy deviated too far away from the experimental data near the inlet section. This points to the inadequacy of the use of high inlet  $\epsilon$ . These results suggested that the Reynolds stress transport model, which implicitly uses the anisotropic turbulent viscosity, seems to have the basic mechanisms capable of more accurately predicting the central separation of swirling flows. The overprediction of the separation size by the RST model may be attributable to the use of Gibson-Lauder pressure-strain model. Computations with more advanced pressure-stain models, such as those by Shih et al.<sup>49</sup> and Speziale et. al.<sup>50</sup>, could clarify the above argument but are not within the scope of this study.



(a) The RST Model



(b) The Standard  $k-\epsilon$  Model



(c) The RNG-Based  $k-\epsilon$  Model

Figure A-12. The Calculated Streamline Plots

The prediction of the corner recirculation zone is less sensitive to the inlet condition. Overall, the RST model provides the best agreement to the experimental data for the corner reattachment length. It is seen that both eddy-viscosity models over predicted the reattachment length, a behavior quite contrary to the case of a sudden expansion flow without swirl. Experimentally, it was found that the reattachment decreased from approximately 8 step heights for the nonswirl flow to about 3.2 step heights for  $S = 0.5$  case. This decrease in the corner recirculation is caused by the rapid expansion of the flow induced by the action of the centrifugal forces. Therefore, the above results suggested that the eddy-viscosity model fails to take the action of the swirl generated centrifugal force into account properly. This may be directly linked to the failure of the model to predict the existence of the central separation zone. It should point out, in passing, that the RNG-based  $k-\epsilon$  model consistently predicted a larger corner recirculation zone than the standard  $k-\epsilon$  model no matter if the flow has swirl or not. If no swirl is present, the RNG model tends to have a good prediction of the reattachment length (see Speziale and Thangam<sup>29</sup>) since the standard  $k-\epsilon$  model underpredicted the reattachment length. As shown in this study, however, the RNG model can predict worse results for the sudden expansion flow with swirl.

Comparisons of the calculated and measured radial variation of the mean axial velocity and the swirl velocity are shown in Figure A-13 and A-14 respectively, at several axial locations. Again, the RST model has the best overall agreement with the experimental data. The results between the standard and RNG-based  $k-\epsilon$  models are essentially similar. For the mean axial velocity component, the major difference between the results of the RST model and that of the eddy-viscosity model are confined to the central separation zone. This is a direct consequence of the failure of the eddy-viscosity model to predict the reversed flow at the center. The most noteworthy difference between the results of different models is the prediction of the mean swirl velocity far downstream of the dump plane ( $x/h > 5.0$ ). As is clear in Figure A-14, the two eddy-viscosity models predicted that the swirling flow will eventually approach to the solid-body-rotation type. This solid-body-rotation flow will remain until the end of the calculation domain. (This is the reason  $x/h$  of 18.0 station is added to Figure A-14). However, the experimental data suggested that the flow retained the strength of its vortex core all the way to the exit and did not evolve to solid-body-rotation flow. This interesting feature was captured quite well by the RST model. The above results indicated that the RST model is able to account for the complicated interaction between swirl and turbulence field and to predict the combined presence of free and forced vortex in the swirling flow. However, the eddy-viscosity model tends to lose the strength of the vortex cone and expand to a solid-body type rotational motion.



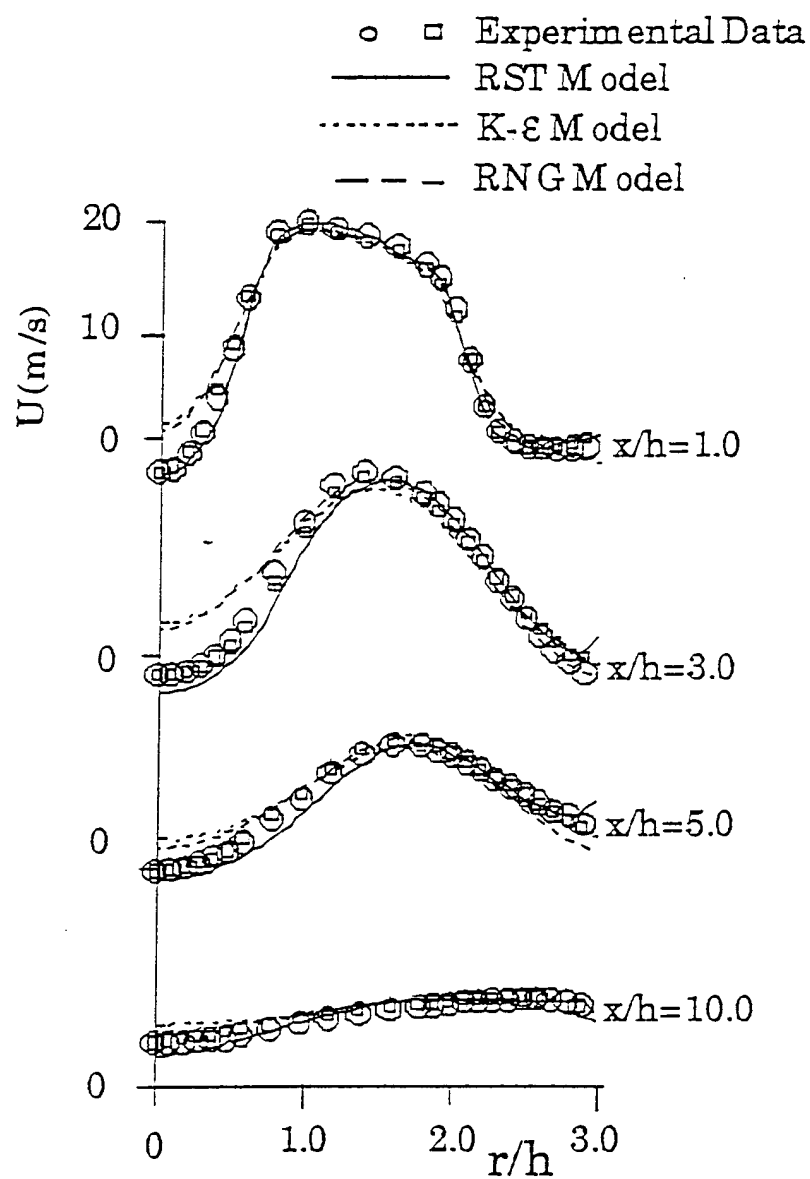


Figure A-13. Radial Variation of the Mean Axial Velocity at Four Axial Locations

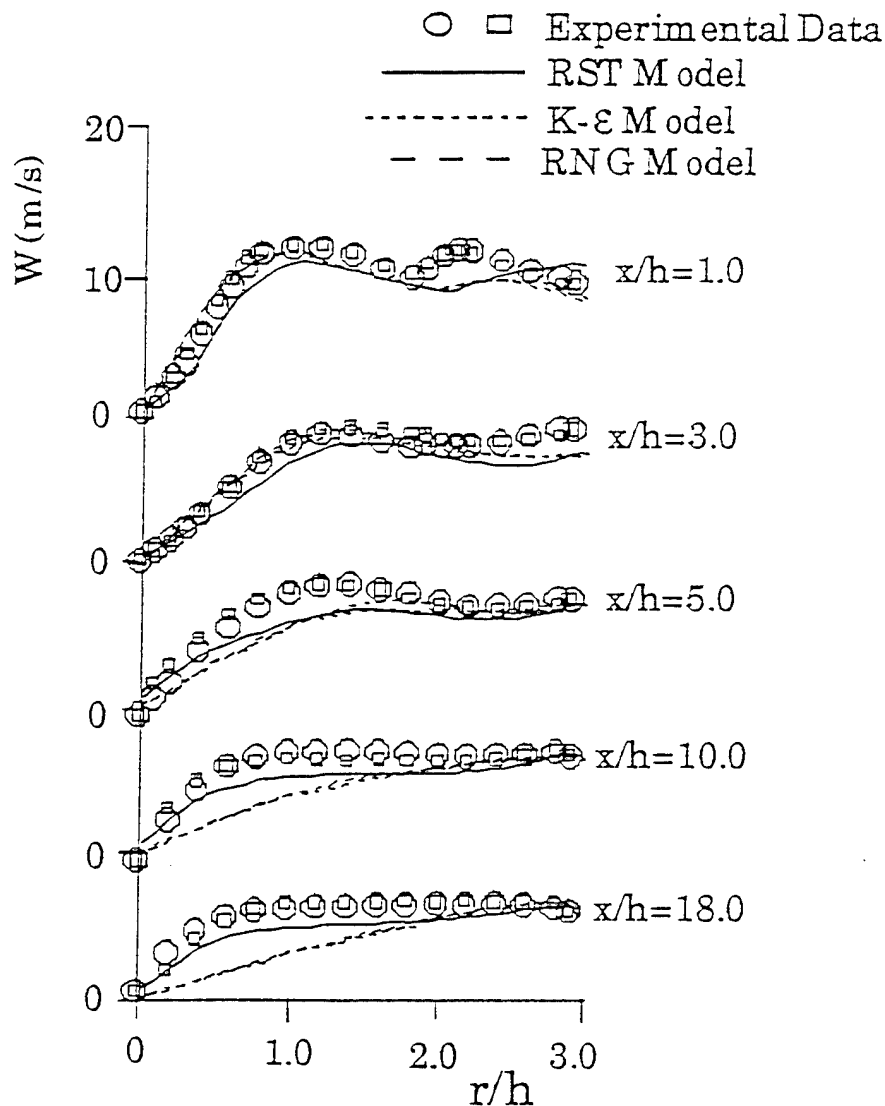


Figure A-14. Radial Variation of the Mean Swirl Velocity at Five Axial Locations

Finally, Figure A-15 shows that comparison of the calculated and measured turbulence kinetic energy. As discussed in the previous section, the turbulence kinetic energy was predicted quite well by all models near the inlet by choosing  $a = 0.36$  for the inlet dissipation rate. ( $x/h = 1.0$  for the present case). But further downstream, the eddy-viscosity models predicted much lower turbulence kinetic energy levels. This underprediction results from the improper modeling of the

swirl and turbulence interaction by the eddy-viscosity model and is probably responsible for the failure of the model to preserve the strength of the vortex core and to predict the reversed flow at the centerline. Again, the RST model provided the best overall prediction. However, large discrepancies could be noticed, particularly around  $x/h$  of 5.0 and near the centerline at downstream locations. The underprediction of  $k$  around  $x/h$  of 5.0 is probably responsible for the overprediction of the central separation zone. With limited information available, no definite conclusion can be drawn with regard to this discrepancy. One major source of error could come from the pressure-strain model.

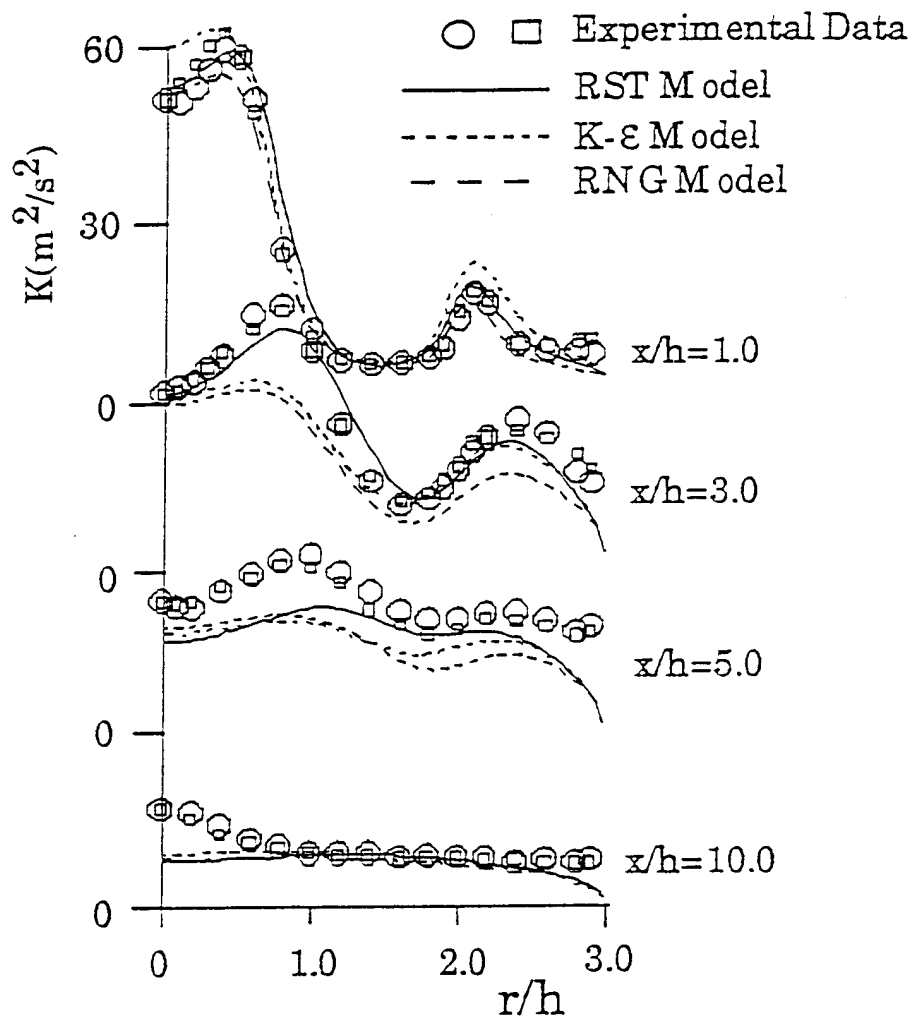


Figure A-15. Radial Variation of the Turbulent Kinetic Energy at Four Axial Locations

## A.5 CONCLUSIONS

The second-moment turbulence closure is implemented into a finite-volume pressure based numerical method on colocated and nonorthogonal grids. Special interpolation scheme is developed to remove the decoupling between momentum and Reynolds stress equations and to provide the strong diffusive contribution of the Reynolds stress force. Three two-dimensional turbulent flows are selected to demonstrate the developed numerical method and the performance of the second-moment closure. The comparison between the second-moment closure and the  $k-\epsilon$  model with the experimental data finds that the second-moment closure does offer advantages over the  $k-\epsilon$  model for complex turbulent flows. For some cases, the difference between the model performances could be remarkable. Due to the increased number of partial differential equations to be solved, the second-moment turbulence will consume more computer resources. For the three flows calculated in this study the increase in CPU time for the second-moment closure is between two to six times that of the  $k-\epsilon$  model.

**APPENDIX B.**  
**LASER DOPPLER VELOCIMETRY**

## B.1 LDV THEORY

Laser Doppler Velocimetry (LDV) has been used for fluid flow measurement since the mid 1960's. Durst, et al.<sup>51</sup> describe the theory and application of LDV at length. LDV is a nonintrusive instrument used to measure turbulent velocity fields without disturbing the flow, and is used where conventional techniques (i.e., hot wire) are not practical. The only added requirement for LDV data acquisition is the presence of seed material in the flow to illuminate the laser beams.

The basic operational principle of the LDV system stems from the creation of a probe volume by crossing two polarized laser beams. At the crossing, the two beams constructively and destructively interfere to create fringes of light as shown in Figure B-1. As the seed particles in the flow pass through the probe volume, the reflected light from the fringes generate an amplitude modulated sinusoidal signal, called a Doppler burst. The scattered light is collected by a lens and focused onto a photomultiplier, which transmits an electrical signal to the signal processor. The LDV signal processors amplify and filter the signals from the photomultiplier, validate the Doppler frequency, and compute the Doppler period which is the reciprocal of the Doppler frequency. The frequency of the scattered light as the particle crosses bright and dark fringes is related to the particle velocity component perpendicular to the fringe direction by the following relation:

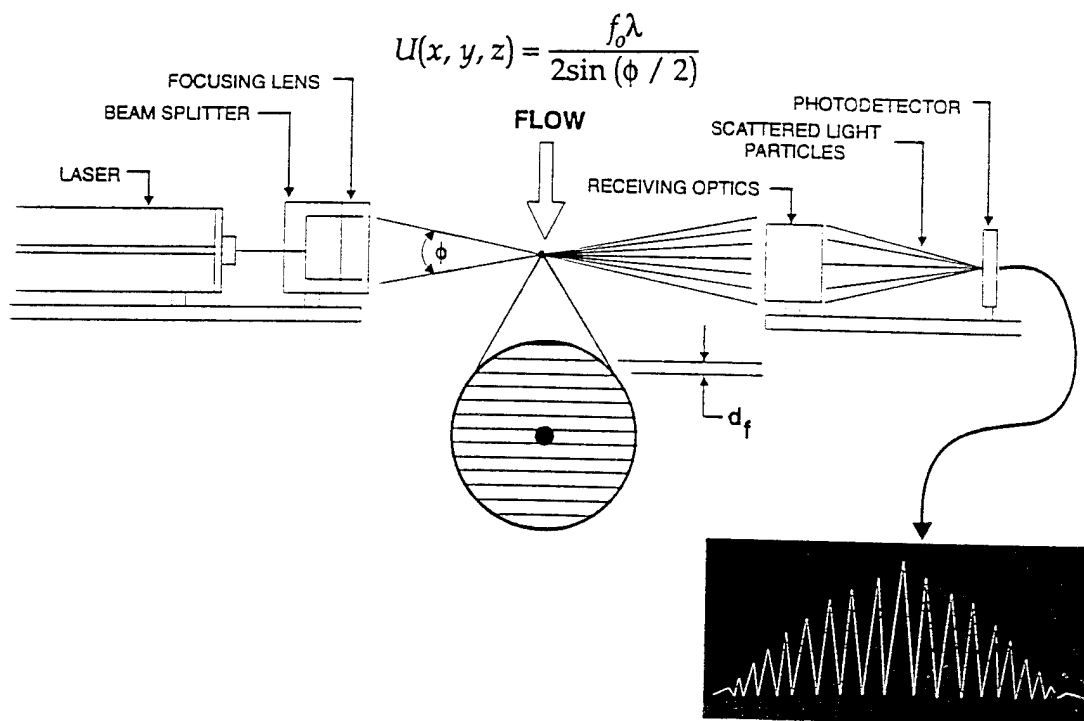


Figure B-1. Typical Dual Beam Laser Doppler Anemometer

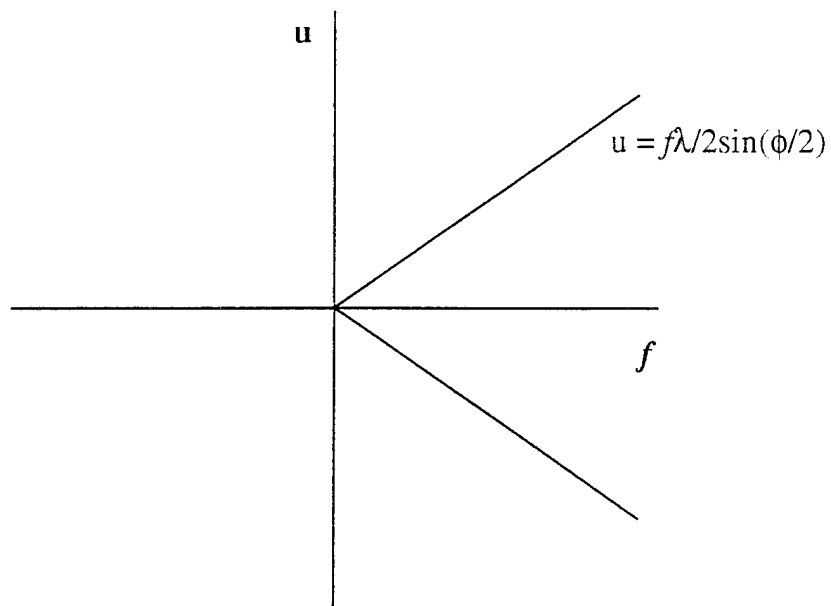
Notice that the velocity is a linear function of the Doppler frequency, since all other terms are constant for a given LDV configuration.

One shortcoming of LDV is that a particle will produce the same frequency regardless of the direction of travel. Therefore a particle traveling at 40 m/s will produce the same frequency as one traveling at -40 m/s since there is not a negative frequency. This is shown graphically in Figure B-2, and is known as aliasing. If negative velocities are expected, the problem can be solved by imposing a frequency shift on the probe volume. The frequency shift causes the fringes in the probe volume to move at a constant rate. A particle sitting at rest within the probe volume will then register a Doppler frequency equal to the frequency shift (typically 40 MHz). This has the effect of shifting the curve up the ordinate in Figure B-2 by 40 MHz. The curve again reflects about  $f=0$ , and aliasing will again occur for particles traveling less than the base velocity ( $u_0$ ). The maximum velocity is limited by the accuracy of the photomultiplier and the signal processor, and is limited by  $f_{max}$ .

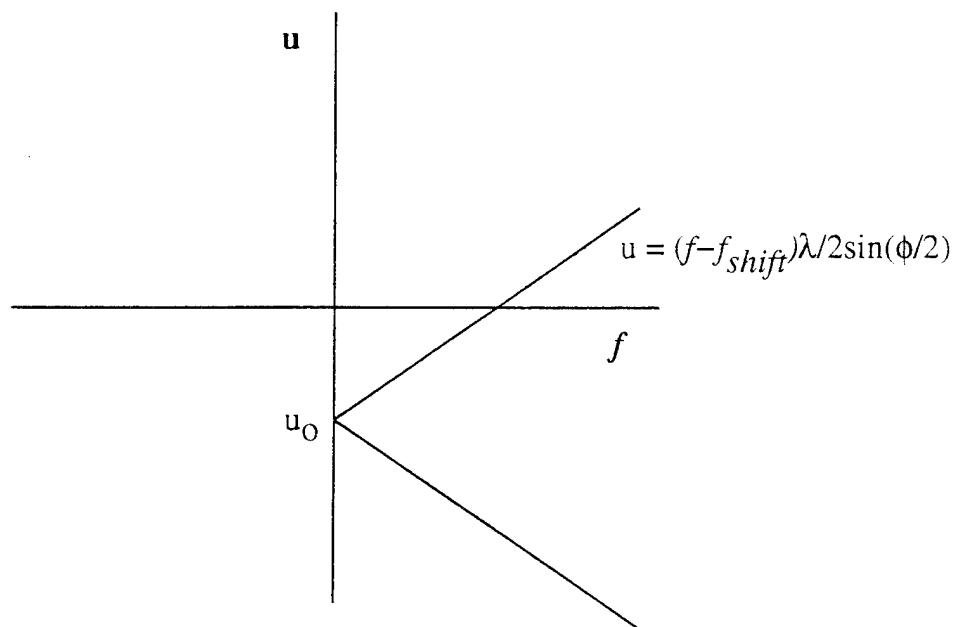
The frequency range can also be shifted in the opposite direction, to increase the peak velocity that the system can measure. This is often done to measure supersonic flows. In short, there is a range of velocity acquisition that falls between  $f=0$  and  $f=f_{max}$ , and that range can be moved along the velocity scale through the use of frequency shifting.

The frequency shifting can be accomplished by several methods, one of which is to pass one of the laser beams through an acoustic oscillator known as a Bragg cell. The Bragg cell creates a diffraction grating using the air density. As the beam passes through the grating, the beam is split into an infinite number of beams, each shifted in frequency by an integer value of the diffraction grating. The first order shifted beam is separated from the rest and is focused to cross with the original beam and form the probe volume.

Two and three dimensional LDV systems are created by focusing additional pairs of laser beams of different colors at the same location, but at different orientations. Each pair of beams must have its own photomultiplier, with appropriate filters so that only the correct color light is registered.



a) without frequency shifting



b) with frequency shifting

Figure B-2. Frequency Shifting Allows the Measurement of Negative Velocities



## B.2 STATISTICAL ANALYSES

LDV systems measure many samples of individual velocity realizations. The most meaningful form of the data comes from standard statistical analysis of the measured data. Since there are inherent errors involved in statistical analysis based on sample population, the statistics are considered estimates, and not actual measurements. A list of the statistical equations used in the current study are as follows:

$$\text{Mean: } \bar{U} = \frac{1}{n} \sum_{i=1}^n U_i \quad \text{or} \quad \frac{1}{n} (U_1 + U_2 + U_3 + \dots U_n)$$

$$\text{RMS: } U_{rms} = \sqrt{\frac{\sum_{i=1}^n U_i^2}{n}} \quad \text{or} \quad \sqrt{\frac{U_1^2 + U_2^2 + U_3^2 \dots U_n^2}{n}}$$

$$\text{SIGMA: } U_{\sigma} = \sqrt{\frac{\sum_{i=1}^n U_i^2}{n} - \left(\frac{\sum_{i=1}^n U_i}{n}\right)^2} \quad \text{or} \quad \sqrt{U_{rms}^2 - \bar{U}^2}$$

where n is the number of samples in the data set.

$$\text{Turbulence intensity (\%): } 100 U_{\sigma} / U_{ref}$$

Second Moments:

$$\begin{aligned} \overline{uv} &= \frac{1}{n} \sum_{i=1}^n ((U_i - \bar{U})(V_i - \bar{V})) \\ &= \frac{1}{n} \sum_{i=1}^n (U_i V_i - U_i \bar{V} - \bar{U} V_i + \bar{U} \bar{V}) \\ &= \left( \frac{1}{n} \sum_{i=1}^n U_i V_i \right) - \left( \bar{V} \sum_{i=1}^n \frac{U_i}{n} \right) - \left( \bar{U} \sum_{i=1}^n \frac{V_i}{n} \right) + (\bar{U} \bar{V}) \\ &= \left( \frac{1}{n} \sum_{i=1}^n U_i V_i \right) - (\bar{V} \bar{U}) = \overline{UV} - \bar{U} \bar{V} \\ &= \left( \sum_{i=1}^n \frac{U_i V_i}{n} \right) - \left( \sum_{i=1}^n \frac{U_i}{n} \right) \left( \sum_{i=1}^n \frac{V_i}{n} \right) \end{aligned}$$

Similarly,

$$\overline{uu} = \left( \sum_{i=1}^n \frac{U_i U_i}{n} \right) - \left( \sum_{i=1}^n \frac{U_i}{n} \right) \left( \sum_{i=1}^n \frac{U_i}{n} \right) = U_{\sigma}^2$$

Triple Products:

$$\begin{aligned}
\overline{uvw} &= \frac{1}{n} \left( \sum_{i=1}^n (u_i - \bar{u})(v_i - \bar{v})(w_i - \bar{w}) \right) \\
&= \frac{1}{n} \left( \sum_{i=1}^n (u_i v_i - u_i \bar{v} - \bar{u} v_i + \bar{u} \bar{v})(w_i - \bar{w}) \right) \\
&= \frac{1}{n} \left( \sum_{i=1}^n (u_i v_i w_i - u_i \bar{v} w_i - \bar{u} v_i w_i - u_i v_i \bar{w} + u_i \bar{v} \bar{w} + \bar{u} v_i \bar{w} - \bar{u} \bar{v} \bar{w}) \right) \\
&= \left( \frac{1}{n} \sum_{i=1}^n u_i v_i w_i \right) - \left( \bar{v} \frac{1}{n} \sum_{i=1}^n u_i w_i \right) - \left( \bar{u} \frac{1}{n} \sum_{i=1}^n v_i w_i \right) + \left( \bar{u} \bar{v} \sum_{i=1}^n \frac{w_i}{n} \right) \\
&\quad - \left( \bar{w} \frac{1}{n} \sum_{i=1}^n u_i v_i \right) + \left( \bar{v} \bar{w} \sum_{i=1}^n \frac{u_i}{n} \right) + \left( \bar{u} \bar{w} \sum_{i=1}^n \frac{v_i}{n} \right) - (\bar{u} \bar{v} \bar{w}) \\
\frac{1}{n} \sum_{i=1}^n uvw &= \sum_{i=1}^n \frac{u_i v_i w_i}{n} \quad ; \quad \bar{v} \frac{1}{n} \sum_{i=1}^n u_i w_i = \bar{v} \sum_{i=1}^n \frac{u_i w_i}{n} \\
\bar{u} \frac{1}{n} \sum_{i=1}^n v_i w_i &= \bar{u} \sum_{i=1}^n \frac{v_i w_i}{n} \quad ; \quad \bar{u} \bar{v} \sum_{i=1}^n \frac{w_i}{n} = \bar{u} \bar{v} \bar{w} \quad ; \quad \bar{w} \frac{1}{n} \sum_{i=1}^n u_i v_i = \bar{w} \sum_{i=1}^n \frac{u_i v_i}{n} \\
\bar{v} \bar{w} \sum_{i=1}^n \frac{u_i}{n} &= \bar{v} \bar{w} \bar{u} \quad ; \quad \bar{u} \bar{w} \sum_{i=1}^n \frac{v_i}{n} = \bar{u} \bar{w} \bar{v} \\
&= \sum_{i=1}^n \frac{u_i v_i w_i}{n} - \bar{v} \sum_{i=1}^n \frac{u_i w_i}{n} - \bar{u} \sum_{i=1}^n \frac{v_i w_i}{n} + \bar{u} \bar{v} \bar{w} - \bar{w} \sum_{i=1}^n \frac{u_i v_i}{n} + \bar{v} \bar{w} \bar{u} + \bar{u} \bar{w} \bar{v} - \bar{u} \bar{v} \bar{w} \\
&= \sum_{i=1}^n \frac{u_i v_i w_i}{n} - \bar{v} \sum_{i=1}^n \frac{u_i w_i}{n} - \bar{u} \sum_{i=1}^n \frac{v_i w_i}{n} + 2(\bar{u} \bar{v} \bar{w}) - \bar{w} \sum_{i=1}^n \frac{u_i v_i}{n}
\end{aligned}$$

Similarly,

$$\begin{aligned}
\overline{uuv} &= \frac{1}{n} \left( \sum_{i=1}^n (u_i - \bar{u})^2 (v_i - \bar{v}) \right) \\
&= \frac{1}{n} \left( \sum_{i=1}^n (u_i^2 u_i - 2u_i \bar{u} + \bar{u} \bar{u})(v_i - \bar{v}) \right) \\
&= \frac{1}{n} \left( \sum_{i=1}^n (u_i^2 v_i - u_i^2 \bar{v} - 2u_i \bar{u} v_i + 2u_i \bar{u} \bar{v} + \bar{u} \bar{u} v_i - \bar{u} \bar{u} \bar{v}) \right) \\
&= \sum_{i=1}^n \frac{u_i^2 v_i}{n} - \bar{v} \sum_{i=1}^n \frac{u_i^2}{n} - 2\bar{u} \sum_{i=1}^n \frac{u_i v_i}{n} + 2(\bar{u} \bar{u} \bar{v})
\end{aligned}$$

Similarly;

$$\overline{u u w} = \sum_{i=1}^n \frac{U_i U_i W_i}{n} - \bar{W} \sum_{i=1}^n \frac{U_i U_i}{n} - 2\bar{U} \sum_{i=1}^n \frac{U_i W_i}{n} + 2(\overline{U U W})$$

$$\overline{u v v} = \sum_{i=1}^n \frac{U_i V_i V_i}{n} - \bar{U} \sum_{i=1}^n \frac{V_i V_i}{n} - 2\bar{V} \sum_{i=1}^n \frac{U_i V_i}{n} + 2(\overline{U V V})$$

$$\overline{v v w} = \sum_{i=1}^n \frac{V_i V_i W_i}{n} - \bar{W} \sum_{i=1}^n \frac{V_i V_i}{n} - 2\bar{V} \sum_{i=1}^n \frac{V_i W_i}{n} + 2(\overline{V V W})$$

$$\overline{u w w} = \sum_{i=1}^n \frac{U_i W_i W_i}{n} - \bar{U} \sum_{i=1}^n \frac{W_i W_i}{n} - 2\bar{W} \sum_{i=1}^n \frac{U_i W_i}{n} + 2(\overline{U W W})$$

$$\overline{v w w} = \sum_{i=1}^n \frac{V_i W_i W_i}{n} - \bar{V} \sum_{i=1}^n \frac{W_i W_i}{n} - 2\bar{W} \sum_{i=1}^n \frac{V_i W_i}{n} + 2(\overline{V W W})$$

$$\overline{u u u} = U_{\sigma}^3$$

$$\overline{v v v} = V_{\sigma}^3$$

$$\overline{w w w} = W_{\sigma}^3$$

3rd Moment (also Skewness);  $\sum_{i=1}^n \frac{U_i^3}{n} - 3\bar{U} \sum_{i=1}^n \frac{U_i U_i}{n} + 2\bar{U}^3$   
 Skewness Coefficient;  $\frac{\text{3rd Moment}}{2\sigma_u^3}$

4th Moment (also Flatness);  $\sum_{i=1}^n \frac{U_i^4}{n} - 4\bar{U} \sum_{i=1}^n \frac{U_i^3}{n} + 6\bar{U}^2 \sum_{i=1}^n \frac{U_i^2}{n} - 3\bar{U}^4$

Flatness Coefficient (Kurtosis);  $\frac{\text{4th Moment}}{\sigma_u^4}$

APPENDIX C.  
FORTRAN LISTING FOR LDV DATA REDUCTION

The following FORTRAN program was written to allow the proper reduction of the LDV data. The program allows for the correction in any angle discrepancies that may be present in a nearly orthogonal laser system. Point-by-point normalization of the data is also possible. The program takes up to two input files in addition to the raw data files produced by the data acquisition program. These files are:

- family.PRN – Header file containing reference conditions for each point. The data must be ordered to match the numerical order of the raw data file.
- master – Optional file that contains all input data to the program such as the family name, number of files to reduce, and correction angles. This allows many files of different families to be reduced in a batch mode. If the file does not exist, the user is prompted for each input.

A sample header file is presented in Table C-1 and is self explanatory. The only value actually used by the program is the reference velocity. The coordinates are not cross-matched to the raw data file. Therefore, the entries in the header file must correspond consecutively with data file 00, 01, 02, etc. Even if the data files do not start with 00, the header file must start with an entry for 00.

Two sets of angles are input to the program. The first set is the correction angles to produce an orthogonal system between the blue and green beams (Figure C-1). The included angle between the beams should always be  $90^\circ + \theta_b - \theta_g$ . Therefore, there is an infinite number of correct combinations of  $\theta_b$  and  $\theta_g$  for a given configuration.

The second set of angles is the rotation and tilt of the LDV system. Rotation ( $\delta$ ) is defined as angle between the green/blue beams and the reference axes (Figure C-2). The tilt ( $\epsilon$ ) is defined as the rotation of the entire LDV system about the x-axis (Figure C-3).

For a typical case,  $\theta_g = 0$ ,  $\theta_b = \text{included angle} - 90$ ,

$$\begin{aligned}\delta &= \text{angle between the green beams and the tunnel x-axis} \\ \epsilon &= 0\end{aligned}$$

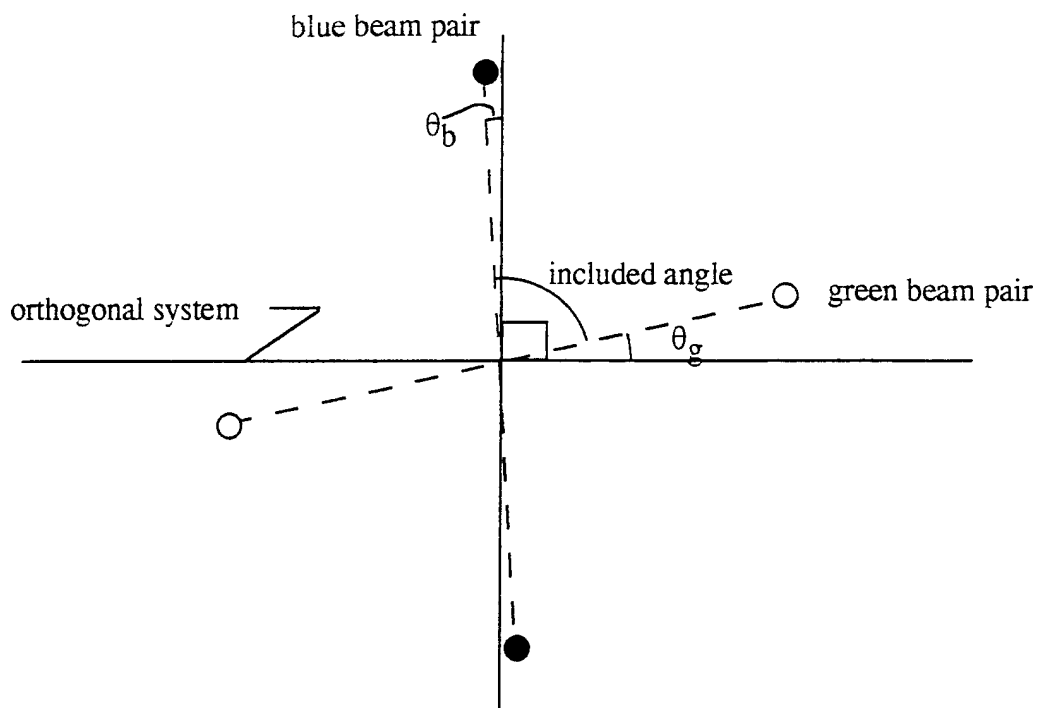


Figure C-1. Definition of Correction Angles ( $\theta_g, \theta_b$ )

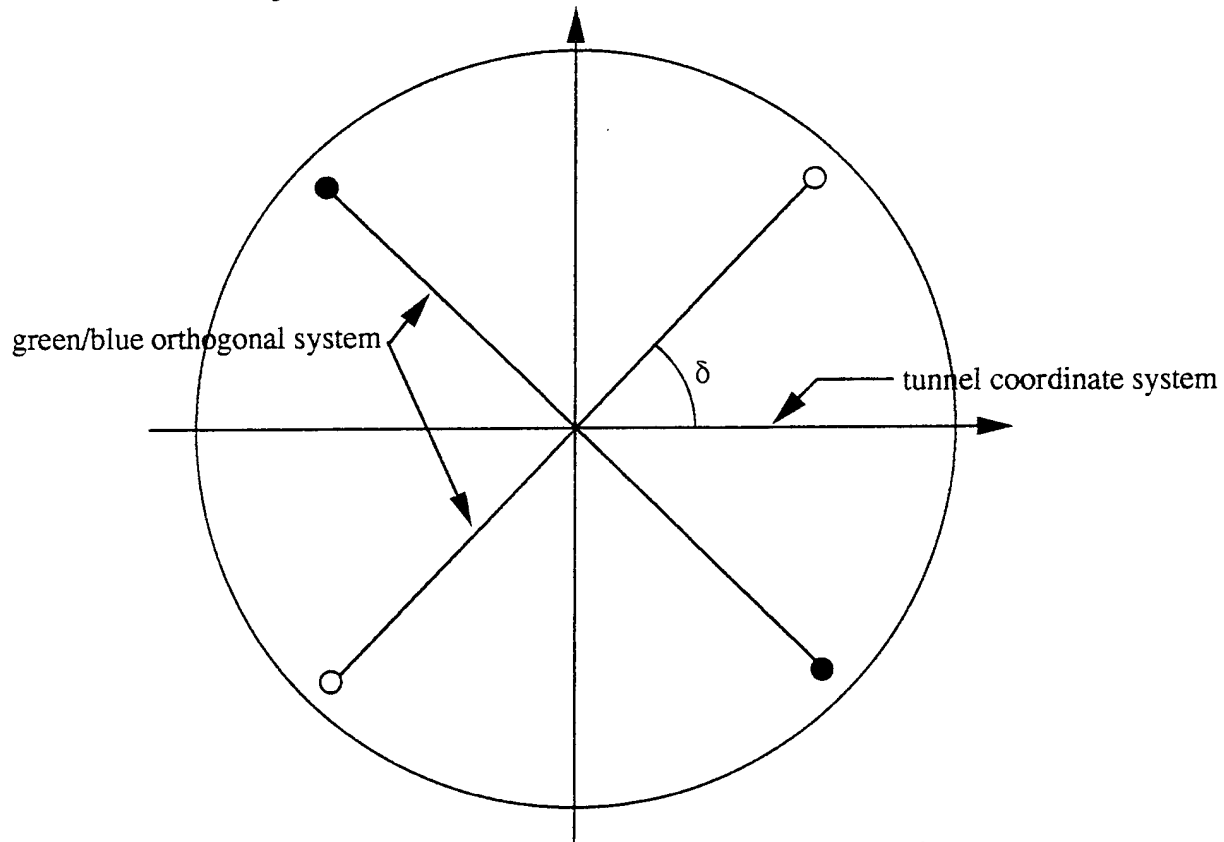


Figure C-2. Definition of Rotation Angle ( $\delta$ )

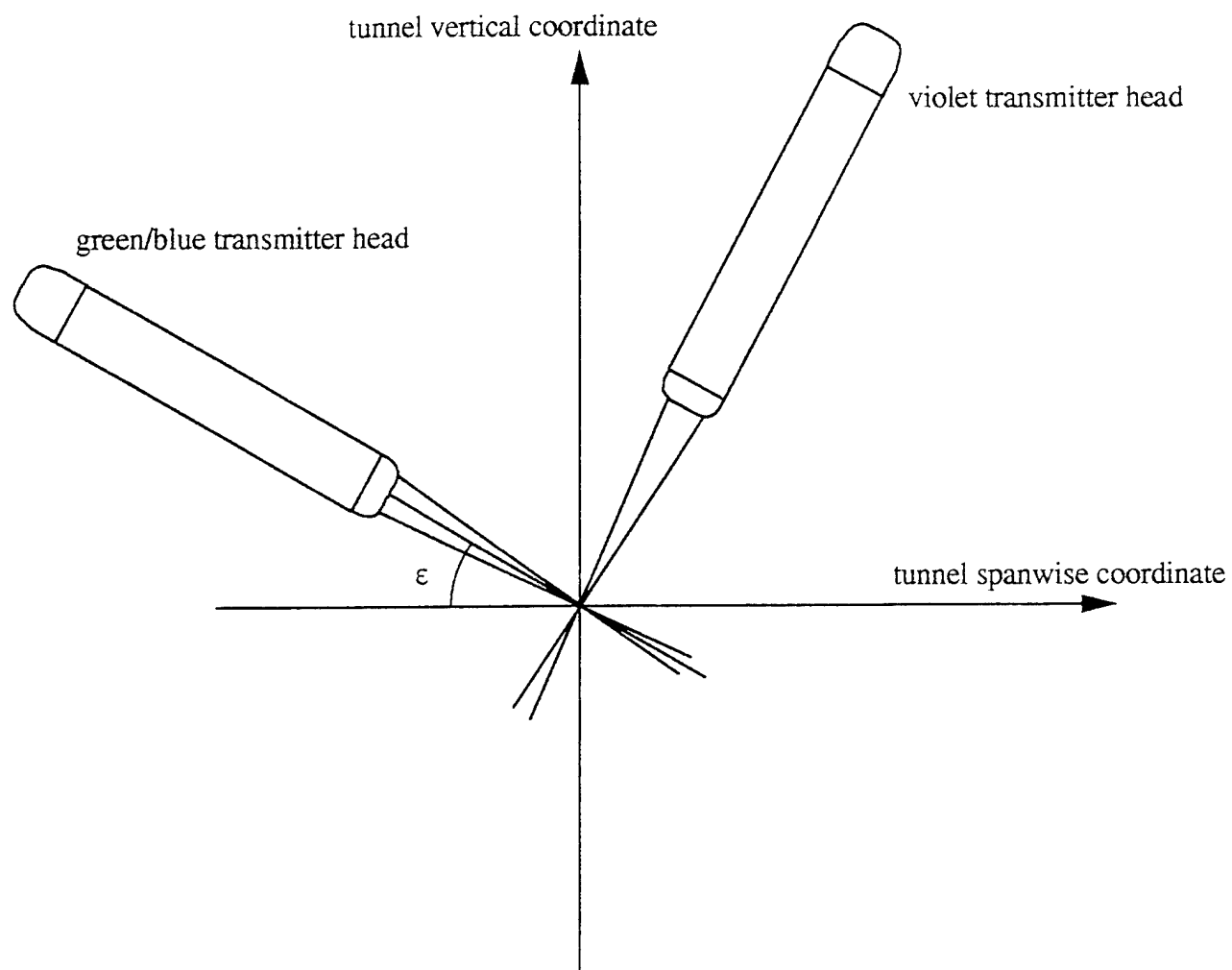


Figure C-3. Definition of Tilt Angle ( $\epsilon$ )

```

c  program name is:round5.for
c  date: 5/31/94
c  program does data reduction for as many files in master
c  program prints raw velocity data with header (.y**)
c  it calculates statistics from raw velocity data (.sta)
c  correlation coefficients, 3rd & 4th moments,
c  skewness & flatness coefficients (.mis)
c  it makes proplot files which are quantities normalized
c  (.pl1): velocities, sigmas & turbulent stresses
c  (.pl2): triple products
c  (.pl3): normal stresses such as uu,vv,ww,uuu,vvv,www
c  execute program from tsi\data
c  header is in tsi\data
implicit double precision (a-h,o-z)
character*80 master,angl,answer
character*80 filer,family,familyn
integer first,last,npts,nsig
logical inter
integer*2 proc2,proc3
  real*8 mom3u(50),mom3v(50),mom3w(50),mom4u(50),mom4v(50),
&mom4w(50),vel(12000,3),tbd(12000)
integer head,raw,yfile,sta,mis,pl1,pl2,pl3
  common/stat/Uiu,Viu,Wiu,Ui2,Vi2,Wi2,UiVi,
  &UiWi,ViWi,UiViWi,UiUiWi,ViViWi,UiViVi,UiUiVi,UiWiWi,ViWiWi,
  &Ui3,Vi3,Wi3,Ui4,Vi4,Wi4,tt,ncount
common/unit/yfile,ista,imis,ipl1,ipl2,ipl3,iyfile
common/angle/anglu,anglv,anglw
dimension h1(50),h2(50),h3(50),h4(50),h5(50),h6(50),h7(50)
dimension ubar(50),vbar(50),wbar(50),uv(50),uw(50),vw(50)
dimension usig(50),vsig(50),wsig(50)
dimension uvw(50),uuw(50),uuv(50),uww(50),uvv(50),
&vvw(50),vww(50)
dimension cocouv(50),cocouw(50),cocovw(50)
dimension flatu(50),flatv(50),flatw(50)
dimension skewu(50),skewv(50),skeww(50)
common/stat2/h4,h5,h6,h7,ubar,vbar,wbar,usig,vsig,wsig,
  &uv,uw,vw,uvw,uuw,uuv,uww,uvv,vvw,vww,cocouv,cocouw,
  &cocovw,flatu,flatv,flatw,skewu,skewv,skeww,
  &mom3u,mom3v,mom3w,mom4u,mom4v,mom4w
mas=05
head=10
raw = 15
yfile=11
sta=21

```



```

mis=41
pl1=51
pl2=52
pl3=53
22 print*, 'please enter master name:(c/r for interactive) '
   read(*,24)master
   if (master.eq.' ')then
   inter=.true.
   else
   inter=.false.
   call opener(mas, master, ' ', 'old ', ierr)
   endif
   if(ierr.ne.0)goto 22
c   OPEN(99,FILE='JUNK\JUNK3.DAT')
   do 296 nm=1,100
   if(inter)print*, 'please enter family name (c/r to end): '
   read(mas,24) family
   if(family.eq.' ')stop
   if(inter)print*, 'please enter first file #: '
   read(mas,*)first
   if(inter)print*, 'please enter last file # (.a. for all): '
   read(mas,24)answer
   if(answer.eq.'a')then
   last=100000
   else
   read(answer,*)last
   endif
   if(inter)PRINT*,
   & 'please enter new family name (c/r for old name): '
   read (mas,24) familyn
24 format (3a)
   if (familyn.eq.' ') familyn=family
   if(inter)print*, 'please enter # of standard of deviations: '
   read(mas,*)nsig
c
   anglu=0.
   anglv=0.
   anglw=0.
   if(inter)print*,
   & 'please enter correction angles:(c/r for:0,0,0) '
   read(mas,24)angl
   if (angl.eq.' ')goto 25
   read(angl,*)anglu,anglv,anglw
25 pi=acos(-1.)

```

```

    anglu=anglu*pi/180.
    anglv=(anglv+90)*pi/180.
    anglw=anglw*pi/180.
    nfiles=last-first+1
c   '.prn' is the header file
    call opener(head,family,'.prn','old',ierr)
    if(ierr.ne.0)stop
    read(head,*)
    read(head,*)
    read(head,*)
    read(head,*)
    do 29 i=1,first
    read(head,*)
29  continue
c   this section reads & prints all in one row in "e-format"
    if(inter)print*,
    &'please enter (y) if you want .sta files:(c/r for none)'
    read(mas,24)answer
    if(answer.ne.'y') goto 77
    ista=1
    call opener(sta,familyn,'.sta','unknown',ierr)
    if (ierr.ne.0) stop
    write(sta,42) 'X','Y','Z','Ts','Ps','Dp','Uref','U/Uref',
    &'V/Uref','W/Uref','Usig/Uref','Vsig/Uref','Wsig/Uref',
    &'UV/Uref^2','UW/Uref^2','VW/Uref^2','UU/Uref^2','VV/Uref^2',
    &'WW/Uref^2','UVW/Uref^3','UUV/Uref^3','UUW/Uref^3','VVU/Uref^3',
    &'VWV/Uref^3','WWU/Uref^3','WWV/Uref^3','UUU/Uref^3',
    &'VVV/Uref^3','WWW/Uref^3','UV-CORR','UW-CORR','VW-CORR',
    &'U-3rd','V-3rd','W-3rd','U-Skew','V-Skew','W-Skew',
    &'U-4th','V-4th','W-4th','U-Flat','V-Flat','W-Flat'
42  format(1X,A3,4X,A3,3X,A3,2X,A3,4X,A3,2X,A3,7X,A5,8X,a6,
    &9x,a6,8x,a6,5x,a9,2(5X,A9),2(5x,a9),2(5X,A9),2(5x,a9),
    &5x,a10,6(4X,A10),4x,a10,4x,a10,4x,a10,
    &6X,A7,6x,A7,7x,a7,9x,a5,9x,a5,10X,A5,
    &7X,A6,8X,A6,8X,A6,3(9x,a5),
    &9X,A6,7x,a6,8x,a6)
    write(sta,53) 'in','in','in','R','psi','in-H2O','m/s',
    &'COEF','COEF','COEF','MOM','MOM','MOM','COEF','COEF',
    &'COEF','MOM','MOM','MOM','COEF','COEF','COEF'
53  format(1X,A3,4X,A3,3X,A3,3X,A2,3X,A4,1X,A6,6X,A3,
    &100x,100x,118x,a4,9x,a4,10x,a4,12x,a3,11x,a3,12x,a3,9x,a4,
    &2(10x,a4),3(10x,a4),11x,a4,9x,a4,10x,a4)
77  if(inter)print*,
    &'please enter (y) if you want .mis files:(c/r for none)'

```

```

read(mas,24)answer
if(answer.ne.'y') goto 96
imis=1
c   this section prints corr. coeff., moments, & misc.
    call opener(mis,familyn,'.mis','unknown',ierr)
if (ierr.ne.0) stop
write(mis,*)
write(mis,*)
write(mis,*)
write(mis,*)
    write(mis,89) 'X','Y','Z','Ts','Ps','Dp','Uref','CoUV',
        &'CoUW','CoVW','3rd','3rd','3rd','SkewU','SkewV',
        &'SkewW','4th','4th','4th','FlatU','FlatV','FlatW'
89 format(1X,A3,4X,A3,3X,A3,3X,A2,2X,A4,1X,A4,3X,A5,
    &4x,a4,4x,a4,4x,a4,6X,A3,6X,A3,6X,A3,5x,a5,4x,a5,4x,
    &a5,6X,A3,7X,A3,7X,A3,4X,A5,3X,A5,3X,A5)
    write(mis,95) 'in','in','in','R','psi','in-H2O',
        &'m/s','Coef','Coef','Coef','MomU','MomV','MomW','Coef',
        &'Coef','Coef','MomU','MomV','MomW','Coef','Coef','Coef'
95 format(1X,A3,4X,A3,3X,A3,3X,A2,2X,A4,1X,A6,2X,A3,
    &5x,a4,4x,a4,4x,a4,6X,A4,5X,A4,5X,A4,5x,a4,5x,a4,5x,a4,
    &6X,A4,6X,A4,6X,A4,3x,a4,4x,a4,4x,a4)
96 if(inter)print*,
    &'please enter (y) if you want .pl1 files:(c/r for none)'
    read(mas,24)answer
    if(answer.ne.'y') goto 99
    ipl1=1
c   this section prints the proplot (.pl1) files
    call opener(pl1,familyn,'.pl1','unknown',ierr)
if (ierr.ne.0) stop
    write(pl1,98) 'X','Y','Z','U/Uref','V/Uref','W/Uref',
        &'Usig/Uref','Vsig/Uref','Wsig/Uref','UV/Uref^2',
        &'UW/Uref^2','VW/Uref^2'
98 format(1X,A3,4X,A3,3X,A3,3(6X,a6),3(4X,A9),3(4X,A9))
c   this section prints the proplot (.pl2) files
99 if(inter)print*,
    &'please enter (y) if you want .pl2 files:(c/r for none)'
    read(mas,24)answer
    if(answer.ne.'y') goto 110
    ipl2=1
    call opener(pl2,familyn,'.pl2','unknown',ierr)
if (ierr.ne.0) stop
    write(pl2,100) 'X','Y','Z','UVW/Uref^3','UUV/Uref^3',
        &'U UW/Uref^3','V VU/Uref^3','V VW/Uref^3','W WU/Uref^3',

```

```

      &'WWV/Uref^3'
100 format(1X,A3,4X,A3,3X,A3,7(4X,a10))
c   this section prints the proplot (.pl3) files
110 if(inter)print*,
      &'please enter (y) if you want .pl3 files:(c/r for none)'
      read(mas,24)answer
      if(answer.ne.'y') goto 108
      ipl3=1
      call opener(pl3,familyn,'.pl3','unknown',ierr)
      if (ierr.ne.0) stop
      write(pl3,133) 'X','Y','Z','UU/Uref^2','VV/Vref^2',
      &'WW/Wref^2','UUU/Uref^3','VVV/Uref^3','WWW/Uref^3'
133 format(1X,A3,4X,A3,3X,A3,6(4X,a10))
c   this section prints the (.y**) files
108 if(inter)print*,
      &'please enter (y) if you want .y** files:(c/r for none)'
      read(mas,24)answer
      if(answer.ne.'y') goto 111
      iyfile=1

111 do 256 n=1,nfiles
      call rdfhdr(raw,family,first,n,npts,vel,tbd,proc2,proc3,del,eps)
      read(head,*,end=257) H1(n),H2(n),H3(n),H4(n),H5(n),H6(n),H7(n)
      if(iyfile.ne.1)goto 125
      write(filer,109)first+n-1
      if(first+n-1.ge.10)write(filer,112)first+n-1
      call opener(yfile,familyn,filer,'unknown',ierr)
      if (ierr.ne.0) stop
109 format('.y0',i1)
112 format('.y',i2)
      write(yfile,118) 'X(in)','Y(in)','Z(in)','Ts(R)','Ps(psi)',
      &'Dp(in-H2O)','Uref(m/s)'
118 format(5X,A7,5X,A7,4X,A7,4X,A7,4X,A8,4X,A11,4X,A11)
      write(yfile,120)h1(n),h2(n),h3(n),h4(n),h5(n),h6(n),h7(n)
120 format(6X,F5.2,7X,F5.2,6X,F5.2,7X,F5.1,4X,F8.4,8X,F4.2,9X,F8.5)
      write(yfile,*)
      write(yfile,124) 'Ni','Ui(m/s)','Vi(m/s)','Wi(m/s)','TBD(s)',
      &'TT(s)'
124 format(3X,A5,8X,A8,6X,A8,6X,A8,10X,A8,10X,A8)
125 stdu=1E28
      stdv=1E28
      stdw=1E28
      ubar(n)=0
      vbar(n)=0

```

```

wbar(n)=0
ksig=2
if(nsig.eq.0) then
ksig=1
endif
iysave=iyfile
do 236 isig=1,ksig
iyfile=iysave+isig-ksig
call statsum(vel,tbd,stdu,stdv,stdw,proc2,proc3,npts,n)
print*,ncount
Ubar(n)=Uiu/ncount
Vbar(n)=Viu/ncount
Wbar(n)=Wiu/ncount
UV(n)=UiVi/ncount-Ubar(n)*Vbar(n)
UW(n)=UiWi/ncount-Ubar(n)*Wbar(n)
VW(n)=ViWi/ncount-Vbar(n)*Wbar(n)
Usig(n)=sqrt(Ui2/ncount-Ubar(n)*Ubar(n))
Vsig(n)=sqrt(abs(Vi2/ncount-Vbar(n)*Vbar(n)))+(1-proc2)
Wsig(n)=sqrt(abs(Wi2/ncount-Wbar(n)*Wbar(n)))+(1-proc3)
STDU=NSIG*USIG(n)
STDV=NSIG*VSIG(n)
STDW=NSIG*WSIG(n)
236 continue
if(ista+ipl2.ge.1)then
UVW(n)=UiViWi/ncount+2*Ubar(n)*Vbar(n)*Wbar(n)-Vbar(n)*
&UiWi/ncount-Ubar(n)*ViWi/ncount-Wbar(n)*UiVi/ncount
UUV(n)=UiUiVi/ncount+2*Ubar(n)*Ubar(n)*Vbar(n)-Vbar(n)*
&Ui2/ncount-2*Ubar(n)*UiVi/ncount
U UW(n)=UiUiWi/ncount+2*Ubar(n)*Ubar(n)*Wbar(n)-Wbar(n)*
&Ui2/ncount-2*Ubar(n)*UiWi/ncount
UVV(n)=UiViVi/ncount+2*Ubar(n)*Vbar(n)*Vbar(n)-Ubar(n)*
&Vi2/ncount-2*Vbar(n)*UiVi/ncount
V VW(n)=ViViWi/ncount+2*Vbar(n)*Vbar(n)*Wbar(n)-Wbar(n)*
&Vi2/ncount-2*Vbar(n)*ViWi/ncount
U WW(n)=UiWiWi/ncount+2*Ubar(n)*Wbar(n)*Wbar(n)-Ubar(n)*
&Wi2/ncount-2*Wbar(n)*UiWi/ncount
V WW(n)=ViWiWi/ncount+2*Vbar(n)*Wbar(n)*Wbar(n)-Vbar(n)*
&Wi2/ncount-2*Wbar(n)*ViWi/ncount
endif
if(ista+imis.ge.1)then
MOM3U(n)=Ui3/ncount-3*Ui2/ncount*Ubar(n)+2*Ubar(n)**3
MOM3V(n)=Vi3/ncount-3*Vi2/ncount*Vbar(n)+2*Vbar(n)**3
MOM3W(n)=Wi3/ncount-3*Wi2/ncount*Wbar(n)+2*Wbar(n)**3
SKEWU(n)=MOM3U(n)/(2*Usig(n)**3)

```

```

SKEWV(n)=MOM3V(n)/(2*Vsig(n)**3)
SKEWW(n)=MOM3W(n)/(2*Wsig(n)**3)
MOM4U(n)=Ui4/ncount-4*Ui3/ncount*Ubar(n)+6*Ubar(n)**2*
&Ui2/ncount-3*Ubar(n)**4
MOM4V(n)=Vi4/ncount-4*Vi3/ncount*Vbar(n)+6*Vbar(n)**2*
&Vi2/ncount-3*Vbar(n)**4
MOM4W(n)=Wi4/ncount-4*Wi3/ncount*Wbar(n)+6*Wbar(n)**2*
&Wi2/ncount-3*Wbar(n)**4
FLATU(n)=MOM4U(n)/USIG(n)**4
FLATV(n)=MOM4V(n)/VSIG(n)**4
FLATW(n)=MOM4W(n)/WSIG(n)**4
COCOUV(n)=UV(n)/(Usig(n)*Vsig(n))
COCO UW(n)=UW(n)/(Usig(n)*Wsig(n))
COCOVW(n)=VW(n)/(Vsig(n)*Wsig(n))
endif
256 continue

257 nfiles=n-1
if(h1(1).ne.h1(2)) then
  call sort(h1,h2,h3,nfiles)
else if(h2(1).ne.h2(2)) then
  call sort(h2,h1,h3,nfiles)
else
  call sort(h3,h1,h2,nfiles)
endif

c  this section prints all
do 260 n=1,nfiles
if (ista.ne.1)goto 243
write (sta,241) h1(n),h2(n),h3(n),h4(n),h5(n),h6(n),h7(n),
&ubar(n)/h7(n),vbar(n)/h7(n),wbar(n)/h7(n),usig(n)/h7(n),
&vsig(n)/h7(n),wsig(n)/h7(n),uv(n)/h7(n)**2,uw(n)/h7(n)**2,
&vw(n)/h7(n)**2,usig(n)**2/h7(n)**2,vsig(n)**2/h7(n)**2,
&wsig(n)**2/h7(n)**2,uvw(n)/h7(n)**3,uuv(n)/h7(n)**3,
&uuw(n)/h7(n)**3,uvv(n)/h7(n)**3,vvw(n)/h7(n)**3,uww(n)/h7(n)**3,
&vww(n)/h7(n)**3,usig(n)**3/h7(n)**3,
&vsig(n)**3/h7(n)**3,wsig(n)**3/h7(n)**3,cocouv(n),cocouw(n),
&cocovw(n),mom3u(n),mom3v(n),mom3w(n),skewu(n),skewv(n),skeww(n),
&mom4u(n),mom4v(n),mom4w(n),flatu(n),flatv(n),flatw(n)
241 format(1x,f5.2,1x,f5.2,1x,f5.2,1x,f5.1,1x,f5.2,1x,f4.2,
&4(1x,e13.6),3(1x,e13.6),3(1x,e13.6),7(1x,e13.6),
&21(1x,e13.6))

c  this section prints moments and miscellaneous(.mis)
243 if(imis.ne.1)goto 244

```

```

        write (mis,249) h1(n),h2(n),h3(n),h4(n),h5(n),h6(n),h7(n),
        &cocouv(n),cocouw(n),cocovw(n),
        &mom3u(n),mom3v(n),mom3w(n),skewu(n),skewv(n),skeww(n),mom4u(n),
        &mom4v(n),mom4w(n),flatu(n),flatv(n),flatw(n)
249 format(1x,f5.2,1x,f5.2,1x,f5.2,2x,i3,1x,f5.2,1x,f4.2,
        &4(1x,f7.4),3(1x,f8.2),3(1x,f8.3),3(1x,f9.2),3(1x,f7.3))
c    this section prints proplot (.pl1)
244 if(ipl1.ne.1)goto 245
        write (pl1,250) h1(n),h2(n),h3(n),ubar(n)/h7(n),vbar(n)/h7(n),
        &wbar(n)/h7(n),usig(n)/h7(n),
        &vsig(n)/h7(n),wsig(n)/h7(n),uv(n)/(h7(n)*h7(n)),uw(n)/(h7(n)*
        &h7(n)),vw(n)/(h7(n)*h7(n))
250 format(1x,f5.2,1x,f5.2,1x,f5.2,3(1x,e11.4),3(1x,e12.5),
        &3(1x,e12.5))
c    this section prints proplot (.pl2)
245 if(ipl2.ne.1) goto 246
        write (pl2,251) h1(n),h2(n),h3(n),uvw(n)/h7(n)**3,uuv(n)/h7(n)**3,
        &uuw(n)/h7(n)**3,
        &uuv(n)/h7(n)**3,vvw(n)/h7(n)**3,uww(n)/h7(n)**3,vww(n)/h7(n)**3
251 format(1x,f5.2,1x,f5.2,1x,f5.2,7(1x,e13.6))
c    this section prints proplot (.pl3)
246 if(ipl3.ne.1)goto 260
        write (pl3,252) h1(n),h2(n),h3(n),usig(n)**2/h7(n)**2,
        &vsig(n)**2/h7(n)**2,
        &wsig(n)**2/h7(n)**2,usig(n)**3/h7(n)**3,vsig(n)**3/h7(n)**3,
        &wsig(n)**3/h7(n)**3
252 format(1x,f5.2,1x,f5.2,1x,f5.2,6(1x,e13.6))
260 continue
296 continue
stop
end

```

```

subroutine sort(x,y,z,npts)
implicit double precision (a-h,o-z)
dimension x(*),y(*),z(*)
dimension h4(50),h5(50),h6(50),h7(50)
dimension ubar(50),vbar(50),wbar(50)
dimension usig(50),vsig(50),wsig(50),uv(50),uw(50),vw(50)
dimension uvw(50),uuw(50),uuv(50),uww(50),uuv(50),
&vvw(50),vww(50)
dimension cocouv(50),cocouw(50),cocovw(50)
dimension flatu(50),flatv(50),flatw(50)
dimension skewu(50),skewv(50),skeww(50)
real*8 mom3u(50),mom3v(50),mom3w(50),mom4u(50),mom4v(50),

```

```

&mom4w(50)
common/stat2/h4,h5,h6,h7,ubar,vbar,wbar,usig,vsig,wsig,
&uv,uw,vw,uvw,uuw,uuv,uww,uvv,vvw,vww,cocouv,cocouw,
&cocovw,flatu,flatv,flatw,skewu,skewv,skeww,
&mom3u,mom3v,mom3w,mom4u,mom4v,mom4w
do 10 i=1,npts-1
  do 10 j=i+1,npts
    if (x(j).lt.x(i))then
      temp=x(i)
      x(i)=x(j)
      x(j)=temp
      temp=y(i)
      y(i)=y(j)
      y(j)=temp
      temp=z(i)
      z(i)=z(j)
      z(j)=temp
      temp=h4(i)
      h4(i)=h4(j)
      h4(j)=temp
      temp=h5(i)
      h5(i)=h5(j)
      h5(j)=temp
      temp=h6(i)
      h6(i)=h6(j)
      h6(j)=temp
      temp=h7(i)
      h7(i)=h7(j)
      h7(j)=temp
      temp=ubar(i)
      ubar(i)=ubar(j)
      ubar(j)=temp
      temp=vbar(i)
      vbar(i)=vbar(j)
      vbar(j)=temp
      temp=wbar(i)
      wbar(i)=wbar(j)
      wbar(j)=temp
      temp=usig(i)
      usig(i)=usig(j)
      usig(j)=temp
      temp=vsig(i)
      vsig(i)=vsig(j)
      vsig(j)=temp

```



```

temp=wsig(i)
wsig(i)=wsig(j)
wsig(j)=temp
temp=uv(i)
uv(i)=uv(j)
uv(j)=temp
temp=uw(i)
uw(i)=uw(j)
uw(j)=temp
temp=vw(i)
vw(i)=vw(j)
vw(j)=temp
temp=uvw(i)
uvw(i)=uvw(j)
uvw(j)=temp
temp=uuv(i)
uuv(i)=uuv(j)
uuv(j)=temp
temp=uuw(i)
uuw(i)=uuw(j)
uuw(j)=temp
temp=uvv(i)
uvv(i)=uvv(j)
uvv(j)=temp
temp=vvw(i)
vvw(i)=vvw(j)
vvw(j)=temp
temp=uww(i)
uww(i)=uww(j)
uww(j)=temp
temp=vww(i)
vww(i)=vww(j)
vww(j)=temp
temp=cocouv(i)
cocouv(i)=cocouv(j)
cocouv(j)=temp
temp=cocouw(i)
cocouw(i)=cocouw(j)
cocouw(j)=temp
temp=cocovw(i)
cocovw(i)=cocovw(j)
cocovw(j)=temp
temp=mom3u(i)
mom3u(i)=mom3u(j)

```

```

        mom3u(j)=temp
        temp=mom3v(i)
        mom3v(i)=mom3v(j)
        mom3v(j)=temp
        temp=mom3w(i)
        mom3w(i)=mom3w(j)
        mom3w(j)=temp
        temp=skewu(i)
        skewu(i)=skewu(j)
        skewu(j)=temp
        temp=skewv(i)
        skewv(i)=skewv(j)
        skewv(j)=temp
        temp=skeww(i)
        skeww(i)=skeww(j)
        skeww(j)=temp
        temp=mom4u(i)
        mom4u(i)=mom4u(j)
        mom4u(j)=temp
        temp=mom4v(i)
        mom4v(i)=mom4v(j)
        mom4v(j)=temp
        temp=mom4w(i)
        mom4w(i)=mom4w(j)
        mom4w(j)=temp
        temp=flatu(i)
        flatu(i)=flatu(j)
        flatu(j)=temp
        temp=flatv(i)
        flatv(i)=flatv(j)
        flatv(j)=temp
        temp=flatw(i)
        flatw(i)=flatw(j)
        flatw(j)=temp
    endif
10 continue
    return
end

```

```

c  subroutine rdfhdr
c  parameters: unit: in - unit number to read file data
c  description: the following reads the file header for a raw
c  or statistics file

```

```

      subroutine rdfhdr(unit,family,first,nfile,totpts,vel,tbd,
&      proc2,proc3,del,eps)
      implicit integer*2 (a-z)
      character*20 drparr(153)
      character*80 filer,family
      character*4 ext
      real*8 fshift(3),df(3),vel(12000,3),tbd(12000),fd,del,eps,
      &anglu,anglv,anglw,pi,sinu,sinv,cosu,cosv,cosw,sinuv,sinvu,
&cosdel,coseps,sindel,sineps,ux,uy,uz,u,v,w
      dimension hword(4),buffer(1000)
      common/angle/anglu,anglv,anglw
      integer*4 temp1,temp2,hword4(2),tottim
      data hword/ 'Z'00FF','Z'0300','Z'4000','Z'0FFF' / ,tottim/0/
      data hword4 / 'Z'FFFFFFF', 'Z'0000FFFF' /
      write(ext,109)first+nfile-1
      if(first+nfile-1.ge.10)write(ext,112)first+nfile-1
109  format('.r0',i1)
112  format('.r',i2)
      call opener(unit,family,ext,'old' ,ierr)
      if (ierr.ne.0)return
      l=length(family)
      write(filer,10)family(1:l),ext
10  format(2a)
      write(*,*)'processing file ',filer
      do 100 i=1,5
        read(unit,399)drparr(i)
100  continue
c      read header
      do 150 i=6,91
        read(unit,399) drparr(i)
150  continue
c      read the dummy
c      information
      do 200 i=92,152
        read(unit,399) drparr(i)
200  continue
      read(unit,499) drparr(153)
c
      close(unit)
      read(drparr(7), 599) totadd
      read(drparr(8),599) tbdflag
      read(drparr(10),599) nkpts
      read(drparr(24),699) df(1)
      read(drparr(25),699) df(2)

```

```

read(drparr(26),699) df(3)
read(drparr(28),699) fshift(1)
read(drparr(29),699) fshift(2)
read(drparr(30),699) fshift(3)
read(drparr(74),799) ttime,proc2,proc3
read(drparr(143),699)del
read(drparr(144),699)eps
totword=totadd*(2+ttime)
proc2=0
proc3=0
if(totadd.eq.2)then
  proc2=1
  proc3=0
else if (totadd.eq.3)then
  proc2=1
  proc3=1
end if
if (tbdflag .ge. 1) totword = totword+2
  open(unit,file=filer,access='direct',recl=840)
  nrec=nkpts*1024*totword/420
  nlast=nkpts*1024*totword-nrec*420
pi=acos(-1.)
sinu=sin(anglu)
sinv=sin(anglv)
cosu=cos(anglu)
cosv=cos(anglv)
cosw=cos(anglw)
sinuv=sin(anglu-nglv)
sinvu=sin(anglv-nglu)
del=del*pi/180.
eps=eps*pi/180.
cosdel=cos(del)
coseps=cos(eps)
sindel=sin(del)
sineps=sin(eps)
noff=0
totpts=0
do 300 lrec=5,5+nrec
do 280 ioff=1,noff
280  buffer(ioff)=buffer(420+noff2-noff+ioff)
  noff2=noff
  if (lrec.eq.5+nrec)noff2=nlast+noff-420
  read(unit,rec=lrec)(buffer(i),i=noff+1,420+noff2)
  ipt=(420+noff2)/totword

```

```

    noff=(420+noff)-ipts*totword
do 300 jpts=1,ipts
    totpts=totpts+1
do 275 iadd=0,totadd-1
    iword=(jpts-1)*totword+1+iadd*(2+ttime)
    ncount=iand(buffer(iword),hword(1))
    if(ncount.eq.0)then
        totpts=totpts-1
    go to 301
    endif
    nadd=ishft(iand(buffer(iword),hword(2)),-8)+1
    mant=iand(buffer(iword+1),hword(4))
    exp=ishft(buffer(iword+1),-12)
    Fd=ncount/(mant*dble(2.0)**(exp-3)*1e-9)*1e-6
    vel(totpts,nadd)=(Fd-Fshift(nadd))*Df(nadd)
275 continue
    if(tbdflag.gt.0) then
        temp1=buffer(iword+2+ttime)
        temp2=buffer(iword+3+ttime)
        temp1=ishft(temp1,16)+iand(temp2,hword4(2))
        tbd(totpts)=(temp1-tottim)
        tottim=temp1
    endif
300 continue
301 continue
    tbd(1)=0.
do 310 i=1,totpts
    Ux=(vel(i,2)*sinu-vel(i,1)*sinv)/sinuv
    Uy=(vel(i,2)*cosu-vel(i,1)*cosv)/sinvu
    Uz=(vel(i,3)*cosw)
    U=Ux*cosdel-Uy*sindel
    V=Ux*coseps*sindel+Uy*coseps*cosdel-Uz*sineps
    W=Ux*sineps*sindel+Uy*sineps*cosdel+Uz*coseps
    vel(i,1)=U
    vel(i,2)=V
    vel(i,3)=W
310 continue
399 format(a20)
499 format(a14)
599 format(i2)
699 format(g20.0)
799 format(9x,i1,6x,2i1)
    return
end

```

c

```

subroutine opener(unit,root,ext,stat,ierr)
character*80 root,fname
character*7 stat
character*4 ext
integer unit
l=length(root)
write(fname,10)root(1:l),ext
10 format(2a)
open (unit,file=fname,status=stat,iostat=ierr)
if(ierr.eq.0) return
write(*,*)'error opening file:',fname
return
end

function lngth(string)
character*(*) string
do 3 lngth=len(string),1,-1
if(string(lngth:lngth).ne.' ')return
3 continue
return
end

subroutine statsum(vel,tbd,stdu,stdv,stdw,proc2,proc3,npts,n)
integer yfile
implicit double precision (a-h,o-z)
dimension rset(23),vel(12000,3),tbd(12000)
common/stat/Uiu,Viu,Wiu,Ui2,Vi2,Wi2,UiVi,
&UiWi,ViWi,UiViWi,UiUiWi,ViViWi,UiViVi,UiUiVi,UiWiWi,ViWiWi,
&Ui3,Vi3,Wi3,Ui4,Vi4,Wi4,tt,ncount
common /unit/yfile,ista,imis,ipl1,ipl2,ipl3,iyfile
equivalence (rset(1),Uiu)
integer*2 proc2,proc3

dimension h4(50),h5(50),h6(50),h7(50)
dimension ubar(50),vbar(50),wbar(50)
dimension usig(50),vsig(50),wsig(50),uv(50),uw(50),vw(50)
dimension uvw(50),uuw(50),uuv(50),uww(50),uvv(50),
&vvw(50),vww(50)
dimension cocouv(50),cocouw(50),cocovw(50)
dimension flatu(50),flatv(50),flatw(50)
dimension skewu(50),skewv(50),skeww(50)
real*8 mom3u(50),mom3v(50),mom3w(50),mom4u(50),mom4v(50),
&mom4w(50)

```

```

common/stat2/h4,h5,h6,h7,ubar,vbar,wbar,usig,vsig,wsig,
&uv,uw,vw,uvw,uuw,uuv,uww,uvv,vvw,vww,cocouv,cocouw,
&cocovw,flatu,flatv,flatw,skewu,skewv,skeww,
&mom3u,mom3v,mom3w,mom4u,mom4v,mom4w
do 15 i=1,23
  rset(i)=0
15 continue
  ncount=0
  z=0.0e-16
  do 20 i=1,npts
    f3=vel(i,1)
    f5=vel(i,2)+(1-proc2)
    f7=vel(i,3)+(1-proc3)
    f8=tbd(i)
    if(i.eq.1)f8=0
    dfc=3.4399
    dfo=3.4399
    f7c=f7*dfc/dfo
    tt=f8+tt
    if(abs(ubar(n)-f3).gt.stdu)f3=z
    if(abs(vbar(n)-f5).gt.stdv)f5=z
    if(abs(wbar(n)-f7c).gt.stdw)f7c=z
    if(iyfile.eq.1)write(yfile,*)i,f3,f5,f7c,f8/1e6,tt/1e6
    if((f3.eq.z).or.(f5.eq.z).or.(f7c.eq.z))go to 20
    if(abs(f3).lt.1e-15)f3=0.0
    if(abs(f5).lt.1e-15)f5=0.0
    if(abs(f7C).lt.1e-15)f7C=0.0
    ncount=ncount +1
    U=f3
    V=f5-(1-proc2)
    W=f7c-(1-proc3)
    Uiu=Uiu+U
    Viu=Viu+V
    Wiu=Wiu+W
    Ui2=Ui2+(U**2)
    Vi2=Vi2+(V**2)
    Wi2=Wi2+(W**2)
    UiVi=UiVi+(U*V)
    UiWi=UiWi+(U*W)
    ViWi=ViWi+(V*W)
    UiViWi=UiViWi+(U*V*W)
    UiUiWi=UiUiWi+(U*U*W)
    ViViWi=ViViWi+(V*V*W)
    UiViVi=UiViVi+(U*V*V)

```

```

    UiUiVi=UiUiVi+(U*U*V)
    UiWiWi=UiWiWi+(U*W*W)
    ViWiWi=ViWiWi+(V*W*W)
    Ui3=Ui3+(U**3)
    Vi3=Vi3+(V**3)
    Wi3=Wi3+(W**3)
    Ui4=Ui4+(U**4)
    Vi4=Vi4+(V**4)
    Wi4=Wi4+(W**4)
20 continue
    return
end

block data
integer yfile
common /unit/yfile,ista,imis,ipl1,ipl2,ipl3,iyfile
data ista,imis,ipl1,ipl2,ipl3,iyfile/6*0/
end

```